

Copyright
by
Sandra Allison Bruce
2017

The Dissertation Committee for Sandra Allison Bruce
certifies that this is the approved version of the following dissertation:

**The Interaction of Solid-Density Nano-Scale Clusters
with High-Intensity XUV Laser Pulses**

Committee:

Todd Ditmire, Supervisor

John Keto, Co-Supervisor

Roger Bengtson

Michael Becker

Bjorn Hegelich

**The Interaction of Solid-Density Nano-Scale Clusters
with High-Intensity XUV Laser Pulses**

by

Sandra Allison Bruce

DISSERTATION

Presented to the Faculty of the Graduate School of
The University of Texas at Austin
in Partial Fulfillment
of the Requirements
for the Degree of

DOCTOR OF PHILOSOPHY

THE UNIVERSITY OF TEXAS AT AUSTIN

August 2017

Dedicated to my parents, Robert and Morita Bruce, who encouraged me to approach the world with a scientific mindset, and to my fiancé, Juan Domínguez, who never stopped picking me up, dusting me off, and pointing me forward.

Acknowledgments

I wish to thank the multitudes of people who helped me to complete this work. Most prominently, I need to thank the UT professors whose help and guidance made this work possible, especially my co-advisors Todd Ditmire and John Keto. Professor Ditmire recruited me to UT with the promise of interesting and challenging work in a world-class laser lab, and that was definitely a promise kept. And I cannot imagine how my experiments would have progressed without the continued interest in my progress shown by Professor Keto. I would also like to thank the other members of my committee, Professors Bengtson, Hegelich, and Becker, for their time, their help, and their support.

Thank you also to the rest of the staff of the Center for High Energy Density Science: Gilliss Dyer, Michael Donovan, Aaron Bernstein, Li Fang, Mikael Martinez, Erhard Gaul, and especially to Hernan Quevedo. Every member of the CHEDS staff offered me quite a bit of guidance and assistance in my journey through these experiments, and I am very grateful. Hernan, specifically, spent many hours in THOR and out, helping to troubleshoot, to parse through confusing results, and generally keeping an eye on everything and helping things to run smoothly.

Likewise, the students of CHEDS were instrumental in my progress. I

would specifically like to thank Ahmed Helal, Matt McCormick, In Tai Kim, and Joel Blakeney, for introducing me to the THOR laser system, and allowing themselves to be dragged into the THOR lab countless times to help with a complicated alignment process or laser maintenance. These senior students were my mentors when I was a brand new student, and the lessons they taught me were invaluable. Additionally, Ahmed and I worked together for many long days to rebuild and realign THOR, learn the quirks of the new HHG beamline, and perform the first experiments with the new setup. The work described here came as an outgrowth of his successful experiments, as hopefully the work following, done by Thanh Ha, will build on mine. Thanh also invested quite a lot of time helping to take this data, and for that I am very grateful.

I would also like to express my gratitude to the technical staff of the RLM third floor. To Allan Schroeder of the RLM machine shop, and all members of his staff, especially Kenny Schneider, Danny Boyd, and Jay Campbell, who manufactured so many parts for my research, as well as Jack Clifford of the student machine shop. They were patient and helpful when my designs went awry, always excited to attempt new and complicated designs, and they saved me many times when I was very short on time. To Ed Baez in the cryo shop, who kept me supplied with compressed gas, distilled water, and liquid nitrogen, leak tested my equipment, fixed our vacuum pumps, and was always willing to answer a barrage of “dumb questions.” It’s no exaggeration to say that THOR wouldn’t have run at all without him. To Gary Thomas and Robert Hasdorff of the electronics shop, who helped troubleshoot electri-

cal components both big and small. Whenever I had an issue with equipment in my lab, my first stop was always on the third floor.

I also need to thank Adam Kennedy in the Welch glass shop, for helping to design and for hand-crafting the particle beds and ablation cells used in my nanoparticle generation experiments.

The RLM and Zone 2 facilities and maintenance staff certainly deserve a mention here, especially Robert Soto, for responding quickly and efficiently time and time again to my water and air temperature emergencies in the lab.

And last, but certainly not least, I need to thank my family, to whom this work is dedicated: my mom and dad, and my fiancé, Juan Domínguez. They kept me sane and kept me motivated, and without their support, I doubt I could have made it this far.

The Interaction of Solid-Density Nano-Scale Clusters with High-Intensity XUV Laser Pulses

Publication No. _____

Sandra Allison Bruce, Ph.D.
The University of Texas at Austin, 2017

Supervisors: Todd Ditmire
John Keto

Studies of the interaction between high intensity, high frequency pulsed lasers and nano-scale material have a broad range of potential applications, from ultrafast biomolecular imaging to fundamental questions of the time scales associated with molecular electronic processes. “Table-top” XUV lasers utilizing HHG to produce a broad range of photon energies are a promising new source of this ultrafast high frequency radiation. Here, we present data generated by the irradiation of nano-scale cluster targets, composed of both solids and van der Waals-bound gases, by high-intensity XUV pulses generated using the new HHG beamline of the UT THOR laser system. On-target intensities are $\sim 1 \times 10^{13}$ W/cm², and photon energies range from 26.4 eV to 32.6 eV. These interactions consistently produce anomalously high charge states in the loosely-bound dense gas clusters; charge states of Xe⁸⁺, Kr⁶⁺, Ar⁵⁺, Ne³⁺, and N²⁺ were observed. The yield ratios of these charge states, as

well as the ion and electron kinetic energies collected during these interactions, help to shed light on the processes of formation and dissociation of these dense plasmas.

Table of Contents

Acknowledgments	v
Abstract	viii
List of Tables	xiv
List of Figures	xv
Chapter 1. Introduction	1
Chapter 2. Laser-Matter Interaction	6
2.1 Keldysh Parameter	7
2.2 $\gamma \ll 1$	8
2.3 $\gamma > 1$	10
2.4 $\gamma \gg 1$	11
Chapter 3. Plasma Theory	12
3.1 Debye Shielding	13
3.2 Plasma Coupling	15
3.3 Collisions in a Plasma	16
3.3.1 Coulomb (Elastic) Collisions	17
3.3.2 Inelastic Collisions	22
Chapter 4. Cluster Theory	25
4.1 Enhanced Photon Absorption in Clusters	26
4.2 Continuum Lowering in High-Density Plasmas	27
4.2.1 Ion Sphere Model	28
4.2.2 Ecker Kröll Model	32
4.2.3 Stewart Pyatt Model	33

4.2.4	Spectroscopic IPD	35
4.3	Inner and Outer Ionization	37
4.4	Conduction Bands and Solid State Phenomena	41
4.5	Cluster Dissociation	44
4.5.1	Coulomb Explosion	44
4.5.2	Hydrodynamic Explosion	46
4.6	Formation of Condensed Gas Clusters	47
4.7	Formation of Metal and Metal Oxide Clusters	50
4.7.1	Laser Ablation of Microparticles	51
4.7.2	Virtual Impactors and Gas Flows	51
Chapter 5. The THOR Laser		55
5.1	The Front End	58
5.1.1	Oscillator	59
5.1.2	Stretcher	60
5.1.3	Fiber	62
5.2	OPCPA	66
5.2.1	Parametric Amplification	66
5.2.2	Benefits and Drawbacks of OPCPA	72
5.2.3	The Design and Construction of THOR's OPCPA	74
5.3	Ti:Sapph Multipass Amplifiers	83
5.3.1	6-Pass Amplifier	83
5.3.2	5-Pass Amplifier	86
5.4	Compression	92
5.4.1	Transform Limited Compression	93
5.4.2	The THOR Compressor	96
5.4.3	Second-Order Autocorrelator	98
5.4.4	Aligning the Compressor	102
Chapter 6. High-Order Harmonic Generation		109
6.1	Theory	111
6.2	THOR HHG Beamline	116
6.3	HHG Optimization	121

Chapter 7. Experimental Setup	123
7.1 XUV Target Chamber	124
7.2 XUV Focusing Mirrors	129
7.3 On-Target Beam Characteristics	130
7.4 ToF Spectrometer	134
7.5 LAM Setup	138
7.5.1 Particle Bed	139
7.5.2 Cascaded Virtual Impactor Assembly	140
7.5.3 Ablation Cell	145
7.5.4 Supersonic Nozzle	148
7.6 Cluster Gas Jet	148
Chapter 8. Results	153
8.1 Nanoparticles	156
8.1.1 Oxygen-Containing Molecular Cluster Data	156
8.1.2 Irradiation with Intense 800 nm Pulses	161
8.1.3 Irradiation with XUV	177
8.1.4 Solid Targets Mounted on Glass	178
8.2 Noble Gas Clusters	188
8.2.1 High Charge-to-Mass Ratio Resolution	191
8.2.2 Detection of High Ion Charge States	195
8.2.3 High Ion Charge States Independent of Cluster Size	200
8.2.4 Sensitivity of Ion Charge States to Photon Energy	212
8.2.5 Cluster Peak Kinetic Energies	227
8.2.6 Ion Kinetic Energy Profiles	237
8.2.7 Electron Kinetic Energy Profiles	245
8.3 Nitrogen Clusters	264
Chapter 9. Conclusions	273
9.1 Solid Targets	274
9.2 High Charge States	275
9.3 Mechanism of Ionization	278
9.4 Continuum Lowering	283

9.5 Cluster Dissociation	284
9.6 Photoelectron Behavior	288
Chapter 10. Future Work	290
Appendices	291
Appendix A. Far Field Analysis of the Astigmatic Beam Out of the THOR Compressor	292
Appendix B. Standard Operating Procedure for LAM Nanopar- ticle Generator	311
Appendix C. Calculation of Flows and Microparticle Diameters	345
Index	348
Bibliography	350
Vita	368

List of Tables

4.1	Conduction band of liquid density noble gases [54, 81, 88] . . .	41
4.2	Cohesive energy of cluster materials used in these experiments [55].	43
4.3	Estimates of characteristics of “magic number” clusters, composed of a given number of complete shells m	48
4.4	K_{ch} parameters for the gases used in this text.	49
7.1	Properties of the cascaded virtual impactor assembly	142
8.1	Photoionization cross sections of noble gases, in Mb [79] . . .	190

List of Figures

2.1	in the $\gamma \ll 1$ regime, the intensity of the laser field is sufficient to distort the Coulomb barrier binding an electron to its parent atom for long enough for an electron to have a reasonable probability of tunneling out of the well (left, tunneling ionization), or in even higher intensities, of suppressing the barrier below the electron energy altogether. Figure from [6]	9
3.1	Cross-sections for electron-electron Coulomb scattering, taking small angle collisions (blue) and large angle collisions (red) into account. The total cross section is shown in gold.	19
3.2	Cross-sections for electron-electron (blue) and electron-ion (red) Coulomb scattering. The total of the two cross sections is shown in gold.	20
3.3	Cross-sections for total electron Coulomb (blue) and electron-neutral (red) scattering. The total of the two cross sections is shown in gold.	21
3.4	Mean free paths for elastic electron scattering through liquid density noble gases, using the total scattering cross sections from Figure 3.3 and the liquid densities of the respective gases. Cross sections include small and large angle Coulombic scattering from ions and electrons, but are dominated by scattering with neutrals, as given by Szmytkowski et al. [92].	22
3.5	Cross sections for electron impact ionization of liquified rare gases. Figure from Reference [81].	24
4.1	Predicted levels of continuum lowering from the ion sphere model as a function of charge state for different values of Z^* (top), and the corresponding effect on the ionization potential of Xe (bottom). The density used in these calculations corresponds to the density of liquid Xe.	31
4.2	Predicted levels of continuum lowering from the ion sphere (solid lines) and Ecker-Kröll (dashed line) models as a function of charge state for different values of Z^* . The density used in these calculations corresponds to the density of liquid Xe, and the electron temperature used was 10 eV.	33

4.3	Predicted levels of continuum lowering from the Stewart-Pyatt model as a function of charge state for different values of Z_p . The density used in these calculations corresponds to the density of liquid Xe, and the Debye length was estimated for an electron temperature of 10 eV.	34
4.4	Simulation of cluster potentials as a function of radial position during the process of charge buildup in an Ar cluster of 10,000 atoms (bottom), along with the electron kinetic energy spectrum associated with the specified outer ionization level (top).	39
4.5	Total number of electrons predicted to be outer ionized and ejected from an Ar cluster (blue lines), versus inner ionized (orange lines) as a function of cluster sizes. At small cluster sizes, (a), the number of ejected electrons is limited by the total number of atoms predicted to be photoionized in a cluster of the given size. However, at large cluster sizes, (b), the total number of outer ionized electrons is limited entirely by the charge buildup on the cluster. The overwhelming majority of photoionization events result in inner ionization.	40
4.6	Predicted potential felt by an electron near the surface of a Ne or He cluster. V_0 is the (positive) potential with respect to vacuum of the conduction band in these unusual materials. Figure from Reference [87].	42
4.7	Maximum Coulomb energy expected if all electrons were outer-ionized, as a function of cluster size for different species of noble gas clusters, illuminated with the 21 st harmonic wavelength (32.6 eV light of fluence 0.028 J/cm ²).	45
4.8	Basic design of a traditional impactor and a virtual impactor, for sorting microparticles by size. Figures from Reference [18].	53
5.1	A schematic layout of the front end (oscillator, stretcher, and amplifiers) of the THOR laser	57
5.2	The front-end oscillator for the THOR laser	59
5.3	(a) THOR's three-piece stretcher grating in its mount. (b) Ray trace diagram of the THOR stretcher (Figure from Reference[31]). Numbers indicate the beam position at each reflection.	61
5.4	(a) A spatial profile of the oscillator beam taken before sending the beam through THOR's optical fiber. (b) A spatial profile taken directly after the fiber output, demonstrating a nearly Gaussian profile.	65

5.5	Far field collimation measurements taken after final adjustment of the fiber output collimation optics. The output beam was directed through a 40 cm focal length lens, and then images were captured (a) 2 cm in front of the focus, (b) at the focus, and (c) 2 cm behind the focus, using 10x magnification. We were able to successfully eliminate astigmatism from this portion of the laser.	65
5.6	Cartoon energy level diagram of the DFG process used in the THOR OPA.	67
5.7	Collinear phase matching wave vector diagram	69
5.8	Collinear phase matching wave vector mismatch as a function of beam angles with respect to the optic axis	70
5.9	Noncollinear phase matching wave vector diagram	71
5.10	Noncollinear phase matching wave vector mismatch as a function of the pump beam angle θ with respect to the optic axis and the angle between the pump and signal beams, α	72
5.11	Curves of optimal values of noncollinear angle α as a function of crystal phase matching angle θ , for different wavelengths, setting $\Delta k = 0$	75
5.12	Small signal parametric gain for small deviations from the optimal values in (a) crystal phase-matching angle θ and (b) noncollinear angle α	77
5.13	Temporal profile of the Continuum pump laser, seeded (green) versus unseeded (blue), as viewed with a fast photodiode. Seeding should result in a reduction of buildup time and a stable, single-mode temporal profile.	78
5.14	Streak camera images of pulses from the Continuum OPCPA pump laser. (a) Viewing the entire duration of the pump beam reveals a “bullet” shape, common in seeded Q-switched lasers such as this one, where the center of the beam appears before the edges in time. (b) A sample of the leading center portion of the pulse, zoomed in to a 1 ns duration streak. With this temporal resolution, we can see temporal modulation in the beam which could imprint themselves in the amplified OPCPA pulse spectrally. (c) A much smoother temporal profile achieved by temperature tuning the Continuum’s seed laser, adjusting its wavelength.	81
5.15	Measurements and simulations done on the amplified output of the 6-pass after converting the 4-pass amplifier to a 6-pass (Figure from Reference [62]). Note that at the time, the output of the OPCPA used to seed the 6-pass, was lower than at the time of publication of this document. Even so, we see the effects of saturation on the output energy.	84

5.16	Damage to the 6-pass Ti:Sapph crystal, caused by deposition of indium onto the surface. What started out as damage around the top edge of the crystal eventually resulted in a full pump beam imprint in the center.	86
5.17	Concentric diffraction rings in the unamplified seed beam after transmission through all 5 passes of the final Ti:Sapph amplification stage. The image is made using a common alignment tool in THOR: an IR-fluorescent “magic wand” tool. (a) Seed beam from the 6-pass amplification stage is unamplified in the 5-pass (the Ti:Sapph crystal is not being pumped). (b) Seed beam being pumped by all three pump beams in the 5-pass, and amplified by the Continuum residual energy (PRO lasers mistimed, not amplifying the beam). (c) Seed beam as in (b), after passing through the spatial filter at the output of the 5-pass amplification stage.	88
5.18	Spectrum of the THOR laser at all stages of amplification. . .	91
5.19	Spatial profile of the beam into the compressor. (Note that the dark spots in the center portion of the beam are from dirt and damage on the camera setup capturing the image, and not on the beam itself.)	93
5.20	(a) Spectra for an example day from the oscillator, after the OPA front end amplifier, and at the output of THOR, after the 5-pass amplifier. (b) Transform-limited temporal pulse shapes for these spectra.	95
5.21	Ray trace diagram of the THOR compressor (Figure from Reference [31]). The setup includes a single large grating, over which the beam passes four times, translated each time by the vertical or horizontal rooftop mirror. Path length through the compressor is adjusted by changing the distance between the horizontal rooftop mirror and the grating.	97
5.22	Camera image of the four bounces of the beams off of the THOR compressor grating. The left two bounces are while the beam is spread spatially into its frequency components, providing a visual diagnostic of the current spectrum of the beam entering the compressor. The top-right spot is the fully compressed beam, which can damage the grating over time. This image was taken before the grating was rotated 180 degrees, to move the main damage spot from the main beam path, as described in Section 5.4.4	98

5.23	(a) The raw camera image from the THOR autocorrelator camera. This image is then captured by a LabVIEW program, shown in (b), and a lineout profile is displayed for the user-selected part of the image. A FWHM calculation is done on the lineout, and the deconvolved FWHM is given as an on-shot measurement or as part of a running average. To facilitate quick compression optimization, this FWHM is also plotted at the bottom of the screen, as the information for each shot arrives.	101
5.24	Image of THOR's compressor grating after rotation, with both damage spots visible - the original on the bottom left, and the new damage/clean spot on the top right.	104
5.25	Layout for testing the parallelism of the horizontal retroreflector without removing it from its place in the compressor chamber.	106
6.1	Typical spectral profile shape of HHG, including a perturbative regime of harmonics up to about the 9 th harmonic, a long, flat plateau, and a cutoff energy of $h\nu_{cut} = I_p + 3.17U_p$, as described in Section 6.1. Figure from Ref [46].	110
6.2	An illustration of the three-step model for HHG generation. First, the slowly-oscillating electric field of a laser induces tunnel ionization. The ejected electron is accelerated by the field back toward the parent ion. Recollision results in the emission of high-frequency harmonics, corresponding to the ultimate kinetic energy of the electron upon recombination. Figure from Ref [75].	112
6.3	Effects of a curved phase front on HHG generation. From Ref [75].	115
6.4	Beam profile of the annular THOR beam after the pickoff mirror. The outer "donut maker" iris was also used to create a circular outer edge. In later experiments, this outer iris was not used, as it did not improve the XUV conversion efficiency. . .	117
6.5	Beam profile of the focus under the HHG gas jet, with the pickoff mirror in place.	118
6.6	The output of the compressor, switched toward the HHG beamline	119
6.7	The $f/200$ loose focus beamline to the HHG-generating Ar gas jet	119
6.8	Foil holder, for 200 nm meshless foil.	120

7.1	The experimental setup in the HHG beamline and XUV target chamber [46]. Harmonics are generated and separated from the fundamental frequency as described in Chapter 6. The desired harmonic is selected and focused onto a target as described in Figure 7.2. Gas cluster and nanoparticle targets are generated in a differentially pumped section of the XUV target chamber, referred to as “the chilipot.” Targets generated in this region must pass through a collimating skimmer before entering the main target chamber.	125
7.2	The experimental setup in the XUV target chamber, as viewed from above. Harmonics of sufficient energy to be transmitted through the Al foil filter pass into the target chamber, and the desired harmonic is selectively reflected and focused by a custom-coated multilayer mirror onto the desired target, in the collection region of a Wiley-McLaren ToF spectrometer. Light not absorbed in the interaction passes to an XUV-sensitive photodiode, providing an on-shot energy measurement.	126
7.3	The experimental setup in the XUV target chamber, as viewed from a windowed port on the side of the chamber. The chilipot, concealing the top skimmer, ToF spectrometer, the lower skimmer, and the XUV photodiode are shown.	128
7.4	Photo-response curve for Opto Diode IRD-AXUV575c photodiode. Figure from [46].	129
7.5	On-target photon energy spectrum reflected by the 17 th harmonic mirror (#3). This data was extracted from a Xe photoelectron spectrum.	130
7.6	Transform-limited temporal pulse profile of the spectrum from Figure 7.5.	131
7.7	Photograph of the physical setup used for the knife edge measurement of beam spot size.	132
7.8	Measurement (blue line) and fit (red dashed line) for the focus of the knife edge measurement of beam spot size. The $1/e^2$ radius for this measurement was 6.4 μm	133
7.9	A cartoon diagram of our time-of-flight	134
7.10	A CAD model of our Wiley-McLaren time-of-flight spectrometer [46]	137
7.11	The LAM apparatus, mounted on the XUV target chamber.	139
7.12	The particle bed for the LAM apparatus. Microparticles are shaken by an unevenly-weighted motor, to maintain fluidity, and a buffer gas is blown from below the particles, to entrain particles in the gas for transport to the virtual impactor assembly.	140

7.13	Diagram of the two-stage virtual impactor used in this work. Figure modified from [41].	141
7.14	The results of using the cascaded virtual impactor on spherical microparticles with a nominal diameter of 1-2 μm . Sub-figures (a) and (c) are SEM images of particles impacted from the entrained microparticle flow, taken before and after the virtual impactors, respectively. Sub-figures (b) and (d) show a histogram of the average particle area, obtained from the SEM images. The medium and large agglomerates which dominate the un-sorted flow are filtered out by the assembly.	144
7.15	Improved ablation cell for nanoparticle generation. The design protect the sides of the ablation cell from becoming damaged by the ablation laser. Entrained microparticle/nanoparticle flows are shown in orange, collimating buffer gas flows in blue, and the path of the ablation laser is shown in green.	146
7.16	Ablation cells displaying the signs of proper microparticle flow and ablation laser alignment. (a) The scattering of the ablation laser at a low energy is viewed by a camera. Scattering is visible from the walls of the ablation cell and the microparticle stream itself. (b) A 532 nm-blocking filter is applied to the camera, and the ablation laser power is increased. Fluorescence from microparticle ablation is clearly visible.	147
7.17	Top/side and pure side view of gas net nozzle used to make target gas clusters.	149
7.18	Diagram of the concentric cooling scheme briefly employed. . .	151
7.19	Heights of the central atomic cluster peak of Ne^+ , as well as the front cluster peaks of Ne^+ and Ne^{2+} , as a function of XUV laser timing with respect to the gas jet trigger. Ne gas jet backing pressure was 40 psi, and the gas jet opening time was set to 1 ms.	152
8.1	Ion ToF data from different cluster sizes of CO_2 , with major ion species labeled.	158
8.2	Ion ToF data from different cluster sizes of CO_2 , plotted as a heat map profile.	159
8.3	Ion ToF data from different cluster sizes of O_2 , with major ion species labeled.	160
8.4	Ion ToF data from different cluster sizes of O_2 , plotted as a heat map profile.	161
8.5	A typical ion ToF signal from N_2 buffer gas only, with no nanoparticles.	164

8.6	A typical ion ToF signal with Ag nanoparticles present in an N ₂ buffer gas. We can see Ag ⁺ , and Ag ²⁺ in this signal. Ag ²⁺ shows possible isotopes, with atomic-type peaks, while Ag ⁺ shows a more cluster-type of broad signal.	165
8.7	A typical signal with Ag nanoparticles present. The signatures for Ag ⁺ , and Ag ²⁺ are similar to those in Figure 8.6. Ag ²⁺ shows possible isotopes, with atomic-type peaks, while Ag ⁺ shows a more cluster-type of broad signal.	166
8.8	An example of a signal with a small amount of Ag ²⁺ , with a large enhancement in the H ⁺ signal as the most prominent sign that we have hit a nanoparticle cloud.	167
8.9	An example of a signal from a dense portion of a nanoparticle cloud, or a microparticle, which significantly disrupts the signal from the N ₂ buffer gas. In this signal, we see Ag ⁺ , and Ag ²⁺ , as well as a new cluster signal at 4 μs, and an enhancement of the H ⁺ signal, which are likely from the microparticles' anti-adhesive coating.	168
8.10	A signal from a dense nanoparticle cloud, with no apparent signal from the N ₂ buffer gas. We can see a signal from Ag ⁺ , atomic and cluster, as well as the cluster signal at 4 μs, as in Figure 8.9, and an additional signal at 8 μs.	169
8.11	A signal from a moderately dense nanoparticle cloud. The N ₂ ⁺ signal is still present, and we have a large atomic Ag ⁺ peak (with both isotopes visible), as well as an unusually-shaped cluster peak. The photon signal in this shot is extremely high, alluding to the high density of the Ag cloud.	170
8.12	A signal from a very dense Ag nanoparticle cloud. Again, we have atomic and cluster signal from Ag ⁺ (with isotopes visible), and the signal at 8 μs exhibits a similar profile. The signal at 4 μs, as well as the H ⁺ and photon peak enhancements, are prominent.	171
8.13	A signal from a dense nanoparticle cloud, showing Ag ⁺ , and then potentially Ag ²⁺ , as well as another signal at 8 μs and at 4 μs. As usual, we have a large H ⁺ peak and photon peak. . .	172
8.14	A signal which is most likely to be a microparticle signature. Note the broad Ag ⁺ peak, lacking any atomic peaks, as well as the extremely large photon peak, which causes ringing in the signal for a significant duration.	173

8.15	Signals from He buffer gas. Dotted lines corresponding to $m/q = 1$ (red), and $m/2 = 2$ and 4 (teal) mark the centers of each common species in the buffer gas. The signal common to all shots without nanoparticles is shown in the top panel. Two modified signals corresponding to two different shots with silver signatures are shown in the bottom two panels.	174
8.16	A trace from a relatively low density nanoparticle cloud, in a He buffer gas. Signals from Ag^+ and Ag^{2+} are present, as is the peak around 4 μs , which was also present in many nanoparticle shots formed in N_2 buffer gas. An additional atomic-type peak has emerged around 6 μs , which is suggestive of a water peak.	175
8.17	A common type of signal from a low-density portion of a silver nanoparticle cloud, showing a prominent Ag^+ peak, as well as an atomic-type peak which is most likely H_2O^+	176
8.18	A typical ion ToF signal from a silver microparticle, in He buffer gas.	177
8.19	Ion ToF m/q spectrum (top), and electron kinetic energy spectrum (bottom) from a 640 μm diameter copper wire. In the top plot, ion species, when known, or estimated m/q is labeled for major peaks.	180
8.20	Ion ToF m/q spectrum (top), and electron kinetic energy spectrum (bottom) from a 200 nm thick copper foil. In the top plot, ion species, when known, or estimated m/q is labeled for major peaks.	181
8.21	Ion ToF m/q spectrum from a 115 nm thick gold foil. No gold ions are present. The trace shows nearly perfect species overlap with Figure 8.20, suggesting that the ions identified as Cu^+ may have actually been surface contaminants.	182
8.22	Ion ToF m/q spectrum (top), and electron kinetic energy spectrum (bottom) from a grid of 5 nm silver nanoparticles written into 10 nm wide wires on a glass substrate. No silver ions are identified. In the top plot, ion species, when known, or estimated m/q is labeled for major peaks.	184
8.23	ToF m/q spectrum from a single-layer film of 5 nm silver nanoparticles on a glass substrate. No silver ions are identified. Ion species, when known, or calculated m/q is labeled for major peaks.	185
8.24	Ion ToF m/q spectrum (top), and electron kinetic energy spectrum (bottom) from Sb and Te microparticles deposited onto a glass slide. No ions from these target microparticles are identified. In the bottom plot, the red lines mark energies from 10 eV to 100 eV, in 10 eV steps.	187

8.25	Height of atomic and front cluster peaks of Ne clusters as a function of gas jet trigger timing with respect to the XUV laser pulse. The x-axis represents laser pulse delay with respect to the detectable beginning of the gas jet (actual gas jet trigger timings are indicated with arrows). A steady state situation, where both atomic and cluster peak heights level out occurs at 810 μ s after the front of the gas jet is detected. Data was taken with the 21 st harmonic mirror, at a backing pressure of 40 psi ($\langle N \rangle = 200$).	189
8.26	ToF m/q spectrum of Xe, cropped to show the Xe ²⁺ uncondensed atomic peak, taken with the 21 st harmonic mirror. All stable isotopes are labeled. The average cluster size for this data set was 200,000 atoms.	192
8.27	ToF m/q spectrum of Xe, cropped to show the Xe ⁺ uncondensed atomic peak, taken with the 21 st harmonic mirror. All stable isotopes are labeled. The average cluster size for this data set was 7,000 atoms. In contrast with Figure 8.26, this data is shown on a log scale, to show that we observe the ¹²⁴ Xe and ¹²⁶ Xe isotopes with natural abundances of 0.095% and 0.089% respectively.	193
8.28	ToF m/q spectrum of Ar, taken with the 21 st harmonic mirror. All major peaks are labeled. The average cluster size for this data set was 1,000 atoms.	194
8.29	ToF m/q spectrum of Ne at $\langle N \rangle = 1,000$, taken with the 17 th harmonic mirror. Front cluster peaks of Ne ions are labeled by charge state.	196
8.30	ToF m/q spectrum of Ar at $\langle N \rangle = 80,000$, taken with the 21 st harmonic mirror. Front cluster peaks of Ar ions are labeled by charge state.	198
8.31	ToF m/q spectrum of Kr at $\langle N \rangle = 90,000$ (blue), taken with the 21 st harmonic mirror. The gold data set is the chamber background signal.	199
8.32	ToF m/q spectrum of Xe, taken with the 21 st harmonic mirror (blue), and chamber background signal (red). For this data set, we accumulated 40,000 shots of Xe, using the higher plate voltage settings. Front cluster peaks of Xe ions are labeled by charge state.	200
8.33	ToF m/q spectrum of Ne at two different cluster sizes, $\langle N \rangle = 200$ (red) and $\langle N \rangle = 1,000$ (blue), taken with the 17 th harmonic mirror. Data is shown cropped in y, log scale (top), and full-scale linear scale (bottom).	202

8.34	ToF m/q spectrum of Ar at different cluster sizes, taken with the 21 st harmonic mirror, presented as a log-scale waterfall plot.	204
8.35	ToF m/q spectrum of Kr at different cluster sizes, taken with the 21 st harmonic mirror, presented as a log-scale waterfall plot.	205
8.36	ToF m/q spectrum of Kr at different cluster sizes, taken with the 21 st harmonic mirror, as shown in Figure 8.35, presented overlaid for direct comparison. Cluster sizes are $\langle N \rangle = 5,000$ (red), 30,000 (teal), 90,000 (blue), and 200,000 (purple). The gold data set is the chamber background signal.	206
8.37	Heights of the front cluster Coulomb peaks at different ionic charges from Kr m/q spectra in Figure 8.36, revealing (a) absolute and (b) relative yields ToF m/q spectrum of Kr at different cluster sizes, taken with the 21 st harmonic mirror.	208
8.38	ToF m/q spectrum of Xe at different cluster sizes, taken with the 21 st harmonic mirror.	209
8.39	ToF m/q spectrum of Xe at different cluster sizes, taken with the 21 st harmonic mirror, as shown in Figure 8.38, presented overlaid for direct comparison. Cluster sizes are $\langle N \rangle = 7,000$ (blue), 20,000 (orange), 90,000 (gold), and 200,000 (purple).	210
8.40	Heights of the front cluster Coulomb peaks at different ionic charges from Xe m/q spectra in Figure 8.39, revealing (a) absolute and (b) relative yields ToF m/q spectrum of Xe at different cluster sizes, taken with the 21 st harmonic mirror.	211
8.41	ToF m/q spectrum of Ne at $\langle N \rangle = 200$, taken with the 17 th (blue) and 21 st (red) harmonic mirror at comparable on-target intensities. It seems that the ionization of the clusters increases at the lower photon energy.	213
8.42	ToF m/q spectrum of Ne at $\langle N \rangle = 200$, taken with the 17 th (blue) and 21 st (red) harmonic mirror at comparable on-target intensities. This plot differs from Figure 8.41 in that it is zoomed in and plotted on a log scale, in order to best display the high charge states. Here, we can see that if we look primarily at the “forward cluster peak,” the signals from the two photon energies are very similar, especially at the higher charge states.	214
8.43	ToF m/q spectrum of Ar at $\langle N \rangle = 30,000$, taken with the 17 th (blue) and 21 st (red) harmonic mirror at comparable on-target intensities. It seems that the ionization of the clusters increases at the lower photon energy. This figure follows the same pattern as Figure 8.41.	215

8.44	ToF m/q spectrum of Ar at $\langle N \rangle = 30,000$, taken with the 17 th (blue) and 21 st (red) harmonic mirror at comparable on-target intensities. This plot differs from Figure 8.43 in that it is zoomed in and plotted on a log scale, in order to best display the high charge states.	216
8.45	ToF m/q spectrum of Ar at $\langle N \rangle = 1,000$, taken with the 17 th (blue) and 21 st (red) harmonic mirror at comparable on-target intensities. The ratios of the front peaks of Ar ²⁺ to Ar ⁺ are the same, 0.2, for the two photon energies, even though the total yield is much higher for the 26 eV 17 th harmonic photons. . .	217
8.46	ToF m/q spectrum of Ar at $\langle N \rangle = 1,000$ (blue), 30,000 (orange), 70,000 (gold), and 200,000 (purple), taken with the 17 th harmonic mirror. Total yield grows much more quickly with illumination from the 17 th harmonic than the 21 st , rapidly expanding the width of the cluster shoulders, and making high charge states indistinguishable from each other.	218
8.47	ToF m/q spectrum of Ar at $\langle N \rangle = 1,000$ (blue), 30,000 (orange), 70,000 (gold), and 200,000 (purple), taken with the 17 th harmonic mirror, zoomed in to show the overlapping shapes of the higher charge states. Total yield grows much more quickly with illumination from the 17 th harmonic than the 21 st , rapidly expanding the width of the cluster shoulders, and making high charge states indistinguishable from each other.	219
8.48	Heights of the front cluster Coulomb peaks at different ionic charges from Ar m/q spectra in Figures 8.46 and 8.47, showing (a) absolute and (b) relative yields ToF m/q spectrum of Ar at different cluster sizes, taken with the 17 th harmonic mirror. . .	220
8.49	ToF m/q spectrum of Kr at different cluster sizes, taken with the 17 th harmonic mirror. Compare to Figure 8.35. Note how smeared out the high charge states are, similar to those traces from much larger cluster sizes taken with the 21 st harmonic mirror.	221
8.50	ToF m/q spectrum of Xe at $\langle N \rangle = 200,000$ (blue), compared to a background spectrum (red), taken with the 17 th harmonic mirror. Front cluster peaks of Xe are labeled. These spectra are taken at the alternate, higher ToF grid voltages, as in Figure 8.32, which was taken with the 21 st harmonic mirror. We can see that the same high charge states are present when the clusters are illuminated with the lower energy photons.	222

8.51	ToF m/q spectrum of Xe at $\langle N \rangle = 200,000$, taken with the 17 th (blue) and 21 st (red) harmonic mirror at comparable on-target intensities. The higher charge states have slightly lower proportional yield in the 17 th harmonic data, although the two data sets seem to overlap very well in general.	223
8.52	ToF m/q spectrum of Xe at $\langle N \rangle = 90,000$, taken with the 17 th (blue) and 21 st (red) harmonic mirror at comparable on-target intensities. Similarly to Figure 8.51, the higher charge states at this smaller cluster size have slightly lower proportional yield in the 17 th harmonic data, although the two data sets seem to overlap very well in general.	224
8.53	ToF m/q spectrum of Xe at $\langle N \rangle = 10,000$ (blue), 90,000 (orange), and 200,000 (purple), taken with the 17 th harmonic mirror, cropped to show only the Xe ⁺ and Xe ²⁺ peaks, including the cluster “wings”. This plot shows well how the “back cluster wing” is much more strongly affected by increasing cluster size than the “front cluster wing.”	225
8.54	Heights of the front cluster Coulomb peaks at different ionic charges from Xe m/q spectra in Figure 8.53, showing (a) absolute and (b) relative yields ToF m/q spectrum of Xe at different cluster sizes, taken with the 17 th harmonic mirror.	226
8.55	ToF m/q spectrum of Xe at $\langle N \rangle = 200,000$, taken with the 17 th harmonic mirror. The top plot shows the entire trace on a linear scale, with an inset highlighting the shape of the front cluster peak. The bottom plot expands this highlighted section to show the Xe ⁺ front cluster peak, as well as the entire Xe ²⁺ peak, including front, central atomic, and back peak.	229
8.56	ToF m/q spectrum of Xe at $\langle N \rangle = 200,000$, taken with the 17 th harmonic mirror, zoomed in to show the isotope peaks present in the Xe ⁺ front cluster peak. Data is the same as shown in Figure 8.55. All peaks show an initial kinetic energy of 118.5 ± 1.5 eV.	230
8.57	ToF m/q spectrum of Xe at $\langle N \rangle = 200,000$, taken with the 21 st harmonic mirror. The top plot shows the entire trace on a linear scale, with an inset highlighting the shape of the front cluster peak. The bottom plot expands this highlighted section to show the Xe ⁺ front cluster peak, as well as the entire Xe ²⁺ peak, including front, central atomic, and back peak.	233
8.58	ToF m/q spectrum of Xe at $\langle N \rangle = 200,000$, taken with the 17 th (red) and 21 st (blue) harmonic overlaid. Data are the same as shown in Figures 8.55 and 8.57.	234

8.59	ToF m/q spectrum of Xe at multiple cluster sizes, taken with the 21 st harmonic mirror, zoomed in to show the Xe ⁺ front cluster peak and unclustered atomic peaks. Data is the same as shown in Figure 8.39. While the forward cluster peak occurs at exactly the same time on each trace, the atomic peaks gradually widen and move forward at larger cluster sizes.	235
8.60	ToF m/q spectrum of Kr at $\langle N \rangle = 200,000$, taken with the 21 st harmonic mirror, zoomed in to show the isotope peaks present in the Kr ⁺ , Kr ²⁺ , and Kr ³⁺ front cluster peaks.	236
8.61	Ar ion kinetic energy signatures, obtained with the 17 th harmonic laser energy. The constant-in-time background has been subtracted from these plots. Only the low-energy signals which are above the background level are plotted.	238
8.62	Kr ion kinetic energy signatures, obtained with the 17 th harmonic laser energy. The figure represents an overview of the trend of cluster size versus kinetic energy, with a scan over cluster sizes from $\langle N \rangle = 8,700$ to $\langle N \rangle = 150,000$, with each cluster size integrating only 200 shots.	239
8.63	Kr ion kinetic energy signatures, at a cluster size of $\langle N \rangle = 200,000$. While the maximum kinetic energies are similar for the two photon energies, the shapes of the two profiles are very different.	240
8.64	Xe ion kinetic energy signature, obtained with the 21 st harmonic laser energy, at a cluster size of $\langle N \rangle = 200,000$	241
8.65	Ne ion kinetic energy signatures, obtained with the 17 th harmonic laser energy.	242
8.66	Ne and Ar ion kinetic energy signatures, at the same cluster size ($\langle N \rangle = 1,000$) obtained with the 17 th harmonic laser energy.	243
8.67	Ne ion kinetic energy signatures, at varied cluster sizes, obtained with the 19 th harmonic laser energy.	244
8.68	Ne ion kinetic energy signatures, at varied cluster sizes, obtained with the 21 st harmonic laser energy.	245
8.69	Argon electron kinetic energy plots, taken with the 17 th harmonic mirror, at different cluster sizes. Data is shown on a linear (a) and log (b) scale. Signals are normalized to their photon peak, effectively normalizing by gas density.	247
8.70	Krypton electron kinetic energy plots, taken with the 17 th harmonic mirror, at two different cluster sizes. Signals are normalized to their photon peak, effectively normalizing by gas density.	248

8.71	Xenon electron kinetic energy plots, taken with the 17 th (blue) and 21 st (green) harmonic mirror, at large cluster size ($\langle N \rangle = 200,000$). Signals are normalized to their photon peak, effectively normalizing by gas density.	249
8.72	Neon electron kinetic energy plots, taken with the 17 th harmonic mirror, at small cluster size ($\langle N \rangle = 100$). The photoelectron peak from the 17 th harmonic is nearly entirely absent from the spectrum.	250
8.73	Ne, Ar, and Xe electron kinetic energy plots, taken with the 17 th harmonic mirror, at 20-30 psig of gas jet backing pressure. Signals are shown on a time, rather than energy, scale, so that their respective photon peaks are visible at $t=0$	252
8.74	Ne electron kinetic energy plots, taken with the 17 th harmonic mirror, at different gas jet backing pressures. Signals are normalized to their photon peak.	253
8.75	Ne electron kinetic energy plots, taken with the 19 th harmonic mirror, at different gas jet backing pressures. Signals are normalized to their photon peak.	255
8.76	Ne electron kinetic energy plots, taken with the 21 st harmonic mirror, at different gas jet backing pressures. Signals are normalized to their photon peak.	256
8.77	Ne electron kinetic energy plots, taken with the 19 th harmonic mirror, at different gas jet timings with respect to the XUV laser. This effectively varies the ratio of uncondensed atomic gas to clusters (the clusters being more prevalent in the center of the gas jet opening time than at the front). Data was taken at 20 psi backing pressure. Signals are normalized to their photon peak.	258
8.78	Ne electron kinetic energy plots, taken with the 17 th harmonic mirror, at different positions of the focusing mirror along the axis of the laser, decreasing the on-target fluence by increasing the laser-gas interaction volume. All data were taken at 50 psi backing pressure. Signals are normalized to their photon peak.	260
8.79	Ne electron kinetic energy plots, taken with the 19 th harmonic mirror, at different positions of the focusing mirror along the axis of the laser, decreasing the on-target fluence by increasing the laser-gas interaction volume. All data were taken at 50 psi backing pressure. Signals are normalized to their photon peak.	261

8.80	Ne electron kinetic energy plots, taken with the 21 st harmonic mirror, at different positions of the focusing mirror along the axis of the laser, decreasing the on-target fluence by increasing the laser-gas interaction volume. All data were taken at 50 psi backing pressure. Signals are normalized to their photon peak.	262
8.81	Ne electron kinetic energy plot, taken with the 19 th harmonic mirror. This data is also shown as the “Center” of the gas jet timing in Figure 8.77. A suggestive envelope is drawn with orange dotted line, which may yield additional hypotheses on the source of our anomalous electron kinetic energy spectra.	263
8.82	Dissociative photoionization cross-sections for N ₂ . Figure from Reference [78]. Cross-sections are 22.15 and 1.12 Mb for the N ₂ ⁺ and the N ⁺ pathway, respectively, for illumination with 17 th harmonic (26 eV) light. Cross-sections are 16.80 and 1.23 Mb for the N ₂ ⁺ and the N ⁺ pathway, respectively, for illumination with 21 st harmonic (33 eV) light	265
8.83	N ₂ ion kinetic energy signatures, obtained with the 21 st harmonic laser energy, for all cluster sizes investigated, including the large sizes in Reference [46].	266
8.84	N ₂ ion kinetic energy signatures, obtained with the 21 st harmonic laser energy. Similarities to Reference [78] allow us to identify the portions of the spectra which represent N ₂ ⁺ and which represent N ⁺	267
8.85	N ₂ ion kinetic energy signatures, obtained with the 17 th harmonic laser energy. The estimated constant-in-time background is plotted as a black dashed line. The estimated break point in the spectra between N ₂ ⁺ and N ⁺ are marked with arrows.	268
8.86	N ₂ ToF m/q spectra, illuminated by the 17 th and 21 st harmonics, at different cluster sizes. Notice that the clusters irradiated with the lower energy light source seem to behave like clusters approximately 5 times their size irradiated with the higher energy source.	269
8.87	N ₂ ToF m/q spectra, illuminated by the 21 st harmonic, at different cluster sizes, zoomed in to give a better view of branching ratios, as well as the presence of N ²⁺	270
8.88	N ₂ ToF m/q spectra, illuminated by the 17 th harmonic, at different cluster sizes, zoomed in to give a better view of branching ratios, as well as the presence of N ²⁺	271
8.89	ToF m/q spectrum of N ₂ at <N> = 3,000, taken with the 17 th (blue) and 21 st (red) harmonic mirror at comparable on-target intensities.	272

9.1	A comparison of xenon ion m/q time-of-flight spectra taken by Wabnitz et al. at a wide range of laser intensities (left) with similar data we took using the THOR XUV beamline at nearly 1×10^{13} W/cm ² at different cluster sizes [96]. Although the Wabnitz experiment used 12.7 eV photons at a fluence of about 7 J/cm ² , while we used 33 eV photons at about 0.028 J/cm ² , the data sets are strikingly qualitatively similar at similar intensities.	276
9.2	We observe high charge states, necessitating some amount of continuum lowering to produce, in each noble gas cluster species studied. Maximal observed charge states are (a) Ne ³⁺ , (b) Ar ⁵⁺ , (c) Kr ⁶⁺ , and (d) Xe ⁸⁺ .	277
9.3	Charge state abundances, determined by the relative heights of forward-going cluster peaks of different charge states for Xe ion m/q spectra, for cluster sizes of $\langle N \rangle = 90,000$ (gold squares) and $\langle N \rangle = 200,000$ (green diamonds). Two model fits for the yield ratios are also shown. The first model (red dot-dashed line) shows the result of a purely random distribution of “lost electrons” for an average ionization state of $Z^* = 1.1$, as might be expected if above-threshold single-photon ionization were dominant. The second model (blue dashed line) shows the results of a Saha distribution, with electron temperature of 8 eV and an average charge state of $Z^* = 1$.	281
9.4	Absolute (left column) and relative (right column) yields of different charge states of krypton (top row) and xenon (bottom row), at different cluster sizes. These data correspond to ionization by the 21 st harmonic.	283
9.5	Calculated average kinetic energies of individual isotopes within the forward-going cluster peaks of xenon ion m/q spectra, at different charge states. These data correspond to ionization by the 21 st harmonic.	286
9.6	Absolute (left column) and relative (right column) yields of different charge states of argon (top row) and xenon (bottom row), at different cluster sizes. These data correspond to ionization by the 17 th harmonic.	287
9.7	Simulated photoelectron kinetic energy spectra (top row) and the associated ultimate cluster potential as a function of radius (bottom row), resulting from different numbers of cluster photoionization events (columns left to right). Simulation is of an argon cluster of 10,000 atoms, irradiated with the expected incident photon spectrum reflected by our 21 st harmonic mirror.	288

Chapter 1

Introduction

Condensed gas clusters, defined as liquid density droplets of STP gases, with between 2 and about 10^6 atoms per cluster, as well as nanoparticles made from solid materials of the same size, are an exciting target for HED and plasma physics explorations. Clusters are unique in their interactions with high-intensity laser fields, as they represent an intermediary between solid and gaseous targets. Their liquid or solid density creates the conditions for high energy absorption, whether through large amounts of photoionization or by resonant heating mechanisms such as those discovered by Ditmire et al [23]. At the same time, their limited size prevents significant energy loss from a nanoplasma cluster to its surroundings. This creates the conditions for unusually energetic plasmas.

Clusters also serve as potential models for large molecules, or biological materials such as protein molecules or viruses. For material which does not crystallize on the large scale, X-ray diffraction imaging may still be possible if the light source is intense enough and fast enough that an image may be captured before the material dissociates. XFEL lasers are the obvious choice of light source for such an endeavor, and quite a bit of progress has been made

towards these goals [69, 84]. However, the energy absorption pathways, ionization methods, and explosion mechanisms, and their associated timescales, which all affect the feasibility of such studies, are still open questions of investigation. “Tabletop” XUV illumination from high-order harmonic generation is helping to provide answers. It shows a lot of promise for ultrafast imaging and control of atomic processes on a sub-femtosecond timescale [10], theoretically as short as 100 as [19].

The chain of events believed to occur during high-intensity XUV-induced ionization of dense clusters at photon energies between 20 and 50 eV is as follows:

1. Single photon photoionization begins to liberate electrons from the neutral clusters. These electrons have sufficient energy to leave the cluster environment entirely (referred to as outer ionization) [59].
2. Charge begins to build up on the cluster, creating an increased barrier potential for outer-ionized electrons [3, 83, 102].
3. Coulomb potential wells due to outer ionization begin to reduce the inter-atomic potential barriers, facilitating increased ionization [59, 102].
4. The charge buildup on the cluster is sufficient to trap photoionized electrons within the cluster boundaries (referred to as inner ionization) [3, 59, 77, 96].

5. Charge screening from inner-ionized electrons simultaneously reduces the Coulomb-induced ionization potential depression and contributes to screening-induced ionization potential depression [59, 86, 100].
6. Electron-neutral and electron-ion collisions create significant amounts of electron impact ionization within the cluster [65].
7. Three-body recombination/heating and the associated increase in photoionization raise the electron temperature within the cluster [53].
8. Evaporative emission from the thermalized inner-ionized electrons contributes a small amount of additional outer ionization [2, 3].
9. The positively charged outer layer(s) of large clusters (or the entire cluster, for smaller clusters), explodes in a Coulomb explosion, ejecting potentially high-energy ions [23, 35, 51, 102].
10. The nearly neutral inner core of larger clusters explodes hydrodynamically, with ions pulled by the expansion of the trapped, hot electrons [23, 51, 52].

In this work, we seek to explore the process of charge buildup, electron trapping, and continuum lowering in these dense clusters. We generate XUV light via high-order harmonic generation, and focus our chosen harmonic (in the range of 26.4 eV to 32.6 eV) onto nano-scale cluster targets. On-target fluences are $\sim 1 \times 10^{-2}$ J/cm², and on-target intensities are $\sim 1 \times 10^{13}$ W/cm².

Targets included silver nanoparticles as well as van der Waals-bound gas clusters. Our Wiley-McLaren time-of-flight spectrometer allows us to observe the final charge state distributions of cluster ions as well as ion and electron kinetic energies, potentially revealing contributions of continuum lowering and electron-ion recombination to the charge state distribution [3, 52], evidence of charge buildup and electron trapping [3, 14, 83], electron plasma temperatures [52], and signs of Coulombic and hydrodynamic ion expansion in the layers of “onion-like” clusters [3, 52].

Our photon energy and laser intensity put us in a rather unique regime, not common to the FEL systems which perform the majority of explorations of these high-density ionization and dissociation mechanisms. Our laser frequencies are presumably high enough to eliminate any significant contribution to the ionization by inverse Bremsstrahlung processes, but not high enough to turn on contributions from Auger ionization. Our moderate intensity allows us to rule out appreciable contributions from two-photon processes. Thus, we may probe the absorption, ionization, and dissociation of clusters within a greatly simplified environment with respect to laser-ionization dynamics.

Employing such a broad range of cluster targets allowed us to scan through the parameter space of cluster density, atom ionization potential, inter-atomic cohesive energy, and solid-density electronic structure. Solid nanoparticles represent a unique type of target for high-intensity XUV lasers. Metal nanoparticles, such as silver, might be expected to behave like a “pre-ionized” plasma, having a significant number of de-localized electrons to con-

tribute to charge screening even before photoionization occurs. Metal *oxide* nanoparticles, such as SiO₂, TiO₂, and SnO₂, should allow us to adjust the number of screening electrons in the plasma in a predictable way, while monitoring effects on the charge state distribution of a single species: the oxygen atoms. This could provide strong evidence for one particular model of continuum lowering over others, a topic of significant debate [21]. These solid oxide nanoparticles have distinct advantages over mixed gas clusters for such experiments, as they would have a known ratio and even distribution of atomic species throughout the cluster.

Employing a broad range of noble gas cluster targets may similarly shed light on the processes of continuum lowering in dense plasmas. The different species provide a wide distribution of sequential ionization potentials. A threshold effect, allowing the ionization to charge state q by illumination with 32.6 eV photons, and only state $(q - 1)$ with 29.5 eV or 26.4 eV (these energies being the span of available focusing mirror reflectivities available to us), would provide a precise value for the amount of IPD in this plasma regime. The lack of such an effect, along with a consistently high maximal charge state, such as we observed, suggests that this simplified model of continuum lowering is insufficient to provide a full description of the ionization dynamics, but also that the actual quantity of continuum lowering may be higher than predicted by any of the reigning models.

Chapter 2

Laser-Matter Interaction

The fundamental processes governing laser-matter interaction are determined by relatively few parameters, such as laser frequency, intensity, and wavefront, and material properties such as the ionization potential, polarizability, centrosymmetry, birefringence, etc. One primary diagnostic of the interaction is the ponderomotive energy, which represents the amount of kinetic energy which is provided to an electron in the material by the oscillating electric field of the laser. The ponderomotive energy is given by

$$U_p = \frac{e^2 E_0^2}{4m_e \omega_0^2} = 9.33 \times 10^{-14} I_0 \lambda_0^2 \quad (2.1)$$

where e and m_e are the charge and mass of an electron, respectively, and E_0 and ω_0 are the electric field amplitude and frequency. Here also, I_0 is the intensity of the laser, in W/cm^2 , and λ_0 is the laser wavelength, in μm , to yield U_p in eV.

For an idealized (spatially and temporally Gaussian) THOR output of 0.6 J, focused as it is by an $f/200$ mirror, we expect a peak focus intensity of $2.5 \times 10^{17} \text{ W}/\text{cm}^2$, giving a maximum ponderomotive energy 15 keV. Whereas the single photon energy at 800 nm, 1.55 eV, is unable to ionize the target Ar gas alone, the ponderomotive energy is well above the ionization potential of

any gas, so we expect the oscillating electric field of the laser itself to be the driving force for electron motion.

In contrast, for an (optimistic) XUV pulse of 21st harmonic light (wavelength 38 nm) of 20 nJ and 0.6 fs, and beam waist radius 2.5 μm , we achieve a maximum intensity of $6.8 \times 10^{14} \text{ W/cm}^2$, but a ponderomotive energy of only 0.09 eV. Since a single photon at this wavelength has an energy of 33 eV, it is clear that in this case, taking a more quantum view of laser interactions (electron interactions with individual photons) is prudent, and the effect of the oscillatory laser field on electrons may be neglected.

2.1 Keldysh Parameter

The Keldysh parameter utilizes the ponderomotive energy to provide a quick diagnostic of the dominant type of interaction between laser light and a transmissive material. It represents the ratio of the ponderomotive energy and the ionization potential, and is written as

$$\gamma = \sqrt{\frac{I_p}{2U_p}} \propto \frac{\omega_o}{E_0} \quad (2.2)$$

where I_p is the ionization potential of the material in question, U_p is the ponderomotive energy created by the incident laser, and ω_0 and E_0 are the frequency and electric field amplitude of the laser, respectively. The Keldysh parameter differentiates between ionization regimes: tunnelling/barrier suppression ionization in the $\gamma \ll 1$ regime dominated by low-frequency, high-intensity lasers, and single-photon/above threshold ionization (ATI) in the

$\gamma \gg 1$ regime, created by high-frequency lasers. In the mid-regime, where $h\nu < I_p$, but $\gamma > 1$, multi-photon ionization (MPI) and ATI are the primary ionization mechanisms. This can occur for moderate-intensity visible and infrared lasers, as well as in the leading edge of a high-intensity pulse with peak intensity in the $\gamma \ll 1$ regime.

2.2 $\gamma \ll 1$

In this regime, lasers tend to be low frequency (commonly near- to mid-IR), and high intensity ($> 10^{14}$ W/cm²). We can treat the laser as an oscillatory electric field. Ionization is dominated by tunneling ionization, or barrier suppression ionization [40].

Tunneling ionization, shown on the left side of Figure 2.1, occurs when the instantaneous magnitude of the oscillating laser field is sufficiently high that it distorts the Coulomb potential well binding an electron to its parent atom. The distortion results in a barrier of finite width and potential, through which the electron may tunnel. Essential to this process is not just the magnitude of the electric field, but also the frequency of oscillation, as the barrier must remain depressed for long enough that the electron has a reasonable probability of tunneling out.

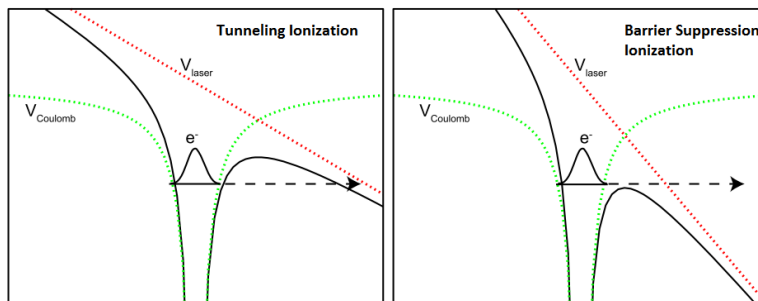


Figure 2.1: in the $\gamma \ll 1$ regime, the intensity of the laser field is sufficient to distort the Coulomb barrier binding an electron to its parent atom for long enough for an electron to have a reasonable probability of tunneling out of the well (left, tunneling ionization), or in even higher intensities, of suppressing the barrier below the electron energy altogether. Figure from [6]

Barrier suppression ionization occurs when the Coulomb field is sufficiently distorted as to temporarily suppress the potential barrier below the electron's ground state energy. This occurs at an electric field E_{BSI} of

$$E_{BSI} = \frac{I_p^2}{4Ze^3} \quad (2.3)$$

where Z is the ionization state of the ion after the loss of the electron, and I_p is the ionization potential of the atom. Then the peak intensity corresponding to this E_{BSI} is given by

$$\begin{aligned} I_{BSI} &= \frac{cE_{BSI}^2}{8\pi} \\ &= \frac{cI_p^4}{128\pi Z^2 e^6} \\ &\simeq 4 \times 10^9 I_p [\text{eV}]^4 Z^{-2} \quad [\text{W}/\text{cm}^2] \end{aligned} \quad (2.4)$$

which typically is on the order of 10^{14} W/cm².

Once an electron is liberated into the continuum, the high ponderomotive energy in this regime will cause additional electron acceleration and can

heat the resulting plasma. In dense media, resonance absorption may occur, resulting in electron kinetic energies of keV and ion energies of MeV [23], as discussed in Chapter 4.

2.3 $\gamma > 1$

This regime, created by low-frequency (visible light and lower), moderate intensity illumination, is dominated by multi-photon ionization and above-threshold ionization. These phenomena involve the absorption of n photons of energy $h\nu$, such that $h\nu < I_p \leq nh\nu$, and ejection an electron of kinetic energy $E_e = nh\nu - I_p$.

Multi-photon ionization is a perturbative phenomenon, where the parent atom absorbs $n = \lceil I_p/(h\nu) \rceil$ photons. The rate of ionization is given by

$$\Gamma_n = \sigma_n I_0^n \quad (2.5)$$

where σ_n is the cross-section for the interaction, and I_0 is the intensity of the incident radiation. Ionization by this method typically becomes relevant above 10^{10} W/cm² [40].

At higher energies, around 10^{12} W/cm², the dominant ionization mechanism may shift from MPI to ATI [40, 57]. In ATI, an electron is able to absorb $n > \lceil I_p/(h\nu) \rceil$ photons. Experimental data has shown that at higher intensities (around 10^{13} W/cm²) more ATI-ejected electrons are detected than MPI. The resulting electron kinetic energy spectrum shifts towards larger values of n , suggesting that ATI is not a perturbative phenomenon [57].

2.4 $\gamma \gg 1$

When $\gamma \gg 1$, we are typically in the regime of high-frequency radiation, resulting in a low ponderomotive energy even at high intensities. Single photon ionization dominates here, with a typical photon-atom interaction resulting in the ejection of an electron with energy $E_e = h\nu - I_p$. If the photon energy is sufficiently high, it may preferentially ionize an inner-shell electron, allowing researchers to observe the electronic structure of atoms and molecules via the resulting relaxation processes (X-ray fluorescence and Auger decay, for example). High-frequency laser light is useful not only as a “pump” for these processes, but also as a “probe.” For photons in the XUV regime and higher frequency, a single period of oscillation can be on the order of 100 as, allowing a correctly shaped few-cycle pulse to probe electron motion within molecules [10, 30, 33, 56, 61].

Chapter 3

Plasma Theory

In standard plasma physics, most of the dynamics of the plasma in question may be derived from four properties for each charged species σ within the plasma: n_σ , the number density, q_σ , the charge, T_σ , the temperature, and m_σ , the mass of the species. Additional parameters may be necessary when collisions with neutrals are probable. These properties govern the reaction of a plasma to an electric field, the characteristic time to reach equilibrium, the energy transfer between species, and energy absorption mechanisms.

One of the most fundamental properties of a plasma is known as the plasma frequency ω_p , and is given by

$$\omega_p^2 = \frac{n_e q^2}{\epsilon_0 m_e}. \quad (3.1)$$

The plasma frequency represents the rate at which electrons in a plasma react to perturbations. The speed at which shielding occurs in a plasma is represented by the inverse of the plasma frequency. In the same vein, an electric field with frequency $\omega_0 < \omega_p$ traversing a plasma will experience “shielding” or compensation by the polarization induced in the medium, and will be unable to propagate.

At high densities such as those seen in a cluster target - around 10^{22} cm^{-3} , we get a plasma frequency of 6 PHz. If we expect to initially photoionize only $\sim 10\%$ of the atoms in a cluster (instead of the 100% assumed above), and to trap most of those electrons inside the cluster, we should still expect a plasma frequency of 2 PHz. A visible or infrared laser would experience high rates of absorption in these high density targets. However, our XUV frequencies are all above the plasma frequency of these dense targets.

3.1 Debye Shielding

One of the most important length scales in plasma physics is given by the Debye length. For a species in a plasma (ion species, electron, etc.) , the Debye length is given by

$$\lambda_\sigma = \sqrt{\frac{\epsilon_0 \kappa T_\sigma}{n_\sigma q_\sigma^2}} \quad (3.2)$$

where ϵ_0 is the vacuum permittivity, n_σ is the density, q_σ is the charge, and κT_σ is the temperature of that species. The Debye length in a plasma composed of multiple species is then

$$\frac{1}{\lambda_D^2} = \sum_\sigma \frac{1}{\lambda_\sigma^2} \quad (3.3)$$

This length scale gives the approximate distance over which charge shielding becomes significant. At $r \ll \lambda_D$, the potential surrounding an arbitrary charged test particle is equal to the potential of that particle in a vacuum, whereas at $r \gg \lambda_D$, the charged particle can be assumed to be completely screened, and the potential due to that particle is zero [12].

One of the fundamental assumptions in standard plasma physics is that the Debye length is long compared to the spacing between particles, or, said another way, there are many particles within a “Debye sphere,” satisfying $\frac{4}{3}\pi\lambda_D^3 n_e \gg 1$. This condition needs to be satisfied for a plasma to be treated as collisionless [12]. However, it is easy to see that as the plasma density increases, the Debye length will shrink, and this assumption will become invalid. Consider the electron Debye length

$$\lambda_{De} = \sqrt{\frac{\epsilon_0 \kappa T_e}{n_e e^2}} \quad (3.4)$$

. which simplifies to

$$\lambda_{De}[\text{m}] \approx 7.44 \sqrt{\frac{T_e[\text{eV}]}{n_e[\text{cm}^{-3}]}} \quad (3.5)$$

. At liquid density $> 10^{22} \text{ cm}^{-3}$, and an electron temperature of 10 eV, $\lambda_{De} \lesssim 2 \text{ \AA}$. Clearly, if the spacing between atoms in a cluster is on the order of 1 \AA , the condition for standard Debye screening is not met.

Equivalently, it is common to define the plasma parameter Λ as a rough estimate of the number of ions within a Debye sphere, that is $\Lambda = (\frac{2}{9})\frac{4}{3}\pi n \lambda_D^3 \approx 0.1$ for our cluster condition of density 10^{22} cm^{-3} and temperature 10 eV. The condition for small angle collisions to dominate over large angle collisions is the same as for the applicability of Debye screening - that $\Lambda \gg 1$. Clearly, weakly coupled plasma assumptions will not hold in this regime.

The other potential region of plasma we are concerned with is the extra-cluster space, which becomes important when considering interactions between, for example, photoelectrons released into the ”continuum” region of

both clustered and uncondensed gas and ions. At our target region, we can estimate a gas density of about 10^{16} cm^{-3} , which would yield a λ_{De} of ≈ 200 nm at 10 eV electron energy or ≈ 10 nm at a room temperature of 30 meV, or equivalently, $\Lambda \approx 100$ or 0.02. Again, at these densities and low temperatures, it is not obvious that the assumption $\Lambda \gg 1$ holds, or that standard Debye screening assumptions are valid.

3.2 Plasma Coupling

Another major diagnostic parameter used to define the physical regime in which a plasma exists is called the electron-electron plasma coupling parameter Γ_{ee} , and is defined as the ratio of the Coulomb to thermal energy in a plasma. That is,

$$\Gamma_{ee} = \frac{E_c}{\kappa T_e} = \left(\frac{e^2}{4\pi\epsilon_0 r} \right) \left(\frac{1}{\kappa T_e} \right) \quad (3.6)$$

where r is commonly estimated as the Wigner-Seitz radius, the radius at which a sphere occupies the mean volume per atom in the material: $r = (\frac{3}{4\pi n})^{1/3}$. For the commonly used units in this field, Equation 3.6 reduces to

$$\Gamma_{ee} \approx 2.32 \cdot 10^{-7} \left(\frac{n[\text{cm}^{-3}]^{1/3}}{T[\text{eV}]} \right) \quad (3.7)$$

At a density of 10^{22} cm^{-3} , and an electron temperature of 10 eV, we obtain $\Gamma_{ee} \approx 0.5$. For the extra-cluster space, a density of 10^{16} cm^{-3} and temperature of 10 eV gives a $\Gamma_{ee} \approx 0.005$.

Additionally, we can define the electron-ion coupling constant, $\Gamma_{ei} = Z\Gamma_{ee}^{3/2}$, which “represents the ratio of ion charge to electron charge within the

Debye-sphere” [53]. For our values listed above, with a singly ionized plasma, we get $\Gamma_{ei} \approx 0.4$. A plasma may be considered to be strongly coupled if its coupling parameters Γ_{ee} and Γ_{ei} are $\gtrsim 0.1$ and 1, respectively [53]. Clearly, our cluster plasma is just over the border of the strongly coupled plasma regime, and we should be leery of applying approximations designed for regimes in weakly coupled plasmas, $\Gamma_{ee} \ll 1$, or solidly strongly coupled plasmas, $\Gamma_{ee} \gg 1$. For the surrounding region of clusters and uncondensed gas at much lower densities, we can safely refer to the plasma as weakly coupled.

3.3 Collisions in a Plasma

Collisions in a plasma determine the rate of energy transfer between and among charged and neutral species, providing timescales for electron-electron and electron-ion thermalization, and shedding light on the evolution of the nanoplasma. Additionally, collision rates factor into the signal we expect to see on our diagnostic instruments. For example, a primary diagnostic used in the experiments described in this dissertation gives the kinetic energy spectra of electrons ejected from photoionized nanomaterial targets. Once an electron is freed from an atom, it is important to consider its probability of making it out of the cluster in which it is born, as well as its probability of traversing the low-density extracuster space between the cluster and the detector, when considering the signal we expect to see at our detector.

Evolution of a plasma occurs on the timescale determined by the inverse of the collision frequency $\nu = \sigma nv$, where σ is the collision cross-section, n is

the target species number density, and v is the thermal velocity $v = \sqrt{\frac{2\kappa T}{m}}$ of the species doing the colliding. It is also important to note the mean free path between collisions $l = 1/(\sigma n)$

According to the Spitzer-Harm theory of electron transport, Coulombic collisions in a plasma occur at a frequency proportional to the Coulomb logarithm, $\ln \Lambda$, where Λ is the plasma parameter, as defined in Section 3.1. Unfortunately, in our clusters, we have a $\Lambda \approx 0.1$, which yields $\ln \Lambda \approx -2.1$, which certainly causes problems in the above equation. However, Baalrud suggests that in this regime, where $1/\Lambda \approx 8$, we can instead use a value for the generalized plasma parameter of $\Xi = \ln(1 + 0.7\Lambda) \approx 0.081$ [8].

Electron thermalization in a plasma occurs at a rate determined by the electron collision frequency, given by

$$\nu_e = \frac{4\sqrt{2\pi}n_e e^4 \ln \Lambda}{3k^2 m_e^{1/2} T_e^{3/2}} \simeq \frac{5 \times 10^{-11} n_e (\text{m}^{-3})}{[T_e (\text{eV})]^{3/2}} \left(\frac{\ln \Lambda}{17} \right) \text{s}^{-1} \quad (3.8)$$

with the the right-hand side a simplified approximation involving density in units of m^{-3} and temperature in units of eV [17]. For a temperature of 10 eV, and a density of 10^{22} cm^{-3} , we get $\tau_{eq} = 1/\nu_{ee} = 13 \text{ fs}$.

3.3.1 Coulomb (Elastic) Collisions

When a charged test particle approaches another charged particle, its trajectory is modified by the Coulomb interaction between the particles. The extent of deflection is determined by the impact parameter, b , the distance of its trajectory of approach from that of a head-on collision, the relative velocity

of the two particles, and the masses and charges of the particles. Collisions are often divided into “large angle collisions” and “small angle collisions,” with a deflection angle of $\pi/2$ marking the boundary between the two. For large angle collisions, the cross-section for Coulombic interaction is given by

$$\sigma_{large} \approx \pi b_{\pi/2}^2 = \pi \left(\frac{q_1 q_2}{4\pi\epsilon_0\mu v_0^2} \right)^2 \quad (3.9)$$

where $b_{\pi/2}$ is the impact parameter corresponding to a deflection angle of $\pi/2$,

$$b_{\pi/2} = \frac{q_1 q_2}{4\pi\epsilon_0\mu v_0^2} \quad (3.10)$$

q_1 and q_2 are the charges of the test particle and target particle, ϵ_0 is the vacuum permittivity, μ is the reduced mass of the test and target particle pair, and v_0 is the relative velocity of the particles [12].

In weakly coupled plasmas, grazing angle scattering is often the primary mode of scattering. To get a cross-section for small angle scattering which we may compare to σ_{large} above, we consider the cumulative effect of many grazing angle collisions, and ask what the effective cross section is for a series of small angle collisions to be equivalent to a single large angle collision. We obtain the small angle cross section

$$\begin{aligned} \sigma_{small} &= \int_{b_{\pi/2}}^{\lambda_D} 2\pi b db [\theta(b)]^2 \\ &= \int_{b_{\pi/2}}^{\lambda_D} 2\pi b db \left(\frac{q_1 q_2}{2\pi\epsilon_0\mu v_0^2 b} \right)^2 \\ &= 8 \ln(2n\lambda_d^3) \sigma_{large} \\ &\approx 8 \ln \Lambda \sigma_{large} \end{aligned} \quad (3.11)$$

where we use $\Xi = \ln(1 + 0.7\Lambda)$ in place of $\ln \Lambda$ in the strongly coupled plasma regime. Figure 3.1 shows the cross-sections for electron-electron scattering at large and small scattering angles in liquid density argon.

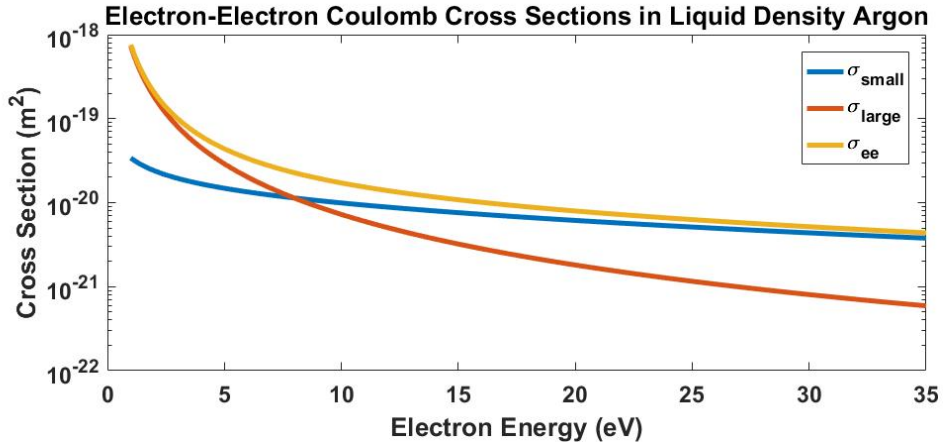


Figure 3.1: Cross-sections for electron-electron Coulomb scattering, taking small angle collisions (blue) and large angle collisions (red) into account. The total cross section is shown in gold.

Likewise, we must take interactions with ions into account. Figure 3.2 shows the total Coulombic scattering cross-sections, from electrons and ions (large and small angle added together).

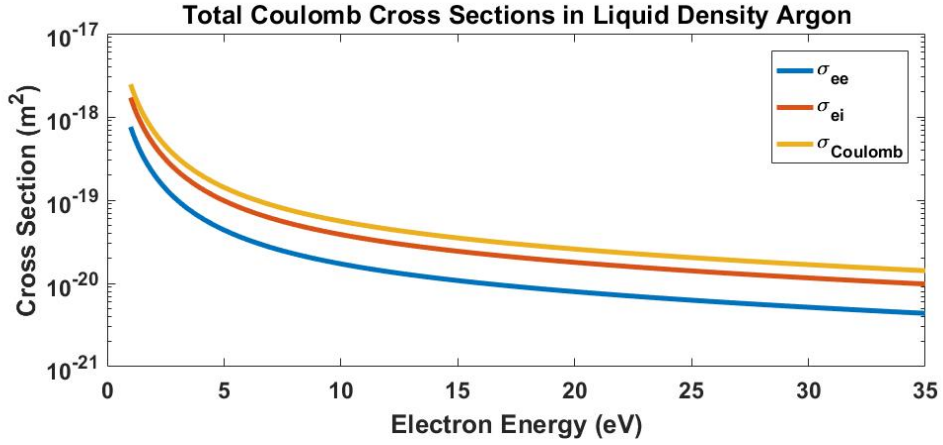


Figure 3.2: Cross-sections for electron-electron (blue) and electron-ion (red) Coulomb scattering. The total of the two cross sections is shown in gold.

Finally, we must consider collisions with neutrals. In a weakly coupled plasma, collisions with neutrals typically are negligible, but in a strongly coupled plasma, they can dominate the total interaction cross-section. Elastic collisions with neutrals has been the observed cause of the isotropic photoemission of electrons from large clusters, instead of the emission being strongly peaked in the electric field direction, as is seen with small clusters and isolated atoms [83]. Figure 3.3 demonstrates how, in liquid argon at our typical electron temperatures, the neutral cross section, taken from Szmytkowski et al. [92] comes to dominate the total scattering cross section. For these, we assume 10% ionization of a liquid density plasma. That is, 90% of our atoms are neutrals, and 10% are singly charged ions.

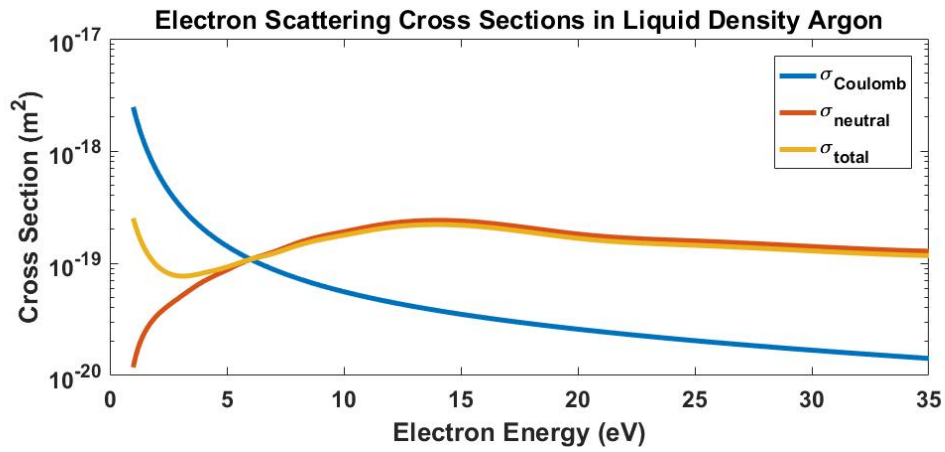


Figure 3.3: Cross-sections for total electron Coulomb (blue) and electron-neutral (red) scattering. The total of the two cross sections is shown in gold.

The resulting mean free path lengths for liquid density noble gas media are shown in Figure 3.4. It is readily apparent that in all of the heavier elements, elastic scattering plays a large role in the electron paths through all but the smallest clusters.

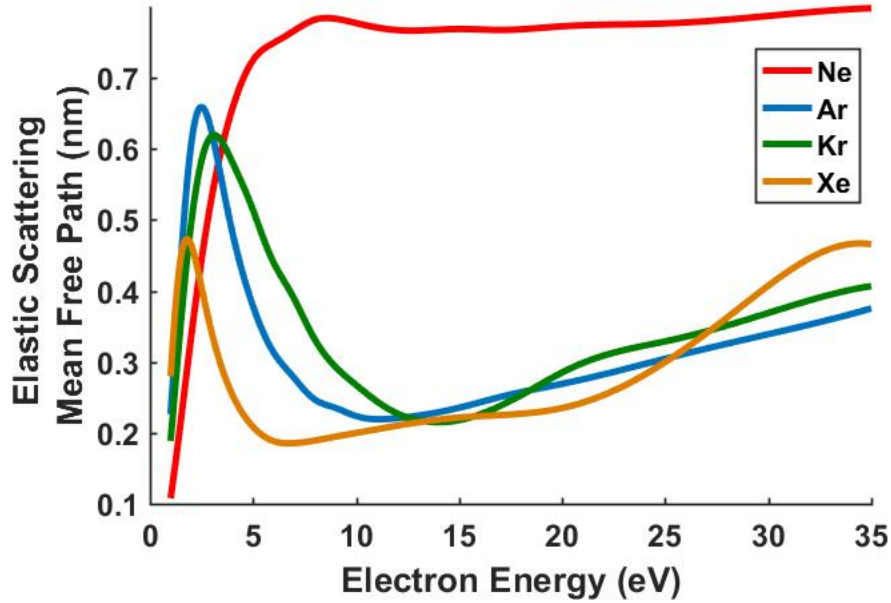


Figure 3.4: Mean free paths for elastic electron scattering through liquid density noble gases, using the total scattering cross sections from Figure 3.3 and the liquid densities of the respective gases. Cross sections include small and large angle Coulombic scattering from ions and electrons, but are dominated by scattering with neutrals, as given by Szmytkowski et al. [92].

3.3.2 Inelastic Collisions

Inelastic interactions of electrons with neutral atoms and ions in the dense cluster environment also play a big role in the rates of inner ionization within the cluster. These interactions include absorption of free electrons by ions (recombination), and electron impact ionization of neutral atoms by inner-ionized electrons.

Recombination is a process which dominates the inner core of large clusters [3, 83]. As will be discussed in the following chapter, van der Waals-

bound cluster dissociation typically proceeds via the Coulombic ejection of the charged outer shell of cluster ions, followed by the much slower hydrodynamic expansion of the quasineutral cluster core. This long expansion time gives the inner-ionized electrons trapped near the core ions ample time to re-combine, typically to excited states. This recombination has been shown to happen on the time scale of 10-100 ps for moderately sized clusters ($\langle N \rangle = 3000$ to 5000) [83]

Electron impact ionization plays a large role in the inner ionization of clusters. Cross sections for electron impact ionization for different liquid rare gas species, as a function of electron energy, are shown in Figure 3.5 [81]. We can see that electron impact ionization is especially prominent in Xe clusters. Electrons photoionized by the 21st harmonic of THOR have a kinetic energy of 20 eV. Neutral atoms then impose an electron impact cross section of about 3×10^{-20} m², resulting in a mean free path in a liquid density cluster of about 3 nm. Given the large amount of elastic scattering described in Section 3.3.1, even a single pass of an inner ionized electron through a moderately sized cluster should result in electron impact ionization. With a small amount of continuum lowering of the height of the potential wells between adjacent atoms, a single photoionization event in a xenon cluster can be expected to yield a total of 3 low energy inner-ionized electrons.

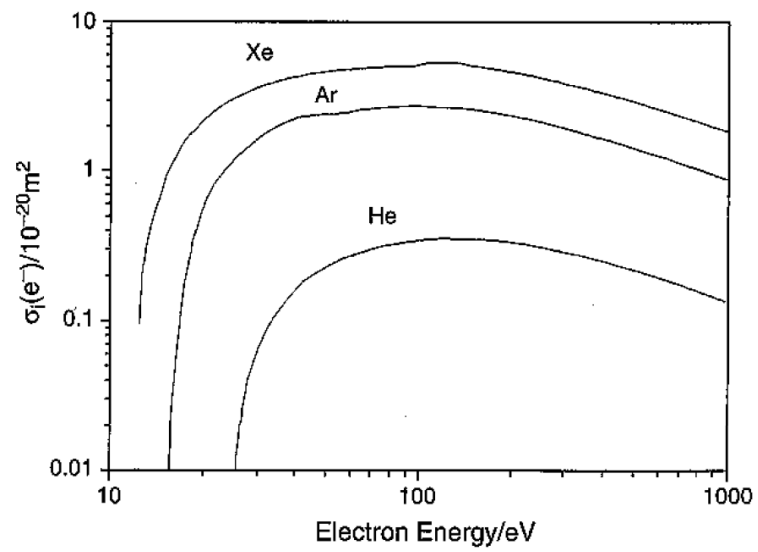


Figure 3.5: Cross sections for electron impact ionization of liquified rare gases. Figure from Reference [81].

Chapter 4

Cluster Theory

Condensed gas clusters, defined as liquid density droplets of STP gases, with between 2 and about 10^6 atoms per cluster, as well as nanoparticles made from solid materials of the same size, are an exciting target for HED and plasma physics explorations. Clusters are unique in their interactions with high-intensity laser fields, as they represent an intermediary between the solid and gaseous targets. Their liquid or solid density creates the conditions for high energy absorption, whether through large amounts of photoionization or by resonant heating mechanisms such as those discovered by Ditmire et al [23]. At the same time, their limited size prevents significant energy loss from a nanoplasma cluster to its surroundings. This creates the conditions for unusually energetic plasmas.

Clusters also serve as potential models for large molecules, or biological materials such as protein molecules or viruses. For material which does not crystallize on the large scale, X-ray diffraction imaging may still be possible if the light source is intense enough and fast enough that an image may be captured before the material dissociates. XFEL lasers are the obvious choice of light source for such an endeavor, and quite a bit of progress has been made

towards these goals [69, 84]. However, the energy absorption pathways, ionization methods, and explosion mechanisms, and their associated timescales, which all affect the feasibility of such studies, are still open questions of investigation.

4.1 Enhanced Photon Absorption in Clusters

Experimental studies of clusters in intense infrared laser pulses have shown unexpectedly large enhancements in photoabsorption, resulting in extremely high electron temperatures [27, 66]. These enhancements were determined to be due to a resonance in the process of inverse Bremsstrahlung absorption. This resonance enhancement of absorption of laser energy via inverse Bremsstrahlung processes occurs at $N_e = 3N_{cr}$ [23, 64], where N_{cr} is the critical density for laser of frequency ω , $N_{cr} = m_e\omega^2/4\pi e^2$. Here, as usual, m_e and e are the mass and electric charge of an electron, respectively. For an 800 nm laser, we obtain $N_{cr} = 1.8 \cdot 10^{21} \text{ cm}^{-3}$, so that as the cluster, which starts around a density of 10^{22} cm^{-3} , expands, different portions of the expanding cluster are at the Bremsstrahlung absorption resonance at different times, increasing the duration over which the cluster laser experiences this enhanced absorption to include the peak intensity portion of a standard 100 fs FWHM laser pulse with a peak intensity of 10^{15} W/cm^2 [64].

If we scale this critical density to our high-harmonic frequencies, we get $N_{cr} = 5 \cdot 10^{23} \text{ cm}^{-3}$ for our 17th harmonic wavelength of 47 nm, and $N_{cr} = 8 \cdot 10^{23} \text{ cm}^{-3}$ for the 21st harmonic wavelength of 38 nm. For the

resonance absorption condition of $N_e = 3N_{cr}$, this puts us above 10^{24} cm^{-3} , which is well above any density we should expect to see from an uncompressed cluster. For reference, the most dense of our noble gas targets, neon, has a liquid density of $3.6 \cdot 10^{22} \text{ cm}^{-3}$.

Inverse Bremsstrahlung absorption enhancement also plays a part in XUV absorption due to this same resonance effect, and is believed to have played a role in the creation of the high charge states of xenon discovered by Wabnitz et al. [80, 96]. However, this effect is expected to be negligible at wavelengths below 100 nm, due to the impossibility of reaching the resonance condition, as well as the ω^{-2} scaling of inverse Bremsstrahlung absorption cross section [14, 103].

4.2 Continuum Lowering in High-Density Plasmas

One universal feature of plasmas is the phenomenon of continuum lowering, or ionization potential depression (IPD). Essentially, the presence of a distribution of free electrons surrounding an ion will screen the ionic charge, resulting in a reduction in the energy level associated with the electron energy continuum, the energy at which an electron will be delocalized from an atom or ion.

As discussed in Section 3.1, in low density plasmas, screening effects occur on the length scale of the Debye length. Within a Debye sphere, we have ionization potential depression. The model for predicting the amount of continuum lowering in this plasma regime, where $n\lambda_D^3 \gg 1$ and $\Gamma \ll 1$ is

known as the Debye-Hückel (DH) model. This model consists of a central ion of charge $Z_m e$ surrounded by an equal number of electrons, distributed within a radially symmetric potential well given by

$$\Phi_{DH}(m) = \frac{Z_m e}{r} e^{-r/\lambda_D}. \quad (4.1)$$

Minimizing the resulting correction to the free energy results in an ionization potential depression of

$$\Delta I_{DH}(m) = -\frac{Z_m e^2}{\lambda_D} \quad (4.2)$$

for the ionization from charge $Z_m e$ to $Z_{m+1} e$ [58].

As previously discussed, our plasma density and temperatures do not put us in this DH regime. When the Debye length encompasses only a single atom, new estimates must be applied.

4.2.1 Ion Sphere Model

The simplest resolution to this issue is to modify the assumed electron distribution to suit the high plasma density - we assume the electrons to be *uniformly* distributed within a sphere surrounding each ion, with the volume of the sphere equal to the ion's share of the volume of the plasma. That is, $\frac{4}{3}\pi R_{IS}^3 = n_m^{-1}$. This model is referred to as the ion sphere (IS) model, and the radius of the sphere, R_{IS} , is called the ion sphere radius. Here, we follow the derivation by Larsen for the ion sphere estimate of the continuum lowering [58].

If we distinguish between Z_m , the charge of a particular (m^{th}) atom,

and Z^* , the average ionic charge in the cluster, then we have $n_e = Z^*n_i$, and $R_m = (3Z_m/4\pi n_e)^{1/3}$ is the ion sphere radius for the m^{th} atom [58]. The potential well around this m^{th} atom is

$$\Phi_{\text{IS}}(m) = \frac{Z_m e}{r} - \frac{Z_m e}{2R_m} \left(3 - \frac{r^2}{R_m^2} \right) \quad (4.3)$$

where the first term represents the potential due to the core ion, and the second represents the potential due to electrons in the sphere. The correction to the free energy due to this potential is then

$$\begin{aligned} \Delta F_m &= -e \int n_e(r) \Phi(r) d^3r \\ &= -4\pi Z_m^2 e^2 n_e \int_0^{R_m} r dr + \frac{1}{4} \frac{Z_m e^2}{R_m} n_e \int_0^{R_m} \left(3 - \frac{r^2}{R_m^2} \right) 4\pi r^2 dr \\ &= -\frac{3}{2} \frac{Z_m^2 e^2}{R_m} + \frac{3}{5} \frac{Z_m^2 e^2}{R_m} \\ &= -\frac{9}{10} \frac{e^2}{R_0} (Z^*)^{1/3} Z_m^{5/3} \end{aligned} \quad (4.4)$$

where $R_0 = (\frac{3}{4\pi n_i})^{1/3} = R_m (Z^*/Z_m)^{1/3}$ represents the radius of a sphere composing an ion's share of the volume in the plasma. The second line in Equation 4.4 includes a factor of 1/2 in the second term, to prevent overcounting in the electron Coulomb energy term. We take the derivative of ΔF_m with respect to Z_m to determine the continuum lowering associated with ionization from Z_m to Z_{m+1} , and we obtain

$$\Delta I_{\text{IS}}(m) = -\frac{3}{2} (Z^*)^{1/3} Z_m^{2/3} \frac{e^2}{R_0}. \quad (4.5)$$

Or, in terms of the known quantity n_i ,

$$\Delta I_{\text{IS}}(m) = -\frac{3}{2} (Z^*)^{1/3} Z_m^{2/3} e^2 \left(\frac{4\pi n_i}{3} \right)^{1/3}. \quad (4.6)$$

Figure 4.1 shows the predicted levels of continuum lowering for different charge states for different values of Z^* , and the effect of this potential lowering on the ionization potential of xenon. The value used for R_0 corresponds to the density of liquid xenon. If applied to photoionization, this lowering could facilitate the direct photoionization of individual ions to Xe^{5+} with only a mean charge state of $Z^* = 1$. This approximation is typically applied to cold, dense (liquid density or greater) plasmas [89].

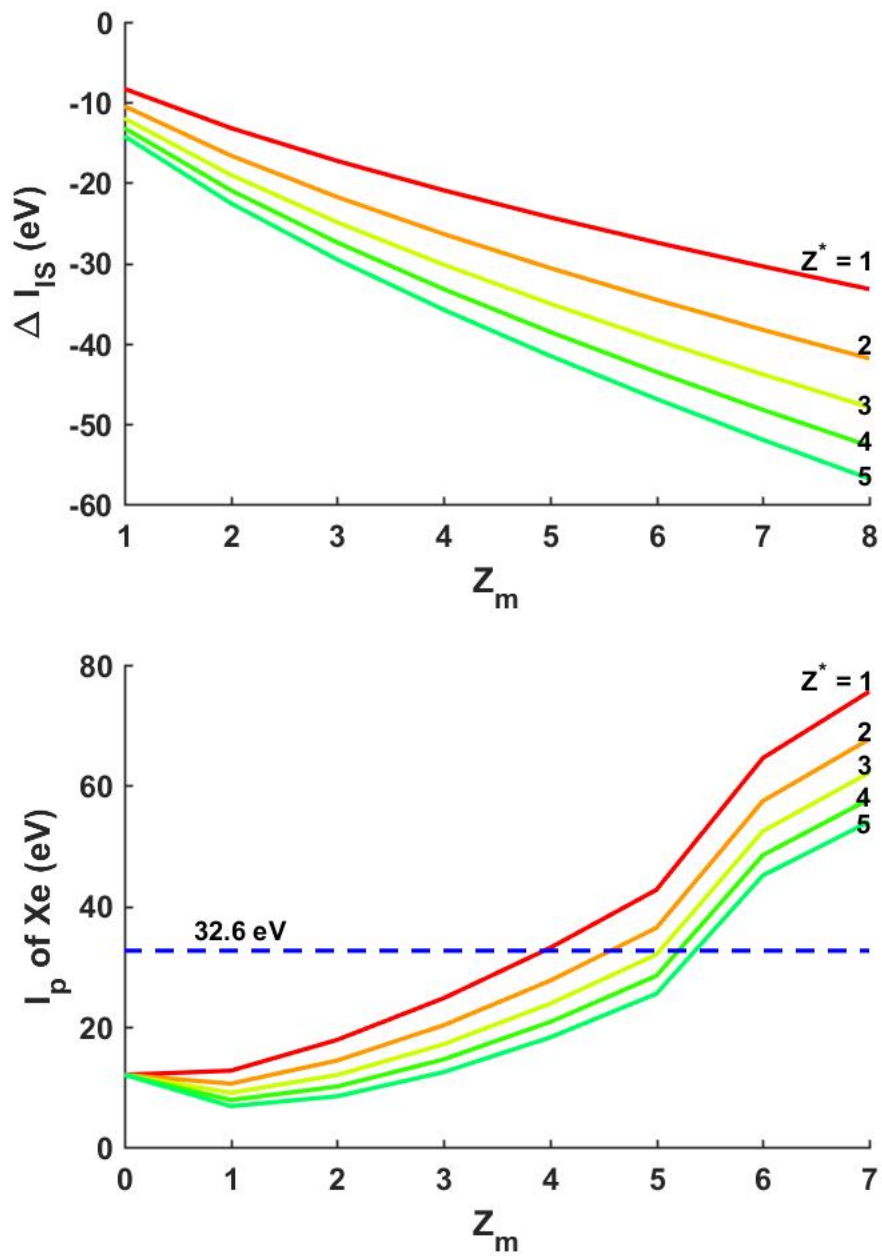


Figure 4.1: Predicted levels of continuum lowering from the ion sphere model as a function of charge state for different values of Z^* (top), and the corresponding effect on the ionization potential of Xe (bottom). The density used in these calculations corresponds to the density of liquid Xe.

4.2.2 Ecker Kröll Model

The continuum lowering model developed by Ecker and Kröll had as primary goals to be both predictive and to be “physically conceivable” - to use the methods of statistical physics to shed light on the processes behind ionization potential depression in plasmas at a wide range of densities [32]. The physics invoked in the derivation of this model is the effect of the instantaneous plasma microfield on a given atom in the plasma.

The Coulomb lowering predicted by this model is given by

$$\Delta I_{\text{EK}}(m) = \begin{cases} -\frac{e^2}{\lambda_D} Z_m & \text{for } n \leq n_c \\ -C \frac{e^2}{R_0} Z_m & \text{for } n > n_c \end{cases}, \quad (4.7)$$

where C is given by

$$C \approx 2.2 \left(\frac{e^2}{k_B T} \right)^{1/2} n_c^{1/6}, \quad (4.8)$$

and n_c is the critical density, defined by

$$n_c = \frac{3}{4\pi} \left(\frac{k_B T}{e^2} \right)^3, \quad (4.9)$$

the density at which the electron-electron coupling parameter is equal to 1 (i.e. the border between the strong and weak plasma coupling regimes) [32, 58]. As determined in Section 3.2, we expect the experiments described in this work to be performed near to the critical density. The EK estimate of continuum lowering for a 10 eV liquid density xenon plasma is shown in Figure 4.2, superimposed on the plot of the ion sphere estimate shown in Figure 4.1. For our plasmas, the EK model performs like the ion sphere model where $Z_m = Z^*$.

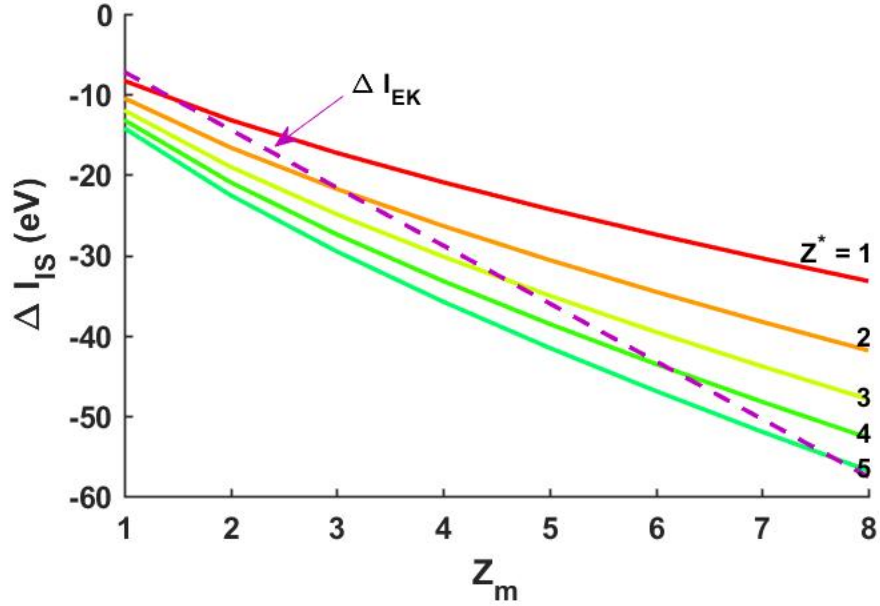


Figure 4.2: Predicted levels of continuum lowering from the ion sphere (solid lines) and Ecker-Kröll (dashed line) models as a function of charge state for different values of Z^* . The density used in these calculations corresponds to the density of liquid Xe, and the electron temperature used was 10 eV.

4.2.3 Stewart Pyatt Model

The continuum lowering/“pressure ionization” model developed by Stewart and Pyatt was another attempt to create a model which accurately interpolated between the two extremes of density and temperature, and which yielded the Debye-Hückel or ion sphere results in each limiting case [89]. Here, they use Fermi-Dirac statistics to model the electrons and Maxwell-Boltzmann statistics to describe the ions. The ionization potential depression predicted by this model is

$$\Delta I_{\text{SP}}(m) = -\frac{3}{2} \left(\frac{Z_m}{Z_p} \right)^{2/3} \frac{Z_p e^2}{R_0} \left\{ \left[1 + \left(\frac{\lambda_{Di}}{R_m} \right)^3 \right]^{2/3} - \left(\frac{\lambda_{Di}}{R_m} \right)^2 \right\}, \quad (4.10)$$

where $Z_p = \langle Z^2 \rangle / \langle Z \rangle$ behaves effectively as the average charge, but is thus prevented from falling below a value of 1 [58, 89]. Figure 4.3 shows the predicted levels of continuum lowering for different charge states for different values of Z_p . The atom density used in these calculations is the density of liquid xenon, and the Debye length is estimated with an electron temperature of 10 eV.

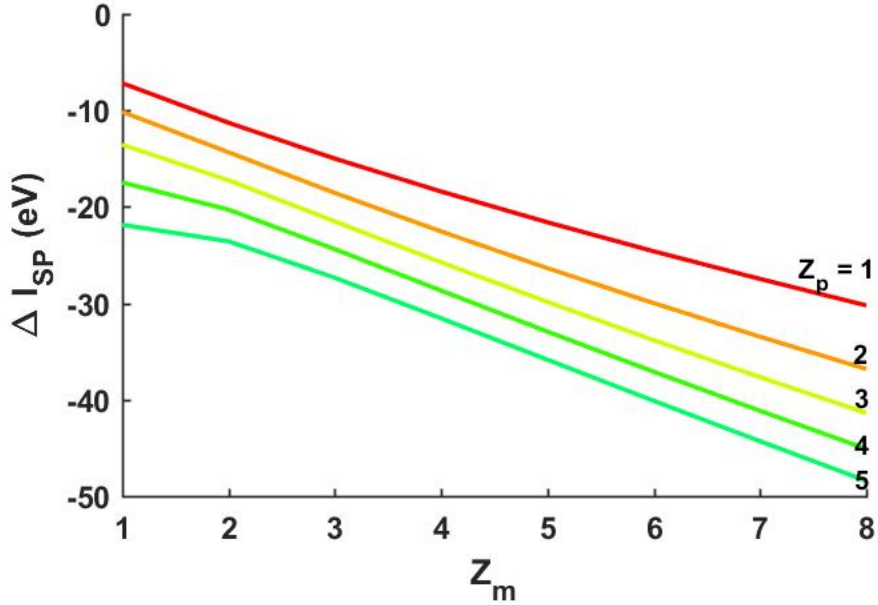


Figure 4.3: Predicted levels of continuum lowering from the Stewart-Pyatt model as a function of charge state for different values of Z_p . The density used in these calculations corresponds to the density of liquid Xe, and the Debye length was estimated for an electron temperature of 10 eV.

4.2.4 Spectroscopic IPD

All of the above models of continuum lowering suffer from the same, largely inaccurate assumption, that ionization in the given plasma is an equilibrium process [21, 58]. As noted by Ecker and Kröll in the paper outlining their estimate of continuum lowering (discussed in Section 4.2.2), “the most frequent mistake is that authors do not carefully distinguish between the lowering of the ionization potential as it occurs in spectroscopic measurements and the lowering of the ionization potential appearing in the Saha equation” [32]. It would be incorrect to apply the estimates described above to the IPD of single photon photoionization processes, as this ionization process occurs on an “instantaneous” time scale with respect to the electrons and ions in a plasma. That is, the electron is liberated before the surrounding electrons and ions “see” it and have a chance to react (a process which takes place on the time scale set by the plasma frequency).

This issue was recognized by Ecker and Kröll, as well as by Crowley, who identified this as the main reason that different measurement techniques, each attempting to identify which model of the preceding three best predicted continuum lowering in solid density plasmas, often came up with significantly different answers [21]. In response to this issue, Crowley developed a fourth model, dubbed spectroscopic IPD (SIPD), which takes into account the non-adiabatic nature of photoionization.

Crowley gives the spectroscopic ionization potential depression as

$$\Delta I_{\text{SIPD}} = \Delta U_j - \Delta\chi + \bar{\epsilon} - \Delta_e \quad (4.11)$$

where $\Delta U_j = \Delta I_{\text{SP}}$ is the “contribution to the potential energy of the bound electron from the surrounding plasma,” $\Delta\chi$ is termed the “relaxation energy,” $\bar{\epsilon}$ is the mean kinetic energy of an electron in the plasma, and $\Delta_e = 3/2k_B T_e$ is a term put in to ensure that ΔI_{SIPD} corresponds to the photoionization threshold [21]. It is worth noting that Crowley assumes electrons are deeply bound, so differences in IPD for different electronic configurations can be neglected.

This model appears to produce results similar to the ion sphere/EK model, (especially in moderately coupled regimes near our atom density) and provides an explanation as for why the EK model in particular seems to best fit the spectroscopic measurements of IPD [21].

The correct model to apply to the plasma evolution of our photoionized clusters is likely to be a dynamic combination of models, with atomic ionization potentials ascribed to the surface atoms, the (slightly lowered) liquid or solid material band gap energy applied to the neutral inner cluster core, and SIPD (without the deeply bound electron assumption) applied to the photoionization, collisional ionization and recombination of the developing inner-ionized plasma.

4.3 Inner and Outer Ionization

Cluster-based plasmas require additional terminology beyond that of large-scale HED plasmas. For one, the distinction between “inner” and “outer” ionization becomes important. The preceding models of continuum lowering predict rates of inner ionization. Inner ionization refers to the delocalization of an electron from a parent atom or ion, within the spatial extent of the cluster. This electron need not have sufficient energy to escape the cluster altogether. Outer ionization refers specifically to those electrons which may escape “to infinity,” and may make it to our detector apparatus without the assistance of an electric field on the extraction region of our time-of-flight [59].

Due to space-charge effects, the rate of inner ionization will be much higher than outer ionization. Providing a high electric field in the extraction region of the time-of-flight allows us to probe the rate of inner ionization by facilitating the separation of delocalized electrons from ions. This may also have the effect of suppressing electron-ion recombination [38].

For standard noble gas clusters in the time frame of the incident XUV laser pulse, it is informative to model the charge buildup on a cluster as a static insulating sphere with uniform charge distribution. Then the charge density $\rho = Q_{tot}/V_{cluster}$, where $Q_{tot} = ne$ is the total number of outer-ionized electrons, and $V_{cluster} = N/\rho_{liquid} = (4/3)\pi r_{cluster}^3$ is the volume of the cluster. As XUV photons are absorbed by the cluster, electrons are outer-ionized to infinity, leaving charge buildup on the cluster. The potential well formed in the cluster is deepest at the center of the cluster, and shallowest on the outer

edge. As the charge builds up, photoionized electrons born near the center of the cluster will be unable to escape, and become inner-ionized electrons. Finally, charge builds up to the point where no further photoionized electrons may escape. Only minimal evaporative emission of internally ionized electrons is possible at this point.

Figure 4.4 shows the process of charge buildup on a 10,000 atom Ar cluster, illuminated by the spectrum we expect from the 21st harmonic mirror (central wavelength and sidebands included) and its effect on the photoionized electron spectra. The cluster potential as a function of a target atom's radius from the center of the cluster is plotted in the bottom graphs. The resulting predicted photoelectron spectrum is shown in the top. The leftmost plots show the predicted potential and photoelectron spectrum resulting from a single photoionization event per cluster. As we move toward the right, we see the gradual effects of positive charge buildup in the cluster, from 5, 10, and 30 photoionization events. By the 30th event, the center of the cluster has exceeded the potential necessary to begin charge trapping - only an average of 28 of the 30 photoelectrons escape the cluster. The buildup of charge creates a growing low energy plateau/tail on the photoelectron peaks. This tail has been predicted and observed by multiple researchers, and it has been suggested that the length of the plateau may be used as an indirect measurement of on-target fluence [2, 3, 14, 83].

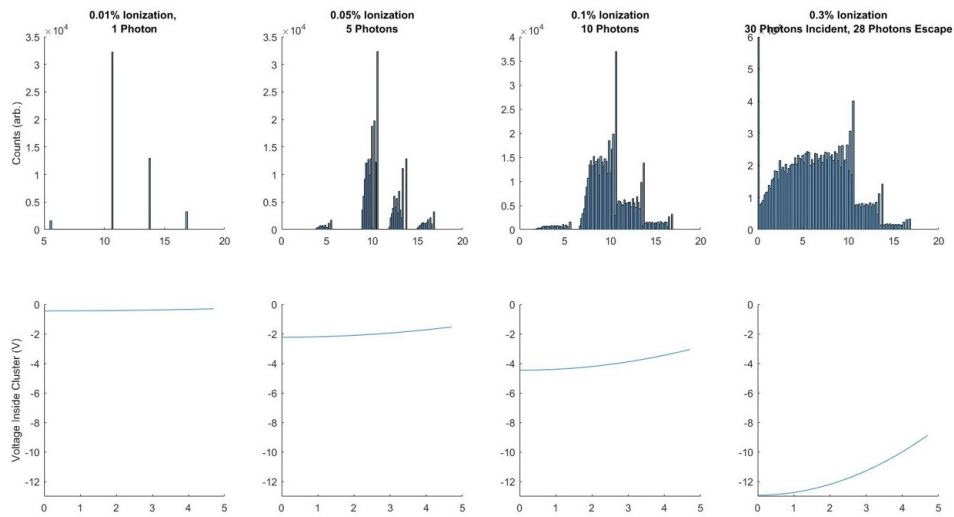
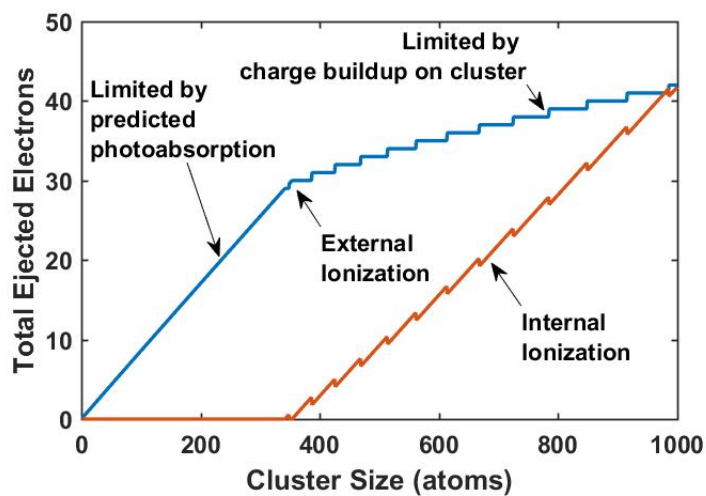
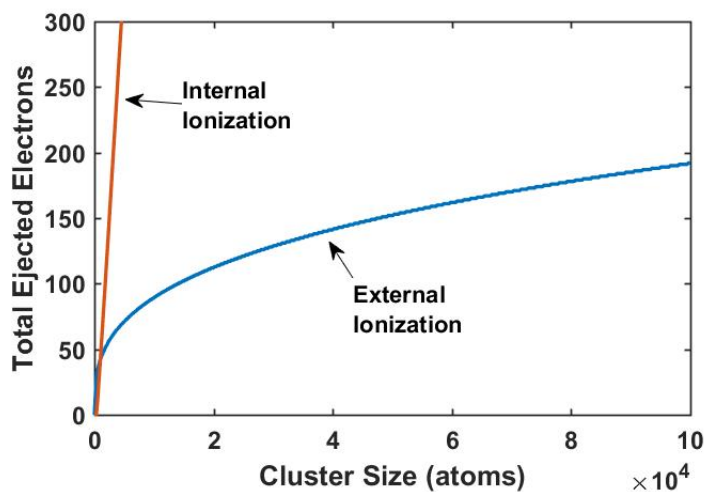


Figure 4.4: Simulation of cluster potentials as a function of radial position during the process of charge buildup in an Ar cluster of 10,000 atoms (bottom), along with the electron kinetic energy spectrum associated with the specified outer ionization level (top).

Figure 4.5 details the total number of electrons we expect to be outer-ionized (and hence detected) as a function of cluster size for argon clusters at our fluences and photons of energy of 26.4 eV. At the lower cluster sizes, the number of electrons detected is a function of the total number of photons absorbed in the cluster - all of the expected photoionization events should lead to outer ionization. As the cluster size increases, charge trapping limits the number of outer-ionized electrons, and the ratio of inner ionization events to outer ionization events increases rapidly. By a cluster size of about 1,000, inner ionization is the dominant result of photoionization.



(a)



(b)

Figure 4.5: Total number of electrons predicted to be outer ionized and ejected from an Ar cluster (blue lines), versus inner ionized (orange lines) as a function of cluster sizes. At small cluster sizes, (a), the number of ejected electrons is limited by the total number of atoms predicted to be photoionized in a cluster of the given size. However, at large cluster sizes, (b), the total number of outer ionized electrons is limited entirely by the charge buildup on the cluster. The overwhelming majority of photoionization events result in inner ionization.

4.4 Conduction Bands and Solid State Phenomena

It is worth noting that even neutral atoms at high densities exhibit a form of IPD by the formation of a conduction band. This allows for inner ionization, as we have defined it, via the delocalization of an electron from an ion within the high density material. With this terminology, we may think of metal clusters as being “pre-ionized,” having an average charge equal to the number of electrons in the conduction band at room temperature, even before a laser pulse strikes them. Likewise, noble gas clusters, while initially maintaining entirely localized electrons, exhibit a lowered inner ionization potential equal to the band gap energy. Below is a table of the band gaps for liquid density noble gas clusters. Note the anomalous band gap in neon, where the conduction band is actually higher than the vacuum level.

Table 4.1: Conduction band of liquid density noble gases [54, 81, 88]

Gas	E_{bg} (eV)	ΔI_{cb} (eV)	E_{vb} (eV)	χ (eV)
Neon	21.58	+0.03	1.3	-1.3
Argon	14.16	-1.61	1.7	-0.4
Krypton	11.01	-2.45	2.3	0.3
Xenon	9.33	-2.93	3.0	0.5

Here, E_{bg} is the band gap energy between the full valance band and the conduction band, ΔI_{cb} is the “IPD” associated with electron delocalization at the conduction band, E_{vb} is the width of the band gap, and χ is the electron affinity.

This anomalous band gap exists for liquid neon and liquid helium. Figure 4.6 shows a predicted potential as a function of distance from the cluster

edge, at $Z = 0$. In this figure, $Z < 0$ represents the interior of the cluster, and $Z > 0$ is the distance from the cluster's edge. A potential well of this form suggests that, until sufficient charge builds up on the cluster to reduce the cluster's internal potential by a magnitude of V_0 , it is energetically favorable for a photoionized electron to escape to infinity, rather than remaining within the cluster.

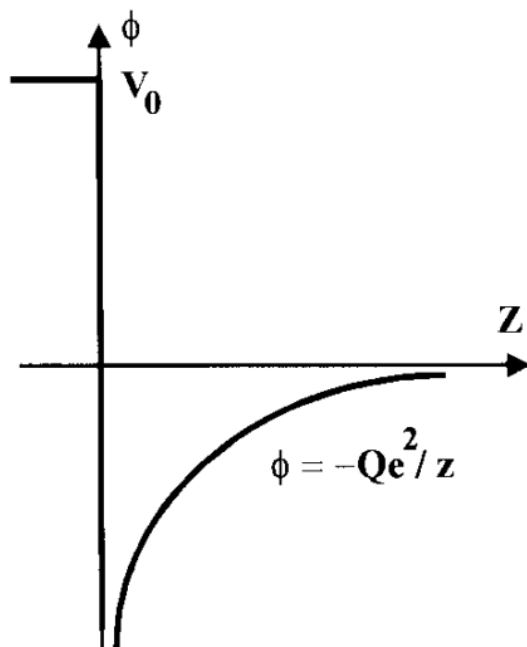


Figure 4.6: Predicted potential felt by an electron near the surface of a Ne or He cluster. V_0 is the (positive) potential with respect to vacuum of the conduction band in these unusual materials. Figure from Reference [87].

Additionally, once that charge builds up, Ne or He clusters remain with deep potential wells just beyond the outer surface of the cluster perimeter. Smolyaninov refers to these electrons as “levitating” above a surface of

solid hydrogen or neon in his experiments [87]. Photoionized electrons with insufficient energy to escape to the continuum should preferentially be found in these regions outside of the cluster. This could lead to unique properties of these clusters. For example, we should expect electron-ion recombination to be stifled, since the electron is not likely to spend much time near to internal ions. Similarly, electron-ion or electron-atom thermalization should be significantly reduced. Instead, we might expect a TNSA-like ion acceleration mechanism, formed by the nearly monochromatic “sheath” of photoionized electrons surrounding clusters.

Another solid state phenomenon which we must take into account when observing cluster dynamics is that of cohesive energy. In a liquid or solid material, a certain amount of energy is required to remove an atom from the material. This is referred to as the cohesive energy of the material. For the complete dissociation of a cluster, the cluster must absorb more energy from the incident laser than $N \times E_{\text{cohesive}}$. The cohesive energies for cluster materials used in this text are given in Table 4.2.

Table 4.2: Cohesive energy of cluster materials used in these experiments [55].

Material	E_{cohesive} (eV/atom)
Neon	0.020
Argon	0.080
Krypton	0.116
Xenon	0.16
Ag	2.95
Sb	2.75
Te	2.23

4.5 Cluster Dissociation

The dissociation of clusters ionized by XUV-regime (10-100 eV) laser pulses typically involves two phases. First, the outer shell of the charged cluster explodes in a Coulomb explosion. Thermalization of the remaining electrons in the quasineutral core results in evaporative outer-ionization of a few more electrons from the cluster [2, 86]. Finally, the inner, quasineutral core expands in a hydrodynamic explosion [50, 95]

4.5.1 Coulomb Explosion

Once a cluster is charged, a small cluster, or the outer shell of a large cluster, typically explodes due to Coulombic repulsion between the ions. Ions are peeled off in layers, with the maximum kinetic energy experienced by the outermost layer [49]. An ion in this outermost shell, with charge Ze experiences the kinetic energy

$$\begin{aligned} E_{max} &= \frac{Q(eZ)}{4\pi\epsilon_0 R} \\ &= \frac{n_l R^2 e^2 Z \bar{Z}}{3\epsilon_0} \end{aligned} \tag{4.12}$$

where $Q = (4/3)\pi R^3 n_l \bar{Z} e$ is the total charge on the cluster, \bar{Z} is the average charge per atom in the cluster, R is the cluster radius, and n_l is the cluster (liquid) density.

In the single photon ionization regime which describes the experiments here, Coulombic explosion yields predictable results. For smaller clusters, the average charge \bar{Z} is determined by the photon fluence on the cluster, and

hence, E_{max} is simply determined by the cluster size and the on-target fluence. However, for larger clusters, charge quickly builds up on the cluster to the point where outer ionization is frustrated. Here, the maximum kinetic energy due to Coulomb explosion is independent of the cluster size, and $E_{max} = h\nu - I_p$.

When the target cluster is embedded in an electric field, as it is when m/q measurements are being recorded, inner-ionized electrons may be separated from the ions by the field, allowing for inner-ionized electrons to contribute to \bar{Z} , and resulting in a higher E_{max} for a Coulombic explosion. Figure 4.7 shows the expected E_{max} due to 100% outer ionization for different cluster sizes and species at our maximum predicted fluences, with illumination by the 21st harmonic at 32.6 eV photon energy.

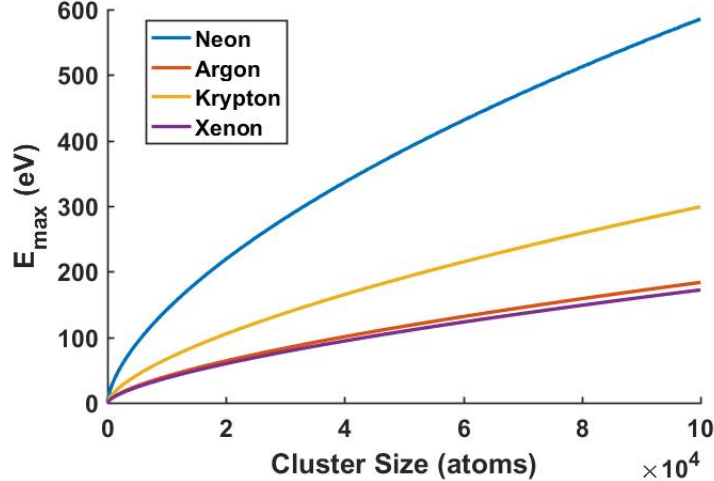


Figure 4.7: Maximum Coulomb energy expected if all electrons were outer-ionized, as a function of cluster size for different species of noble gas clusters, illuminated with the 21st harmonic wavelength (32.6 eV light of fluence 0.028 J/cm²).

4.5.2 Hydrodynamic Explosion

In the single-photon ionization regime, with negligible ponderomotive energy from the incident laser field, clusters become rapidly charged above the photoelectron energy, leading to a cessation of outer ionization. After the outer, charged shell of the cluster is removed via Coulomb explosion, the inner, quasineutral plasma core remains. Expansion of this core happens via hydrodynamic explosion. The warmer, trapped electron cloud expands beyond the boundaries of the cold ion cluster, creating an ambipolar electric field, and pulling the ions with them as they expand [23]. The speed of this hydrodynamic expansion can be approximated by the plasma sound speed

$$c_s = \left(\frac{\gamma Z k T_e}{m_i} \right)^{1/2} \quad (4.13)$$

where γ is the adiabatic index of the material (5/3 for a monatomic gas), Z is the average ion charge state, kT_e is the electron temperature, and m_i is the mass of the cluster ions. For an Ar cluster of 10,000 atoms (cluster radius 4.8 nm), illuminated with 0.028 J/cm² of 32.6 eV light, this yields a sound speed of approximately 31 m/s. So an expansion of 1 nm would require about 32 ps.

One telltale sign of hydrodynamic expansion is a strong exponential contribution to an electron energy spectrum (as opposed to plateau-like structure which indicates multistep photoionization and suggests a Coulombic shell explosion) [3]. Similarly, a nearly-featureless, continuously negatively sloped ion kinetic energy spectrum suggests a hydrodynamic expansion, while strongly

oscillatory behavior points to a Coulomb explosion. In our wavelength regime, simulations predict hydrodynamic contributions to ion kinetic energy spectra from inner shells of larger clusters, while the Coulomb explosion of the outermost shell contributes the majority of the distinguishable spectral features [3].

4.6 Formation of Condensed Gas Clusters

Condensed gas clusters are formed by supersonic expansion of compressed gas into a vacuum. The gas expands adiabatically, resulting in cooling and condensation into clusters. These clusters tend to form in an “onion-like” layered fashion, with each layer consisting of an icosahedral or cuboctahedral “shell,” with the icosahedral dominating at small cluster sizes, $\lesssim 750$ atoms, and cuboctahedral dominating larger clusters, forming the transition to a large scale bulk fcc crystal structure [36] [94]. Both shell shapes contain the same number of atoms per shell, where the total number of atoms N in a cluster with m complete shells is given by [13] [94]

$$N = \frac{1}{3}(2m - 1)(5m^2 - 5m + 3) \quad (4.14)$$

and the number of atoms in the m^{th} shell is

$$N_m = 10m^2 - 20m + 12 \quad (4.15)$$

where $m > 1$. $N_1 = 1$ for the single first layer core atom. Employing these formulae, Table 4.3 below shows the various sizes of clusters for different av-

erage N and shell number m .

Table 4.3: Estimates of characteristics of “magic number” clusters, composed of a given number of complete shells m .

m	N_m	N	N_m/N	d_{shell} (nm)				d_{liquid} (nm)			
				Ne	Ar	Kr	Xe	Ne	Ar	Kr	Xe
1	1	1	1	N/A				N/A			
2	12	13	0.92	0.5	0.6	0.7	0.7	1.0	1.1	1.1	1.2
3	42	55	0.76	1.0	1.2	1.4	1.3	1.6	1.7	1.8	2.0
4	92	147	0.62	1.5	1.8	2.1	2.0	2.2	2.4	2.5	2.8
5	162	309	0.52	2.0	2.4	2.8	2.6	2.8	3.0	3.2	3.5
7	362	923	0.39	3.1	3.7	4.2	3.9	4.0	4.4	4.7	5.1
12	1212	5083	0.24	5.6	6.7	7.8	7.2	7.1	7.7	8.2	9.0
15	1962	10179	0.19	7.1	8.6	9.9	9.1	9.0	9.7	10.4	11.3
17	2562	14993	0.17	8.2	9.8	11.3	10.4	10.2	11.1	11.8	12.9
19	3242	21127	0.15	9.2	11.0	12.7	11.7	11.5	12.4	13.3	14.4
20	3612	24739	0.15	9.7	11.6	13.5	12.4	12.1	13.1	14.0	15.2
21	4002	28741	0.14	10.2	12.2	14.2	13.0	12.7	13.8	14.7	16.0
26	6252	55301	0.11	12.8	15.3	17.7	16.3	15.8	17.1	18.3	19.9
27	6762	62063	0.11	13.3	15.9	18.4	17.0	16.4	17.8	19.0	20.6

We estimate the number of atoms in the outermost shell, N_m , the total number of atoms in the cluster, N , the ratio of surface to total cluster atoms, N_m/N , the diameter of the outermost shell, d_{shell} , and the diameter of the cluster in a random configuration with bulk liquid density, d_{liquid} . Ar/Kr/Xe

For an estimate of the intershell distance d_{liquid} , we use, as in [94], the distance between layers in the bulk fcc (111) solid of the noble gas [94] [47]. These interatomic distances are 0.255 nm, 0.306 nm, 0.354 nm, and 0.326 nm for Ne, Ar, Kr, and Xe, respectively [94].

Clusters produced by this method of adiabatic expansion into vacuum exhibit a lognormal distribution of radii [5], with a predictable average number of atoms per cluster $\langle N \rangle$. To estimate the average number of atoms in

each cluster, we use the Hagena relationship [43–45], with the correction for small cluster sizes developed by Buck [16], and corrections for large cluster sizes developed by Dorchies [29]. The formula developed by Hagena uses the gas jet nozzle parameters of diameter and cone angle, as well as gas species, temperature, and backing pressure, to estimate the average cluster size formed by the rapid expansion of that species into vacuum.

The so-called Hagena parameter, Γ^* is given by

$$\Gamma^* = K_{ch} \frac{p_0 d_{eq}^{0.85}}{T_0^{2.2875}} \quad (4.16)$$

where p_0 is the backing pressure of the nozzle, T_0 is the temperature of the gas before expansion, K_{ch} is a gas-dependent parameter which characterizes its tendency to cluster, and d_{eq} is the equivalent diameter of the gas jet nozzle. For a conical nozzle such as those used in the experiments described here, d_{eq} is given by $d_{eq} = 0.74d / \tan(\theta)$, where θ is the cone half-angle [16, 29, 43]. Table 4.4, below, gives the K_{ch} parameters for the gases used in this text.

Table 4.4: K_{ch} parameters for the gases used in this text.

Gas	K_{ch}
Neon	185
Argon	1650
Krypton	2890
Xenon	5550
N ₂	528
O ₂	1400
CO ₂	3660

The average number of atoms in a cluster, $\langle N \rangle$, is then determined as a function of the Hagena parameter, as shown in Equation 4.17. The original relationship, developed by Hagena, is given as $\langle N \rangle = 33 \cdot (\Gamma^*/1000)^{2.35}$, and is applied for $1800 < \Gamma^* < 10^4$. The relationships for other conditions were developed later by other researchers, when exploring the more extreme experimental parameters.

$$\langle N \rangle = \begin{cases} a_0 + a_1\Gamma^* + a_2(\Gamma^*)^2 + a_3(\Gamma^*)^3 & \text{for } \Gamma^* < 350 & [16] \\ 38.4 \cdot (\Gamma^*/1000)^{1.64} & \text{for } 350 < \Gamma^* < 1800 & [16] \\ 33 \cdot (\Gamma^*/1000)^{2.35} & \text{for } 1800 < \Gamma^* < 10^4 & [16, 45] \\ 100 \cdot (\Gamma^*/1000)^{1.8} & \text{for } 10^4 < \Gamma^* < 10^6 & [5, 29] \end{cases} \quad (4.17)$$

Where $a_0 = 2.23$, $a_1 = 7.00 \cdot 10^{-3}$, $a_2 = 8.30 \cdot 10^{-5}$, and $a_3 = 2.55 \cdot 10^{-7}$, as experimentally determined by Buck [16].

4.7 Formation of Metal and Metal Oxide Clusters

In addition to Van der Waals-bound gas clusters, we also investigate laser interaction with clusters made of typically solid materials. While the Hagena-style of cluster generation has been applied to materials such as metals, we instead employ the laser ablation of microparticles (LAM) method pioneered by Nichols, Lee, Keto, Brock, and Becker [70–73], along with the systemic designs and improvements developed by Gleason [41] and Erickson [34] to generate these nanoparticle cluster targets.

4.7.1 Laser Ablation of Microparticles

In order to generate nanoparticles of a predictable size, with a narrow size distribution, we ablate spherical microparticles which have been entrained in an inert buffer gas. An ablation laser, with fluence $> 2 \text{ J/cm}^2$ intersects a laminar stream of entrained microparticles and ablates the surface of the microparticles, initiating a shockwave which traverses the bulk of the particle and causes disintegration [60].

Nanoparticles condense in the region of gaseous target material in the rarefaction behind the shockwave. Their ultimate size is determined by the properties of the surrounding buffer gas, with heavier/denser gases restricting the expansion of the target material cloud, facilitating condensation and ultimately resulting in larger nanoparticles [72]. For the 1 atm of buffer gas pressure typical of the experiments discussed in this text, the 2 μm diameter silver microparticles used can be expected to ablate into nanoparticles of 5, 7, and 9 nm diameter for buffer gases of helium, nitrogen, and argon, respectively [72]. Their size distribution can be represented as a narrow lognormal distribution [34]. The nanoparticles produced by this method have been shown to be spherical and non-agglomerated [72].

4.7.2 Virtual Impactors and Gas Flows

Ablation of microparticles proceeds more predictably if the target microparticle aerosol is composed of particles of uniform size. While the microparticle “feed stock” used here is composed largely of spherical particles

of uniform size, agglomeration of these particles is common. To remove agglomerates and small pieces of dust or contaminant from the microparticle stream, we employ a two-stage virtual impactor system, described by Gleason [41]. This design follows the criteria laid out by Chen, for optimal nozzle and collector probe design, as well as optimal flow ratios to each impactor stage [18].

Impactors are inertial particle sorters. They sort aerosolized particles by size by impacting large particles onto a plate. A traditional impactor is shown in Figure 4.8(a) (Figure from [18]). Small particles are entrained in a buffer gas, which is directed through a nozzle and directly toward a plate. Particles are sorted via their momentum, as larger particles cross the gas streamlines and impact the plate, sticking to it and removing themselves from the stream of entrained particles. When used for long periods of time, the functionality of these impactors may change, as particles build up on the plate, potentially changing or obstructing the streamlines.

A virtual impactor, on the other hand, creates a virtual plate, still maintaining the smaller particles entrained in the major flow, while allowing the larger particles to be removed from the system in a minor flow through a receiving probe, as shown in Figure 4.8(b) (Figure also from [18]). This reduces sources of contamination of the major flow stream. Alternatively, it allows one to select for larger particles, directing the minor flow to the desired location downstream.

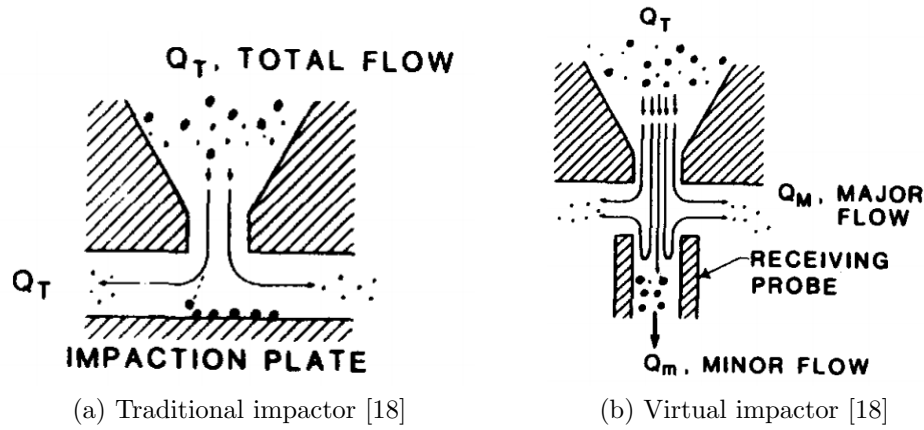


Figure 4.8: Basic design of a traditional impactor and a virtual impactor, for sorting microparticles by size. Figures from Reference [18].

Each virtual impactor has an input flow and an equal output flow. The output flow is partitioned into a minor flow, which flows through the receiving probe below the input nozzle, and a major flow, which flows out around the probe. Chen determined experimentally that the optimum ratio of receiving probe (minor) flow to input flow was 8% [18].

Thus, in a cascaded virtual impactor such as ours, where the major flow of the first stage becomes the input flow of the second stage, all flows are ultimately determined by a single set parameter. In our case, this is the major flow of the second stage, which flows unchanged through the ablation cell and through the continuous flow nozzle below, into a vacuum chamber. The flow of atmospheric pressure buffer gas through a 150 or 250 μm nozzle into vacuum sets the flows for each stage of our impactor.

The flows through the virtual impactor system and the dimensions of

the impactor nozzles and probes are related to the diameters of the sorted entrained microparticles by the Stokes number associated with the gas traversal through the input nozzle.

$$St = \frac{\rho_p v_0 C D^2}{9\mu d} \quad (4.18)$$

where ρ_p is the density of the particle material, v_0 is the gas velocity at the input nozzle throat, C is the Cunningham slip factor, D is the particle diameter, μ is the gas viscosity, and d is the nozzle diameter [18, 41]. For the particle cutoff diameter, the diameter at which half of the particles will go through the minor flow and half through the major flow, the optimal Stokes number is $St = 0.83^2$ [18, 41]. Thus, once the flows and buffer gas have been determined, the optimal nozzle diameter, d , for a given microparticle cutoff diameter D is

$$d = \left(\frac{4\rho_p C D^2 Q}{9\pi\mu(0.83^2)} \right)^{1/3} \quad (4.19)$$

Once the flows and nozzle diameters have been determined, the remaining dimensions of the virtual impactors are specified in terms of d [18]. Additional information about the cascaded virtual impactor assembly is contained in Section 7.3.2, and in [41].

Chapter 5

The THOR Laser

The Texas High-intensity Optical Research (THOR) laser, located on the 12th floor of RLM, is a Ti:Sapphire-based ultrafast laser system designed, constructed, and used primarily by CHEDS students, under the guidance of CHEDS faculty and staff. Operating at 800 nm, with a repetition rate of 10 Hz, THOR produces output pulses of up to 1.3 J. A recent re-design of the first amplifier stage, substituting a four crystal, two stage optical parametric chirped pulse amplification system (OPCPA) for the previous Ti:Sapphire-based regenerative amplifier, has increased our pulse bandwidth to over 60 nm, allowing us to achieve a final compressed pulse duration of less than 30 fs (FWHM).

The OPCPA upgrade had a myriad of benefits in addition to facilitating tighter pulse compression. Primary among these is the increased pulse contrast achieved. While the previous regenerative amplifier was itself the source of a string of prepulses in our compressed beam, an OPCPA not only does not generate these prepulses, but actually achieves significant “cleaning” of existing prepulses due to its nonlinear characteristics.

After the OPCPA stages, the still-stretched THOR pulses pass through

two multipass Ti:Sapphire amplification stages, dubbed “The 6-Pass” and “The 5-Pass,” each setup in a bowtie configuration. A pinhole spatial filter is employed after each stage of amplification, to maintain a good spatial profile. The telescopes containing the pinholes are designed to employ relay imaging of the beam, to decrease the maximum “lever arm” in the system and dramatically increase pointing stability. The fully amplified THOR beam is 1.3 J per pulse, before compression. Figure 5.1 shows a cartoon of the lab setup before the beam is transported through a wall and into the compressor chamber.

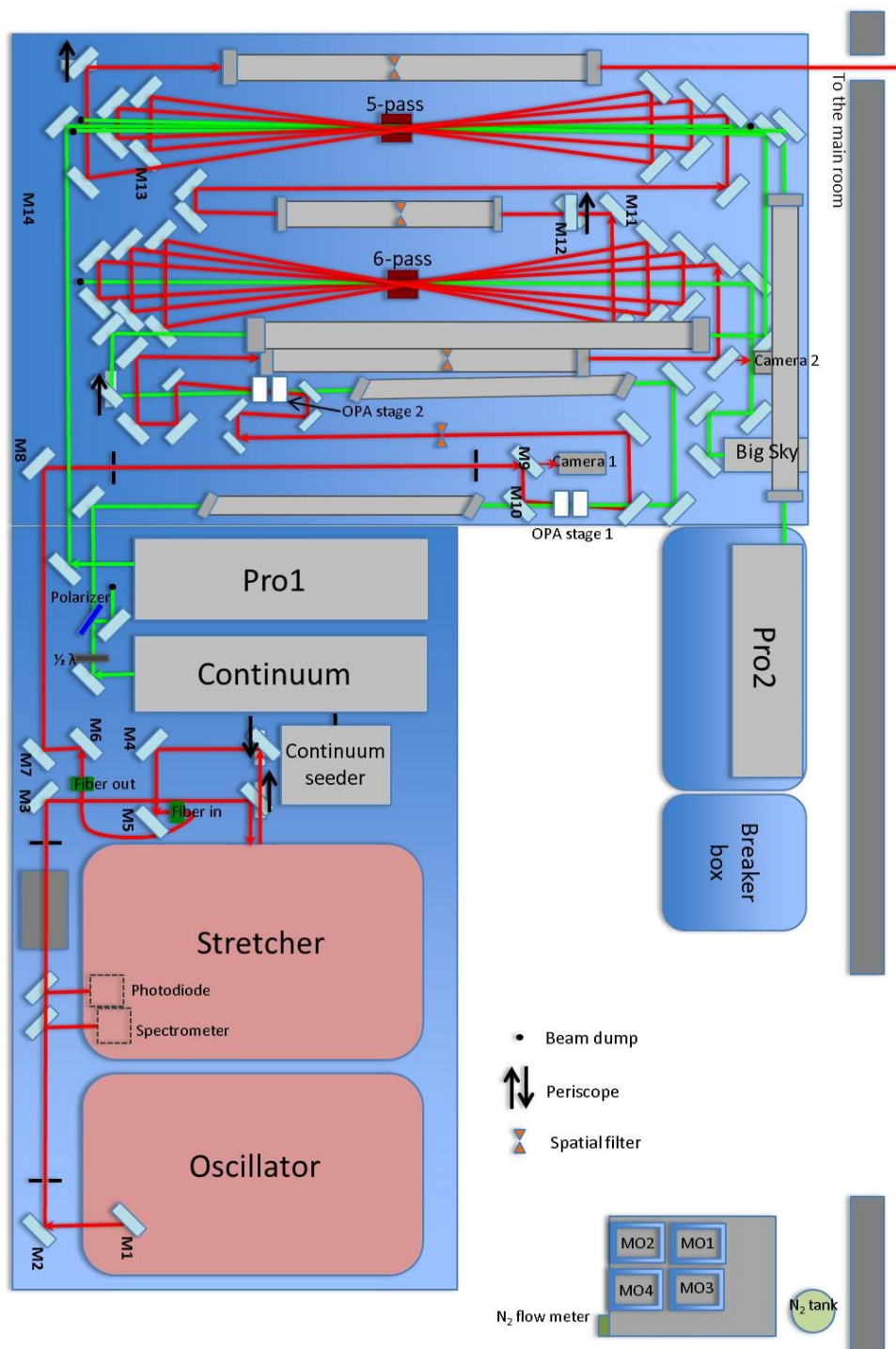


Figure 5.1: A schematic layout of the front end (oscillator, stretcher, and amplifiers) of the THOR laser 57

The fully amplified and compressed THOR beam can be used in either of two configurations, which may be quickly and easily toggled between, allowing two experimental setups to be present in the lab at once, and maximizing user efficiency of the facility. The “solid target beamline” utilizes THOR’s full energy at 800 nm, and allows the user to focus this energy directly onto a target of her choice. Using THOR’s $f/3$ off-axis parabola, a spot size of 6 microns has been measured, giving a peak intensity of $> 10^{19}$ W/cm². The “high harmonic beamline” allows the user to send the THOR beam through a long focus ($f/200$) beamline to a pulsed argon gas jet, to generate high-order harmonics of the 800 nm light up through the XUV regime (up to 48 eV). These harmonics may be separated from the fundamental frequency, and then individually reflected, to result in a tunable frequency XUV laser source. At 32.6 eV, we measured a pulse energy of up to 18 nJ on target.

5.1 The Front End

Before amplification, the THOR beam, generated by a Femtosome oscillator cavity, is pared down to a 10 Hz repetition rate, chirped in a stretcher, and sent through an optical fiber to optimize the the dispersion and spatial profile of the 800 nm beam. A Faraday isolator after the fiber output protects the front end from potential intensity spikes caused by a back-reflected beam.

5.1.1 Oscillator

The THOR oscillator is based on a Femtosource Ti:Sapphire cavity pumped by a 5 W (typically pumped at 4.5 W) Spectra-Physics Millennia VsJS 532 nm CW diode-pumped laser. The oscillator is passively modelocked via Kerr lens modelocking. Its final output is 8 nJ pulses at 800 nm, with a bandwidth of 40 nm FWHM, resulting in a 24 fs pulse duration.

The oscillator outputs pulses at a repetition rate of 73 MHz, which is immediately cut to 10 Hz, by sending the beam through a pulse slicer before the sending the pulses into the stretcher. The pulses from the THOR oscillator act as the master clock (timing trigger) for the rest of the laser system. Figure 5.2 shows the setup of the THOR oscillator.

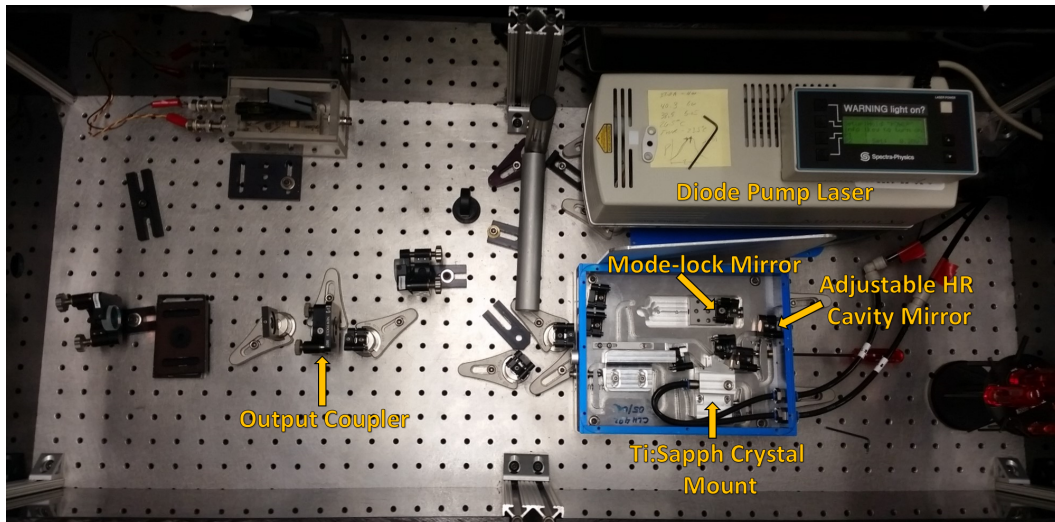


Figure 5.2: The front-end oscillator for the THOR laser

5.1.2 Stretcher

The development of chirped pulse amplification (CPA) by Strickland and Mourou [90] allowed for a dramatic increase in laser pulse energy. Broadband ultrafast pulses are first positively “chirped,” introducing a greater path length for high frequency components than lower frequency components, spreading the pulse energy out in time. The pulse can then be amplified, giving it a large total pulse energy while maintaining a low instantaneous intensity on optical components. This allows for the prevention of unwanted nonlinear interactions between the beam and transmissive material, thermal distortions, and damage to optical components. After amplification, pulses must then be sent through a compressor with negative group velocity dispersion, reversing the original chirp.

The THOR stretcher, designed with a folded Banks-Perry geometry [11], utilizes a large, rectangular grating (1480 lp/mm) with a flat mirror stripe at its center (see figure 5.3 (a)), along with one large spherical mirror (113 cm focal length), a separate flat mirror, and a vertical “rooftop” retroreflector to achieve a stretched pulse, with a total of four passes over the grating (two on the top half and two on the bottom). This results in positively chirped pulses which have been stretched in duration from 24 fs to 600 ps. Figure 5.3 (b) shows the setup of the THOR stretcher, with the numbers acting as a “connect the dots” to indicate beam position. The numbers indicating the beam on the grating are split into three rows, indicating the beam hitting the top grating, center mirror stripe, and bottom grating.

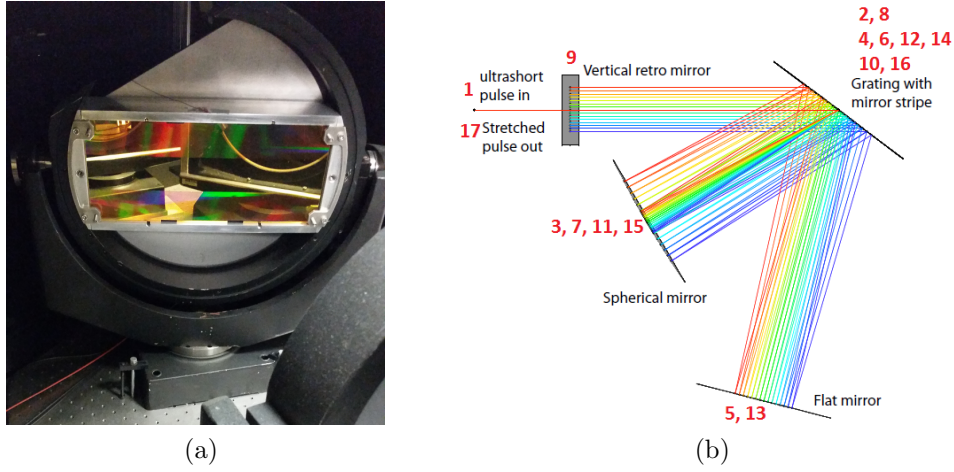


Figure 5.3: (a) THOR’s three-piece stretcher grating in its mount. (b) Ray trace diagram of the THOR stretcher (Figure from Reference[31]). Numbers indicate the beam position at each reflection.

This geometry sidesteps some of the issues with using a more traditional double-grating stretcher, such as the necessity of having two perfectly matched gratings. Theoretically, it allows a similarly-designed compressor to perfectly compensate for distortions in the spectral phase introduced up to the third order. Phase $\phi(\omega)$ can be expanded as a Taylor series in frequency ω about the center frequency ω_0 as:

$$\begin{aligned} \phi(\omega) = \phi_0 + \left. \frac{\partial \phi}{\partial \omega} \right|_{\omega_0} (\omega - \omega_0) + \frac{1}{2!} \left. \frac{\partial^2 \phi}{\partial \omega^2} \right|_{\omega_0} (\omega - \omega_0)^2 + \frac{1}{3!} \left. \frac{\partial^3 \phi}{\partial \omega^3} \right|_{\omega_0} (\omega - \omega_0)^3 \\ + \frac{1}{4!} \left. \frac{\partial^4 \phi}{\partial \omega^4} \right|_{\omega_0} (\omega - \omega_0)^4 + \frac{1}{5!} \left. \frac{\partial^5 \phi}{\partial \omega^5} \right|_{\omega_0} (\omega - \omega_0)^5 + \dots \quad (5.1) \end{aligned}$$

The zeroth order is inconsequential to the pulse shape, as it is just a constant. The first order represents the group delay, a shift in time of the entire pulse, also not affecting the ultimate pulse shape. The second order term represents

group delay dispersion (a temporal “chirp” in the pulse), and additional higher orders are referred to as “ n^{th} order dispersion,” where n is the number of the order being referred to. Ideally, each order above the first should sum to zero, when including the characteristics of the stretcher, the laser amplification path, and the compressor. This would result in a perfect transform-limited pulse at the system’s output. Non-zero elements can result in pulse duration broadening (FWHM), flat pedestal-type pre- and post-pulses (even orders) and oscillatory wing pre- and post-pulses (odd orders) [39].

In the THOR system, we use a combination of compressor path length (distance between the grating and the horizontal rooftop mirror, as described in Section 5.4.4), the compressor grating angle, and the dispersive characteristics of a variable length of fused silica fiber to best minimize the compressed pulse duration. Note that this can mean increasing the absolute value of the accumulated dispersion of one order to decrease the effects of another similarly even or odd order [39, 42].

5.1.3 Fiber

After being stretched, a laser continues to accumulate phase distortions from the dispersive characteristics of the additional optics (and air) in the system through which it passes. Thus, building a compressor with the identically opposite dispersive characteristics of the system’s stretcher cannot be expected to yield a transform-limited compressed pulse [39]. Additionally, a single-grating compressor, such as the one used in THOR, cannot on its

own compensate for the accumulated dispersion above the third order [68]. We employ a dispersive optical fiber to assist in zeroing the total accumulated dispersion, and allow us to approach a transform-limited compressed pulse duration. The primary benefit of the fiber is in decreasing the fourth order dispersion, which was found to be created in abundance via spherical aberration in the stretcher [42].

Directly after stretching the pulses, we send the THOR beam through an optical fiber (Thorlabs P1-780PM-FC-2: fiber patch cable, FC/PC connectors, 780 nm central wavelength, polarization maintaining, panda-style, 2 m length), which was experimentally determined to give the shortest pulse duration out of the compressor. This fiber allows us to adjust the dispersion added as changes are made to the overall THOR beam path, without needing to adjust other optics in our system. The delay accumulated in traveling through a material with index of refraction n and length l can be represented as

$$\tau(\omega) = \frac{l}{c} \frac{d}{d\omega} n(\omega) \omega \quad (5.2)$$

where l is the length of the material through which the beam passes, c is the speed of light in vacuum, and n is the index of refraction of the material, which may be calculated through the Sellmeier equation, given as a function of wavelength $\lambda = 2\pi c/\omega$ by

$$n^2(\lambda) = 1 + \sum_i \frac{B_i \lambda^2}{\lambda^2 - C_i} \quad (5.3)$$

where $\sqrt{C_i}$ are the wavelengths of absorption resonances in the material of strength B_i . Thus, by varying the length of the fiber, we are able to adjust the

total amount of accumulated fourth and higher order phase delay, to further optimize our pulse compression downstream.

The original fiber length for the THOR system which included a regenerative amplifier front end was determined by calculation by Will Grigsby [42]. The accumulated phase delay changed as the laser design was updated, and a decision was made to make an experimental discovery of the optimum fiber length for the new system. To determine the optimum fiber length, we vented the compressor to atmosphere, put the desired fiber in place after the stretcher, and minimized the pulse duration from the compressor by systematically scanning through the full angular range of the compressor grating, adjusting the path length of the compressor at each angle by changing the position of the horizontal rooftop in the compressor until the shortest pulse duration was achieved. Once the minimum pulse duration at the optimum angle was determined, this process was repeated with a new length of fiber. This process is described in more detail in Section 5.4.

Additionally, the fiber acts as a spatial filter for the oscillator beam, giving a near-ideal Gaussian output profile (see Figure 5.4). This mitigates the risk of hot spots in the amplified beam, which could damage optical coatings. The fiber output mount also gives us the ability to verify and adjust the collimation of the infrared beam before we send it to the amplifier stages, as shown in Figure 5.5. Directly after the optical fiber, we employ a Faraday isolation unit, to protect the fiber and upstream optics from stray reflections traveling upstream, which could damage them.

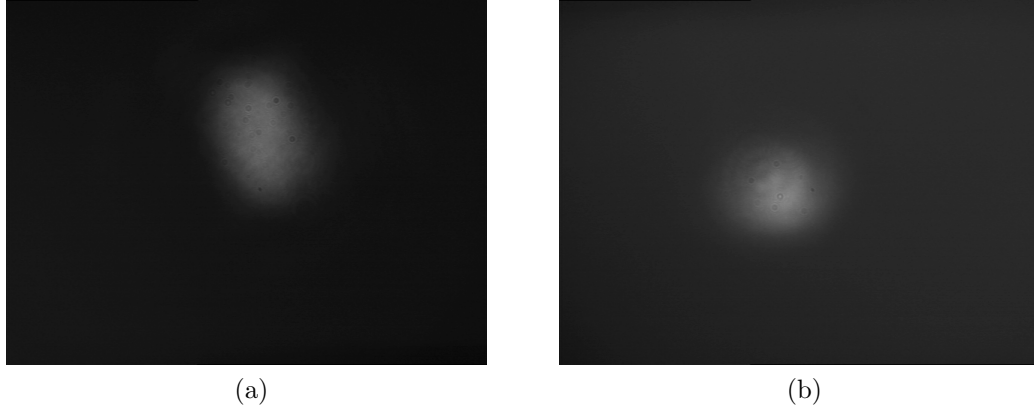


Figure 5.4: (a) A spatial profile of the oscillator beam taken before sending the beam through THOR's optical fiber. (b) A spatial profile taken directly after the fiber output, demonstrating a nearly Gaussian profile.

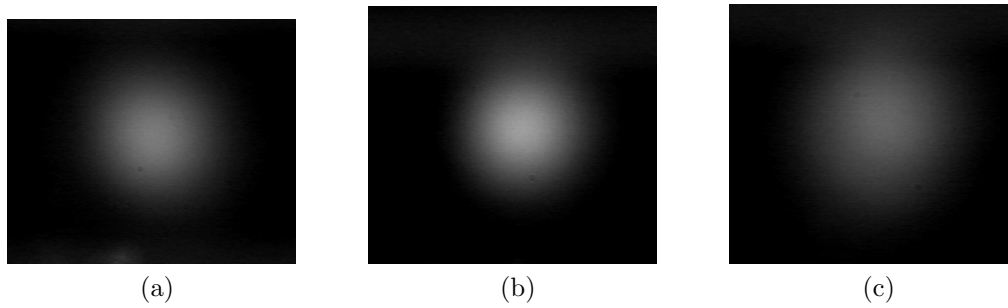


Figure 5.5: Far field collimation measurements taken after final adjustment of the fiber output collimation optics. The output beam was directed through a 40 cm focal length lens, and then images were captured (a) 2 cm in front of the focus, (b) at the focus, and (c) 2 cm behind the focus, using 10x magnification. We were able to successfully eliminate astigmatism from this portion of the laser.

5.2 OPCPA

The most influential component of the THOR upgrade was changing the design of THOR’s front-end amplifier. Originally a Ti:Sapph-based regenerative amplifier, we upgraded to a two-stage BBO-based optical parametric chirped pulse amplifier (OPCPA) design. The design consists of two pairs of β barium borate (BBO) crystals, each with dimensions of 10 mm x 10 mm x 12 mm length. Each pair is matched in length, with the second crystal having an optic axis opposite to the first, to ensure walkoff compensation.

The OPCPA amplifies the approximately 1 nJ pulses (cut down from 8 nJ out of the oscillator by the optics in the stretcher, fiber, and Faraday isolator) chirped pulses to up to 20 mJ, and broadens the originally Gaussian spectral profile from 40 nm FWHM to up to 80 nm FWHM. This allows for us to compress the pulse to shorter pulse durations than was previously possible, even with minor gain narrowing in the following Ti:Sapph amplification stages. Parametric amplification, as a nonlinear amplification process, also provides the benefit of pulse cleaning for any prepulses which may have been generated.

5.2.1 Parametric Amplification

Optical parametric amplification (OPA) is an application of the second-order nonlinear optical process of difference frequency generation (DFG). In OPA, the DFG conversion of a higher frequency, high-intensity “pump beam” is seeded with a lower-frequency beam to preferentially optimize the conversion to the seed frequency. This results in the amplification of the seed beam and

the production of an idler beam at the photon energy $E_{idler} = E_{pump} - E_{seed}$.

An energy-level diagram of this process is shown in Figure 5.6.

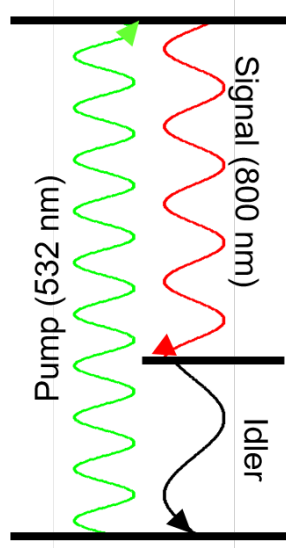


Figure 5.6: Cartoon energy level diagram of the DFG process used in the THOR OPA.

The complex material polarization $\tilde{P}(t)$ induced in a material that gives rise to the phenomenon of DFG/OPA can be expanded as a Taylor series as

$$\begin{aligned}\tilde{P}(t) &= \tilde{P}^{(1)}(t) + \tilde{P}^{(2)}(t) + \tilde{P}^{(3)}(t) + \dots \\ &= \epsilon_0[\chi^{(1)}\tilde{E}(t) + \chi^{(2)}\tilde{E}^2(t) + \chi^{(3)}\tilde{E}^3(t) + \dots]\end{aligned}\tag{5.4}$$

where ϵ_0 is the permittivity of free space, χ is the optical susceptibility, and E is the complex electric field incident on the material. If there are two laser beams present (pump and seed), with electric fields \tilde{E}_p and \tilde{E}_s , then the total electric field can be written as

$$\tilde{E}(t) = E_p e^{-i\omega_p t} + E_s e^{-i\omega_s t} + c.c.\tag{5.5}$$

where ω_p and ω_s represent the frequencies of the pump and seed laser, respectively, and c.c. represents the complex conjugate. Then the second order nonlinear polarization $\tilde{P}^{(2)}$ is

$$\begin{aligned} \tilde{P}^{(2)}(t) = & \epsilon_0 \chi^{(2)} [E_p^2(t) e^{-2i\omega_p t} + E_s^2(t) e^{-2i\omega_s t} \\ & + 2E_p E_s e^{-i(\omega_p + \omega_s)t} + 2E_p E_s e^{-i(\omega_p - \omega_s)t} + \text{c.c.}] \\ & + 2\epsilon_0 \chi^{(2)} [E_p E_p^* + E_s E_s^*] \end{aligned} \quad (5.6)$$

where the component representing difference frequency generation, and hence OPA, is highlighted in red [15]. The combination of the pump and the seed laser create the conditions for the generation of a third beam known as the idler at the frequency $(\omega_p - \omega_s)$. In the process, a pump photon is converted into an idler photon and a seed photon, to maintain conservation of energy. Thus the seed beam is amplified.

While this process is possible, Equation 5.6 shows that, for example, sum frequency generation (generation of a beam at frequency $(\omega_p + \omega_s)$) is also equally plausible, as is frequency doubling either of the two input beams. Which, if any, of these processes is selected for is dependent on the phase matching conditions. Phase matching refers to the minimization of the wave vector mismatch between the propagating pump beam and the generated/amplified signal and idler beams. Figures 5.7 and 5.9 show wave vector diagrams of the two types of phase matching, collinear and noncollinear, as they propagate through a (dispersive) nonlinear medium.

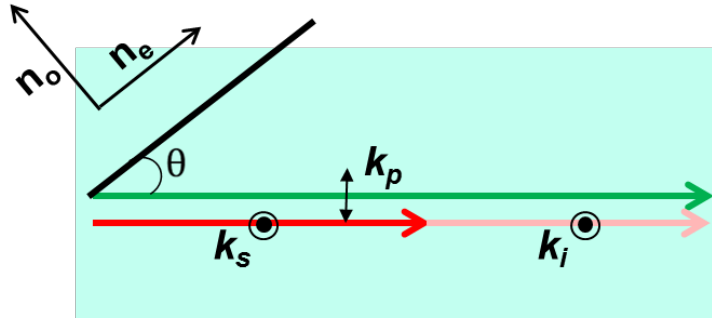


Figure 5.7: Collinear phase matching wave vector diagram

Collinear phase matching, as used in the GHOST laser, and as diagramed in Figure 5.7, refers to an alignment where the pump, seed, and idler beams are collinear, and have parallel wavevectors. While this makes alignment of the system much easier, Figure 5.10 shows why we could not use this system in THOR. Figure 5.10 shows a diagram of the wave vector mismatch Δk through a 10 mm BBO crystal (typical of the size and material we would need to use to achieve the desired gain in our system) as a function of seed beam wavelength for different angles of beam propagation to the crystal optic axis. (Since BBO is a birefringent crystal, this angle tunes the effective index of refraction these beams experience.) Here, a y-value of > 1 indicates that the crystal is longer than our coherence length L_{coh} is $L_{coh} = \pi/(\Delta k)$, and thus the wave vector mismatch is too large to allow for significant amplification.

At a seed wavelength of 1064 nm, as used in GHOST, we can see that a wide phase matching bandwidth may be achieved at an angle of slightly less than 23° . Unfortunately, at 800 nm, as in THOR, we would need exactly

22.233° to achieve any amplification at all, and its gain bandwidth would be severely, fundamentally restricted.

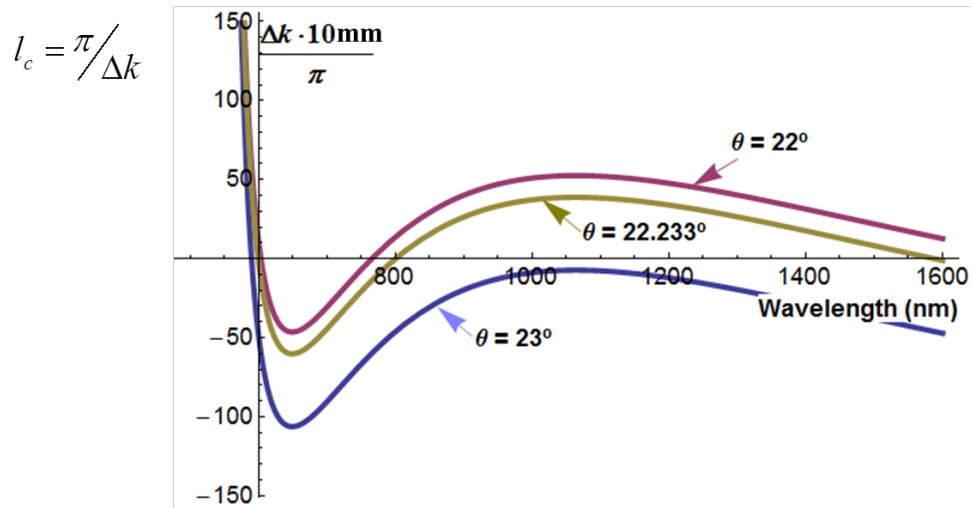


Figure 5.8: Collinear phase matching wave vector mismatch as a function of beam angles with respect to the optic axis

Noncollinear phase matching, as diagrammed in Figure 5.9, gives us another “knob to turn” to minimize the wave vector mismatch. In addition to varying the angle, θ , between the pump beam and the crystal optic axis, we may also adjust the angle, α , between the seed beam and the pump beam. Figure 5.9 shows specifically an example of Type I phase matching, where the seed and idler beams have the same (ordinary) polarization, and the pump beam is polarized perpendicularly, in the plane of the optic axis. Thus, it is the pump’s wave vector through the crystal that is adjusted by changing angle θ .

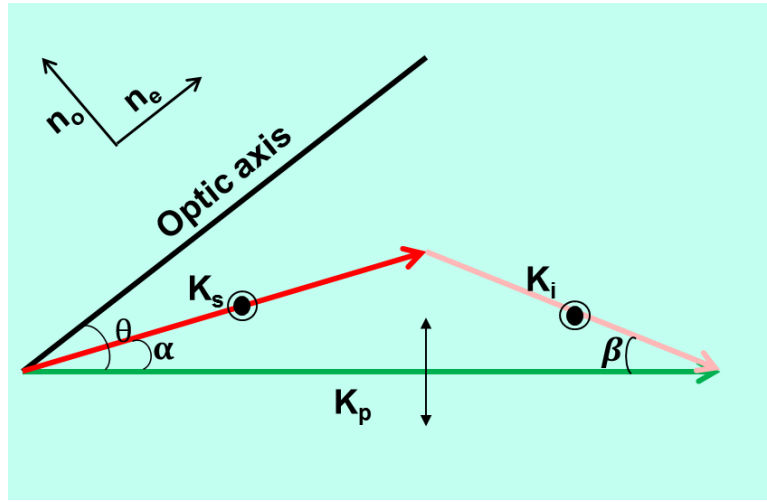


Figure 5.9: Noncollinear phase matching wave vector diagram

Figure 5.10 shows the wave vector mismatch with different adjustments in θ and α . With this scheme, we can adjust the local minimum in the graph in Figure 5.10 to fall around 800 nm, allowing us to minimize the wave vector mismatch over a broad spectral width (note the change in y-axis scale between the collinear and noncollinear figures). In Figure 5.10, the pink curve represents a minimization of Δk around 800 nm, maximizing gain here, while compromising overall gain bandwidth. A set of angles closer to our chosen set of angles for THOR are shown in the purple curve, exhibiting a tradeoff between bandwidth and amplification at the central wavelength. Section 5.2.3 has additional wave vector and gain calculations specific to our chosen setup.

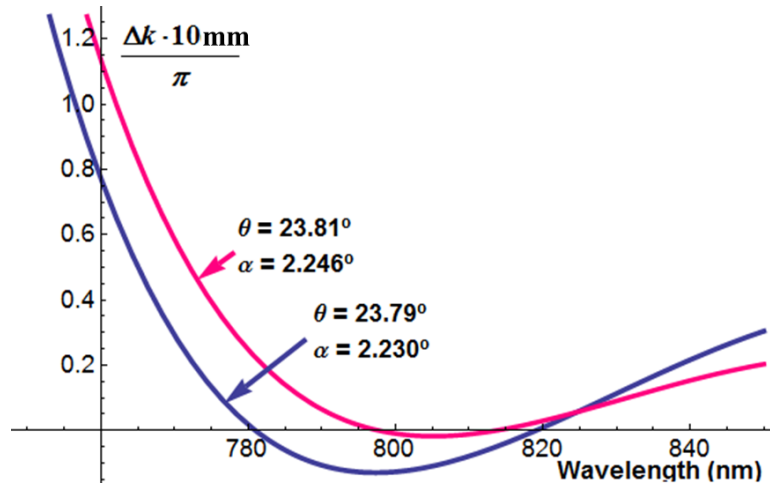


Figure 5.10: Noncollinear phase matching wave vector mismatch as a function of the pump beam angle θ with respect to the optic axis and the angle between the pump and signal beams, α .

5.2.2 Benefits and Drawbacks of OPCPA

The benefits of using OPCPA are manifold. Its high gain per length of gain medium allows for small, compact crystals to provide extremely high gain. Other than the obvious benefit of achieving high gain, this also allows a laser to reduce its path length through dispersive media, thus reducing the accumulated nonlinear phase shift (B-integral). Also, because parametric amplification is a second order nonlinear process, lower intensity portions of the beam, such as prepulses, reflections, and pulse pedestals, are not amplified to the same degree as the main pulses. This provides active pulse cleaning, in contrast to the prepulse train which was inherent in the regenerative amplifier replaced by the OPCPA.

Another benefit over laser-based amplifiers is the broad gain band-

width. At proper phase matching conditions, OPCPA can provide extremely high gain bandwidth. Conversely, laser-based amplifiers such as the Ti:Sapph regenerative amplifier create gain narrowing, due to their relatively narrow gain spectra, peaked around electron transition energies. Saturation in the OPA, in contrast, actually increases the bandwidth, continuing to amplify the low-intensity “wings” of the originally Gaussian spectrum after the main portion has become saturated, creating a flat-top spectral profile, which then experiences minor rounding via gain narrowing in the following laser-based multipass amplifiers.

Lastly, because parametric amplification involves no energy storage, there is negligible heat load deposited in the gain medium. This means that the BBO crystals in our OPCPA may be mounted in non-ablating, soft Teflon, instead of wrapped in indium, mounted in copper, and even actively cooled, such as our Ti:Sapph stages are. Teflon makes a mount which is forgiving to both the physical stresses on a crystal, as well as the alignment through the crystal; a misalignment through the multipass amplifiers risks ablating indium and copper from the crystal mount and depositing them on the surface of the crystal. Lack of heat buildup also means that the warmup time for the OPCPA stage to reach thermal equilibrium is negligible. Lastly, it means that thermal lensing, an effective gradient index focusing lens caused by the increased temperature (and hence increased index of refraction) in the center of the crystal as opposed to the actively cooled edges, is not a problem in an OPCPA.

Although there are many benefits to using OPCPA in place of standard laser-based amplification techniques, as with any design decision, the utilization of OPCPA is not without drawbacks. The high gain bandwidth achieved with the noncollinear phase-matching scheme employed in THOR also makes the amplifier extremely sensitive to the relative angles between the pump and signal beam and the optic axis of the gain medium. Temporal and spatial overlap of the pump and seed beams is also critical in OPCPA.

The lack of energy storage in the medium which makes for negligible thermal considerations in the amplification stage also means that the temporal intensity profile of the pump beam at the instant of overlap between the pump and seed is imprinted on the (chirped) seed beam, affecting both the temporal and spectral characteristics of the amplified seed, as discussed in Section 5.2.3. An unstable pump beam can cause a factor of 10 or more in shot-to-shot energy variation of the amplified beam, and may imprint oscillatory modulation into the spectral profile, affecting compression and potentially causing damage to downstream optics via intensity spikes.

5.2.3 The Design and Construction of THOR's OPCPA

Due to its high nonlinear susceptibility, its transparency in our wavelength range, and its ability to be manufactured to our physical specifications, β barium borate (BBO) was chosen as the OPCPA medium. As described in Section 5.2, our goal then was to find the correct crystal optic axis angle θ and crossing angle α to minimize the wave vector mismatch between the seed and

idler beam and the pump beam. With a goal of a bandwidth of 80 nm around a central wavelength of 800 nm, we can plot curves for each wavelength, setting $\Delta k = 0$, and finding the value of α as a function of θ . These curves are plotted in Figure 5.11. As is immediately obvious from Figure 5.11 (a), there exists a narrow optimum region of angle-space where these curves overlap, indicating that phase matching is near-optimum for each of our target wavelengths.

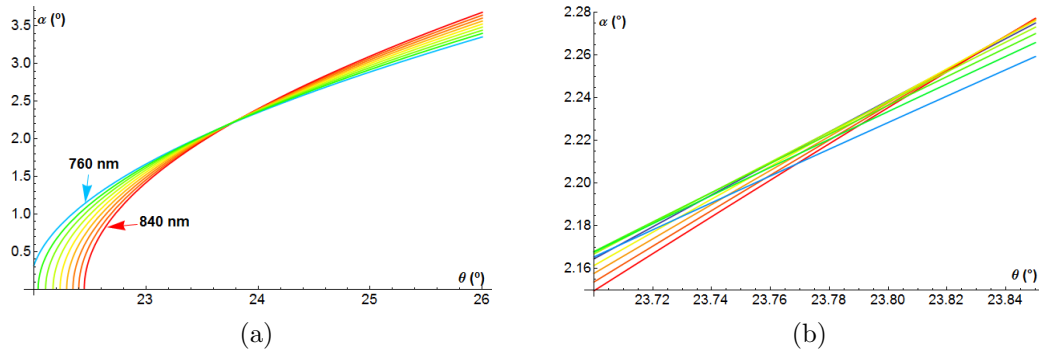


Figure 5.11: Curves of optimal values of noncollinear angle α as a function of crystal phase matching angle θ , for different wavelengths, setting $\Delta k = 0$.

As we zoom in on that near-optimal region in Figure 5.11 (a), we see in Figure 5.11 (b) that there is no single set of “magic angles” that perfectly match all wavelengths. This should be apparent also from Figure 5.10, as there is no perfectly flat region of the plot of wave vector mismatch, nor should we expect such a thing - an index of refraction which remains perfectly constant for a wide wavelength range.

Figure 5.12 shows the small signal parametric gain profiles for the chosen values for chosen set of angles, $\alpha = 2.38^\circ$ and $\theta = 23.83^\circ$. Just a small

angular deviation of 0.015° is enough to significantly distort the spectral profile and decrease the gain at 800 nm. The coupled equations which govern parametric amplification of this nature are

$$\begin{aligned}\frac{\partial}{\partial z}A_s &= \kappa A_i^* A_p e^{-i\Delta kz} \\ \frac{\partial}{\partial z}A_i &= \kappa A_s^* A_p e^{-i\Delta kz} \\ \frac{\partial}{\partial z}A_p &= -\kappa A_s A_i e^{-i\Delta kz}\end{aligned}\tag{5.7}$$

where A_s , A_i , and A_p are the complex amplitudes of the signal, idler, and pump, respectively, and κ is a constant term proportional to the d_{eff} of the material, associated with its nonlinear susceptibility. If the Δk for the desired signal/idler wavelengths are too large, for example due to their angles being misaligned, these equations can easily become the relevant equations for the “new” signal and idler caused by amplified parametric fluorescence (amplified spontaneous parametric downconversion).

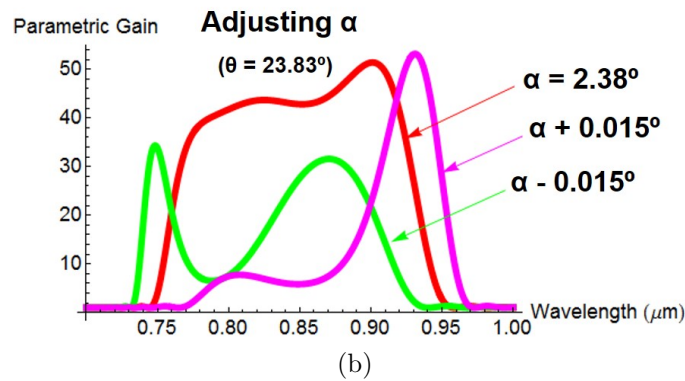
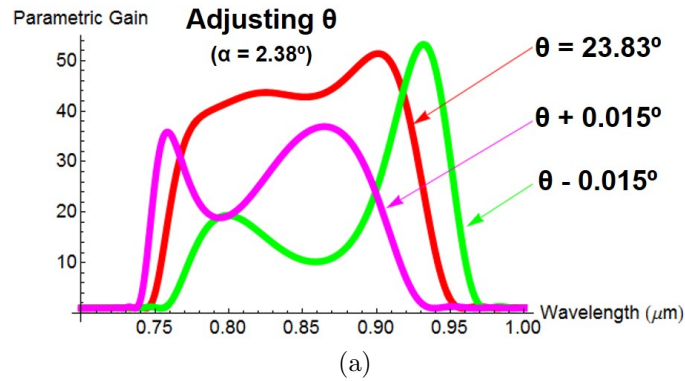


Figure 5.12: Small signal parametric gain for small deviations from the optimal values in (a) crystal phase-matching angle θ and (b) noncollinear angle α

These are the main factors taken into account in designing the OPCPA stages. Comprehensive details on the modeling and design of THOR’s OPCPA are contained in the doctoral dissertation of Ahmed Helal [46].

Extreme sensitivity to the phase-matching angle and noncollinear angle were not the only major hurdles in achieving a robust, properly-functioning OPCPA front-end for THOR. The other critical challenge proved to be the temporal stability of the Continuum Q-switched frequency-doubled YAG laser

used as the pump beam in the OPCPA stages. On first inspection, ensuring temporal overlap between a 600 ps seed beam and an approximately 10 ns pump beam does not seem like a difficult proposition. If the temporal pump profile were Gaussian, you would have to be within 1-2 ns of the peak to obtain good amplification efficiency. However, for a Q-switched laser, proper seeding of the oscillator cavity is critical for creating and maintaining a smooth, single-mode temporal profile which has good shot-to-shot temporal stability (low “jitter”). An example of a profile of an un-seeded shot from the Continuum laser is shown by the blue trace in Figure 5.13.

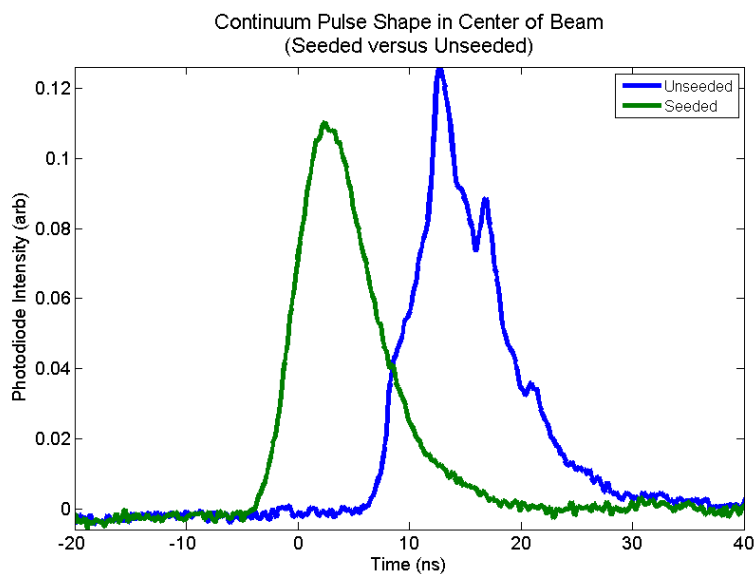


Figure 5.13: Temporal profile of the Continuum pump laser, seeded (green) versus unseeded (blue), as viewed with a fast photodiode. Seeding should result in a reduction of buildup time and a stable, single-mode temporal profile.

To achieve a well-seeded temporal profile such as the one shown in green in Figure 5.13, the Continuum laser has a CW diode laser, which may

be temperature-tuned to the desired wavelength, injected into the oscillator cavity. The alignment of this laser through the cavity is crucial, and the optimization of this alignment was a first priority in attempting to maintain a smooth, stable temporal profile.

To further optimize the seeder beam alignment, we modified the layout of the seeder injection into the Continuum oscillator cavity, assembling a new, more stable and adjustable mount for the seeder fiber output, and adding in an additional mirror, to allow for better positioning of the beam, as well as a half-wave plate, allowing us to fine tune the polarization of the seed beam to match that of the oscillator.

In addition to the physical position of the beam in the oscillator cavity, matching the wavelength of the seed beam (and hence the seeded pulsed oscillator output) to the cavity length is also crucial. Changes in room temperature, thermal properties of the gain medium, and other factors may affect this wavelength-cavity length matching. To maintain that matching in real time, the Continuum employs a feedback loop. A fiber positioned behind the high-reflector cavity mirror captures leak-through of the oscillator pulse through the mirror, and uses that to measure the build-up-time (BUT) of the pulse. The BUT is the time from the flashlamp trigger to the rising edge of the pulse, and minimization of this BUT is a good sign of a well-seeded pulse. Reduction of BUT with seeding can also be seen in Figure 5.13.

To minimize the BUT, software within the seed laser module controls a piezoelectric element attached to the high-reflector cavity mirror, which main-

tains a constant back-and-forth dithering motion, and continuously moves the mirror towards the direction which minimizes the BUT. The amplitude of the dither and magnitude of correction controlled manually via DIP switches on the seed laser box.

Another parameter featuring in the wavelength-cavity length matching is the actual wavelength of the seed laser. This wavelength setting is manually controlled with and monitored by an included computer software package. The desired wavelength is maintained by temperature control by a heater within the seed laser module.

The dramatic results which may be achieved by optimizing the seed wavelength are shown in Figure 5.14. Here, streak camera images of the output (amplified and doubled) Continuum pump laser pulses are shown. The horizontal axis represents a spatial dimension, and the vertical axis represents time. In Figure 5.14 (a), the “bullet-shaped” spatio-temporal profile, typical of Q-switched lasers, is shown. The BUT for the more intense (central) regions of the beam is shorter than for the edges. Figures 5.14 (b) and (c) show a temporally zoomed-in portion of the central leading edge, which gives a before and after image, respectively, of an adjustment to the temperature-wavelength tuning of the seed beam. The result of this tuning is a dramatic reduction to the intensity modulation in the pump laser. Because of the parametric nature of OPCPA, this modulation will imprint itself onto the amplified (chirped) seed beam, and potentially cause both intensity spikes and spectral modulation in the seed beam.

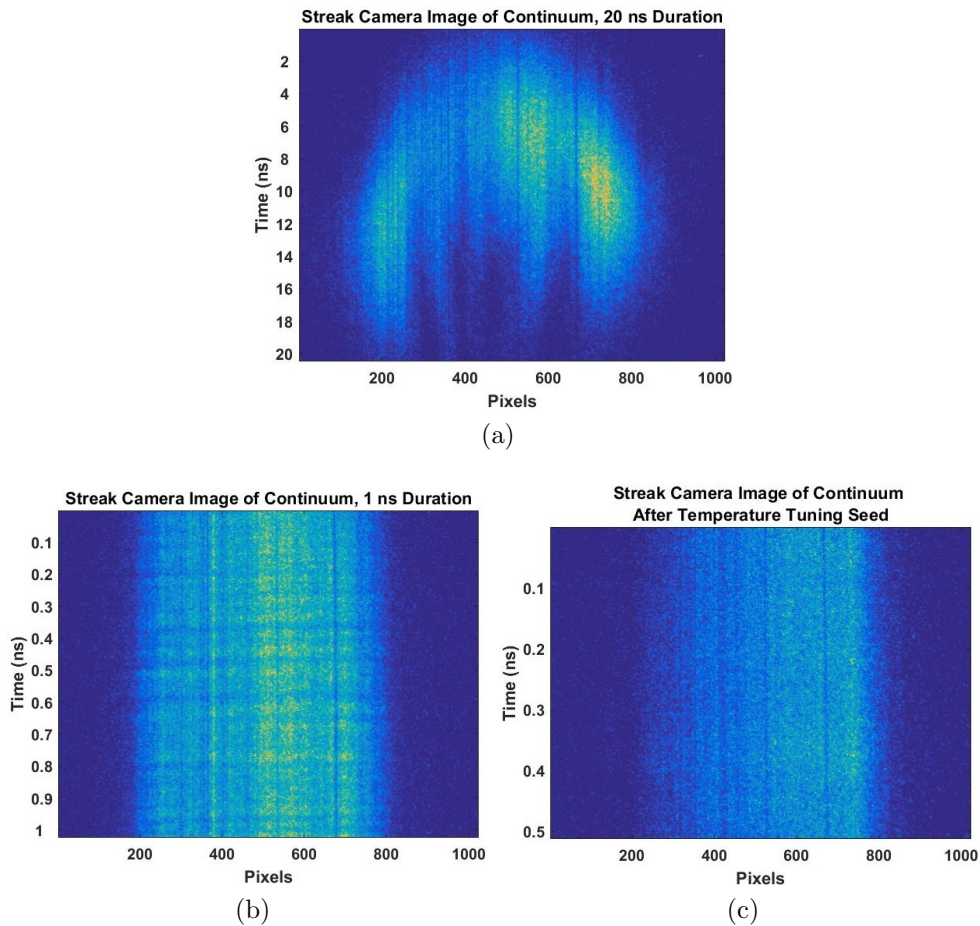


Figure 5.14: Streak camera images of pulses from the Continuum OPCPA pump laser. (a) Viewing the entire duration of the pump beam reveals a “bullet” shape, common in seeded Q-switched lasers such as this one, where the center of the beam appears before the edges in time. (b) A sample of the leading center portion of the pulse, zoomed in to a 1 ns duration streak. With this temporal resolution, we can see temporal modulation in the beam which could imprint themselves in the amplified OPCPA pulse spectrally. (c) A much smoother temporal profile achieved by temperature tuning the Continuum’s seed laser, adjusting its wavelength.

Once these fundamentals were solved, the THOR OPCPA alignment

was finalized. The overall layout of the THOR OPCPA is shown in Figure 5.1. The OPCPA BBO crystals (dimensions $10\text{ mm} \times 10\text{ mm} \times 12\text{ mm}$) were cut with their optic axis at 23.83° to the front surface. The full, 1 J, 7 ns, 532 nm Continuum pump beam is relay-imaged from the output of the laser to the plane between the first stage OPCPA crystals, in order to minimize potential ringing in the beam from damage or other hard edges (the flat-top spatial profile of the pump beam itself constitutes a hard edge). While the (physically larger, more energetic) pump beam is aligned straight through the OPCPA crystals, the seed beam is aligned at a crossing angle of 2.387° internal to the crystal, which translates to 3.968° externally, when the change in index of refraction is taken into account.

After crossing within the two first-stage crystals, the beams are separated via a dichroic mirror. The pump beam takes the external path, and is once again relay imaged, with the plane between the first stage crystals imaged to the plane between the second stage crystals. The seed beam is likewise imaged for stability, and passes through a pinhole at its focus to provide spatial filtering and to remove any co-propagating idler or fluorescence. It has extra path length added in an adjustable stage, to shift the portion of the pump beam which is converted to seed between the two stages, thus removing the effects of pump depletion in the first stage. The beams are aligned through the second stage crystals as through the first. They are separated downstream, where their crossing angle results in a sufficient physical separation to permit the use of two separate mirrors.

In the two-stage OPCPA, the seed pulses are amplified to 20 mJ of energy, and up to 80 nm of bandwidth in a somewhat flat-top profile as shown in Figure 5.18. Because of the non-absorptive nature of OPCPA, the approximately 500 mJ of unconverted 532 nm light from the Continuum laser is available to increase the pump energy on the 5-pass amplifier further downstream (see Section 5.3.2 for details).

5.3 Ti:Sapph Multipass Amplifiers

After the OPCPA stages, the now 20 mJ, still-chirped THOR pulses travel through two additional amplification stages, to increase pulse energy and energy stability. These stages are both multipass Ti:Sapph amplifiers, in a bowtie configuration. Ideally, they are both run in the saturation regime, to ensure shot-to-shot energy stability. Energy stability and stable gain bandwidth characteristics are the primary benefits of this form of stored-energy CPA. The minor drawbacks include a slight red-shift of the amplified beam, as well as some minor bandwidth narrowing.

Additional details concerning the modeling and design of THOR's multipass amplifiers are contained in the doctoral dissertation of Matthew McCormick [62].

5.3.1 6-Pass Amplifier

The 6-pass amplifier boosts the pulse energy from the output of the OPCPA from 20 mJ to 70 mJ. Run heavily saturated, the 6-pass can decrease

the shot-to-shot energy fluctuation from 50% of the pulse energy out of the OPA to less than 10%. The Ti:Sapph crystal used for this amplification stage is a 1 cm diameter x 1 cm long cylinder, with both faces cut at Brewsters angle. It is pumped by a 532 nm 200 mJ (at 532 nm) Quantel Big Sky CFR-400 Nd:YAG laser. The spatial profile and pass-by-pass energy measurements of the 6-pass are shown in Figure 5.15

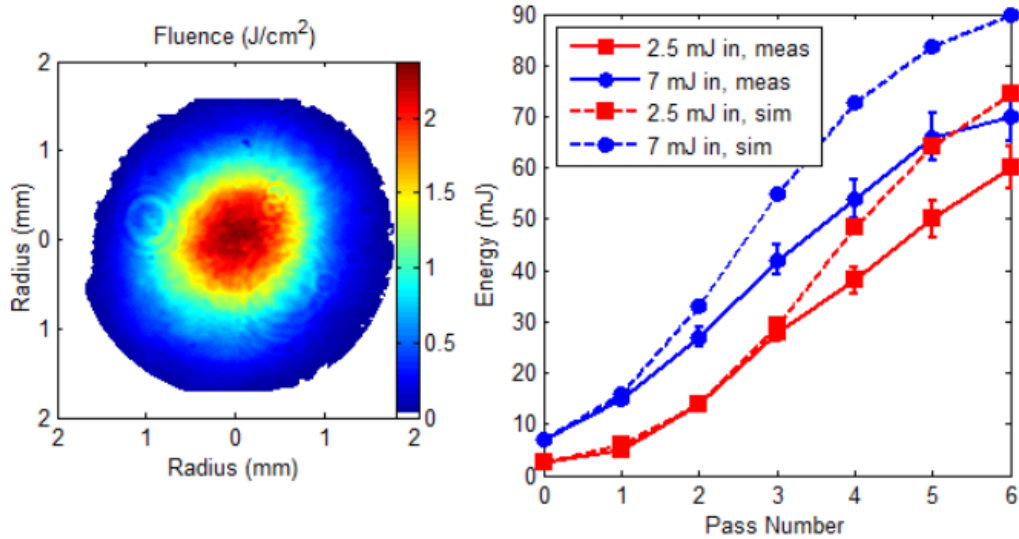


Figure 5.15: Measurements and simulations done on the amplified output of the 6-pass after converting the 4-pass amplifier to a 6-pass (Figure from Reference [62]). Note that at the time, the output of the OPCPA used to seed the 6-pass, was lower than at the time of publication of this document. Even so, we see the effects of saturation on the output energy.

After the last OPCPA stage, the beam is directed through an expanding telescope, constructed with a 75 cm focal length lens and a 90 cm focal length lens, with a 400 μm diameter pinhole at the focal plane of the first

lens, providing spatial filtering and magnification of the beam. It then passes through the amplifying Ti:Sapph crystal six times (increased from four during the recent THOR re-design), in a bowtie configuration, starting at a small angle, and working to the outside of the bowtie, as shown in Figure 5.1.

For mitigation of thermal effects, the amplifier crystal is mounted in a solid copper mount, and good thermal contact between the mount and the crystal is maintained by a layer of indium foil sandwiched around the crystal in the mount. The output profile of the 6-pass is shown in Figure 5.15. Due to the small tolerances in the design, and the large angles at the later amplification passes, damage to the surface of the Ti:Sapph crystal is the most common problem with this part of the THOR system. Small misalignments in one or more passes, from a sagging mirror or a misalignment at the input, can result in ablation of indium and copper from the crystal's mount, and deposition of this material onto the crystal surface. If not inspected and cleaned on a regular basis, this accumulation can lead to damage to the crystal itself, as seen in Figure 5.16. For this reason, we do not recommend amplifying the 6-pass to 80 mJ, as this increases the likelihood of damage.

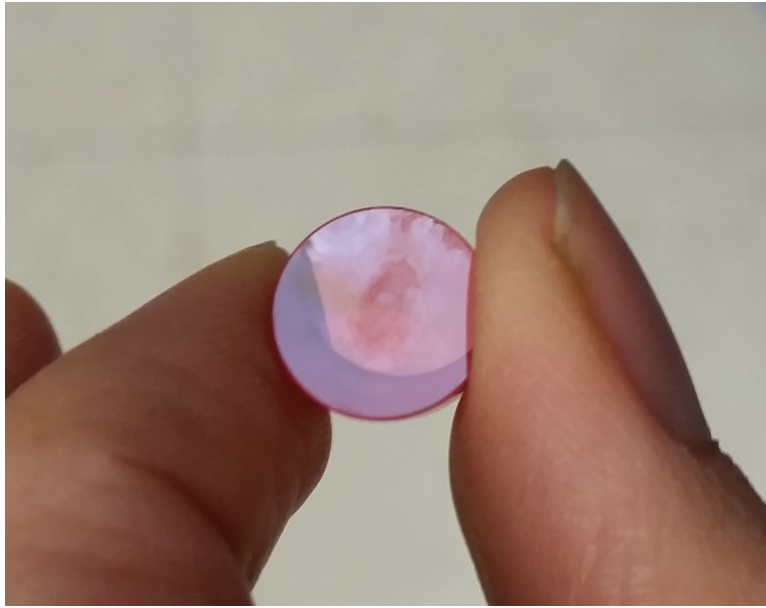


Figure 5.16: Damage to the 6-pass Ti:Sapph crystal, caused by deposition of indium onto the surface. What started out as damage around the top edge of the crystal eventually resulted in a full pump beam imprint in the center.

5.3.2 5-Pass Amplifier

After going through the 6-pass Ti:Sapph amplifier the THOR beam is again sent through a spatial filter (a 200 μm pinhole), to improve the spatial profile of the beam and to remove any accumulated hot spots. The spatial filter is at the focus of a magnifying telescope created with a 30 cm focal length front lens and a 1.25 m focal length lens at the output. While the first lens is mounted on a lens tube, the second lens is free, to allow translation. This is because the 5-pass seed beam is made intentionally diverging, to compensate for the thermal lensing which occurs in every pass of this final amplifier stage. The exact position of the second lens was determined experimentally, to pro-

duce a collimated output beam profile. The second lens is positioned 96.5 cm from the focal plane of the first lens (the position of the spatial filter pinhole).

The still-expanding seed beam slightly over-fills 1 inch diameter 5-pass crystal. This allows the beam to be aligned through the 5-pass amplifier by using the diffraction rings created on each pass. The “bull’s-eye” pattern created on each pass should be overlapped with each other to form a concentric pattern. The concentric ring pattern, as viewed with an IR-fluorescent “magic wand” tool, can be seen in Figure 5.17(a).

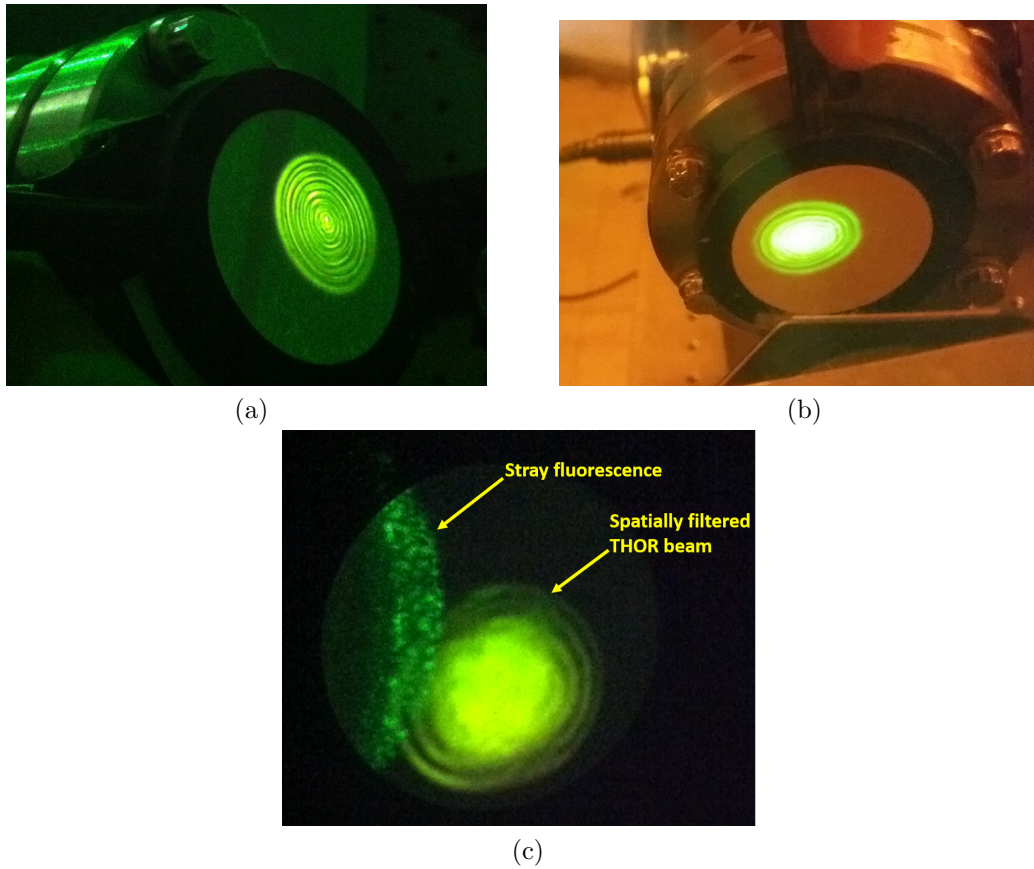


Figure 5.17: Concentric diffraction rings in the unamplified seed beam after transmission through all 5 passes of the final Ti:Sapph amplification stage. The image is made using a common alignment tool in THOR: an IR-fluorescent “magic wand” tool. (a) Seed beam from the 6-pass amplification stage is unamplified in the 5-pass (the Ti:Sapph crystal is not being pumped). (b) Seed beam being pumped by all three pump beams in the 5-pass, and amplified by the Continuum residual energy (PRO lasers mistimed, not amplifying the beam). (c) Seed beam as in (b), after passing through the spatial filter at the output of the 5-pass amplification stage.

The 5-pass amplifier is pumped with about 2.9 J of 532 nm pulses from three Q-switched frequency-doubled Nd:Yag lasers. As in the pre-upgrade

THOR design, two Spectra-Physics PRO350 lasers, each with an optimal output of 1.2 J at 532 nm impinge on the 5-pass Ti:Sapph crystal, one from each side. Each of these beams travels through a telescope, relay imaging the end surface of the last amplifier rod in the laser onto the surface of the 5-pass crystal. This relay imaging serves to minimize potentially damaging hot spots in the pump beams on the crystal. These spots develop from mid-field ringing about a damage spot in one or more of the laser rods. Imaging the damage spot onto the crystal surface prevents this ringing. Additionally, these telescopes magnify the pump beams on the crystal to 13 mm diameter.

During the THOR upgrade from a regenerative amplifier to an OPCPA, the lab obtained another 1 J output (at the frequency-doubled 532 nm) Q-switched Nd:YAG laser, to pump the OPCPA. Because parametric processes do not involve energy absorption and storage by the amplifier crystal, the energy not converted to signal and idler in the amplification process was available to pump the 5-pass. The excess energy, after conversion in the OPCPA as well as some losses from optics in the transport from the OPCPA to the 5-pass ends up about an extra 500 mJ on the 5-pass crystal. After the OPCPA, the residual light from the Continuum pump beam is raised to the height of the 5-pass with a periscope, then expanded in a vacuum telescope to 13 mm on the 5-pass crystal, to optimize spatial overlap with the other two pump beams.

Once these three pump beams are confirmed to be properly aligned on the crystal surface (using their low power or long pulse modes), and the seed beam is correctly aligned through the 5-pass path, the three pump beams

are Q-switched and raised to full power. At this point, a thermal lens develops in the crystal, resulting in a spatially compressed, distorted, but roughly collimated diffraction pattern in the seed beam, as seen in Figure 5.17(b).

Thermal lensing develops due to the change of index of refraction of common materials, such as Ti:Sapph due to their temperature. At the 10 Hz THOR repetition rate, the absorption of nearly 3 J of pump light results in nontrivial heat buildup within the crystal. If not properly managed, this heat buildup could produce thermal instability in the amplified beam, or could even lead to stress fracturing in the crystal itself. In THOR, this heat buildup is controlled by placing the 5-pass crystal in a copper mount, which is actively cooled by a constant flow of water from a chiller. Thermal contact is maintained between the crystal and the mount by a layer of indium foil sandwiched between the two.

The net result of this is a tolerable, stable thermal profile in the crystal after pumping with all pump beams for a short (few minute) warm-up period. Since the crystal is cooled only on its outer diameter, and pumped only in its center, a radially-dependent gradient develops in its index of refraction, with a higher index near the center of the crystal, and a lower index near the edges. An index gradient of this nature creates a converging beam, in the same fashion as a GRIN lens. Due to imperfect indium contact along the entire outer circumference of the crystal, the final, roughly-collimated seed beam has an “egg” shape, where one half of the beam converges more than the other half, as seen in Figure 5.17(b).

After passing through the 5-pass amplification stage, the beam is sent through another spatial filter, to remove the still prominent diffraction pattern caused by the finite crystal diameter. The filtered beam is shown in Figure 5.17(c). Removing these rings removes intensity spikes in the beam which may damage optics, and results in better compression characteristics.

An example of the spectrum of the THOR beam at all stages of amplification is shown in Figure 5.18. The spectrum out of the fully amplified laser closely follows the spectrum measured out of the OPA. In the 6-pass spectrum before and after turning on the Big Sky pump laser, we can see some evidence of the red-shift which characterizes such stored-energy stimulated emission amplification techniques as our Ti:Sapph crystals, when employed on a chirped seed beam. The spectrum out of the 5-pass amplification stage is significantly blue-shifted, and its bandwidth is lower than expected. This was partially alleviated by a re-alignment of the amplification stage.

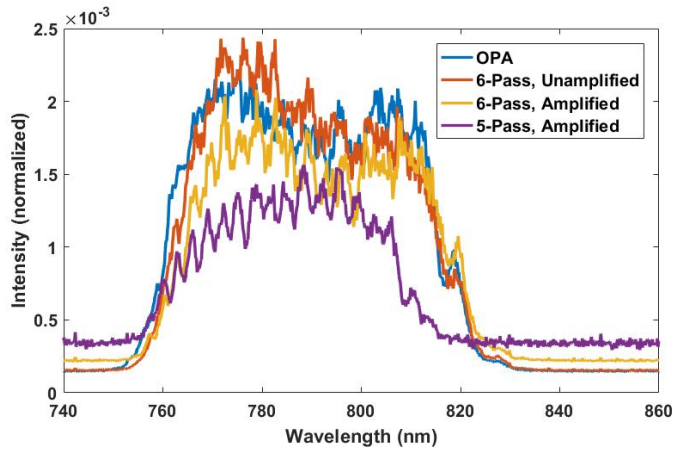


Figure 5.18: Spectrum of the THOR laser at all stages of amplification.

5.4 Compression

After amplification, the THOR beam is sent into the central room in the THOR lab to be re-compressed in a manner opposite to the way it was originally stretched. With quite a bit of adjustment to the compressor, to the dispersion-compensating fiber after the stretcher, and to the frequency spectrum of the amplified beam, we obtained pulse durations of less than 30 fs FWHM, as measured by a second-order autocorrelator.

For optimum compression, it is imperative that the beam be properly characterized for size, spatial uniformity, and collimation before being sent to the compressor. Figure 5.19 shows the beam profile before compression. It is large enough to avoid damage to the optics and is largely spatially “flat top,” without any major hot spots or ringing from diffraction. The beam shown in Figure 5.19 was then transmitted across the THOR lab, propagating 10 m from the plane of the first image, and another image was taken, with an identical size profile, down to the pixel, confirming proper collimation.

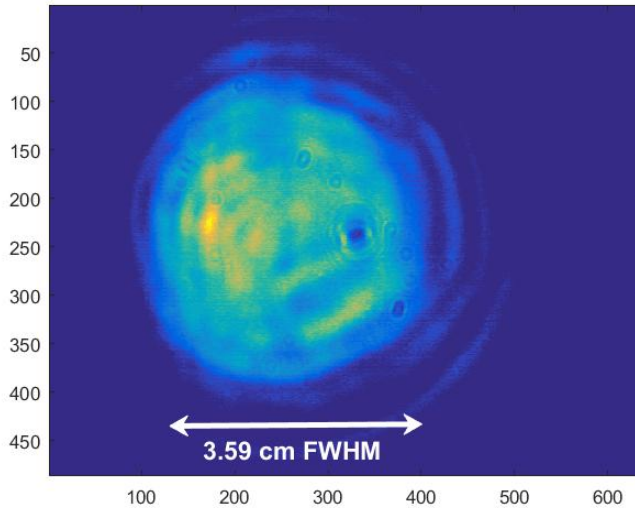


Figure 5.19: Spatial profile of the beam into the compressor. (Note that the dark spots in the center portion of the beam are from dirt and damage on the camera setup capturing the image, and not on the beam itself.)

The final compressor throughput is 50% of the input pulse energy, without the pickoff mirror or outer shaping iris. The best compressed pulse duration measured was below 30 fs FWHM. We have observed that the compressor optics impart a measurable amount of astigmatism to the fully compressed output beam.

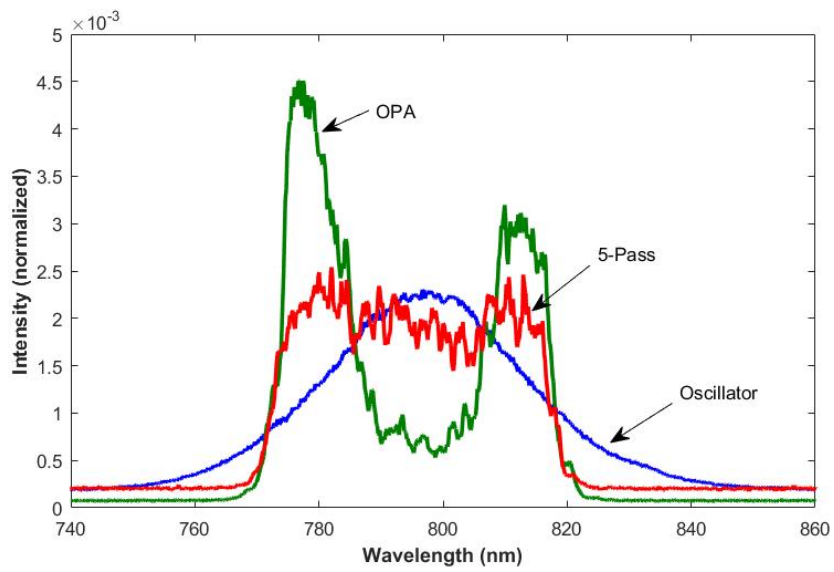
5.4.1 Transform Limited Compression

As discussed above, the ideal pulse out of the compressor would be of transform-limited duration. That is, we could predict the exact temporal profile of each pulse from a measurement of the spectrum out of the last amplification stage of THOR, assuming zero relative phase delay for each spec-

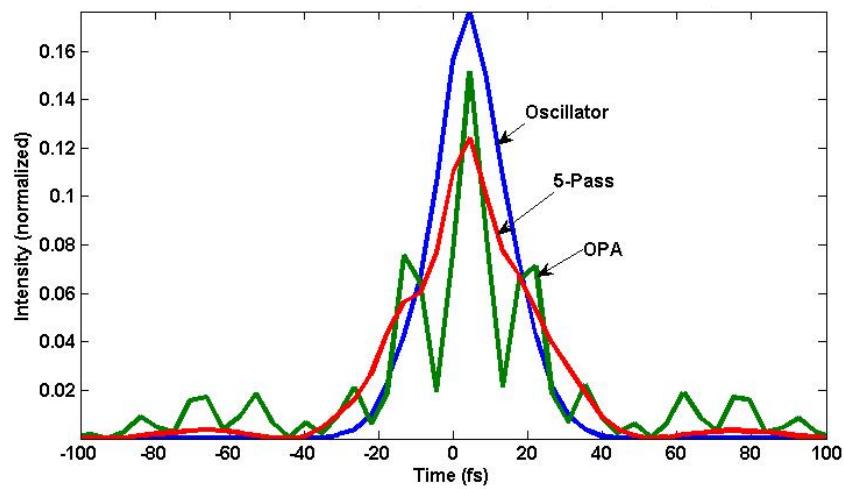
tral component. Examples of transform-limited pulse shapes are shown in Figure 5.20. The electric field of a laser pulse as a function of time, $E(t)$, can be decomposed into its spectral components using a Fourier transform, $E(\omega) = \mathcal{F}\{E(t)\}$. Because $I(t) = (E(t))^2$, if we assume that there is no residual phase delay as a function of frequency left after compression, we can calculate the temporal pulse shape of a transform-limited pulse using only its measured spectrum $I(\omega)$ using

$$I(t) = (\mathcal{F}^{-1}\{I(\omega)^{1/2}\})^2 \quad (5.8)$$

where $I(t)$ and $I(\omega)$ are the intensity as a function of time and frequency, respectively.



(a)



(b)

Figure 5.20: (a) Spectra for an example day from the oscillator, after the OPA front end amplifier, and at the output of THOR, after the 5-pass amplifier. (b) Transform-limited temporal pulse shapes for these spectra.

From these spectra, we can see that FWHM bandwidth is only one important consideration when attempting to shape the compressed output pulse. While the near-Gaussian oscillator spectrum results in a similarly Gaussian short-duration output pulse, pushing the OPCPA into an extreme broad spectrum mode where back-conversion exists for the high-intensity spectral components of the seed beam results in a temporal beating of the two ends of the spectrum, creating intensity oscillations which extend out for potentially over 100 fs. Likewise, the wide, relatively flat-top spectrum we see from the 5-pass amplifier (a good measurement of the final THOR output) does not compress to a sub-30 fs Gaussian pulse, but actually has a much broader FWHM, as well as “wings” which peak about 70 fs before the main pulse. These are all factors to consider when adjusting a the laser output spectrum (primarily via the OPCPA) for a given application.

5.4.2 The THOR Compressor

Because of the ultimate intensities involved, self-phase modulation and other undesirable interactions would be expected were we to propagate the compressed THOR pulses through any medium, including atmosphere. Because of this, the compressor, as well as all post-compression beam propagation, is maintained under vacuum, and only reflective optics are utilized. The layout and ray trace diagram of the THOR compressor is shown in Figure 5.21 [31].

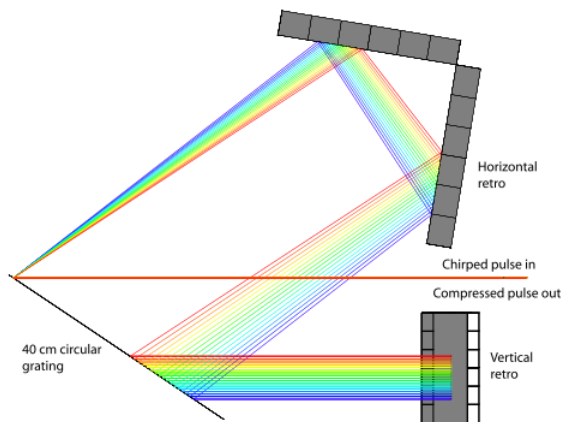


Figure 5.21: Ray trace diagram of the THOR compressor (Figure from Reference [31]). The setup includes a single large grating, over which the beam passes four times, translated each time by the vertical or horizontal rooftop mirror. Path length through the compressor is adjusted by changing the distance between the horizontal rooftop mirror and the grating.

The chirped, amplified pulses enter the compressor through a port window and pass directly to the bottom-right section of the 40 cm diameter circular gold grating, with (1480 lp/mm). The first-order diffracted beam travels to the horizontal retroreflector “rooftop” mirror, and is translated back to the grating, to hit the bottom-left section. It is then diffracted to the vertical retroreflector, translated up, and sent back to top-left portion of the grating. From this third bounce off of the grating, it is translated horizontally once again by the horizontal retroreflector, and then back to the top-right portion of the grating. Finally fully compressed, it exits the compressor in a path just above its entrance, and is directed to a remotely-controlled steering mirror, to be directed to either the solid target beamline or the high harmonic generation

beamline. Figure 5.22 shows an example of the real-time camera diagnostic which shows the beams on the grating.

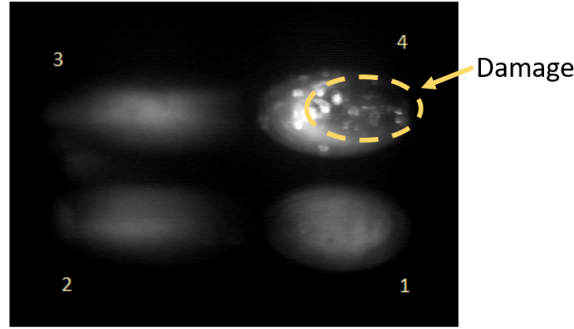


Figure 5.22: Camera image of the four bounces of the beams off of the THOR compressor grating. The left two bounces are while the beam is spread spatially into its frequency components, providing a visual diagnostic of the current spectrum of the beam entering the compressor. The top-right spot is the fully compressed beam, which can damage the grating over time. This image was taken before the grating was rotated 180 degrees, to move the main damage spot from the main beam path, as described in Section 5.4.4

5.4.3 Second-Order Autocorrelator

The second-order autocorrelator is, as of the writing of this dissertation, THOR's only temporal diagnostic tool. When the laser is used with the HHG beamline, it is able to provide an on-shot estimate of the THOR temporal duration and profile. The center of the THOR beam is sampled at the output of the compressor using a mirror suspended on wires. The mirror is elliptical in shape, such that when angled at 45 degrees with respect to the laser axis, its projection onto the beam profile is a 0.5" circular shadow. This shadow is necessary for the proper functioning of the harmonic generation beamline, as

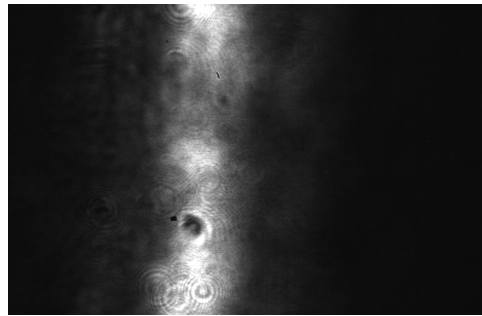
described in Section 6.2, so the beam is sampled on every shot.

The sampled portion of the beam is directed downward to a mirror below it, and two more mirrors are employed to transport the beam at the correct position and angle into the autocorrelator. The beam is split, using a 50/50 beamsplitter, and one of the beams is sent at a 3 degree angle to the surface of a thin β barium borate (BBO) crystal. The other is directed through a delay stage with an encoded motor, and then to the surface of the crystal, overlapping the first beam, and crossing at the same angle to the crystal surface, but from the opposite direction.

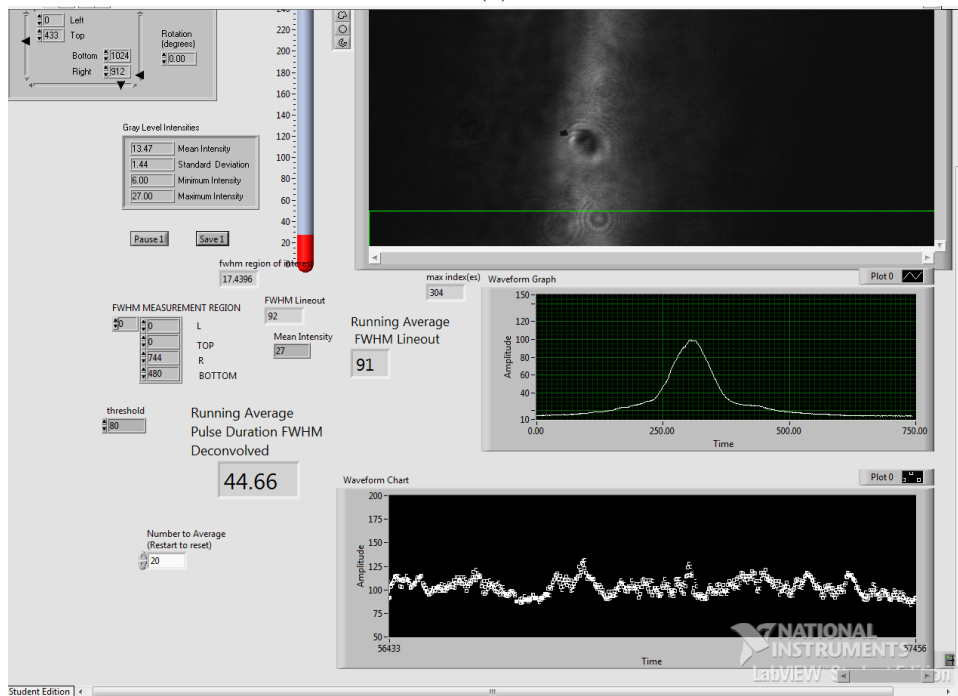
The nonlinear crystal properties produce doubled blue light from each beam. Since doubling is intensity-dependent, when the two beams are overlapped temporally, that is, the delay stage is in such a position as to create zero time delay between the two beams, the overlapped (in time and space) portions of the beams produce a much brighter blue line, traveling in a direction halfway between the two angled beams. The width of this line represents the duration of overlap, and hence the duration of the beam itself. The line at the back surface of the crystal is imaged with a single lens and periscope to the plane of the CCD camera mounted just outside a port window. Once on the camera, the pixels-to-time conversion may be done by translating the encoded stage forward and backward a known distance, and watching the line move a corresponding number of pixels left and right on the camera.

The image on the camera is captured by a labVIEW program, as shown in Figure 5.23. This program obtains a lineout of the user-selected portion of

the camera image and displays this lineout. This may give the user an idea of the overall shape of the pulse, and whether it might have “wings.” The full width at half maximum (FWHM) of this lineout is measured, and a Gaussian deconvolution factor applied, along with the known pixel-to-time calibration. This number is displayed as the estimated pulse FWHM. The FWHM in pixels is plotted in a running chart at the bottom of the program GUI, to give the user a good idea of the general trend and stability of the pulse duration.



(a)



(b)

Figure 5.23: (a) The raw camera image from the THOR autocorrelator camera. This image is then captured by a LabVIEW program, shown in (b), and a lineout profile is displayed for the user-selected part of the image. A FWHM calculation is done on the lineout, and the deconvolved FWHM is given as an on-shot measurement or as part of a running average. To facilitate quick compression optimization, this FWHM is also plotted at the bottom of the screen, as the information for each shot arrives.

5.4.4 Aligning the Compressor

In the upgrade involving switching the front end THOR amplifier from a regenerative amplifier to an OPCPA format, as well as changing the number of passes through the first multipass Ti:Sapph amplification stage, the dispersion experienced as the beam traverses the system was also affected, making adjustments necessary both to the compressor alignment as well as the length of dispersion-compensating fiber introduced for optimum compressed pulse duration. The adjustment process was done experimentally, fixing problems as they arose and working toward optimum energy throughput and pulse compression.

Upon the initial recommissioning of the THOR compressor following the upgrade, we went through the first order optimization routine of adjusting the compressor input and output steering mirrors for optimum alignment, as well as performing a full angle scan with the compressor grating. An angle scan consists of the iterative process of setting the angle of the grating to the incoming beam at the estimated optimum angle, adjusting the compressor path length by moving the horizontal retroreflector mirror pair (on an encoded, motorized translation stage) toward and away from the compressor until the minimum pulse duration is achieved, recording this pulse duration, and then adjusting the grating angle by a small amount and repeating the process. In this way, the user determines the angle and path length combination which produce the best compression.

When we finished this procedure, we discovered that the throughput

of the compressor, the pulse energy at the output with respect to the pulse energy at the input, was very low - only 30%. Predicting that the grating had become contaminated with hydrocarbon deposition (perhaps from the oil-lubricated Sargent Welch turbomolecular pump on the compressor chamber, which had experienced a failure and produced a backflow of lubricant into the compressor vacuum chamber), we attempted to clean the grating, and the inside of the compressor in general, with long exposure to a UV-producing lamp. Unfortunately, this failed to improve the throughput.

The final bounce of the compressed beam onto the compressor grating had left a noticeable damage spot on the grating, as shown in the bottom left corner of the grating in Figure 5.24, from long-term exposure to the high-intensity pulses. This damage spot, being 100% overlapped with our laser energy, could cause our throughput problems. To mitigate this loss, we rotated the compressor grating 180° in its mount, so that the damage spot would overlap with only a portion of the spectrally expanded bounce on the bottom left portion of the grating. This indeed improved the compressor throughput to 40%.

Additional sources of energy loss from the compressor were discovered as we continued the optimization of the compressed pulse duration by changing the length of our dispersion-compensating fiber after the compressor. It appeared that we should be able to get better compression with shorter fiber lengths, but shorter fibers produced spectral clipping on the vertical retroreflector. The spatially-expanded spectrum would walk off of the retro mirror

pair at the grating angles required for best compression, yielding both low throughput and poor compression. To fix this, we adjusted the position of the motorized rail holding the horizontal retroreflector pair sideways (rotationally about the grating) to adjust the total horizontal distance the beams would be translated, and thus translate the beams back onto the vertical retroreflector. Following another scan through the available fiber lengths (with a full angle scan for each fiber), we achieved 56% throughput in the compressor. Additional attempts at cleaning this with the UV lamp decreased this throughput to its final value of 50%.

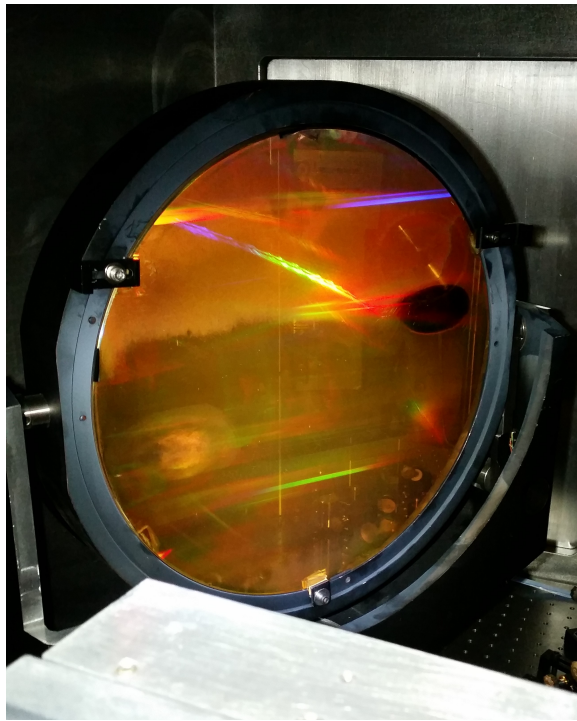


Figure 5.24: Image of THOR's compressor grating after rotation, with both damage spots visible - the original on the bottom left, and the new damage/clean spot on the top right.

While characterizing the compressed far-field, using the long-focus HHG beam path, we discovered what appeared to be an astigmatism, but what might more accurately be called angular chirp. The beam focused well when sending the 800 nm alignment diode through the compressor, but focused to a line when sending the full THOR spectrum through the system. Additionally, when blocking a small portion of the center of the oscillator spectrum by placing a thin post in front of the vertical retroreflector in the stretcher, a corresponding dimming of the center of the line focus was observed.

Angular chirp such as this could be caused by a misalignment of the horizontal retroreflector, so we set up a diagnostic to verify the 90 degree angle between the two mirrors. The setup for this is shown in Figure 5.25. As shown in the figure, we did discover that the horizontal rooftop was misaligned - the input and output beams of our diagnostic were not parallel, but were in fact converging. We adjusted the retroreflector until the two beams were parallel to each other and in a plane parallel to the optical breadboard in the compressor. However, this did not alleviate the angular chirp observed in the far field.

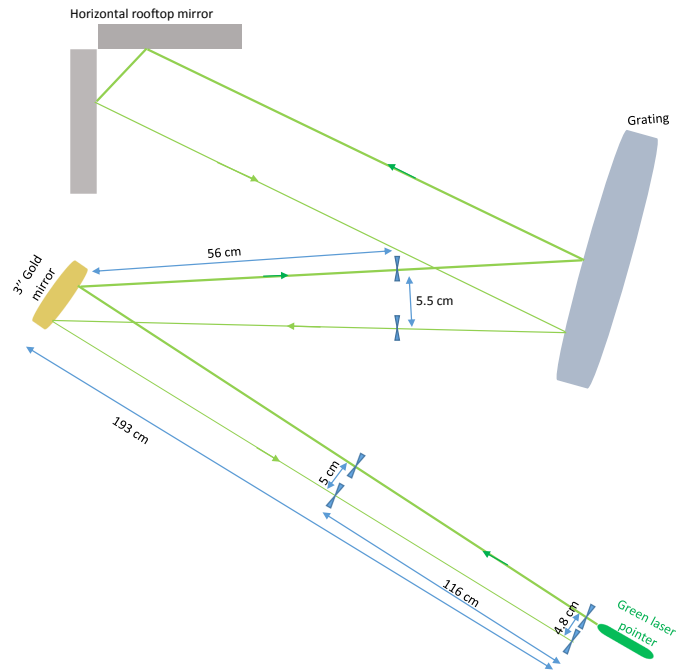


Figure 5.25: Layout for testing the parallelism of the horizontal retroreflector without removing it from its place in the compressor chamber.

With the expectation that our diagnostic was not sufficiently accurate, we removed both the horizontal and vertical retroreflector pairs from the compressor, and put them on an empty optical table. We discovered that the springs on the mirror mount holding the (large, heavy) horizontal retro mir-

rors had fatigued over time, so we replaced these springs and also improved the rigidity of the fine-pitch adjustment screws on the mount. Having verified that both retros were properly aligned and at the correct height, we replaced them in the compressor. Unfortunately, this did not solve our angular chirp issue.

In a final attempt to track down the source of the astigmatism or chirp, we removed the optics from the HHG beamline, up to the focusing mirror, and reassembled the beamline outside of their vacuum tubes. This would facilitate swapping suspected warped mirrors out for other mirrors, and also allow us to send the uncompressed THOR beam through the same beamline. With this optical setup, we were able to confirm that the 800 nm alignment diode experienced no astigmatism, the uncompressed THOR beam (already confirmed to be collimated) experienced no astigmatism, and the compressed THOR beam experienced the same astigmatism/chirp as we had seen previously. In exchanging mirrors, we narrowed down the possible issues to mirrors for which we had no replacements: the gold retroreflectors or the grating itself. All of these optics were confirmed to be only tenuously held by their mounts, to avoid warping them, with the exception of the top half of the vertical retroreflector, which requires force to keep it from falling.

Having exhaustively confirmed that we had no recourse for this problem, we characterized the beam profiles, as shown in Appendix A. These images show the round focus of the beam before compression, to a minimum diameter of 107 μm , as well as the horizontal (upstream) and vertical (down-

stream) astigmatic foci of the compressed beam, separated in distance by 10 cm. The former has dimensions of $95\ \mu\text{m}$ by $601\ \mu\text{m}$, and the latter $125\ \mu\text{m}$ by $454\ \mu\text{m}$. Additionally, unfocused beam profiles obtained before and after 10 m of propagation show that the beam is actually slightly diverging after compression.

Chapter 6

High-Order Harmonic Generation

The discovery of high-order harmonic generation (HHG) by Mcpherson *et al.* revolutionized the push in optics towards coherent high-energy radiation, enabling tabletop lasers to produce a broad range of spectra up to and beyond the extreme ultraviolet [63]. While typical harmonic generation is a perturbative process, with the intensity of each successive harmonic less than the last, the typical envelope of an HHG spectrum, shown in Figure 6.1, with a long plateau of harmonics beginning around order 9, and continuing potentially up to orders of hundreds, dispelled the original assumption that the process was perturbative [15, 74].

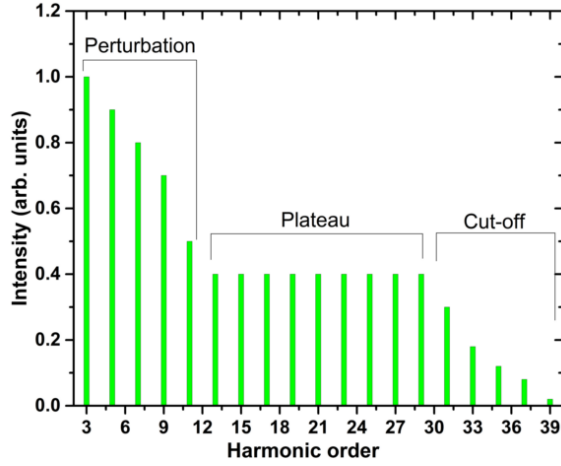


Figure 6.1: Typical spectral profile shape of HHG, including a perturbative regime of harmonics up to about the 9th harmonic, a long, flat plateau, and a cutoff energy of $h\nu_{cut} = I_p + 3.17U_p$, as described in Section 6.1. Figure from Ref [46].

To generate the XUV laser source necessary for our experiments, we utilize high-order harmonic generation (HHG), by focusing the fully amplified, compressed THOR pulse onto a pulsed Ar gas jet. This generates a “comb” of coherent harmonics which extends up to an observed cutoff energy of 48 eV. We separate the high harmonic wavelengths from the un-converted fundamental frequency via a combination of mask/inverse mask system and a 200 nm-thick Al foil. By inserting a 1 mm thick glass slide into the beam in combination with the foil, we confirm that there is no infrared light on target.

6.1 Theory

HHG is a nonlinear parametric optical effect, which may occur when the Keldysh parameter $\gamma \ll 1$. That is, the frequency and intensity of an incident laser are sufficiently low and high (respectively) to impose an oscillatory behavior on electrons in a gaseous (or other) medium.

The “three step model,” first proposed by Corkum, is commonly used to describe the process of HHG [15, 20, 75]. First, a distortion of the Coulombic potential results in ejection of an electron into the continuum via tunnelling ionization. The electron may then be treated classically, accelerated by the instantaneous electric field of the laser. If ejected at the correct phase of the laser cycle, the oscillating field may drive it to recombine with the parent ion, or an adjacent ion. The collision results in the emission of coherent harmonics. Figure 6.2 illustrates this process.

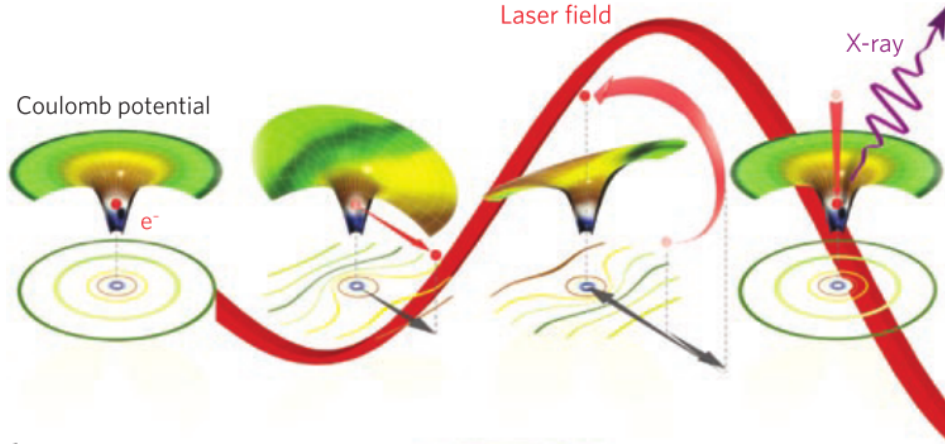


Figure 6.2: An illustration of the three-step model for HHG generation. First, the slowly-oscillating electric field of a laser induces tunnel ionization. The ejected electron is accelerated by the field back toward the parent ion. Recollision results in the emission of high-frequency harmonics, corresponding to the ultimate kinetic energy of the electron upon recombination. Figure from Ref [75].

The field phase at which the electron is ejected determines its path, and whether and with what kinetic energy it recombines with the parent ion. Ejected at a phase of 17° (or 197°), the electron will recombine with its maximum kinetic energy, $3.17 U_p$ [20]. This results in the maximum (cutoff) energy for harmonic generation,

$$h\nu_{cut} = I_p + 3.17U_p \approx I_L\lambda_L^2 \quad (6.1)$$

where I_p is the ionization potential of the gas medium, I_L is the laser intensity, and λ_L is the laser wavelength, which generate the ponderomotive energy U_p for a free electron in the laser field. The centrosymmetry of a gaseous medium

means that the electrons are emitted at 17 degrees and 197 degrees equally, leading to harmonics emission every half-cycle of the fundamental frequency electric field. In the Fourier domain, this means that harmonic frequencies are spaced at 2ω , odd frequencies only.

To optimize conversion efficiency in HHG, many factors must be taken into account. The most obvious of these is the ponderomotive energy. Given that the fundamental frequency is fixed, in order to increase the cutoff energy of the generated harmonics, it is necessary to obtain high laser intensities (typically $> 10^{14}$ W/cm²). However, at very high intensities, the temporal shape of the envelope of the fundamental frequency laser pulse must also be considered. If a prepulse, pedestal, or rising edge of the laser pulse is has sufficient intensity and duration to ionize the majority of the gas via multiphoton ionization, conversion efficiency from the peak pulse intensity will be low. Thus, “clean” few-cycle laser pulses are ideal for conversion efficiency.

A more subtle factor affecting HHG conversion efficiency is phase matching. HHG is a coherent process, with coherence length L_{coh} is $L_{coh} = \pi/(\Delta k_q)$, where $\Delta k_q = |qk_1 - k_q|$ is the wave vector mismatch between the fundamental frequency light and the frequency of the q^{th} harmonic. After a distance of L_{coh} , the generated harmonics will begin to destructively interfere with the previously generated, leading to an oscillatory amplitude with a conversion efficiency of zero at $2L_{coh}$.

Although this wave vector mismatch is inherent in propagation through any dispersive medium, including the target gas and plasma through which the

laser passes, there are additional contributions to the accumulated mismatch which involve the beam geometry, as shown in Figure 6.3. To achieve the intensities necessary to generate a high cutoff energy, it is common to bring the generating laser beam to a focus. This results in wave vector mismatch via the Guoy phase shift near the focus. Since higher frequencies are less divergent, they accumulate the total π phase shift over a longer distance. A steep intensity gradient, such as in a rapidly focusing beam also affects phase matching [9].

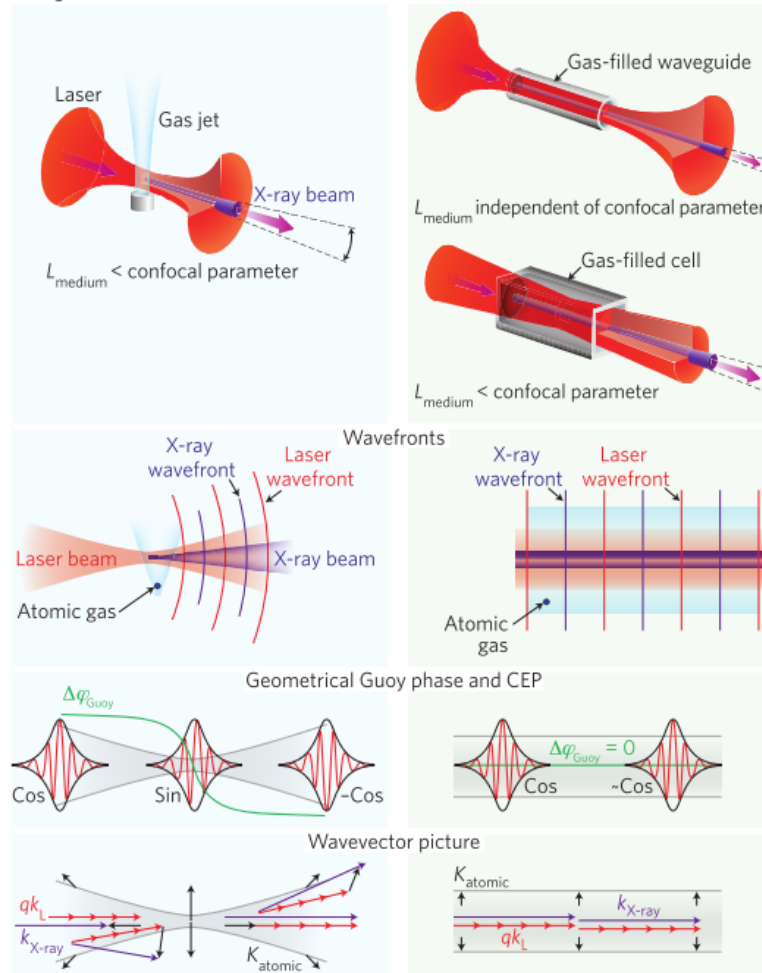


Figure 6.3: Effects of a curved phase front on HHG generation. From Ref [75].

To optimize conversion to the XUV regime, we have optimized the THOR laser to produce short (< 30 fs) high-energy (1.3 J) pulses, and implemented an OPCPA front-end amplifier, to provide pulse cleaning and eliminate the prepulses which were characteristic of the laser's initial regenerative amplifier. The high peak power allows us to utilize a long, loose focus ($f/200$) into

a gas jet. We determined our optimal gas jet position to be over a Rayleigh length before the focus, minimizing Guoy phase shift and intensity gradient, and allowing us to decrease the target gas density due to the large spatial extent of the beam in the interaction region. Our gas jet interaction length on the order of 1 cm, keeping the length of the medium well below the confocal parameter.

We utilize the method developed by Peatross for the initial gross separation of the fundamental frequency from the harmonics [74]. Because HHG is an intensity-dependent process, harmonic generation emerges from a laser focus as if from a spatial filter, strongly peaked along the laser axis. Additionally, because divergence is wavelength-dependent, the higher harmonics diverge significantly less than the fundamental frequency light. Thus, we use an annularly-shaped beam profile, focused just behind a harmonic-generating gas jet, to generate harmonics, and we can remove the majority of the fundamental frequency from the beam propagation via an inverse-mask aperture at the image plane of the original “donut-shaping” beam block.

6.2 THOR HHG Beamline

Post-compression, the THOR laser beam may be routed to one of two beamline configurations: the “solid target beamline,” which utilizes the full THOR beam and an $f/3$ off-axis parabola to generate high intensities on target, or the “HHG beamline,” which utilizes high-order harmonic generation to convert THOR’s energy to higher frequencies. Figures 6.6 and 6.7 show the

path of the HHG beamline.

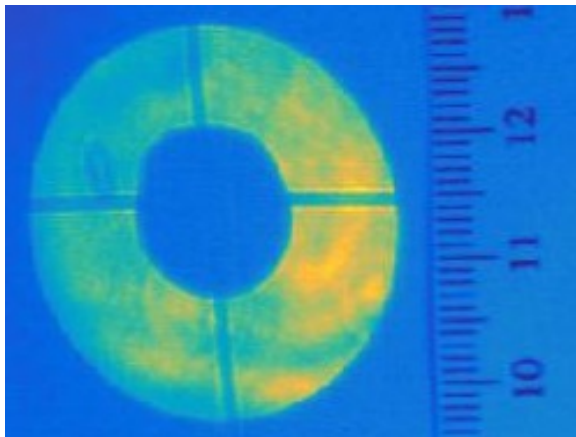


Figure 6.4: Beam profile of the annular THOR beam after the pickoff mirror. The outer “donut maker” iris was also used to create a circular outer edge. In later experiments, this outer iris was not used, as it did not improve the XUV conversion efficiency.

Within the compressor chamber, the fully compressed THOR laser beam is shaped into an annular profile with a mirror suspended at a 45° angle placed in the center of the beam. The ellipsoidal mirror profile casts a circular shadow in the beam profile, as shown in Figure 6.4. This mirror is inserted as a mask, used for the HHG beamline. The reflected center portion of the beam is directed downward, and is transported to the second-order autocorrelator, allowing us an on-shot measurement of the beam compression characteristics. The masked beam contains 80% of the energy of the unmasked, compressed THOR beam.

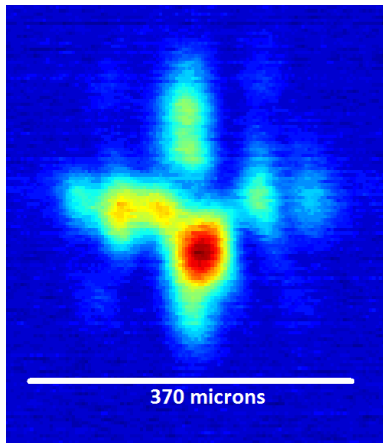


Figure 6.5: Beam profile of the focus under the HHG gas jet, with the pickoff mirror in place.

The masked “donut beam” is directed to a 45° mirror, then to a 0° mirror several meters away, and reflected back to a 0° spherical focusing mirror, with focal length 6 m (nominal focal length 5.5 m). This $f/200$ focusing mirror is targeted onto a pulsed (Parker General Valve Series 9) Ar gas jet, to generate harmonics. The gas jet (790 μm diameter) is outfitted with a slit nozzle attachment of dimensions 6.57×0.635 mm, to increase the interaction distance between the laser and the gas.

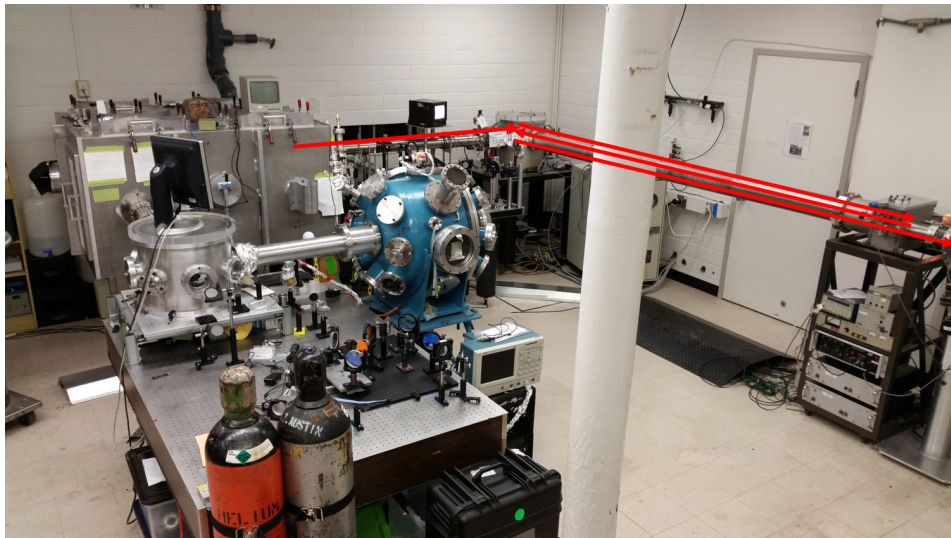


Figure 6.6: The output of the compressor, switched toward the HHG beamline

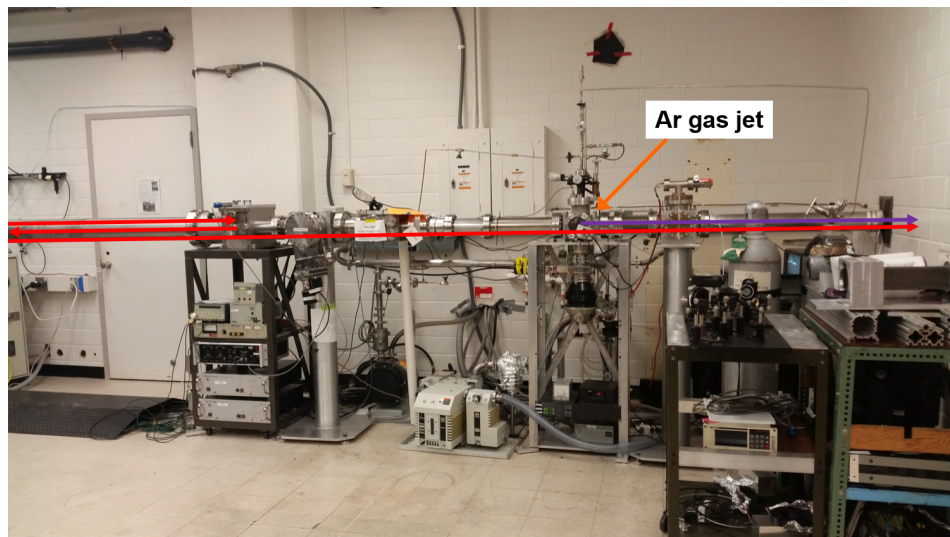


Figure 6.7: The $f/200$ loose focus beamline to the HHG-generating Ar gas jet

The harmonics co-propagate with the laser, with the shorter wavelengths generated peaked along the laser axis and diverging less rapidly, so that at the image plane of the annular mask, they occupy primarily the central region shadowed by the mask. The vast majority of fundamental frequency light is then separated from the high harmonics via an inverse mask (a large iris) near the image plane of the mask. A 200 nm thick Al foil rejects the remaining 800 nm light, as well as lower harmonics, in the XUV target chamber

Figure 6.8 shows the design of the Al foil holder, which holds a Luxel 200 nm Al meshless film, mounted on a TF111-15.9-Al-BA 1 inch diameter mount. The holder seals against an iris which covers the input of the XUV target chamber, and cuts the background gas load flowing from the HHG gas jet to the target chamber by 90%.

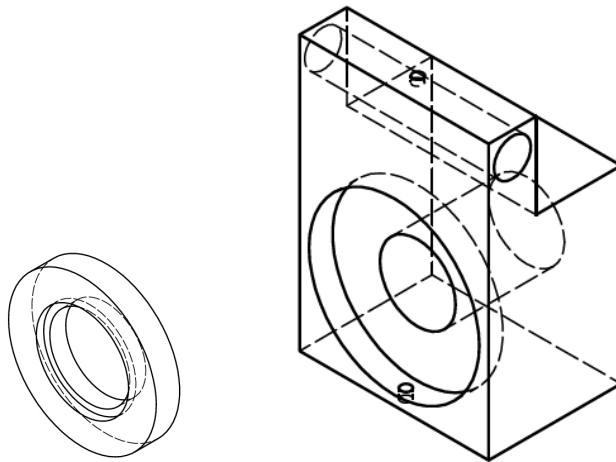


Figure 6.8: Foil holder, for 200 nm meshless foil.

6.3 HHG Optimization

To obtain the highest conversion efficiency from the fundamental frequency in the infrared to the XUV regime, we optimized the XUV output over several parameters, with the use of an XUV spectrometer. The spectrometer consists of a curved grating and a flat mirror, designed to operate at grazing incidence, along with a detector, made of two 2 inch MCPS mounted in a chevron configuration, backed by a phosphor screen. We used a camera, triggered via a LabVIEW program, to capture and store images of the phosphor screen. Design and use of the spectrometer are described in [68] and [46].

The variables over which we were able to optimize include gas jet position with respect to the beam focus (Z position), gas jet position with respect to the beam axis (X and Y position), gas jet backing pressure and nozzle pulse duration, and THOR pulse compression. These variables were often adjusted iteratively, with one variable being adjusted incrementally, and the others optimized at that setting, to obtain the best combination of settings.

The Z position of the gas jet with respect to the beam focus proved to be the most complicated variable to adjust, as it required breaking vacuum to rearrange pieces of the actual beamline tube. The Z-adjustment length made possible by adjusting the vacuum translation stage on the HHG focusing mirror and the manual Z adjustment on the HHG gas jet itself is only about 6 inches. Because the uncertainty about the optimal position was greater than this range, the HHG beamline tube was designed with several smaller pieces of varying lengths, which could be arranged “upstream” or “downstream” of the

gas jet-containing tube segment. The design was created around the nominal focal length of the focusing mirror (5.5 m), but, likely due to a small positive divergence which emerges within the compressor, the actual focal length of the mirror was 6 m. Ultimately, all of the rearrangeable tube segments were set in front of the HHG gas jet segment, and the gas jet position was optimized about three Rayleigh lengths (13 cm, with an estimated Rayleigh length of 4 cm) in front of the beam focus.

The other two dimensions perpendicular to the laser axis were far easier to optimize, and were often adjusted (minimally) when harmonic energy appeared to drop. Adjustment of these axes is done via the manual translation stages attached to the gas jet input to the vacuum line. Full plots of harmonic intensity as a function of gas jet position are shown in [46]. At these positions, it was determined that maximum XUV generation occurred at the highest THOR pulse energy output, as well as the best possible pulse compression. Optimal HHG gas jet stagnation pressure was originally determined to be 90 psig, but after several years at this pressure, new conditions appeared to instead favor 72 psig.

Chapter 7

Experimental Setup

The main goal of the experiments described here was to measure the m/q ratio of ions ejected from nano-clusters of STP gases or nano-scale solid targets when hit with a high-intensity XUV laser pulse of adjustable photon energy. With the chamber setup we chose, our detector, a Wiley-McLaren time-of-flight spectrometer [99], was also able to measure the kinetic energies of the ions and electrons from these same interactions.

The XUV target chamber and experimental setup were designed to minimize target signal contamination by maintaining ultralow chamber background pressures. Differential pumping schemes, along with up to 5 turbomolecular pumps, yielded a background pressure (with no target gas jet firing) of 2×10^{-8} Torr.

Cluster targets were injected into the target chamber through a nozzle mounted in a differentially-pumped region of the chamber dubbed “the chilipot.” A skimmer separating the main chamber from the chilipot served to collimate the target cluster beam. Gas clusters were formed via adiabatic expansion of gas into vacuum, using the Hagen parameter for cluster size estimation. Solid nanoparticle targets were generated via the laser ablation

of microparticles method, and injected, along with a buffer gas, through a continuous flow nozzle.

The XUV comb from high-order harmonic generation was filtered for the desired harmonic and focused using a narrow-band dielectric mirror, with a focal length of 12.5 cm. We measure up to 17.7 mJ on target energy at the 21st harmonic, with a spot size of $6.4 \mu\text{m } 1/e^2$ radius, yielding an intensity on the order of 10^{13} W/cm^2 .

7.1 XUV Target Chamber

One of the main design goals of the XUV target chamber is to maintain a low level of background gas in the laser interaction region. To this end, the target chamber is effectively separated into two halves - the laser interaction area and the gas jet output area, known as “the chilipot.” This allows us to employ a differential pumping scheme, to keep gas background in the laser area to a minimum. A diagram of the target chamber is shown in Figure 7.1 [46], where the chamber itself encompasses all portions of othe diagram “downstream” of the 200 nm Al foil filter. The differential pumping “chilipot” enclosure is shown with the cluster-forming gas jet shooting downwards toward a skimmer. The bottom of the chilipot is also visible in Figure 7.3.

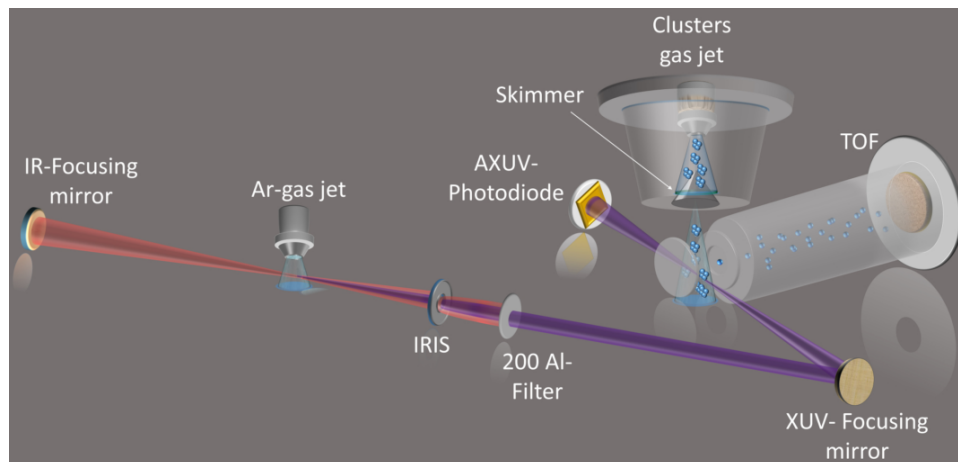


Figure 7.1: The experimental setup in the HHG beamline and XUV target chamber [46]. Harmonics are generated and separated from the fundamental frequency as described in Chapter 6. The desired harmonic is selected and focused onto a target as described in Figure 7.2. Gas cluster and nanoparticle targets are generated in a differentially pumped section of the XUV target chamber, referred to as “the chilipot.” Targets generated in this region must pass through a collimating skimmer before entering the main target chamber.

This skimmer forms the only direct opening between the two regions of the chamber, and serves to shave the gas jet output into a thin column of nearly uniform density. The removal of the outer portions of the jet output serves to increase charge-to-mass and kinetic energy resolution in the time-of-flight spectrometer by minimizing the uncertainty in the position at which a charged particle is created, as well as by limiting the effects of charge exchange on the way to the detectors.

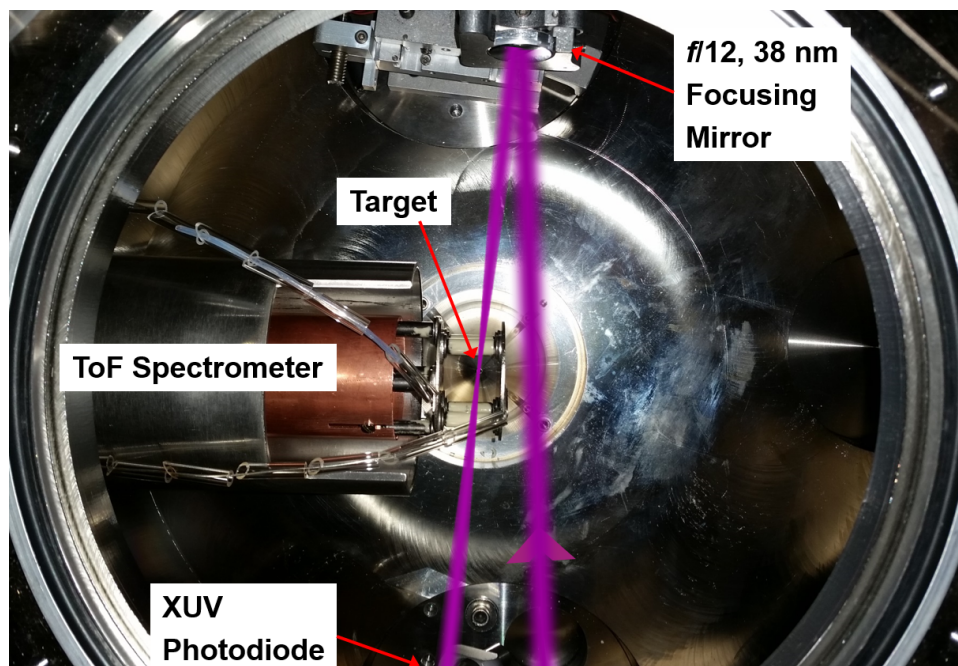


Figure 7.2: The experimental setup in the XUV target chamber, as viewed from above. Harmonics of sufficient energy to be transmitted through the Al foil filter pass into the target chamber, and the desired harmonic is selectively reflected and focused by a custom-coated multilayer mirror onto the desired target, in the collection region of a Wiley-McLaren ToF spectrometer. Light not absorbed in the interaction passes to an XUV-sensitive photodiode, providing an on-shot energy measurement.

The chipot has a dedicated turbomolecular pump, backed by a roots blower and mechanical pump. The turbo pump facilitates the rapid clearing of gas from the chipot and prevents backflow into the interaction region from the roots blower. Likewise, after the skimmed gas cluster beam passes through the interaction region of the time-of-flight, it is directed through another skimmer below, designed to accept the majority of the pre-skimmed gas beam. This area

below the bottom skimmer also has a turbomolecular pump backed by a dry scroll pump, and is also pumped directly by the roots blower and mechanical pump.

The main interaction region of the target chamber has another two turbomolecular pumps of its own, to keep gas density in this region as low as possible. These turbos are backed by a scroll pump. The largest remaining source of background pressure in the target chamber is from the Ar HHG gas jet, about 6 m away. The seal between the Al foil filter holder and the input to the target chamber was improved to minimize this contamination source. After baking the target chamber with heat tape, the ultimate background pressure was 2×10^{-8} Torr.

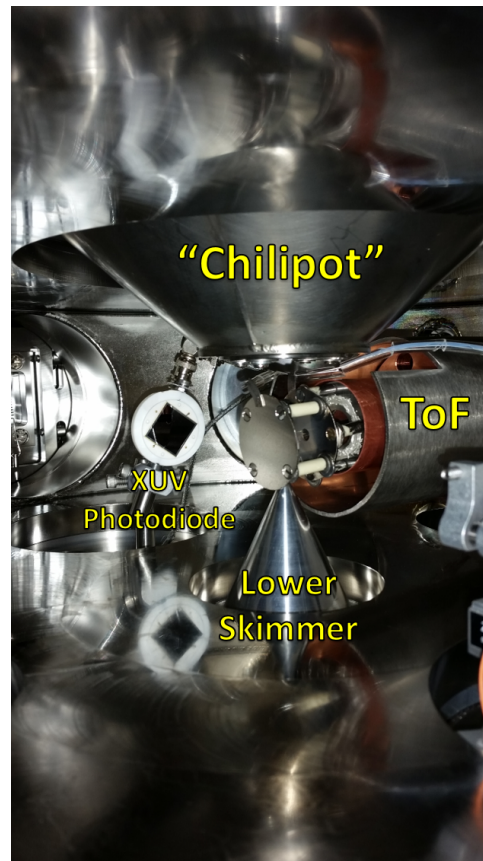


Figure 7.3: The experimental setup in the XUV target chamber, as viewed from a windowed port on the side of the chamber. The chilipot, concealing the top skimmer, ToF spectrometer, the lower skimmer, and the XUV photodiode are shown.

Figure 7.2 shows the target chamber from a top-down perspective. This photo, taken with the chilipot removed from the top of the target chamber, shows the path of the XUV laser in this experimental configuration. The laser enters the chamber through the Al foil holder, reflects from a spherical focusing mirror, and is focused onto the target, which flows in a collimated stream

through the center of the interaction region of a Wiley-McLaren time-of-flight (ToF) spectrometer. With gas cluster and nanoparticle targets, the vast majority of the incident light is transmitted through the target and hits an Opto Diode IRD-AXUV575c photodiode, which has a calibrated photo-response curve for XUV wavelengths. This diode provides an on-shot measurement of the XUV energy on target. As shown in Figure 7.4, the photo-response curve is a nearly flat 0.26 A/W in our range of interest, corresponding to a conversion of $V_{measured} [\text{mJ}] = 0.67 E_{XUV} [\text{nJ}]$ when terminated into 50Ω .

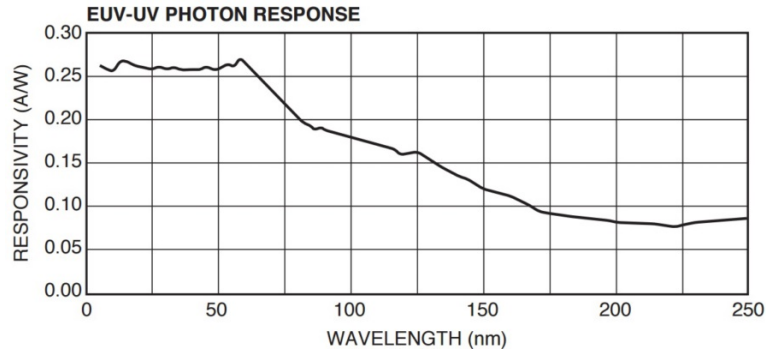


Figure 7.4: Photo-response curve for Opto Diode IRD-AXUV575c photodiode. Figure from [46].

7.2 XUV Focusing Mirrors

The XUV focusing mirror selects the harmonic wavelength of interest in our experiments. These multi-layered dielectric mirrors were custom-coated by the Lebedev Physical Institute in Moscow, Russia [46]. They are composed of layers of Si, Cr, and Sc, and engineered to selectively reflect a single harmonic, as well as small amounts (about 20% or less of the fundamental frequency

energy) of the adjacent sidebands, as shown in Figure 7.5. These mirrors are spherical focusing mirrors with a focal length of 12.5 cm.

7.3 On-Target Beam Characteristics

A typical on-target spectrum for the 17th-harmonic-reflecting mirror is shown in Figure 7.5. Sidebands have a maximum intensity of 10-20% of the center harmonic.

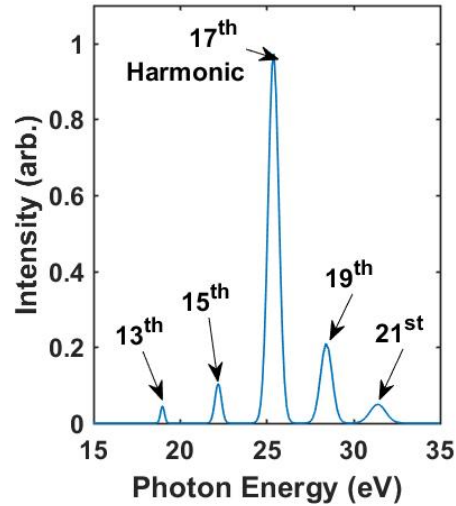


Figure 7.5: On-target photon energy spectrum reflected by the 17th harmonic mirror (#3). This data was extracted from a Xe photoelectron spectrum.

The actual temporal profile of the XUV pulses remains an estimated quantity. An ideal pulse, represented by the Fourier transform of the spectrum in Figure 7.5 has a FWHM pulse duration of 600 as, with prominent sidebands. Due to the long ~ 10 optical cycle pulse duration and lack of carrier envelope

phase stabilization, as well as the focused HHG geometry with a less-than-ideal wavefront, the actual pulse duration is likely to be longer. An upper bound of the pulse duration is the estimated width of the harmonics envelope, $(30 \text{ fs})/\sqrt{q} \approx 7 \text{ fs}$.

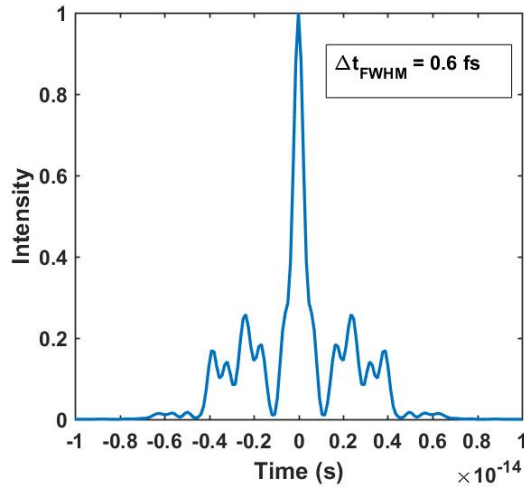


Figure 7.6: Transform-limited temporal pulse profile of the spectrum from Figure 7.5.

The spatial extent of the beam focus was determined via a knife edge measurement. A knife edge was attached to an encoded translation stage with $1 \mu\text{m}$ step size and positioned near the focus of the XUV beam. The Z-adjustment was done by translating the focusing mirror towards and away from the knife edge, in steps of 50 to 200 μm . A photo of the setup is shown in Figure 7.7.

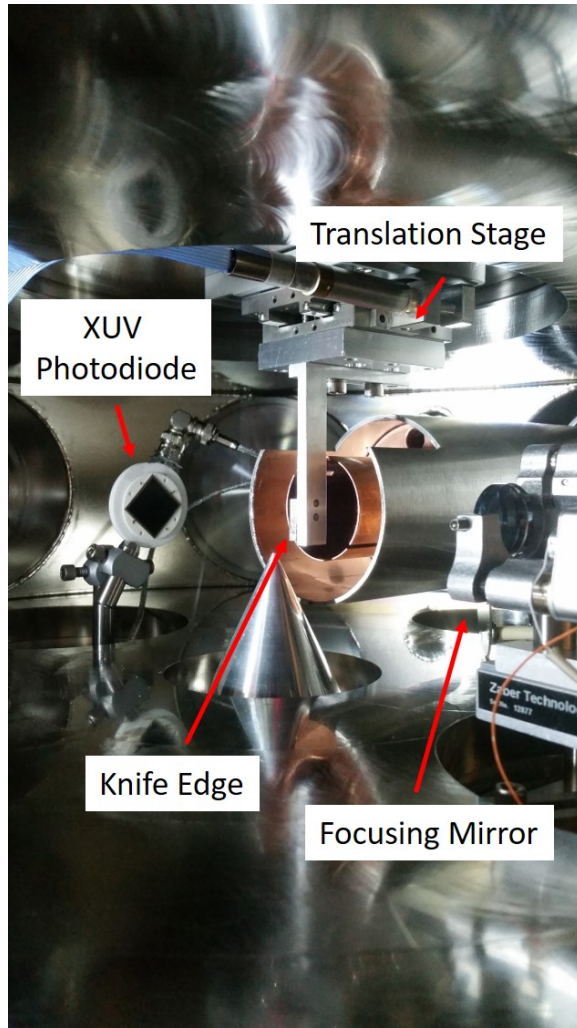


Figure 7.7: Photograph of the physical setup used for the knife edge measurement of beam spot size.

For this measurement, the equation for the energy on the diode E as a function of knife position x is

$$E(x) = E_{tot}/2 \left[1 - \operatorname{erf} \left(\frac{\sqrt{2}x}{w_x} \right) \right] \quad (7.1)$$

Where E_{tot} is the total, unobstructed energy on the diode, and w_x is the $1/e^2$ radius [7]. The fit gives us a $1/e^2$ radius of $6.4 \mu\text{m}$. The data and fit equation corresponding to the smallest measured beam radius is shown in Figure 7.8, yielding a $1/e^2$ radius of $6.4 \mu\text{m}$.

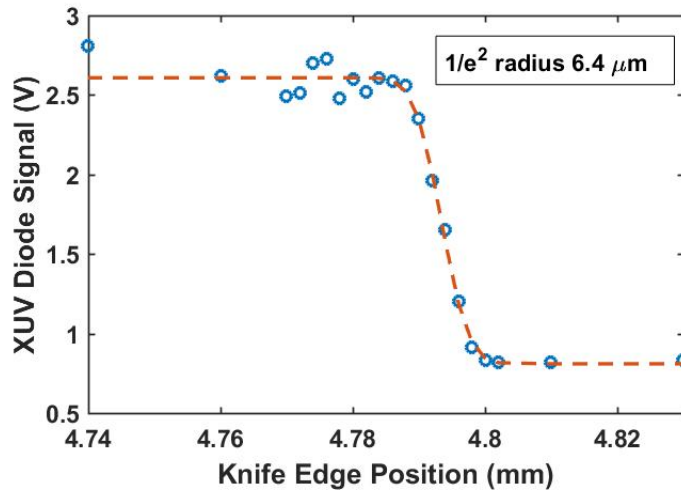


Figure 7.8: Measurement (blue line) and fit (red dashed line) for the focus of the knife edge measurement of beam spot size. The $1/e^2$ radius for this measurement was $6.4 \mu\text{m}$.

The maximum measured laser pulse energy was 17.7 nJ [46], although in later experiments, the output was as low as $1\text{-}2 \text{ nJ}$. With a spot size of $6.4 \mu\text{m}$, this yields a maximum on-target fluence of $2.8 \times 10^{-2} \text{ J/cm}^2$. With our optimistic (600 as) and pessimistic (7 fs) estimates of pulse duration, we get on-target intensities of $9.2 \times 10^{13} \text{ W/cm}^2$ and $7.9 \times 10^{12} \text{ W/cm}^2$, respectively.

7.4 ToF Spectrometer

We used a Wiley-McLaren-type time-of-flight spectrometer [99] to allow us to measure the ion charge-to-mass distributions, ion kinetic energies, and electron kinetic energies of the plasma resulting from our laser-target interactions. A diagram of the spectrometer is shown in Figure 7.9. When possible, when describing the apparatus, I have used the notation from the original Wiley-McLaren paper [99].

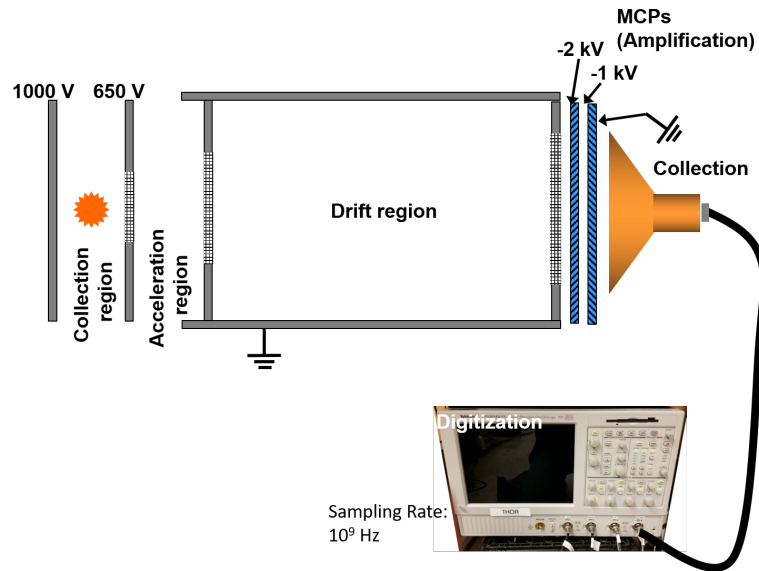


Figure 7.9: A cartoon diagram of our time-of-flight

The laser is focused onto a target within the collection/ionization region, which is bounded by the “front plate” and “center aperture” of the ToF. The voltages on these plates are typically 1000 V and 650 V, respectively, for maximum m/q resolution. The distance between these plates, x , is 2.51 cm,

which produces a relatively uniform field in the region of 13.9 kV/m. the distance within the collection region between the ionization region (target) and the center aperture, s , is variable, but commonly 9 mm. Ions are accelerated by this field toward and through the center aperture, which has an aperture in the center covered by a gold mesh with greater than 90% transmissivity.

The ions travel into the acceleration region of the ToF, bound by the center aperture plate and a similarly designed aperture plate, which are typically held at 650 V and ground, respectively. The length of the acceleration region, d , is 2.11 cm. This gives a uniform electric field of 30.8 kV/m. The voltages on the front plate and center aperture, which determine the electric fields in the collection and acceleration region, were determined experimentally to yield the highest m/q resolution of our ToF spectrometer. The presence of two regions, instead of simply one, allows for some amount of compensation for the finite spatial distribution, Δs , of the interaction, as well as the distribution of initial kinetic energies of exploding clusters.

After passing through the acceleration region, ions enter a field-free drift region, bounded by two grounded plates with large mesh apertures. The length of the drift region, D , is 49.6 cm. This unusually long drift region allows for a high m/q resolution, by allowing additional distance for the accelerated ions to sort themselves by their final velocities (determined by their masses and charges), translating into a larger spread in time.

After the drift region, the ions are accelerated into a pair of uncoated Photonis microchannel plates (MCPs), to produce an electron avalanche which

is collected in on the copper anode behind the MCPs. The MCPs are oriented in a chevron configuration for maximum signal amplification. They are held near their maximum specified voltages, with the front of the first MCP held at -1900 V, the back of the second MCP and the anode grounded, and the voltage divider circuit on the ToF power supply providing half of the voltage (-950 V) between the two MCPs.

In different voltage configurations, the ToF can be used to detect the unaccelerated kinetic energy of ions or electrons. For the ion configuration, all voltages are the same as specified above, except for the ToF front plate and center aperture plate, which are instead grounded. For the electron configuration, the front plate and center aperture are also grounded, but the MCPs and anode must be set up to collect negatively charged electrons instead of positively charged ions. For this, we ground the front of the first MCP, set the region between the MCPs to +1000 V, and the back of the MCPs to +2000 V. The anode is increased to +2100 V, to achieve the highest possible signal level. Connecting this configuration to an oscilloscope requires attaching a differentiating circuit box between the anode and the scope, so that the 2.1 kV DC signal is filtered out.



Figure 7.10: A CAD model of our Wiley-McLaren time-of-flight spectrometer [46]

A CAD diagram of the actual ToF used in the experiments in this dissertation is shown in Figure 7.10. The acceleration plates/grids are made of stainless steel, with transmissive gold mesh over all apertures, which was secured to the plates with conductive epoxy or graphite aerosol. The plates are attached to each other via ceramic posts. The drift region is made of a copper tube, which is grounded to the flange which mounts it onto the vacuum chamber. Surrounding the entire ToF is an outer mumetal tube, which shields electrons from the Earth's magnetic field, as well as any stray magnetic fields

in the target chamber. With 2" MCP collectors and an approximately 50 cm fly distance, our ToF collects roughly 0.25 % of electrons or ions in a field-free (un-accelerated) configuration.

7.5 LAM Setup

To supply a steady stream of nanoparticle targets to our laser target chamber, we utilize the laser ablation of microparticles (LAM) apparatus as described in [41]. Microparticles of the desired target material (here we use a DuPont powder of spherical silver microparticles 1-2 μm in diameter, formulation P-311J) are entrained in a buffer gas within the particle bed assembly. The particles are then sorted by size within the cascaded virtual impactor assembly, to remove agglomerated microparticles, as well as particle fragments and excess buffer gas.

The optimally-sized microparticles are then ablated by a laser in the ablation cell. They nucleate and re-condense into nanoparticles, with the size of the resulting nanoparticles determined by the choice of buffer gas. These nanoparticles are then injected into the target vacuum chamber via a continuous-flow supersonic nozzle. The LAM apparatus, mounted on the XUV target chamber, is shown in Figure 7.11. Additional details on the design, use, and safety of the system are in Appendix B.

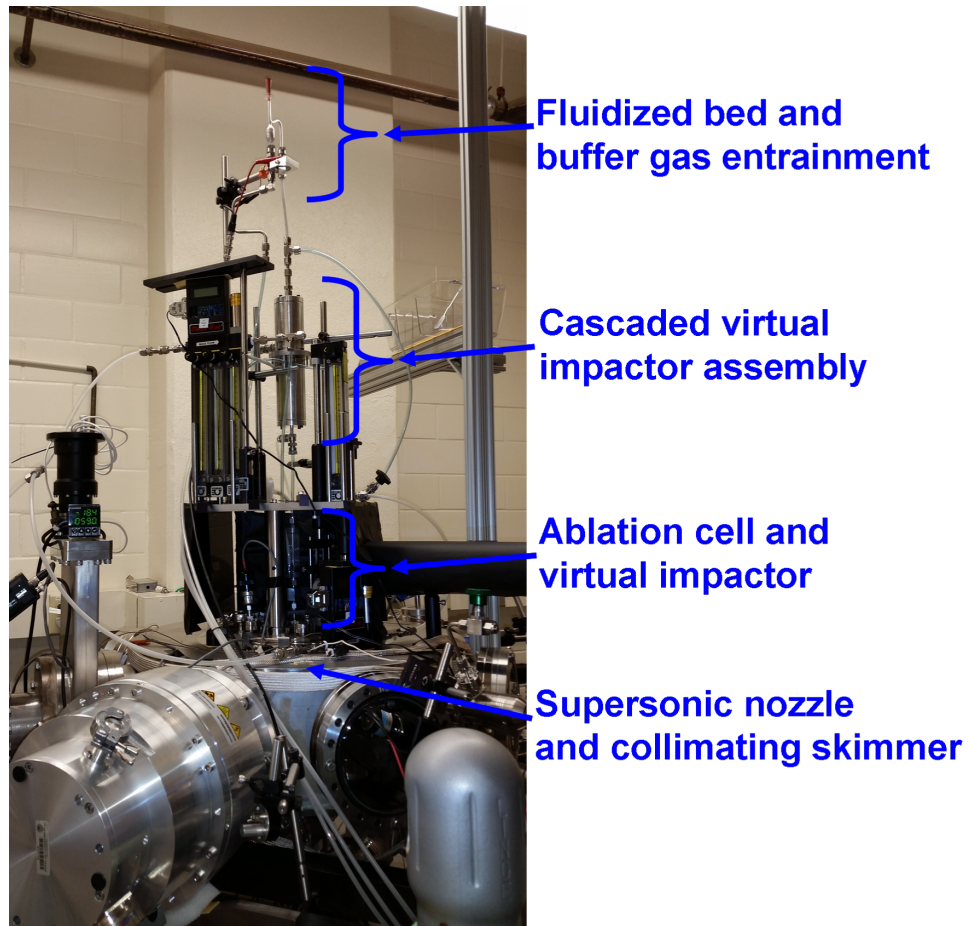


Figure 7.11: The LAM apparatus, mounted on the XUV target chamber.

7.5.1 Particle Bed

Microparticles of the target material are delivered to the glass particle bed via a funnel in the top of the apparatus. They sit in a conical region with a 250 μm diameter orifice at the bottom of the bed, through which a buffer gas flows. The particles are shaken with an unevenly-weighted motor, to maintain

their fluidity and to keep them from sticking together. The buffer gas flows up through the bottom of the particle bed, producing a cloud of entrained particles in the top of the particle bed chamber. These particles follow the flow of the buffer gas into the virtual impactor assembly.

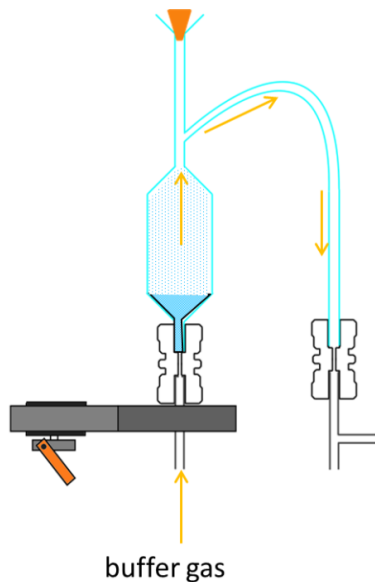


Figure 7.12: The particle bed for the LAM apparatus. Microparticles are shaken by an unevenly-weighted motor, to maintain fluidity, and a buffer gas is blown from below the particles, to entrain particles in the gas for transport to the virtual impactor assembly.

7.5.2 Cascaded Virtual Impactor Assembly

The virtual impactor pair used in the following experiments follows the design used by Chen [18], and employs the cascaded virtual impactor assembly designed and built by Gleason [41], and shown in Figure 7.13. In the first stage of the virtual impactor, large agglomerates of microparticles are filtered out

of the system. The minor flow is removed from the impactor assembly, and the microparticles entrained in this flow are deposited into paper particulate filters. The major flow is directed into the second stage of the cascaded virtual impactor assembly.

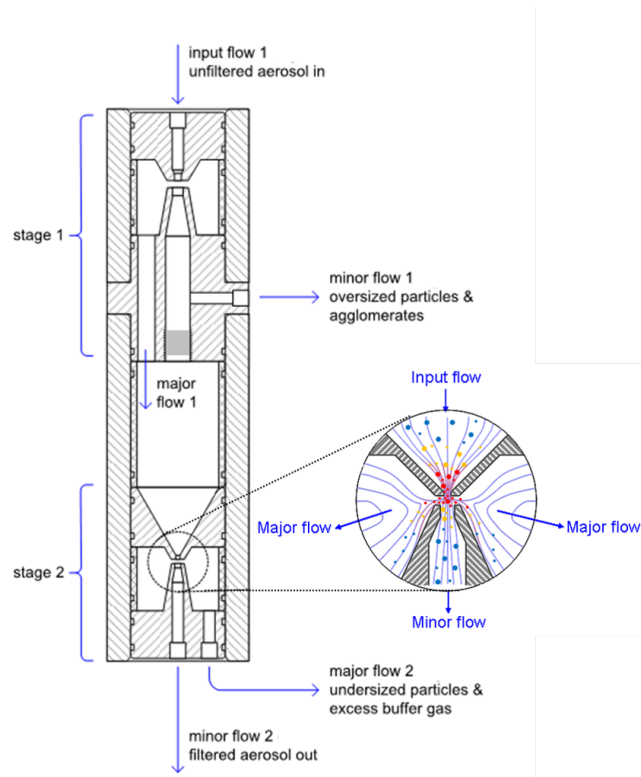


Figure 7.13: Diagram of the two-stage virtual impactor used in this work. Figure modified from [41].

In the second stage, particulate fragments and excess buffer gas are removed from the system. It is the minor flow which is directed through filters and exhausted from the system, while the major flow, now containing

only unagglomerated microparticles, passes into the ablation cell. Additional details concerning the design and construction of the cascaded virtual impactor are found in [70] and [41].

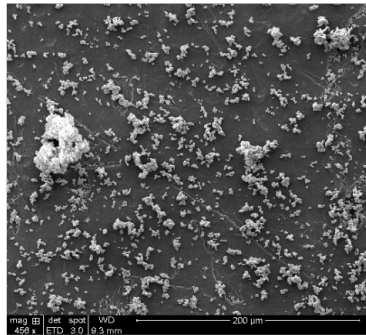
For the setup described here, all flows are ultimately determined by the expansion into vacuum by the 150 μm diameter nozzle, backed by atmospheric pressure nitrogen buffer gas. Working backwards from this point, we determine the following flows through the system for the initial trials and the final setup:

Table 7.1: Properties of the cascaded virtual impactor assembly

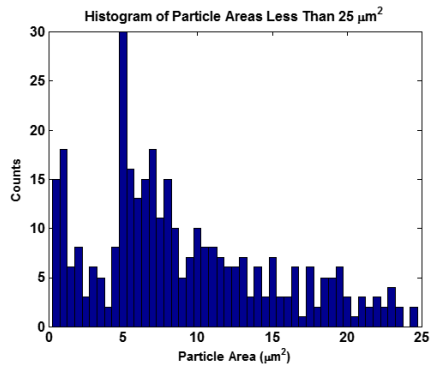
Parameter	Initial Value	Final Value
Gas	He	N ₂
Supersonic nozzle diameter (μm)	250	150
Input flow 1 (sccm)	2717	2772
Major flow 1 (sccm)	2500	2550
minor flow 1 (sccm)	217	221
Major flow 2 (sccm)	2300	2346
Minor flow 2 (sccm)	200	204
Ag particle min diameter (μm)	0.7	0.8
Ag particle max diameter (μm)	1.7	1.8

For the unmodified virtual impactor assembly described by Gleason, with input nozzle diameters of 0.268 cm and 0.163 cm for the first and second stage, respectively [41], we have also included in Table 7.1 the minimum and maximum diameters transmitted through the system for a spherical silver microparticle. The flows and diameters in this table were calculated with the MATLAB code given in Appendix C.

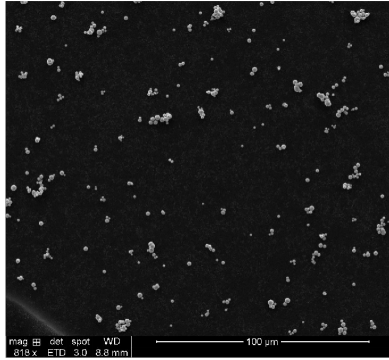
As shown in Table 7.1, the modifications in buffer gas and supersonic nozzle diameter necessary to make the LAM compatible with our high vacuum target chamber do not affect the cutoff diameters appreciably. They remain compatible with the 1-2 μm Ag feedstock employed in these experiments. Figure 7.14 shows the successful results of employing the virtual impactor assembly.



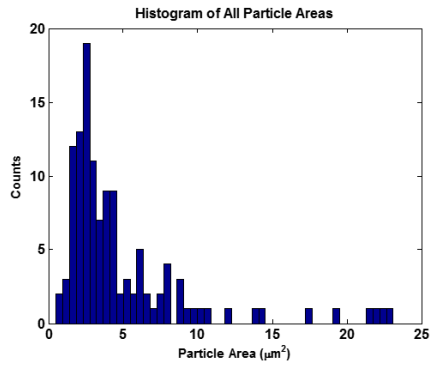
(a)



(b)



(c)



(d)

Figure 7.14: The results of using the cascaded virtual impactor on spherical microparticles with a nominal diameter of 1-2 μm . Sub-figures (a) and (c) are SEM images of particles impacted from the entrained microparticle flow, taken before and after the virtual impactors, respectively. Sub-figures (b) and (d) show a histogram of the average particle area, obtained from the SEM images. The medium and large agglomerates which dominate the un-sorted flow are filtered out by the assembly.

7.5.3 Ablation Cell

After the microparticles are sorted, the unagglomerated microparticles, still entrained in buffer gas, are sent to the ablation cell. The newest iteration of the ablation cell is shown in Figure 7.15. Within the cell, there is a break in the tubing carrying the microparticles. The particles are maintained in a laminar flow from the input tube to the slightly larger output tube below by a coaxial sheath flow of buffer gas in the cell.

We focus the ablation laser (a Quanta-Ray GCR) to a line focus with a cylindrical lens, and direct it onto the microparticles in this region. The profile of the particle stream is adjusted by compressing the tubing ends into an oblong shape, thus allowing the laser to interact with the majority of the particles present in the flow when the laser fires. The GCR runs at 10 Hz, with its Q-switch triggered by the THOR laser, and thus ablates only about 1/4 of the microparticle flow.

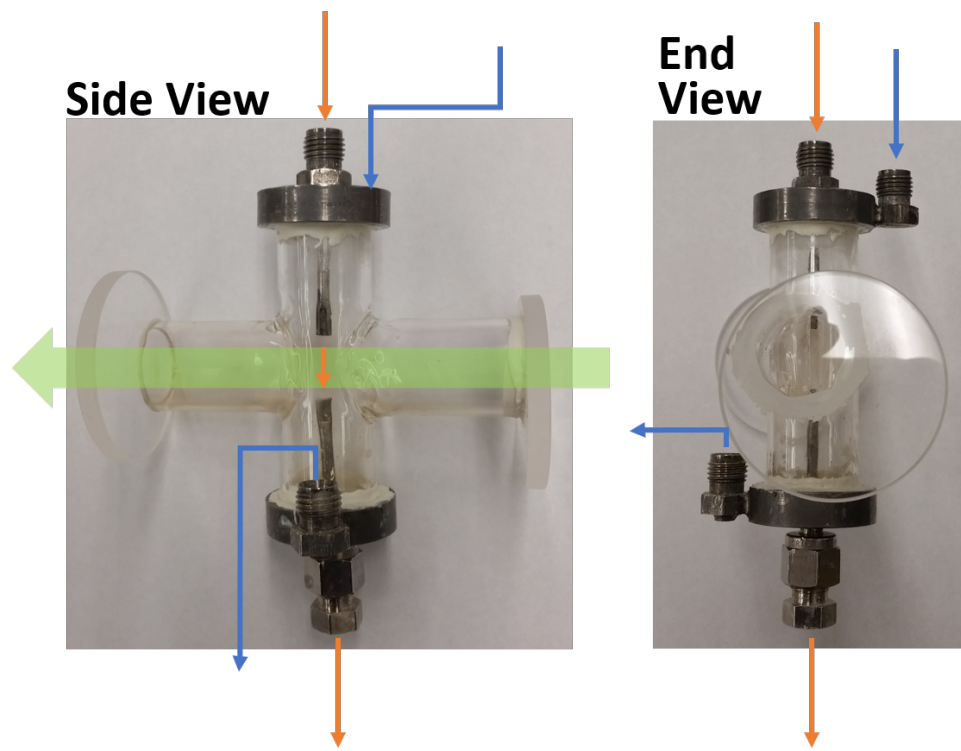
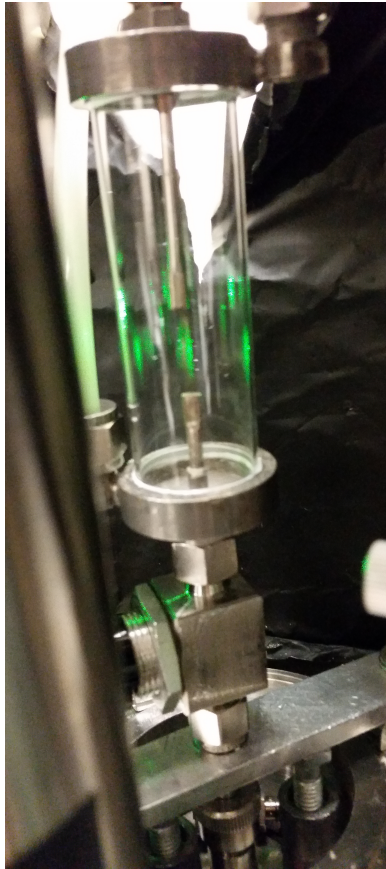


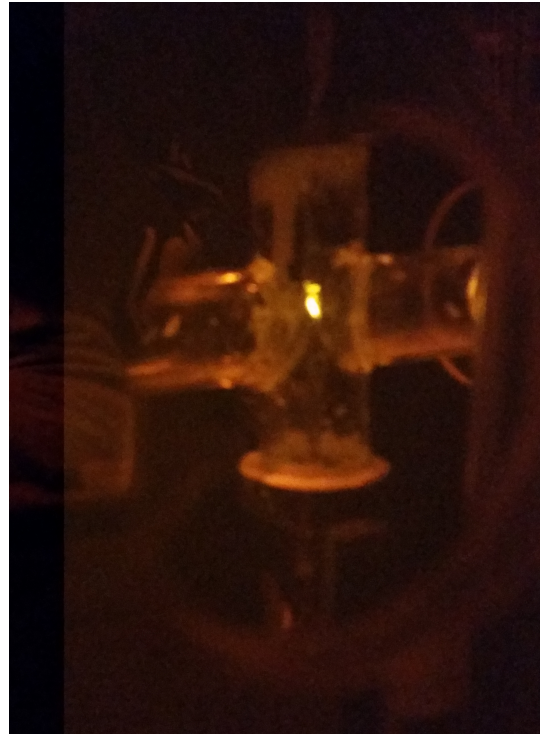
Figure 7.15: Improved ablation cell for nanoparticle generation. The design protect the sides of the ablation cell from becoming damaged by the ablation laser. Entrained microparticle/nanoparticle flows are shown in orange, collimating buffer gas flows in blue, and the path of the ablation laser is shown in green.

The original ablation cell design, as shown in Figure 7.16 (a), required modification, as the intensity needed to ablate the nanoparticles was close to the damage threshold of the exterior 1" diameter quartz tube, and damage to the tube walls became common. To remedy this, a slit was cut in the sides of the quartz tube, about 2 mm wide and 25 mm long, to allow the laser to enter while causing minimal disruption to the microparticle stream.

A second 1" diameter quartz tube was added in a cross shape, as shown in Figure 7.15, and windows with 532 nm antireflective coating were added using vacuum-compatible epoxy.



(a) Ablation cell showing scattering of the ablation beam at low energies.



(b) Ablation cell showing fluorescence from ablation.

Figure 7.16: Ablation cells displaying the signs of proper microparticle flow and ablation laser alignment. (a) The scattering of the ablation laser at a low energy is viewed by a camera. Scattering is visible from the walls of the ablation cell and the microparticle stream itself. (b) A 532 nm-blocking filter is applied to the camera, and the ablation laser power is increased. Fluorescence from microparticle ablation is clearly visible.

7.5.4 Supersonic Nozzle

After ablation, the nanoparticles (and unablated microparticles) flow through a Swagelok ball valve (allowing the vacuum chamber to be sealed off and pumped down when the LAM is not in use) and into the continuous flow supersonic nozzle. The nozzle we ultimately used was a flat plate nozzle with a 150 μm diameter opening. Although the original design of the LAM system used a 250 μm nozzle, this provided far too much gas load on the turbomolecular pumps in the XUV target chamber, especially when used with a difficult-to-pump buffer gas such as neon. In fact, even the 150 μm nozzle created problems for the turbo pumps when used with a neon buffer gas.

The continuous flow nozzle was positioned in the chilipot section of the XUV target chamber, 2 cm above a 1.2 mm diameter skimmer. The gas flow lines created by the nozzle provide some focusing direct the nanoparticles and microparticles, so that they easily flow through the skimmer, into the target chamber, while excess buffer gas is removed from the system via differential pumping in the chilipot.

7.6 Cluster Gas Jet

To form our gas cluster targets, we utilized a solenoid-driven pulsed conical gas jet (Parker General Valve Series 9) attached to a nozzle aperture with a 5° half-angle and a 790 μm throat diameter, resulting in an effective nozzle diameter of $d_{eff} = 6.682$ mm. The nozzle attached to the gas jet is shown in Figure 7.17. Gas jet backing pressures ranged between 2 psi and 200

psi, to create a broad range of cluster sizes.

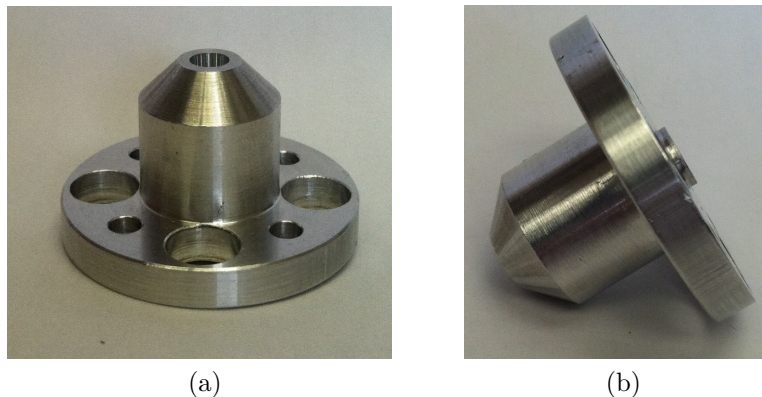


Figure 7.17: Top/side and pure side view of gas jet nozzle used to make target gas clusters.

When larger cluster sizes or higher condensation ratio were necessary, we employed a cooling jacket, made of multiple turns of 1/4 in Cu tubing wrapped around the gas jet body, and in thermal contact with the nozzle via a sandwiched layer of indium foil. The temperature of the nozzle was measured via a thermocouple embedded in the foil. We directed a flow of cooled nitrogen gas through the cooling jacket. The gas was cooled by first sending the flow through many turns of 1/4 in Cu tubing submerged in a bath of liquid nitrogen. The ultimate nozzle temperature was adjusted with the flow through the cooling line, by adjusting the N₂ gas cylinder pressure regulator between 5 and 50 psi output.

An alternate cooling system was also developed, which employed a concentric flow of cooled gas down the center of the tube carrying the target gas, as shown in Figure 7.18. This would prolong the thermal interaction of

the target gas with the cooled gas. Unfortunately, there were problems with this setup. The size of the target gas line severely restricted the sizes of the cooling gas lines, and consequently, their maximum flows were limited.

While we were able to achieve gas temperatures well below 0° C with this method (using N₂ as a cooling gas) when the gas jet was separated from the target chamber for maintenance, the physical constraints associated with its position on the target chamber further restricted the flows, and resulted in condensation of the cooling gas in the cooling line. Condensation and rapid evaporation when contacting a warmer part of the line resulted in cyclical, uncontrollable pressure spikes in the cooling line. Substituting He for the cooling gas, to prevent condensation, did not provide adequate cooling to the target gas. No significant temperature drop was achieved.

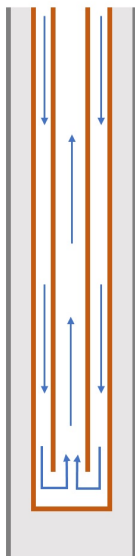


Figure 7.18: Diagram of the concentric cooling scheme briefly employed.

The gas jet nozzle was positioned within a differentially pumped section of the target chamber, 12 mm above a conical knife-edge skimmer of 1.2 mm diameter.

Gas jet opening times were controlled with a General Valve Iota One pulse driver triggered by the 10 Hz THOR laser, and delayed relative to the laser pulses with a Stanford Research Systems DG535 digital delay box. The gas jet poppet was held open for a duration of 1 ms, to allow for steady-state cluster formation, while minimizing target gas usage as well as gas load on the target chamber turbomolecular pumps. Figure 7.19 characterizes the cluster/gas mixture in the collection region of our ToF spectrometer as a function

of gas jet trigger timing. Gas is first detectable in the target region 160 μs after the gas jet fires. About 810 μs after that, the density of the uncondensed target gas and clusters each appear to have reached a steady state.

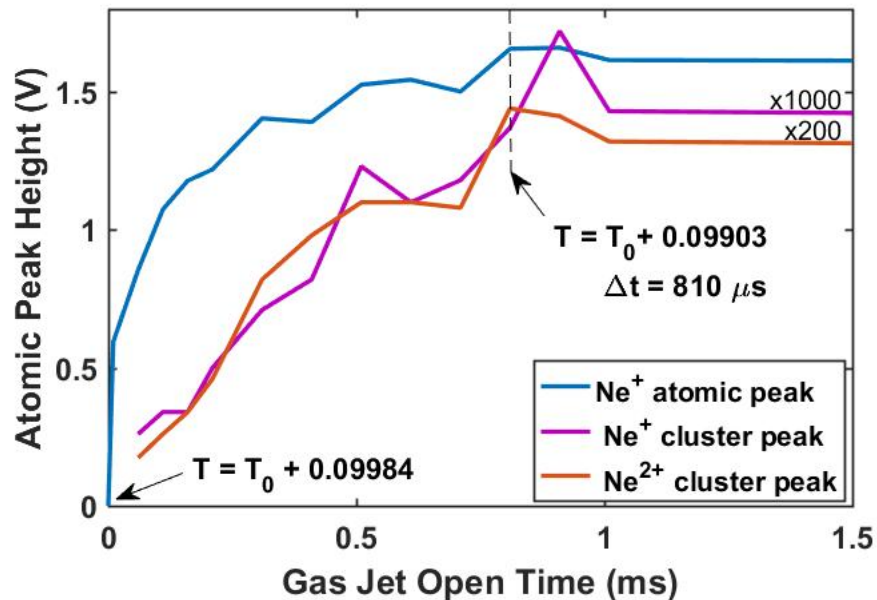


Figure 7.19: Heights of the central atomic cluster peak of Ne^+ , as well as the front cluster peaks of Ne^+ and Ne^{2+} , as a function of XUV laser timing with respect to the gas jet trigger. Ne gas jet backing pressure was 40 psi, and the gas jet opening time was set to 1 ms.

Chapter 8

Results

Here we present the results of nanometer-scale clusters irradiated with intense XUV light composed primarily of energies from 26.4 eV to 32.6 eV, fluences of $\sim 1 \times 10^{-2}$ J/cm², and on-target intensities of $\sim 1 \times 10^{13}$ W/cm². Targets included silver nanoparticles, as well as van der Waals-bound gas clusters.

Although we were able to create silver nanoparticles via the LAM method, and to deliver them to the interaction region of the target chamber, we were not able to provide sufficient on-target XUV intensity to enable these clusters to absorb the energy necessary for complete nanoparticle dissociation. Microparticles and nanoparticles mounted on glass, as well as nano-scale thin film targets proved similarly inconclusive. Therefore, our XUV-illuminated nanoparticle data is not able to contribute as we had hoped to the experimental investigations of high frequency laser ionization of solid metallic clusters. However, the m/q time-of-flight spectra obtained by irradiating these clusters with the higher-intensity 800 nm THOR laser demonstrate that the experimental design and execution are otherwise viable. Additionally, these IR measurements may provide some insight into the development and dissociation of

metallic nanoparticle plasmas.

Due to their dramatically lower cohesive energies, noble gas clusters, generated via Hagen-type expansion of pressurized gas into vacuum and irradiated with high-intensity XUV pulses, became the main focus of our investigation. With these clusters, we confirmed the improved charge-to-mass ratio resolution of our Wiley-McLaren time-of-flight spectrometer. This enhanced m/q resolution, in addition to the signal acquisition and processing techniques which produced over seven orders of magnitude in yield resolution, enabled us to confidently identify high charge states in each noble gas and molecular gas cluster we studied.

The maximal charge states we report are Xe^{8+} , Kr^{6+} , Ar^{5+} , Ne^{3+} , and N^{2+} , each well above the maximum achievable charge for an isolated ion in a low-density plasma. These high charge states persist, seemingly independent of cluster size or photon energy within the ranges of each available to us. Yield ratios of the different charge states do, however, seem to be modified by cluster size. At larger cluster sizes, the dominant charge state appears to shift from 1+ to 2+, and fractional yields from higher charges begin to drop off, potentially demonstrating the effects of recombination in the cores of larger clusters. Lower incident photon energies appear to reproduce m/q data corresponding to larger cluster sizes at higher photon energies. This effect persists uncorrelated with the energy dependence of photoabsorption cross sections.

The identifying feature of high charge states is the forward-going peak

associated with high energy (about 100 eV) cluster dissociation. As we expect, no sharp, central peaks associated with uncondensed gas are observed at charge states higher than achievable via multistep single photon ionization with the given photon energy. One prominent feature of these forward-going peaks, believed to be unique to this work, is the presence of identifiable contributions from different isotopes. This is most visible in the studies of xenon and krypton, due to their multiple stable isotopes at comparable natural abundances.

In addition to m/q spectra, we were able to record ion kinetic energy spectra for these gas clusters using field-free drift measurements. For the most part, these spectra exhibit similar trends, with small cluster sizes producing only low-energy ions. The maximum ion energy increases with cluster size, until saturating around a value near $h\nu - I_p$ for the given material. Neon ion kinetic energy spectra obtained with illumination from 25.4 eV XUV pulses are an anomaly, in that they seem to be peaked *sharply* around a value near $h\nu - I_p$, independent of cluster size. We hypothesize that this is due to the unusual electronic structure of solid-density neon.

Lastly, we recorded electron kinetic energy spectra from the clusters under investigation. Here we observe what appears to be a kinetic energy-dependent “filtering” mechanism, which strongly suppresses detection of electrons below about 10 eV, while potentially amplifying signal from photoelectrons generated by much higher harmonics, the contributions of which should be negligible.

8.1 Nanoparticles

The main goal of experiments using the LAM apparatus to generate nanoparticle targets for THOR's HHG-generated XUV pulses was to be able to generate metal oxide nanoparticles, such as SiO_2 , TiO_2 , and SnO_2 , and to use these to observe a shift in the maximum achievable charge state of the constituent oxygen atoms. Presumably, we could identify higher oxygen charge states from clusters with higher- Z metal atoms. These metals would donate higher number of screening electrons, contributing to increased continuum lowering, and resulting in a higher achievable charge state for all atoms, including the oxygen.

To test the component assumptions of this experiment, we started by looking at the ionization states of oxygen when irradiating clusters of gas molecules containing oxygen: CO_2 , followed by pure atmosphere (obviously containing O_2 molecules), and then by pure O_2 . The results of these experiments are contained in Section 8.1.1.

8.1.1 Oxygen-Containing Molecular Cluster Data

To get an idea of what type of signal we could expect from XUV-irradiated metal oxide nanoparticles, and whether the resulting ionization state of oxygen could be used as a marker of the degree of continuum lowering in said nanoparticles, we decided to shoot gas clusters containing oxygen. We started with CO_2 gas, with which we could easily and safely vary the cluster size of the targets. When this did not produce charge states of oxygen above

singly charged, we decided that O_2 might make a better target for this test.

For safety's sake, we started by shooting pure, uncompressed atmosphere, for which it is difficult to determine the cluster size and relative abundances of species within a cluster. When this still did not yield oxygen ions more than singly charged, we employed a bottle of compressed O_2 . This still did not yield high charge states of oxygen. For this reason, using oxygen ionization as a marker for continuum lowering in a metal oxide nanoparticle may need to be rethought.

Figures 8.1 and 8.2 show the ion time-of-flight data from compressed CO_2 , at mean cluster sizes of 3,000 to 530,000, spanning the achievable range of backing pressures of CO_2 with our setup, and covering close to the entire expected size range (7 nm to over 39 nm) of our metal oxide nanoparticles. At low cluster sizes (and hence low backing pressures), we have a signal from background N_2 in our target chamber. This signal seems to be incorporated into a contaminated bottle of CO_2 gas, as the N_2^+ signal increases with pressure along with the CO_2^+ , as is best seen in Figure 8.2.

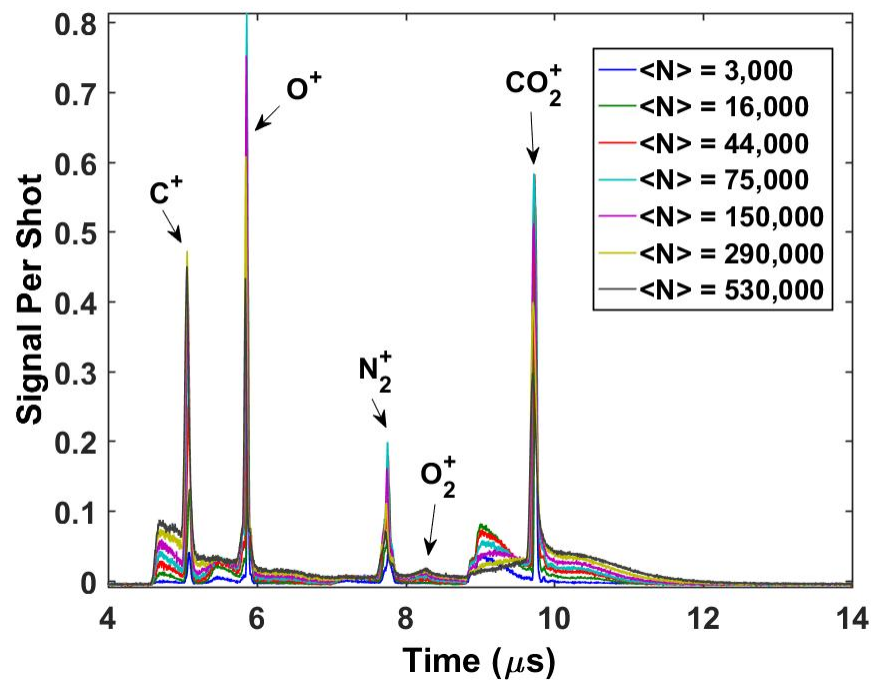


Figure 8.1: Ion ToF data from different cluster sizes of CO_2 , with major ion species labeled.

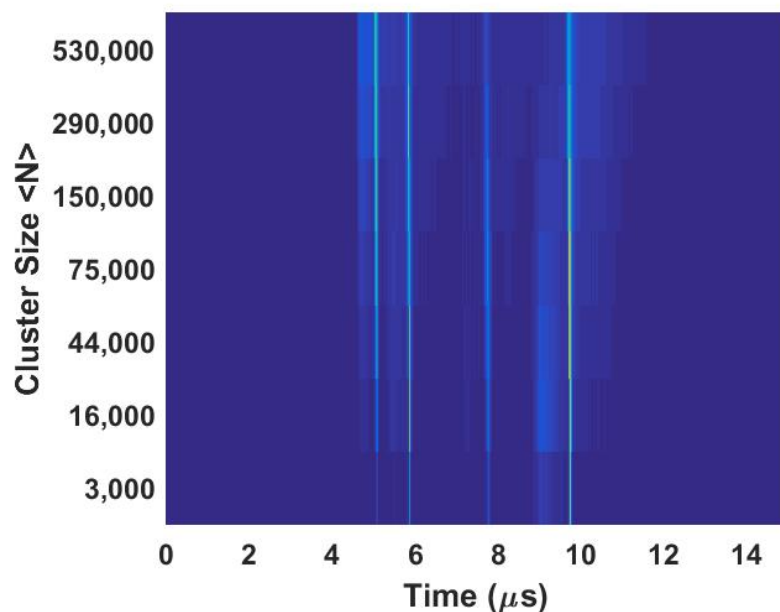


Figure 8.2: Ion ToF data from different cluster sizes of CO_2 , plotted as a heat map profile.

As you can see in Figures 8.1 and 8.2 above, larger cluster sizes yield a slightly higher fragmentation ratio, from CO_2^+ to C^+ and O^+ , and we do have quite a bit of pure O^+ signal, we do not see any evidence of O^{2+} , or any higher charge states of oxygen. In an attempt to produce these higher charge states, a similar set of data, spanning a large range of cluster size, was taken with compressed pure O_2 , as shown below in Figures 8.3 and 8.4.

These peaks are, unsurprisingly, very similar to data we have collected with N_2 . With increasing cluster size, the ratio of O^+ to O_2^+ also increases. The main O_2^+ cluster peak shifts from primarily a forward peak, before the central atomic peak, to more evenly distributed between forward and backward peaks.

The O^+ peak remains dominated by its forward peak, although it exhibits the same trend at large cluster sizes. It is apparent that the N_2^+ visible in these oxygen cluster spectra is not from target gas contamination, but from background signal from stray gas in the target chamber, as the signal decreases rapidly with increasing O_2 backing pressure. These trends with cluster size may most easily be seen in Figure 8.2.

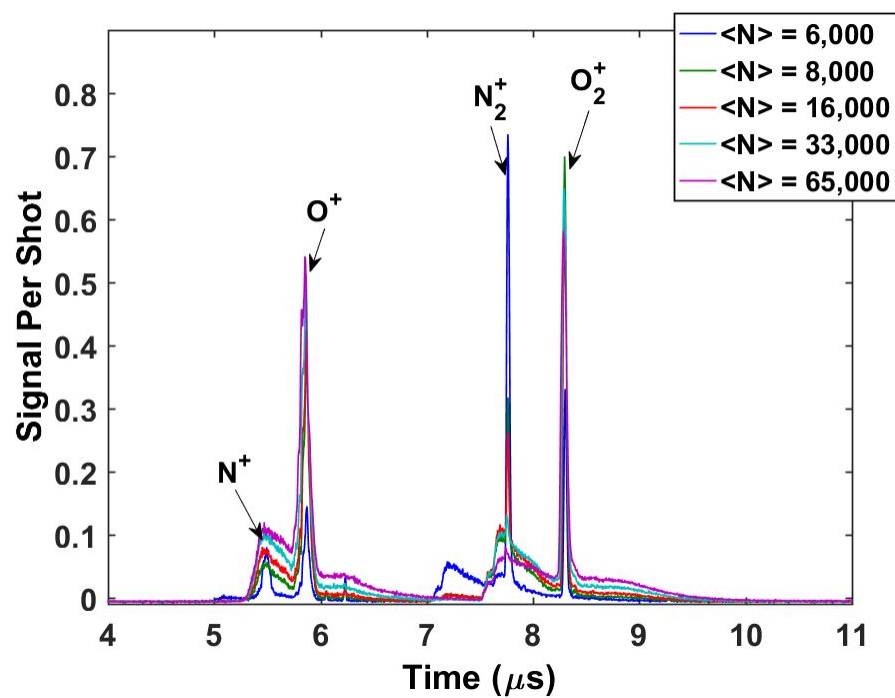


Figure 8.3: Ion ToF data from different cluster sizes of O_2 , with major ion species labeled.

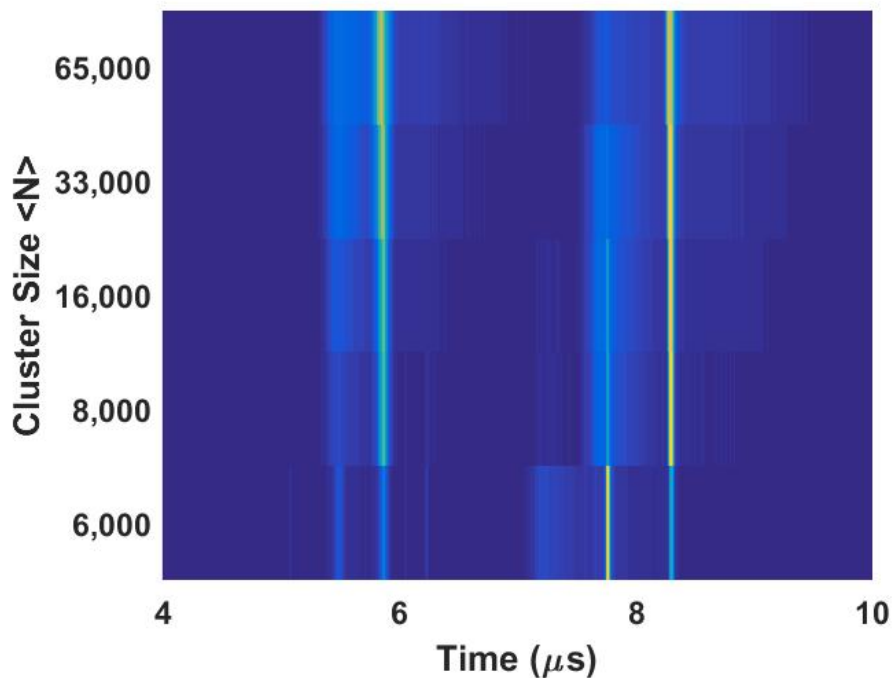


Figure 8.4: Ion ToF data from different cluster sizes of O_2 , plotted as a heat map profile.

Unfortunately, what is notably absent from these O_2 cluster data is higher charge states of oxygen. We still have not observed charge states above O^+ in these time-of-flight spectra.

8.1.2 Irradiation with Intense 800 nm Pulses

Undeterred by the lack of high oxygen ionization states in molecular gas clusters, we continued on to the LAM-generated silver nanoparticle targets. When initial attempts to try to view signals from XUV irradiation of ablated silver nanoparticles did not yield results, we needed to confirm that

our experimental apparatus worked properly - that we were indeed generating nanoparticles with our LAM apparatus, and injecting them into the focus of the laser.

To confirm this, we switched from using the generated XUV light as our ionization source to using a portion of THOR's compressed 800 nm beam. We removed the pickoff mirror from the compressor output beamline, and allowed the center of the beam, which would have been masked by the pickoff mirror, to travel down the HHG beamline, without the harmonic gas jet active. The 200 nm aluminum foil was removed, but the inverse mask iris was left in place, making the portion of THOR's IR beam transmitted into the XUV target chamber equal in diameter to the XUV beam. This means that only 20% of the compressed THOR energy was available on target, less than 130 m J, 4 TW, or $4 \cdot 10^{18}$ W/cm².

Using this setup, we were able to confirm that all parts of the system were working properly. We observed signatures on our time-of-flight spectrometer from nanoparticles, microparticles, and uncondensed silver gas. Uncondensed Ag gas was identifiable by the two prominent silver isotopes - ¹⁰⁷Ag, with 51.8% abundance in nature, and ¹⁰⁹Ag, with 48.2% abundance. Nanoparticle signatures occurred at a rate 14 times higher than those of the microparticles (7% versus 0.5% of shots). We used both nitrogen and helium as a buffer gas, in order to observe the different signatures from differently-sized nanoparticles. There does not seem to be a correlation between buffer gas or the on-shot laser energy and the type of signal we get from the silver particles.

Each particle produced a signature on only a single shot of our 10 Hz data acquisition, and each individual shot yielded a different signature, making averaging or accumulation of shots impossible. These particle signatures may be organized broadly into categories, with each category displaying a distinct set of features in its trace. In many data sets, especially those from dense nanoparticle clouds or microparticles, is difficult to get an accurate measurement of m/q , as the presence of silver frequently distorts the time scale for both silver and other species, and in fact, frequently distorts the appearance times and profiles associated with the buffer gas.

Figure 8.5 shows the typical ion ToF signal for nitrogen buffer gas, without evidence of silver. This profile is extremely repeatable between shots. In fact, a distortion in this buffer gas signal was often the most prominent sign of a nanoparticle shot. The signal from ionized hydrogen and a growth in the photon peak are the most sensitive and reliable markers for a particle in a shot. Nearly unnoticeable in background shots, the signal for both increases dramatically when we get on or near a silver particle. The hydrogen signal is most likely due to the proprietary anti-adhesive coatings on the silver microparticles from DuPont.

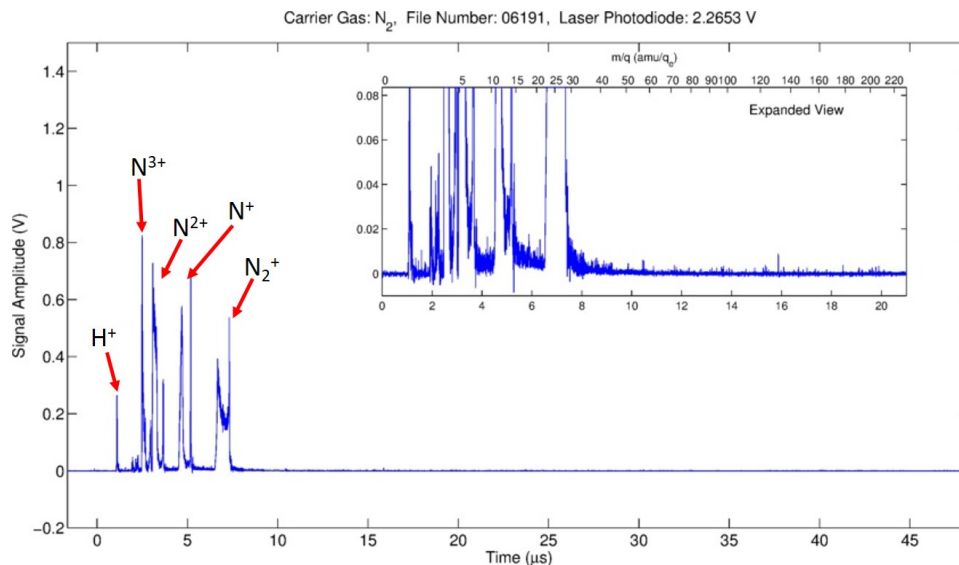


Figure 8.5: A typical ion ToF signal from N₂ buffer gas only, with no nanoparticles.

Unlike shots consisting solely of background gas, signatures of the laser interacting with a cloud of LAM-ablated nanoparticles likely formed by a single microparticle are varied in their signature traces, and can be grouped into about 10 different profile types. Figure 8.6 shows one typical signature of a nanoparticle shot. In this signal pattern, the Ag signal is not strong enough to disrupt the nitrogen signature, although there is a notable increase in the hydrogen peak. You can see a prominent Ag⁺ and Ag²⁺ signal. The Ag²⁺ signal is actually higher than the Ag⁺ signal, and exhibits more of an atomic peak signature, with possible isotope separation, while the Ag⁺ signal has a broad, cluster signature. This pattern was common.

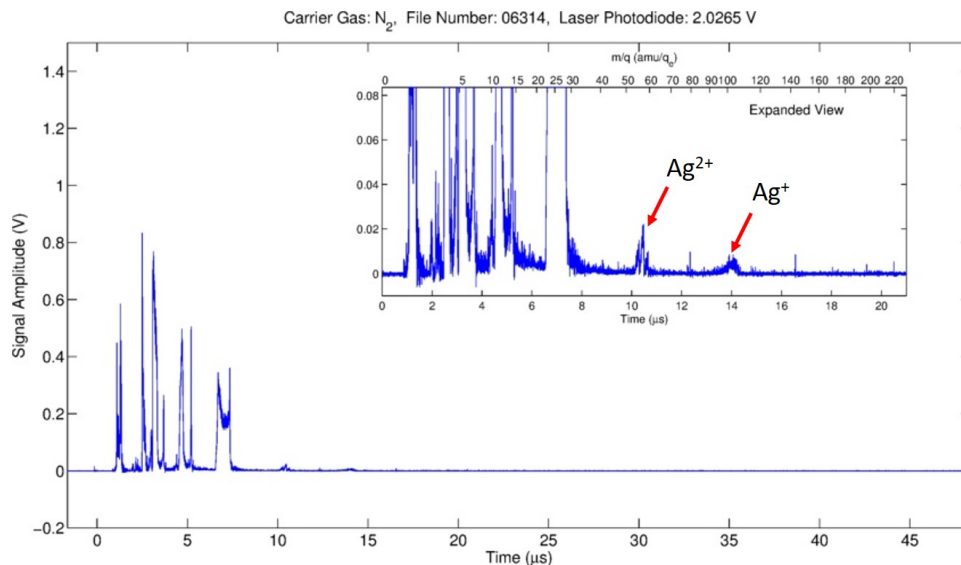


Figure 8.6: A typical ion ToF signal with Ag nanoparticles present in an N_2 buffer gas. We can see Ag^+ , and Ag^{2+} in this signal. Ag^{2+} shows possible isotopes, with atomic-type peaks, while Ag^+ shows a more cluster-type of broad signal.

Figure 8.7 shows a prominent silver ion ToF nanoparticle signature, in a nitrogen buffer gas, with a cluster and atomic peak for Ag^+ , and atomic peaks for Ag^{2+} , with visible isotope separation. Additionally, we see a new peak around $m/q = 26$, as well as a distortion in the background cluster gas signal, including a reduction in the N^+ cluster signal, and a dramatic increase in the H^+ signal.

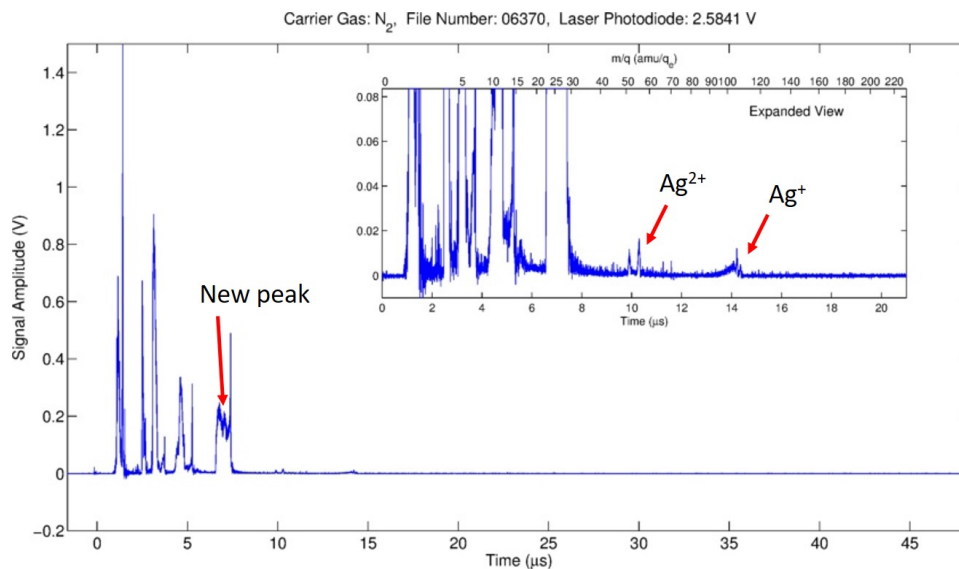


Figure 8.7: A typical signal with Ag nanoparticles present. The signatures for Ag⁺, and Ag²⁺ are similar to those in Figure 8.6. Ag²⁺ shows possible isotopes, with atomic-type peaks, while Ag⁺ shows a more cluster-type of broad signal.

A third representative profile of a signal from small nanoparticles, which does not significantly affect the background buffer gas signal (with the exception of H⁺), is shown in Figure 8.8. It shows signal from Ag²⁺ as a broad cluster profile, but shows no appreciable amount of Ag⁺.

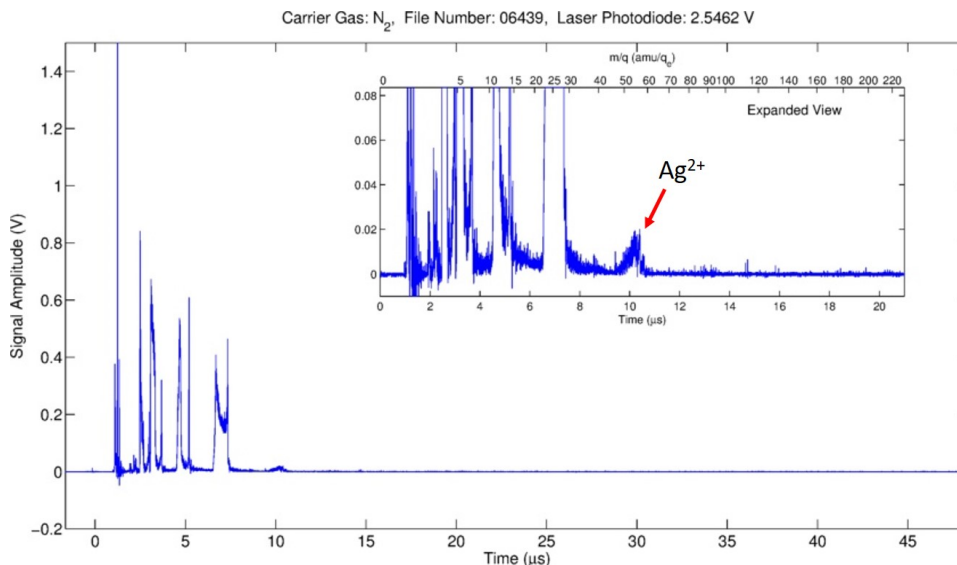


Figure 8.8: An example of a signal with a small amount of Ag^{2+} , with a large enhancement in the H^+ signal as the most prominent sign that we have hit a nanoparticle cloud.

Other common signals show a large change in the average background signal, decreasing the signals from nitrogen significantly. We have seen this effect in gas cluster experiments as well, when an exploding cluster effectively “blows away” the contaminant gas in the target chamber. In silver, this effect could come from hitting a dense cloud of nanoparticles, or from hitting a single larger nanoparticle or unexploded microparticle. Further research is needed to distinguish between these cases. Figure 8.9 shows one such case. We can see cluster peaks from Ag^+ , and Ag^{2+} , and a huge increase in the signal from H^+ . The signal from nitrogen is nearly gone, and we have picked up another cluster peak at 4 μs . This 4 μs peak is a common feature of dense silver shots, in both N_2 and He buffer gas, indicating that it could represent a a fragment

of the coating present on microparticles to keep them from clumping together.

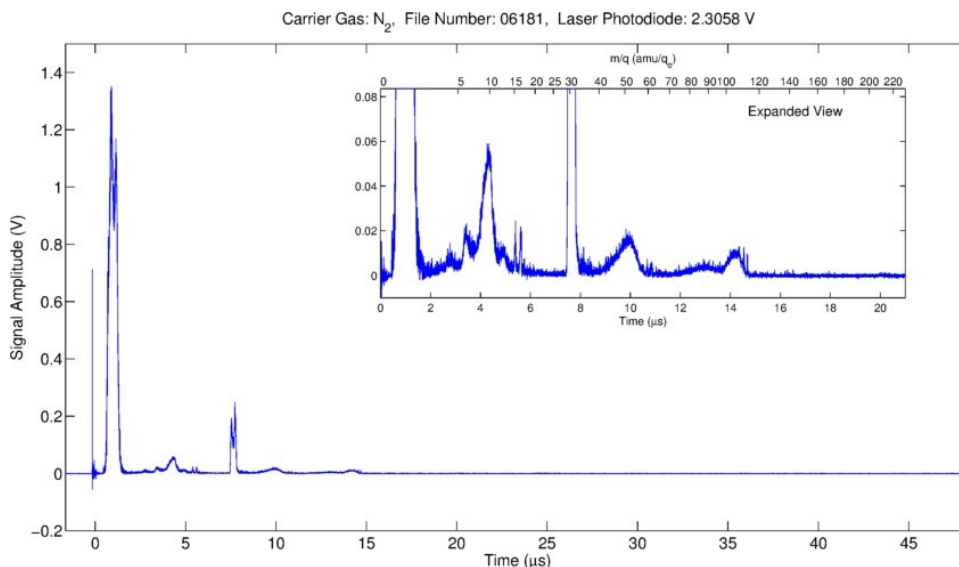


Figure 8.9: An example of a signal from a dense portion of a nanoparticle cloud, or a microparticle, which significantly disrupts the signal from the N_2 buffer gas. In this signal, we see Ag^+ , and Ag^{2+} , as well as a new cluster signal at $4 \mu s$, and an enhancement of the H^+ signal, which are likely from the microparticles' anti-adhesive coating.

The trace in Figure 8.10 represents another common profile of a dense silver shot with N_2 buffer gas. In this profile, the easily distinguished nitrogen signals are all but gone. We see a large cluster peak of Ag^+ ions, with an atomic peak on the trailing side. The large cluster peak at $4 \mu s$ is even more prominent than in Figure 8.8, and we have a similar peak at $8 \mu s$, which is also a common feature of dense silver cluster shots. This could be indicative of Ag^{3+} , or of another microparticle coating fragment. In these profiles with large silver signals, we can see that the m/q scale is probably incorrect. The

time scale on these shots is distorted, with the Ag^+ atomic peaks falling at a later time than on shots at lower density.

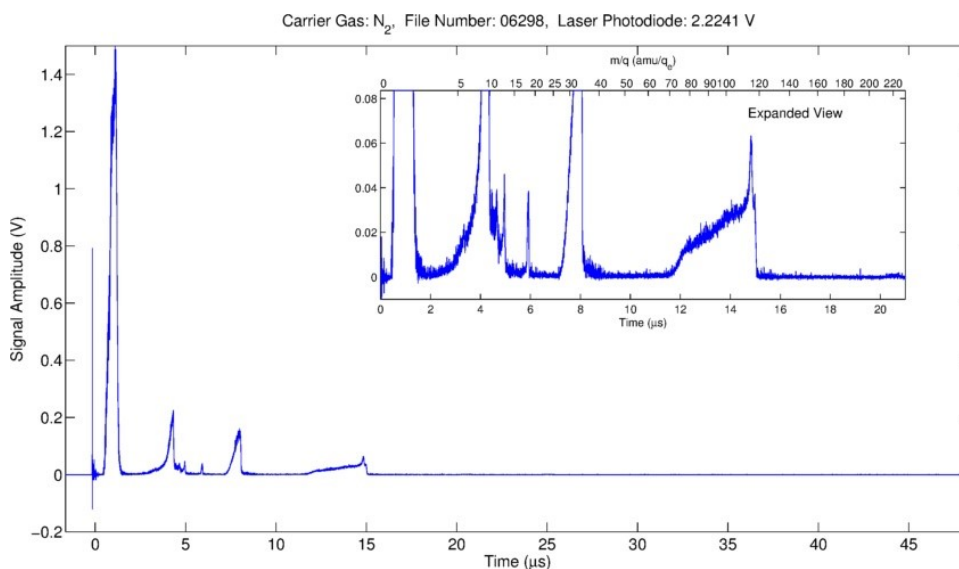


Figure 8.10: A signal from a dense nanoparticle cloud, with no apparent signal from the N₂ buffer gas. We can see a signal from Ag^+ , atomic and cluster, as well as the cluster signal at 4 μs , as in Figure 8.9, and an additional signal at 8 μs .

A much more unusual trace is shown in Figure 8.11. It seems clear that, in this shot, we hit a particularly dense part of the nanoparticle cloud, yielding a large signal from uncondensed atomic Ag^+ (with each isotope visible), as well as a low, broad cluster peak. No higher charge states of silver are visible, but we do still have a prominent signal from the microparticle coatings at 4 μs , and a large increase in both the H^+ and photon signals.

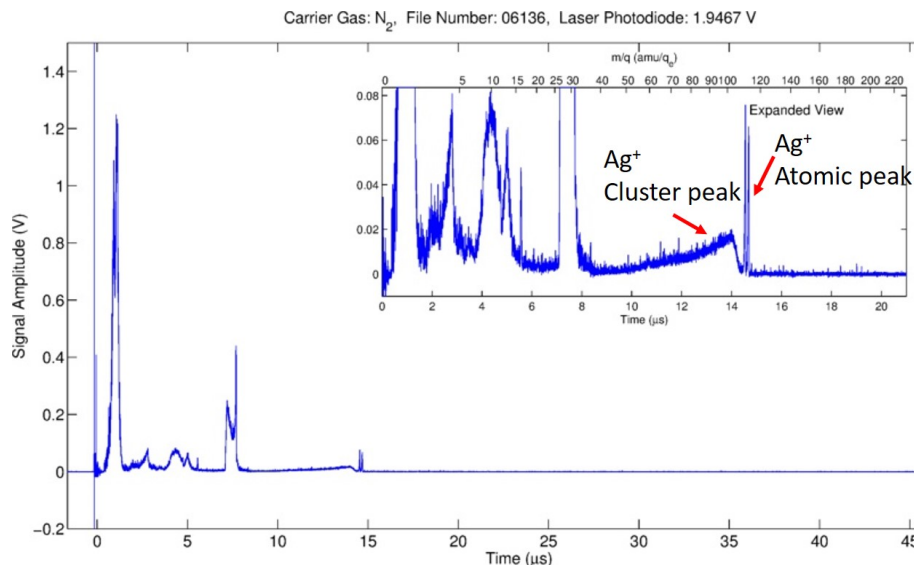


Figure 8.11: A signal from a moderately dense nanoparticle cloud. The N₂⁺ signal is still present, and we have a large atomic Ag⁺ peak (with both isotopes visible), as well as an unusually-shaped cluster peak. The photon signal in this shot is extremely high, alluding to the high density of the Ag cloud.

Figure 8.12 shows another unusual signal profile. Again, we have both atomic Ag⁺ and a large cluster peak preceding it. This time, the peak at 8 μs takes the same shape as the Ag⁺ peak, leading to suspicion that it could actually be Ag³⁺. It could also be oxygen, if we were to re-scale the m/q scale for the new position of the silver atomic peaks on this particular shot. The nitrogen signal is undetectable, having presumably been entirely displaced by the nanoparticle cloud formed by an exploded microparticle. The signal at 4 μs is still very prominent, and again, we have very significant increases in the hydrogen and photon peaks.

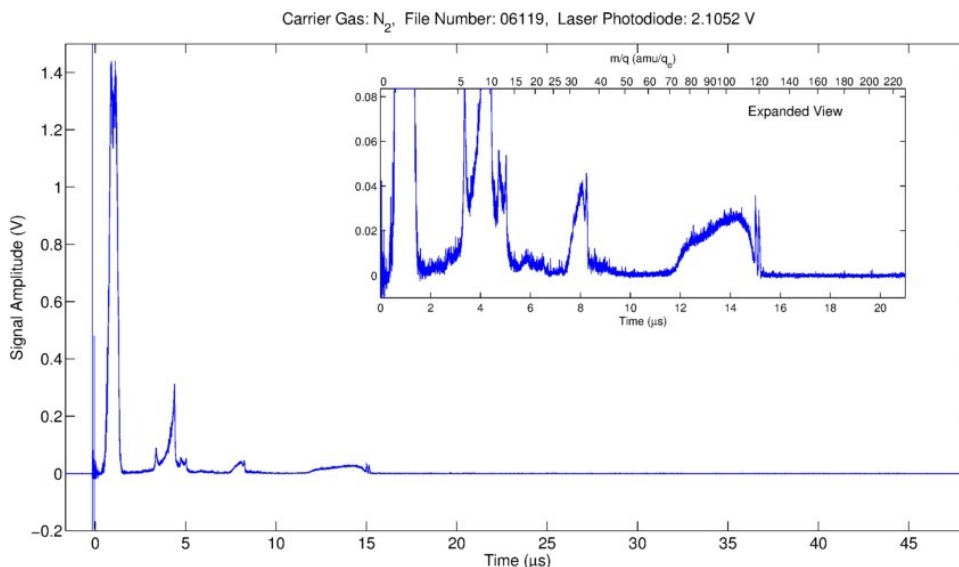


Figure 8.12: A signal from a very dense Ag nanoparticle cloud. Again, we have atomic and cluster signal from Ag^+ (with isotopes visible), and the signal at 8 μs exhibits a similar profile. The signal at 4 μs , as well as the H^+ and photon peak enhancements, are prominent.

The signal profile in Figure 8.13 may shed some light on the identity of the peaks at 10 μs and 8 μs , as they are both present in this shot. Again, we see the atomic Ag^+ , and a large cluster peak preceding it, and the peak at 8 μs takes the same shape. The peak closer to 10 μs is cluster only. We can see from the position of the Ag^+ peak that, in dense shots such as these, the time and m/q scales may become distorted, and as in this shot, there is not often a N_2^+ peak with which to confirm the scale.

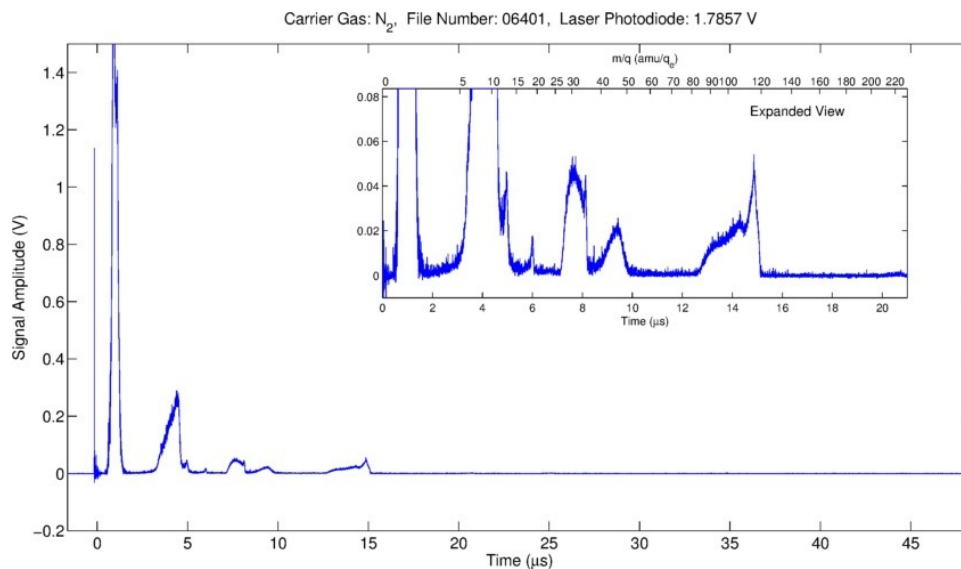


Figure 8.13: A signal from a dense nanoparticle cloud, showing Ag^+ , and then potentially Ag^{2+} , as well as another signal at $8 \mu\text{s}$ and at $4 \mu\text{s}$. As usual, we have a large H^+ peak and photon peak.

Figure 8.14 is the signature which is most likely to be a microparticle. We see no atomic peak from the Ag^+ or Ag^{2+} (now located suggestively around $8 \mu\text{s}$) signals. The Ag^+ signal is extremely broad. No trace of buffer gas signal is visible. The photon peak is much higher than in other shots. These signals appear in about 7% of the traces with silver signal.

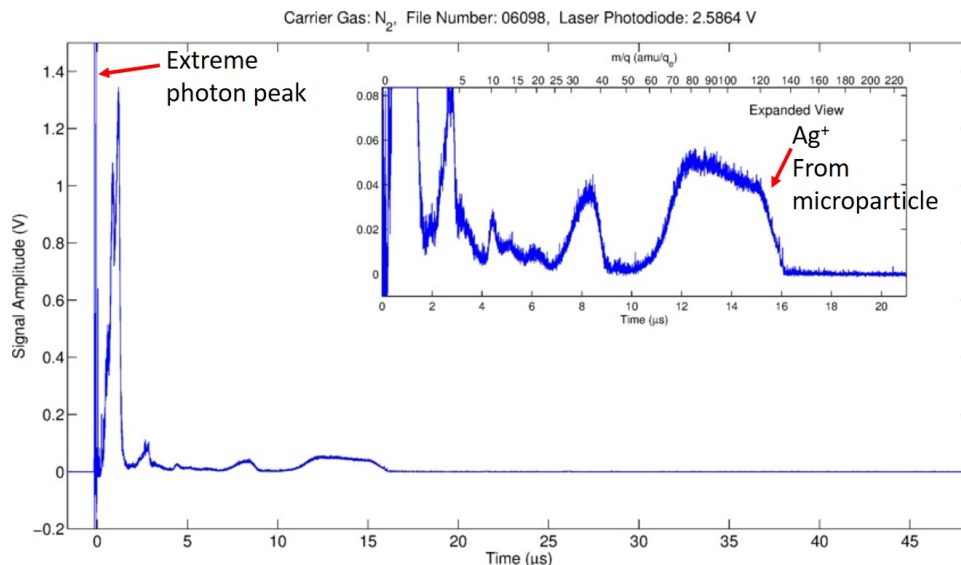


Figure 8.14: A signal which is most likely to be a microparticle signature. Note the broad Ag⁺ peak, lacking any atomic peaks, as well as the extremely large photon peak, which causes ringing in the signal for a significant duration.

Signals using a He buffer gas are similar to those with a N₂ buffer gas. As in the N₂ signals, deviations in the background gas signal were often the most reliable signs of hitting a silver nanoparticle. Figure 8.15 shows a typical buffer gas signal, as well as two signals where silver particles were also found. The signals are zoomed in, to inspect the traces from $m/q = 1, 2,$ and $4,$ which are marked with dotted lines. All three are triple peaks, with a front, center, and back peak. When only the buffer gas is present, the signals are skewed toward the front and center peaks (as seen on the top panel of Figure 8.15). When we hit a nanoparticle, or parts of a nanoparticle cloud, the signals shifted, sometimes with an increase to the back peak (as in the bottom left panel of Figure 8.15), and sometimes to further favor the front peak (as in the

bottom right panel of Figure 8.15).

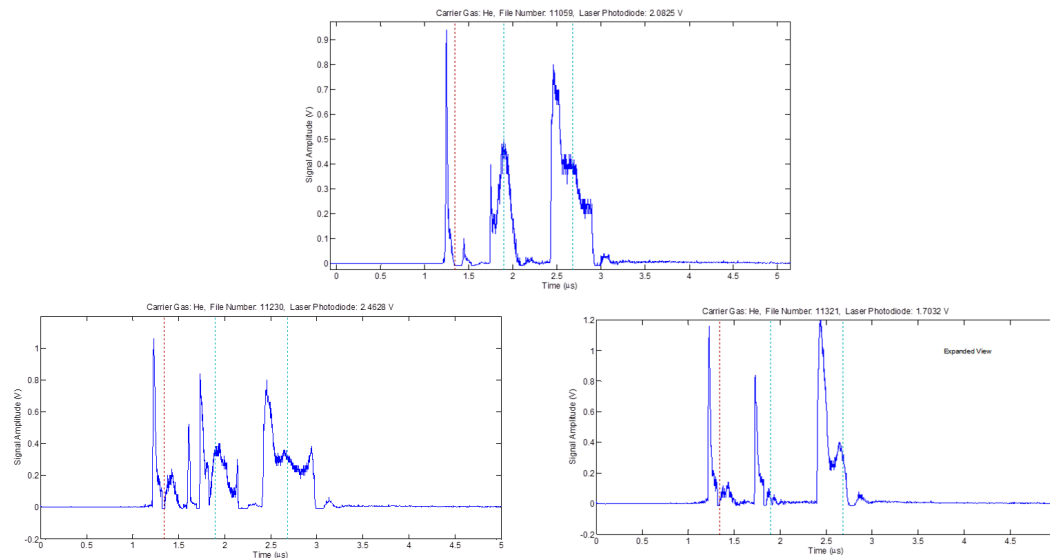


Figure 8.15: Signals from He buffer gas. Dotted lines corresponding to $m/q = 1$ (red), and $m/2 = 2$ and 4 (teal) mark the centers of each common species in the buffer gas. The signal common to all shots without nanoparticles is shown in the top panel. Two modified signals corresponding to two different shots with silver signatures are shown in the bottom two panels.

Figure 8.16 gives a good example of a trace made by silver nanoparticles in a He buffer gas which shares many similarities with traces made with N_2 buffer gas. Because the mass of He is only 4 amu, these traces give us a larger range of m/q space in which signal from a nanoparticle cloud may be easily distinguished from background signal. In Figure 8.16, we see a well-defined Ag^+ and Ag^{2+} signal. The Ag^+ signal looks as if it may have some atomic peaks, in addition to its more prominent forward cluster peak. The large cluster peak at $4 \mu s$, so common in the traces with N_2 buffer gas, is also

present in this trace. It appears that this could well be attributable to C^+ , leading us to conclude that a large portion of the anti-adhesive coating on the original microparticles may be hydrocarbon-based. This would also help explain the consistent increase in the H^+ peak in nanoparticle shots with either buffer gas. These He buffer gas shots also help us to distinguish a sharp peak around $m/q=18$, suggesting that there is a non-negligible amount of adsorbed H_2O on the microparticles. This peak is visible in many of the traces from N_2 buffer gas, but the He buffer gas traces confirm that this is from the silver particle cloud itself, and not a remnant of the buffer gas.

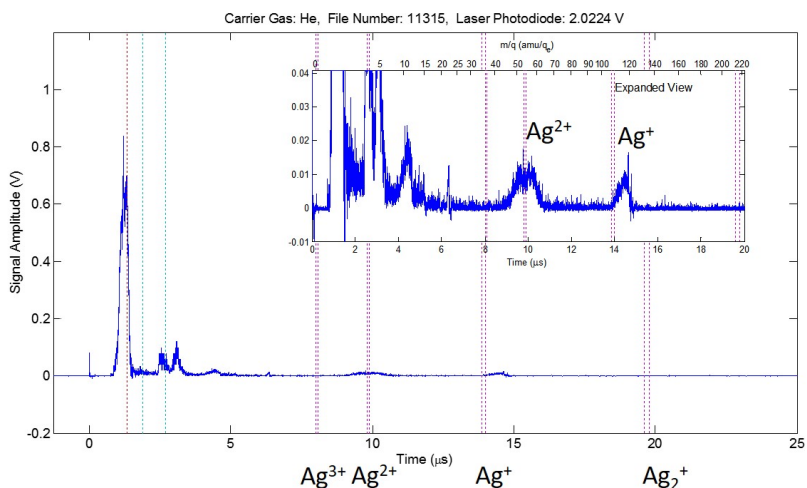


Figure 8.16: A trace from a relatively low density nanoparticle cloud, in a He buffer gas. Signals from Ag^+ and Ag^{2+} are present, as is the peak around $4 \mu s$, which was also present in many nanoparticle shots formed in N_2 buffer gas. An additional atomic-type peak has emerged around $6 \mu s$, which is suggestive of a water peak.

Figure 8.17 gives a better example of the potential water peak. This signal appears to be from a less dense portion of a nanoparticle cloud, judging from the sizes of the photon and H^+ peaks. Nevertheless, we observe a large, atomic-like peak around $m/q=18$, which would correspond to H_2O^+ . This trace also shows a common-looking silver peak, with a possible small contribution from atomic Ag^+ .

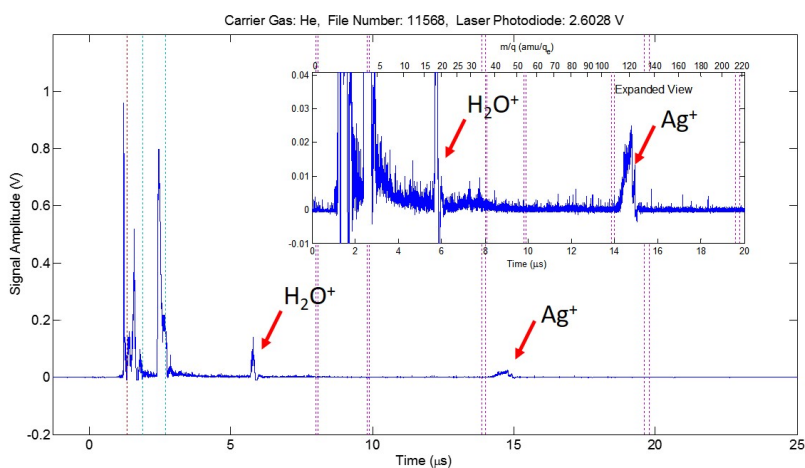


Figure 8.17: A common type of signal from a low-density portion of a silver nanoparticle cloud, showing a prominent Ag^+ peak, as well as an atomic-type peak which is most likely H_2O^+ .

Although using different buffer gases helps to provide a complimentary set of information on nanoparticle targets, shots with unablated microparticles typically look very similar for different buffer gases. In these shots, the buffer gas is usually completely absent, “blown out” of the active area completely. Figure 8.18 shows an example of a typical microparticle shot in He buffer gas. It looks very similar to dense, or microparticle signals in N_2 buffer gas, such

as in Figure 8.14, but the atomic peak that was previously around $m/q = 18$ (now closer to looking like a C^+ peak at $m/q = 12$, except that we remember that peaks shift in large/dense particle shots) is prominent, and not obscured by buffer gas signals.

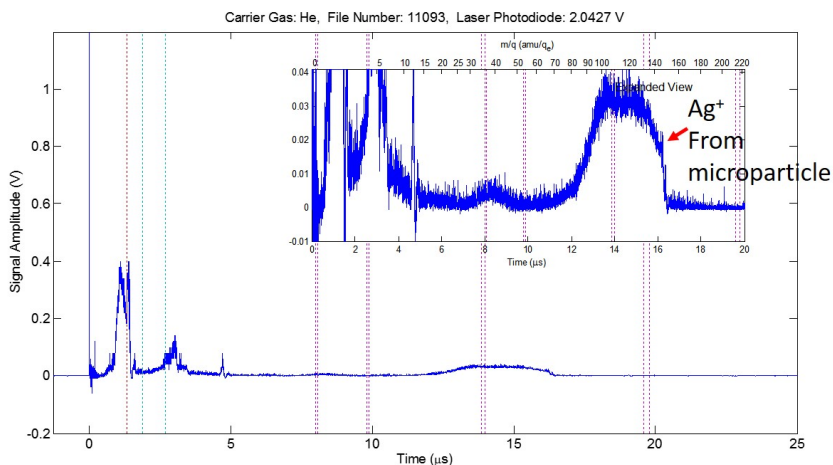


Figure 8.18: A typical ion ToF signal from a silver microparticle, in He buffer gas.

8.1.3 Irradiation with XUV

The experiments detailed in Section 8.1.2 confirmed that we were able to generate silver nanoparticles and deliver them into the target area, in the interaction region of our ToF spectrometer, and that we were able to detect signals from dissociated silver nanoparticles when we hit one with our laser focus. Unfortunately, when switching back to using XUV pulses instead of THOR's high-intensity fundamental frequency, we were still unable to observe any signal from silver particles. This suggests that few if any signals we observe

in the infrared are from unagglomerated silver atoms, as these should still be easily ionized by XUV and observed in our spectrometer.

We believe the reason for this lack of data from nanoparticles with XUV ionization is the large cohesive energy associated with solid materials. Solid silver has a cohesive energy of 2.95 eV/atom, so the bare minimum amount of energy absorbed by the cluster to achieve dissociation with 32.6 eV/photon would be about 9% photoionization. This assumes no energy lost through other mechanisms. In comparison, liquid argon has a cohesive energy of 0.08 eV/atom, and the most tightly bound of the noble gases, xenon, has a cohesive energy of 0.16 eV/atom. Using the absorption cross section and density of liquid argon, we expect a 5 nm diameter particle to experience only 2% primary photoionization at 32.6 eV, but this represents an average of over nine times the cohesive energy necessary for dissociation into each individual atom. In contrast, for silver we expect about 13% photoionization of a similar 5 nm particle, but this represents only about 1.5 times the cohesive energy needed for full dissociation. These numbers are for our best observed XUV energy of 20 nJ per shot. It is possible that under our more common, less ideal conditions, we are simply unable to provide enough energy for full dissociation of the particle into ions.

8.1.4 Solid Targets Mounted on Glass

It is apparent from Section 8.1.2 that perhaps the two main difficulties with observation of ToF signals from nanoparticles are the large signal from

the surrounding buffer gas and the lack of consistent nanoparticle signals from shot to shot. This confuses ion data and makes electron data, which is always orders of magnitude less intense, impossible to collect. Therefore, to further explore the lack of observed signal from LAM-generated nanoparticles in our XUV beamline, we chose to simplify the situation by measuring data from nano-scale targets mounted on glass slides. This eliminates the background gas, and ensures that you hit a particle on each shot.

Our first target was a portion of a pure, single crystal silicon wafer, mounted in the interaction region of the ToF, with standard ion acceleration voltages applied. No ions were observed ejected from this target. Next, we mounted a 640 μm diameter copper wire in the interaction region and attempted to find an ion signal from the copper or copper oxide on the surface. As shown in Figure 8.19, we were able to identify a small number of copper ions in a 200-shot integrated signal. So it may be that we have enough energy to eject a single ion from a metal surface such as a silver nanoparticle, but that the low signal, coupled with the extreme shot-to-shot uncertainty of LAM nanoparticle data, made the signal difficult to isolate. Figure 8.20 shows the remarkably similar ion and electron spectra we accumulated while shooting a 200 nm thick copper foil instead of the wire.

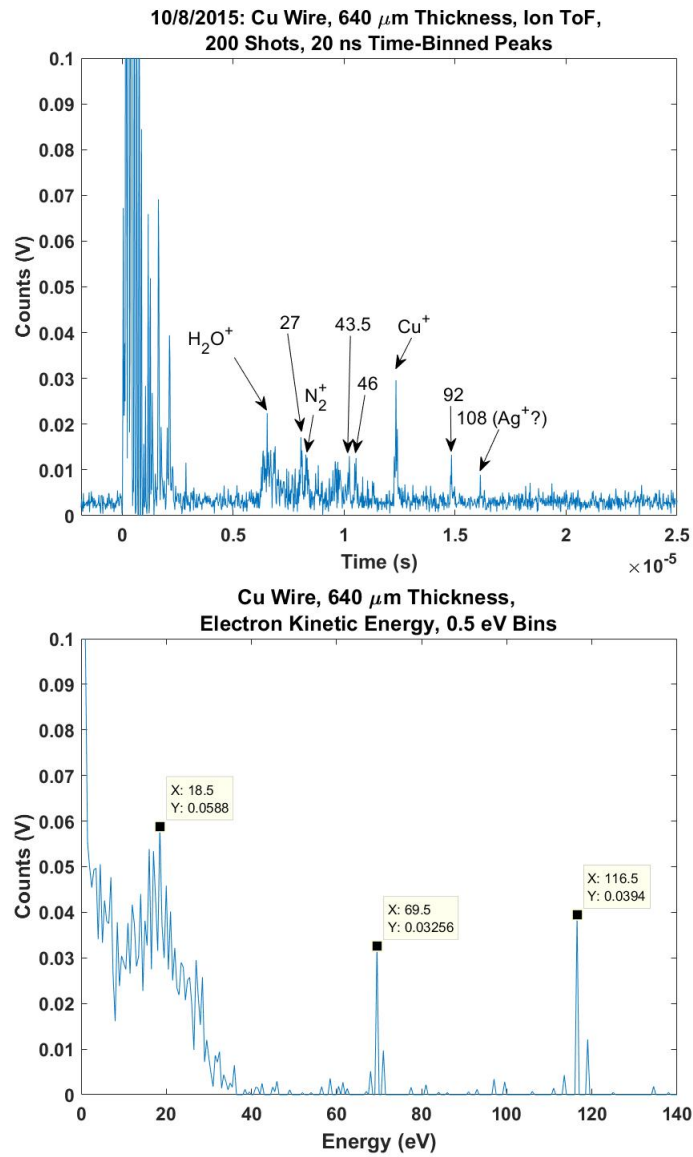


Figure 8.19: Ion ToF m/q spectrum (top), and electron kinetic energy spectrum (bottom) from a 640 μm diameter copper wire. In the top plot, ion species, when known, or estimated m/q is labeled for major peaks.

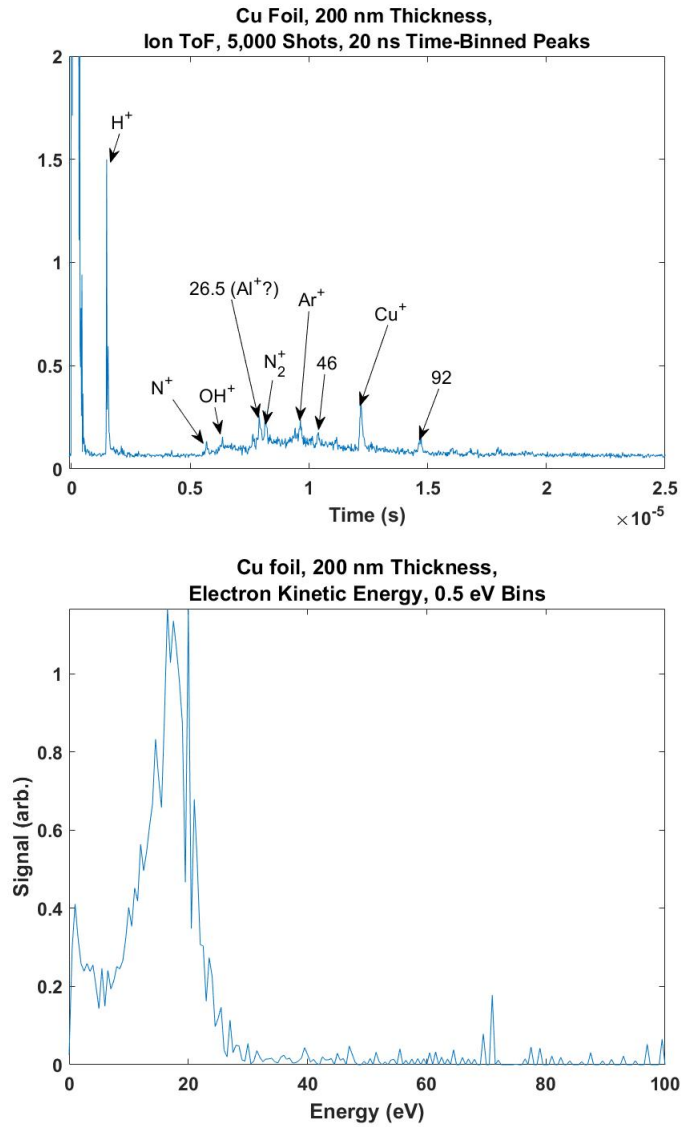


Figure 8.20: Ion ToF m/q spectrum (top), and electron kinetic energy spectrum (bottom) from a 200 nm thick copper foil. In the top plot, ion species, when known, or estimated m/q is labeled for major peaks.

With these promising spectra in mind, we switched from the 200 nm thick copper foil to a 115 nm thick gold foil. Figure 8.21 shows the results of the ion ToF trace from the gold foil. The results overlap almost exactly with the results from the copper foil, shown in Figure 8.21, but with a slightly lower count rate. No gold ions are present, and the overlap of the signals draws into question whether the "copper" ions we found from the foil and wire were actually copper, or some surface contaminants common to both targets.

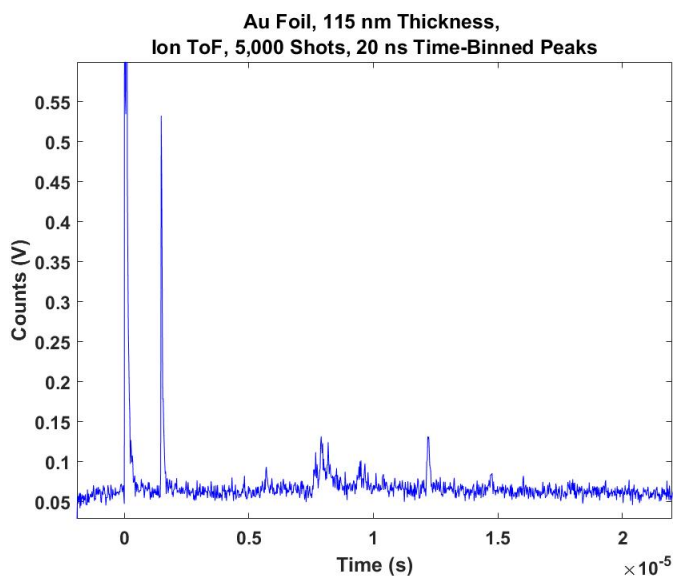


Figure 8.21: Ion ToF m/q spectrum from a 115 nm thick gold foil. No gold ions are present. The trace shows nearly perfect species overlap with Figure 8.20, suggesting that the ions identified as Cu^+ may have actually been surface contaminants.

We then attempted to replace the copper targets with pure SiO_2 , in the form of a piece of 1 mm thick glass mounted in the interaction region of the ToF. We obtained a small ion trace from surface contaminants, but no signal

from silicon, oxygen, or ionized molecular SiO_2 . Likewise, the only electrons collected from this target appeared to be low-energy stray electrons in the target chamber.

The preceding macro-scale targets may have allowed for energy to be carried away before ablation could occur. We attempted to investigate this by instead employing targets of 5 nm silver nanoparticles written onto a glass slide. Our first such target had the 5 nm diameter silver nanoparticles written onto a glass slide in a grid of 10 nm wide wires. We scanned across this target with the 21st harmonic mirror, hitting both the wires (dense regions of nanoparticles), and the regions between the wires, which contained many isolated stray nanoparticles. As with all of the solid targets, we accumulated a few ions per shot. The results of the ion time-of-flight measurement are shown in Figure 8.22, with ion species or calculated m/q identified. No silver ions were found.

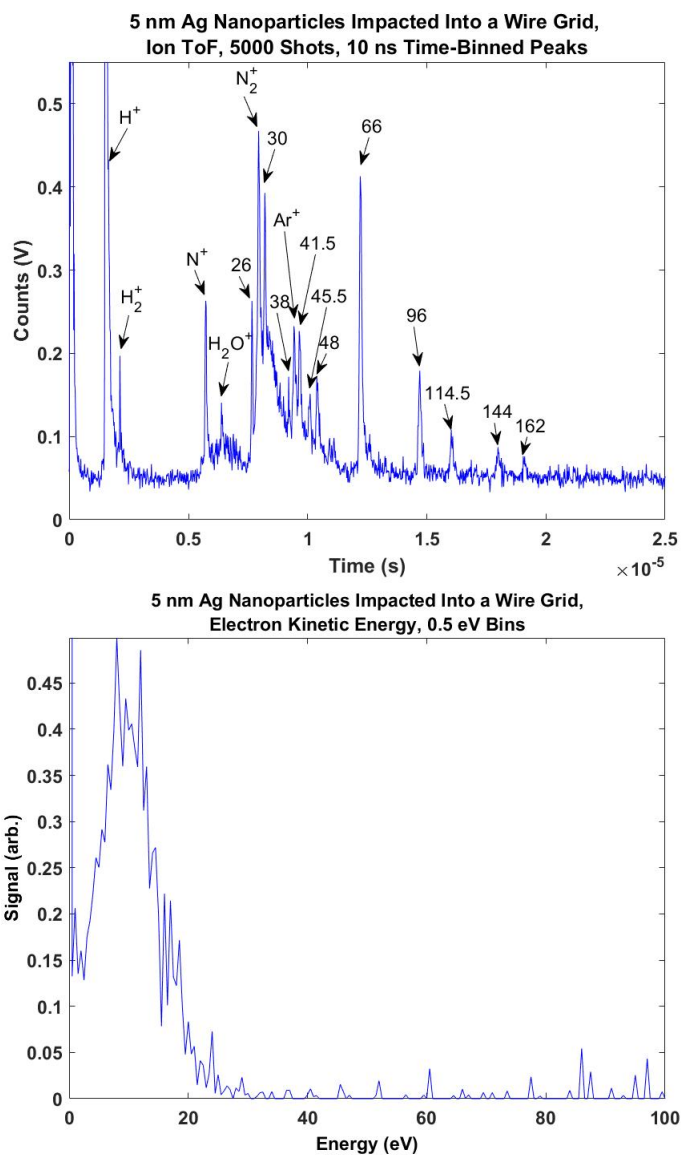


Figure 8.22: Ion ToF m/q spectrum (top), and electron kinetic energy spectrum (bottom) from a grid of 5 nm silver nanoparticles written into 10 nm wide wires on a glass substrate. No silver ions are identified. In the top plot, ion species, when known, or estimated m/q is labeled for major peaks.

Similarly, we obtained a target made of the same 5 nm silver nanoparticles written into a single-layer thin film on a glass slide. Results of an ion ToF measurement of this target are shown in Figure 8.23. They look almost identical to the signal from the Ag nano-wire target in Figure 8.22. No silver ions were found.

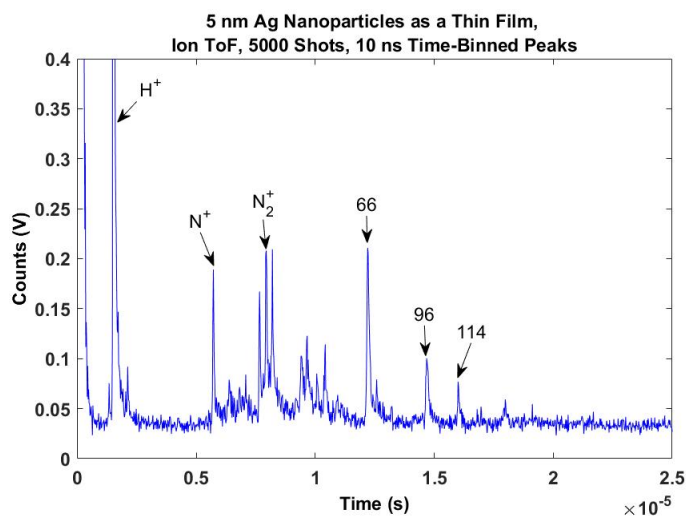


Figure 8.23: ToF m/q spectrum from a single-layer film of 5 nm silver nanoparticles on a glass substrate. No silver ions are identified. Ion species, when known, or calculated m/q is labeled for major peaks.

We employed evaporative deposition to create a 10 nm thick layer of silver on a glass slide. At this thickness, isolated nano-scale pools of silver are common. No silver ions could be identified from this target in our standard time-of-flight configuration either. Similarly, when we mounted a Wollaston wire, with a 50 μm outer cladding of silver, and an inner 2 μm platinum core,

in the focus of the XUV beam, we saw no silver ions. When we mounted an etched wire (2 μm diameter of platinum only), we saw no sign of platinum.

Lastly, we obtained microparticles of antimony and tellurium, to use as targets with similar electronic properties to xenon. We immersed the particles in isopropanol, decanted the smaller particles twice, and deposited these smallest particles onto a glass slide. The results of ion ToF and electron kinetic energy measurements are shown in Figure 8.24. Neither ions of antimony nor tellurium were detected. The spectra from both the ions and electrons appear to be from isopropanol residues, instead of the intended targets.

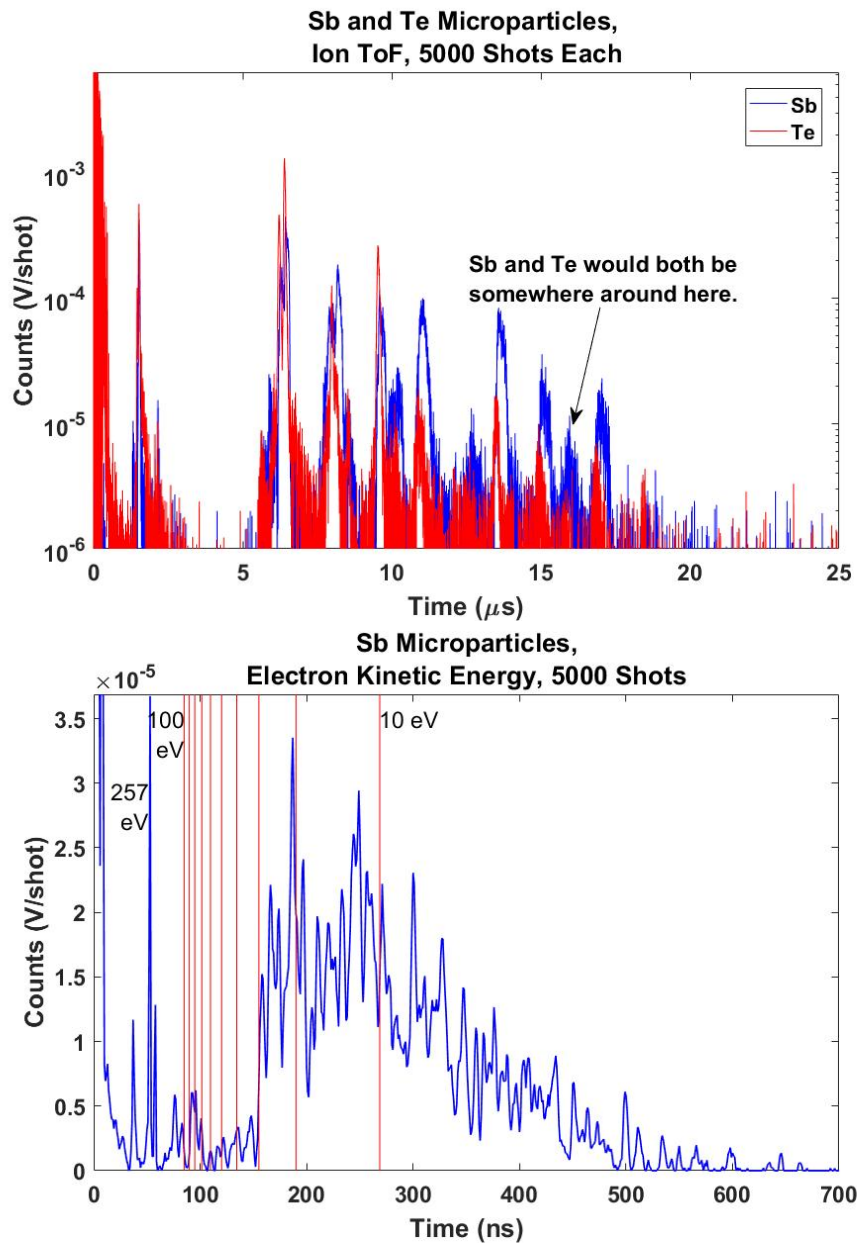


Figure 8.24: Ion ToF m/q spectrum (top), and electron kinetic energy spectrum (bottom) from Sb and Te microparticles deposited onto a glass slide. No ions from these target microparticles are identified. In the bottom plot, the red lines mark energies from 10 eV to 100 eV, in 10 eV steps.

8.2 Noble Gas Clusters

Noble gas clusters provide well-studied nano-scale solid-density targets with low inter-atomic binding energies. For this reason, they became the primary targets used in our experiments. Clusters were formed by adiabatic expansion of gas into vacuum, and their sizes characterized by the gas jet nozzle shape, backing pressure, and temperature, as described in Section 7.5.

To reach a nearly steady-state situation where these equations are relevant, and where condensation ratio is largest, we timed the gas jet to open well before the laser fired, and took data at a timing in the middle of the gas jet's open duration. Figure 8.25 shows a characterization of the relative intensities of signals from the unclustered atomic peaks and forward-going cluster-related peaks, as a function of laser and gas jet timings.

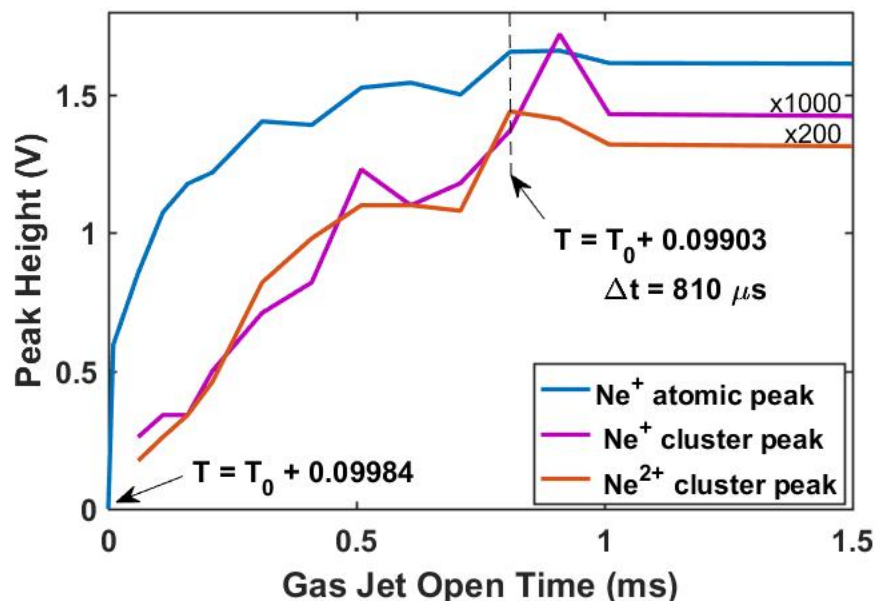


Figure 8.25: Height of atomic and front cluster peaks of Ne clusters as a function of gas jet trigger timing with respect to the XUV laser pulse. The x-axis represents laser pulse delay with respect to the detectable beginning of the gas jet (actual gas jet trigger timings are indicated with arrows). A steady state situation, where both atomic and cluster peak heights level out occurs at $810 \mu\text{s}$ after the front of the gas jet is detected. Data was taken with the 21st harmonic mirror, at a backing pressure of 40 psi ($\langle N \rangle = 200$).

The data detailed in this Section uses as targets clusters of different noble gases, at multiple cluster sizes and incident photon energies. Table 8.1 shows the relevant photoionization cross-sections for atomic gas at the approximate photon energies used in this experiment. Note that while the neon cross-section is relatively flat in this energy regime, argon, krypton, and xenon exhibit a decrease in cross-section by a factor of two to three over this energy span. It is also important to note that there are no known absorption

resonances for any of our noble gases at our photon energies. The cross-sections in Table 8.1 may be used as an initial estimate, but the photoionization cross section may differ from the atomic cross section listed at high densities such as in our cluster targets.

Table 8.1: Photoionization cross sections of noble gases, in Mb [79]

Gas	17 th Harmonic (26.4 eV)	19 th Harmonic (29.5 eV)	21 st Harmonic (32.6 eV)
Neon	8.38	8.92	9.13
Argon	32.7	22.7	13.9
Krypton	24.9	18.2	11.9
Xenon	13.8	8.3	4.8

In the following sections, I will show that the improved resolution in charge-to-mass ratio achieved by our unusually long ToF spectrometer resulted in some interesting new findings for gas cluster targets illuminated with XUV laser pulses. The most prominent of these is that we observe charge states up to Xe^{8+} , Kr^{6+} , Ar^{5+} , and Ne^{3+} , each well above the maximum achievable charge for an isolated ion in a low-density plasma. These maximal charge states are unaffected by cluster size or incident photon energy, although yield ratios for different charges do suggest a change in plasma dynamics at large cluster sizes. The appearance time of the cluster-related peaks which we use to identify high charge states are, strangely, unaffected by cluster size or photon energy, however the kinetic energy suggested by their rising edges, as well as their shape, suggest that these are from a Coulomb explosion of the charged outer cluster shells. These peaks also show identifiable contributions from

different isotopes of the target atom, which, to our knowledge, has not been observed previously.

Kinetic energies of electrons and ions ejected from expanding plasma were also measured via field-free drift time measurements. For electrons, an unusual, energy-dependent “filtering mechanism” was observed, which seemed to decrease contributions from electrons with kinetic energies below about 10 eV and to shift them to lower kinetic energies, while leaving higher-energy electrons unaffected or even amplified. For ions, we see cluster size-dependent spectra, centered in the hundreds of meV at low cluster sizes, and broadening to a saturation cutoff energy of around $h\nu - I_p$ for each species investigated, with the exception of neon. For neon, ions appeared peaked strongly about $h\nu - I_p$, independent of cluster size. This may be because of the unusually high band gap in liquid or solid density neon, which is actually above the ionization potential of neon. This may prevent electron-ion recombination in the cluster, and cause a different spatial distribution of Coulombically trapped inner-ionized electrons within the charged cluster.

8.2.1 High Charge-to-Mass Ratio Resolution

As described previously, one of the main upgrades made to the experimental setup used to collect the data in this dissertation was improved charge-to-mass resolution of our Wiley-McLaren time-of-flight spectrometer (ToF). This was achieved primarily by increasing the length of the drift region of the ToF to approximately 50 cm, and experimentally adjusting the voltages

of the plates defining the extraction region and the acceleration region until the best resolution was achieved, as described in [99].

Figure 8.26 provides an example of the resolution achieved by these improvements. The data was taken with large clusters ($\langle N \rangle = 200,000$) of xenon, which typically decreases the achievable resolution. Here, we zoom in on the isotope peaks of Xe^{2+} , resulting primarily from uncondensed atomic Xe gas. Even with $q = 2$, we still easily resolve all common isotopes of xenon, in their equilibrium concentration ratios, demonstrating a m/q resolution of $< 1 \text{ amu/e}^-$ in the region of 64 amu/e^- .

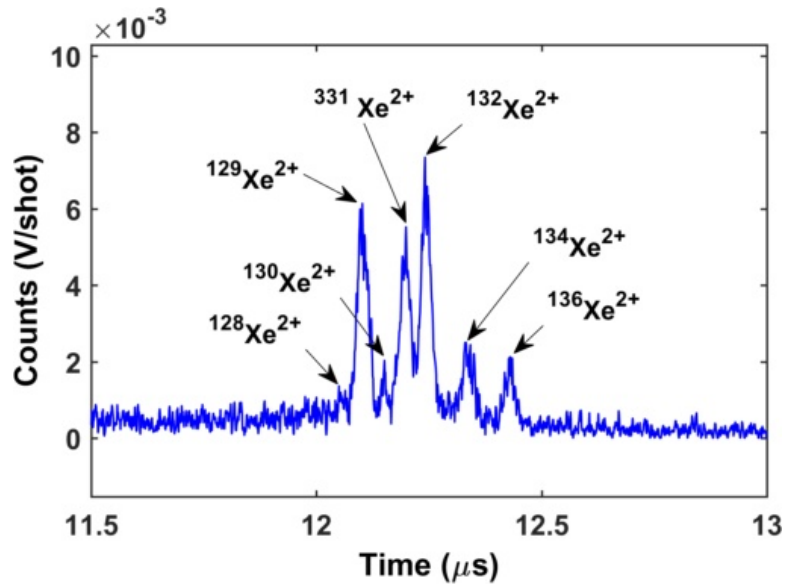


Figure 8.26: ToF m/q spectrum of Xe, cropped to show the Xe^{2+} uncondensed atomic peak, taken with the 21st harmonic mirror. All stable isotopes are labeled. The average cluster size for this data set was 200,000 atoms.

It is also useful to look at the resolution available at the highest m/q

ratios we are interested in, given by Xe^+ . Figure 8.27 shows this region of interest, looking at the uncondensed singly ionized xenon gas from a dataset with low cluster sizes ($\langle N \rangle = 7,000$). (Note the log scale on this particular figure, used to reveal the presence of observable $^{124}\text{Xe}^+$ and $^{126}\text{Xe}^+$ isotopes, with natural abundances of 0.095% and 0.089% respectively.) While we can still easily resolve below 1 amu/ e^- in this range, as shown by the $^{131}\text{Xe}^+$ and $^{132}\text{Xe}^+$ isotopes, we can see that the lineshapes, especially in species of high abundance, may obscure adjacent peaks with significantly lower abundances, as shown by the $^{128}\text{Xe}^+$ peak, as well as the lack of a peak at $^{130}\text{Xe}^+$, as we saw in Figure 8.26.

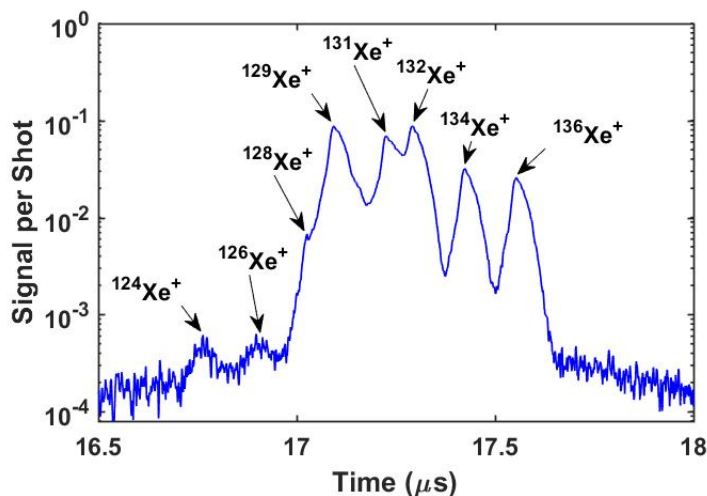


Figure 8.27: ToF m/q spectrum of Xe^+ , cropped to show the Xe^+ uncondensed atomic peak, taken with the 21st harmonic mirror. All stable isotopes are labeled. The average cluster size for this data set was 7,000 atoms. In contrast with Figure 8.26, this data is shown on a log scale, to show that we observe the ^{124}Xe and ^{126}Xe isotopes with natural abundances of 0.095% and 0.089% respectively.

Argon clusters give us another opportunity to confirm the resolution of our detector. Figure 8.28 demonstrates that we can easily resolve all common isotopes of argon as Ar^+ . Unlike xenon, these argon isotopes are each separated by 2 amu. However, the sharp peaks visible in Figure 8.28, each separated by more than their width, allow us to confirm a resolution of $< 1 \text{ amu}/e^-$ in the region of $40 \text{ amu}/e^-$. Additionally, we can easily identify in Figure 8.28 OH^+ and H_2O^+ , as well as H^+ and H_2^+ , thus confirming this resolution over our entire range of interest for these gas cluster experiments.

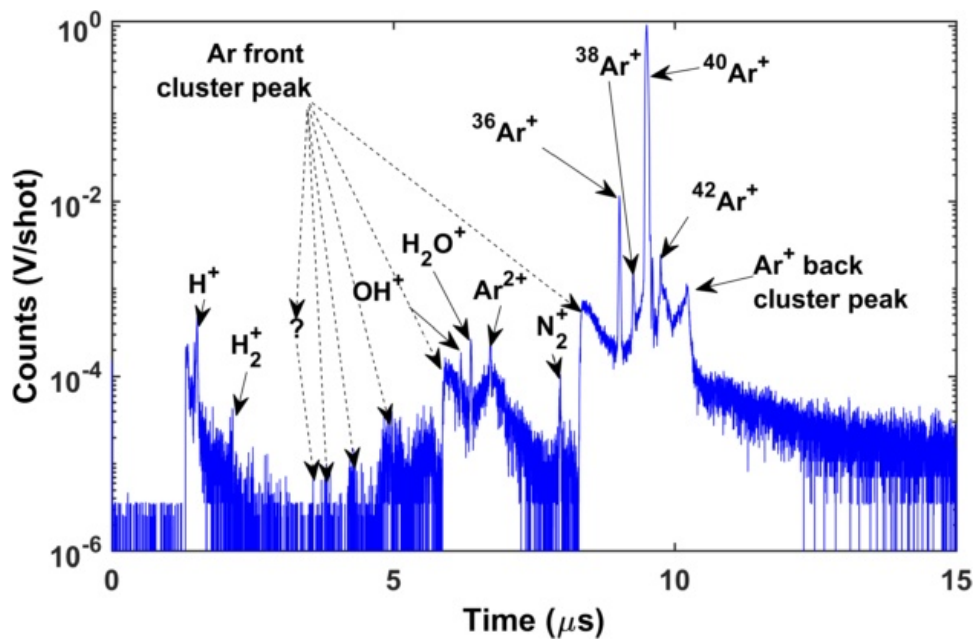


Figure 8.28: ToF m/q spectrum of Ar, taken with the 21st harmonic mirror. All major peaks are labeled. The average cluster size for this data set was 1,000 atoms.

Other features of interest identified in Figure 8.28 are the “forward” or “front” cluster peaks. Present only in data from clusters, these peaks indicate

ions ejected directly toward our detector during cluster dissociation. The front cluster peaks proved to be the best indicators of highly charged ions, as the position of the sharp cutoff at the leading edge of the peak is extremely consistent with cluster size, although the height and shape of the peak may vary. This cutoff position reliably follows the same time-to- m/q scaling as the atomic peaks, with the cutoff for Ar^{2+} falling at time $t_{\text{Ar}^{2+}} = \sqrt{2}t_{\text{Ar}^+}$, and higher charge states following the same pattern. We were fortunate to observe this trend, as we should not expect to observe sharp atomic peaks from the high charge states formed within a cluster.

The “back” cluster peak, resulting from ions ejected from clusters directly away from the detector (and subsequently slowed and accelerated back to the detector by the electric field in the extraction region), is also identified in Figure 8.28 for Ar^+ . Its height, position, and shape varies strongly with cluster size and charge state, making it an unreliable indicator of highly charged ions.

8.2.2 Detection of High Ion Charge States

As described in Section 8.2.1, we rely on the forward cluster peaks of our ion species to identify each charge state detected. This is especially necessary, as the central “atomic” peak is not (and should not be) present in the anomalously high charge states we are interested in observing. Additionally, as seen in Figure 8.29, due to the width of these cluster peaks, peaks from different ionization states of the same species frequently overlap with each other,

making the sharp rise of the front cluster peak the only visible signature of charge states greater than 1+ or 2+.

Figure 8.29 shows the easily identifiable presence of Ne^{3+} in data obtained via the irradiation of small ($\langle N \rangle = 1,000$) clusters with the 21st harmonic of our laser, which should primarily yield photons of 32.6 eV. An isolated Ne^+ ion requires 41.0 eV of energy for the transition to Ne^{2+} , and another 63.4 eV to go from Ne^{2+} to Ne^{3+} , so the presence of Ne^{3+} is anomalous [1].

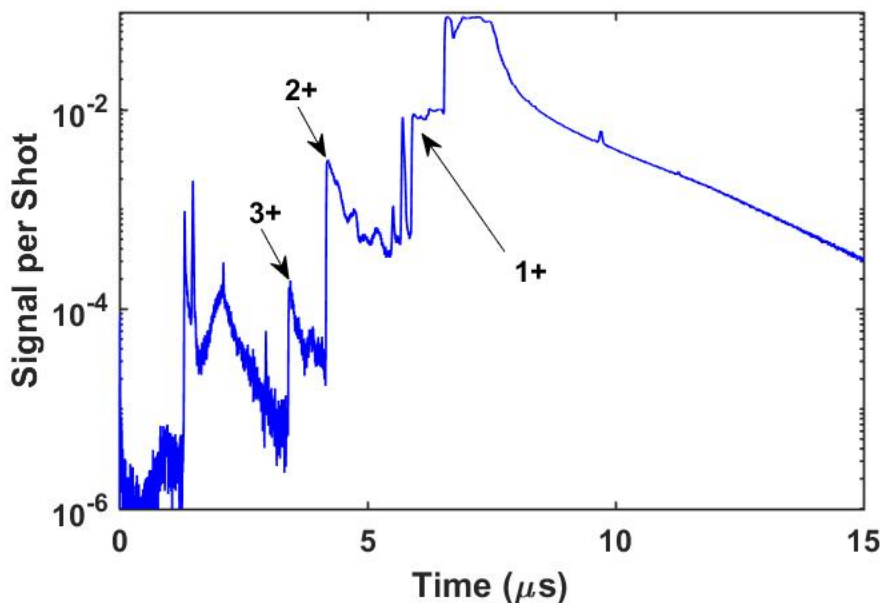


Figure 8.29: ToF m/q spectrum of Ne at $\langle N \rangle = 1,000$, taken with the 17th harmonic mirror. Front cluster peaks of Ne ions are labeled by charge state.

The lack of peak from Ne^{4+} puts a hard upper limit on the amount of potential continuum lowering, or combination of other effects, we can expect to observe to achieve these anomalously high charge states. The transition from

Ne^{3+} to Ne^{4+} requires 97.2 eV of energy, so, while we can achieve charge states at about the same energy as provided by two photons, we cannot observe a charge state which would require three [1]. Alternately, we may observe over 30 eV of continuum lowering, but less than 64 eV.

Continuing down the right hand side (noble gas column) of the periodic table, we performed a similar experiment with Ar. Figure 8.30 shows that we produce charge states up to Ar^{5+} with the 21st harmonic focusing mirror. This may further refine our estimates of potential continuum lowering, and rule out a multi-photon explanation for these charge states, as the transition from Ar^{4+} to Ar^{5+} requires 74.8 eV, well over the energy of two 32.6 eV photons. The transition from Ar^{5+} to Ar^{6+} requires 91.3 eV, which maintains our “unachievable” range at around 90 eV [1].

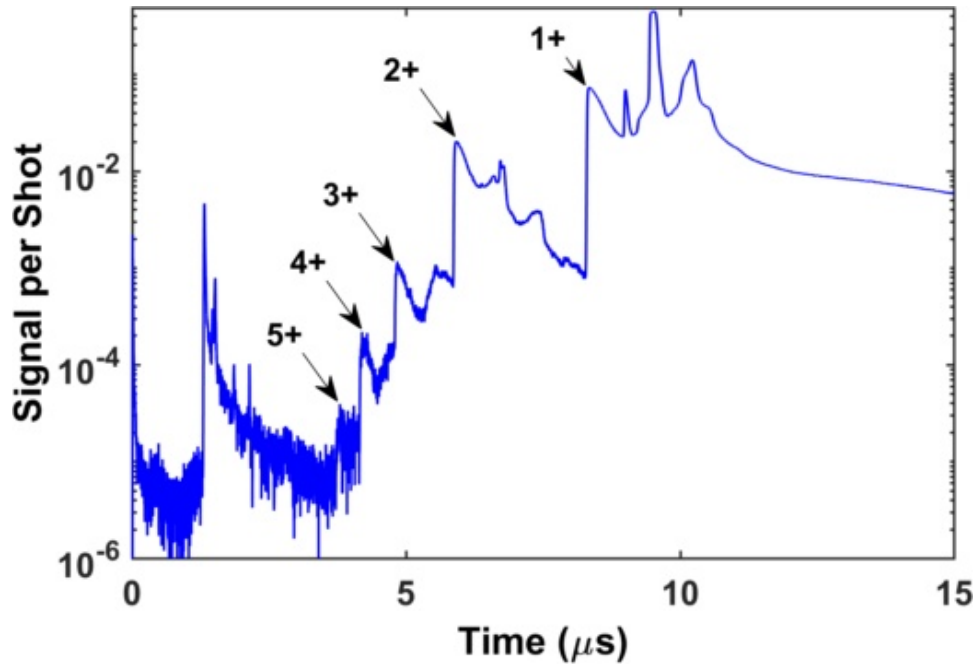


Figure 8.30: ToF m/q spectrum of Ar at $\langle N \rangle = 80,000$, taken with the 21st harmonic mirror. Front cluster peaks of Ar ions are labeled by charge state.

The data from krypton clusters continues this trend. In Figure 8.31, we see evidence of Kr^{6+} , requiring 78.5 eV to achieve from a Kr^{5+} ion, but not Kr^{7+} , which would require an additional 109.1 eV. Thus far, the maximum ionization state achieved in a given cluster has been consistent with a state of continuum lowering of between 78 and 91 eV [1]. It is also consistent with a model of increasing potential lowering with increasing atomic number.

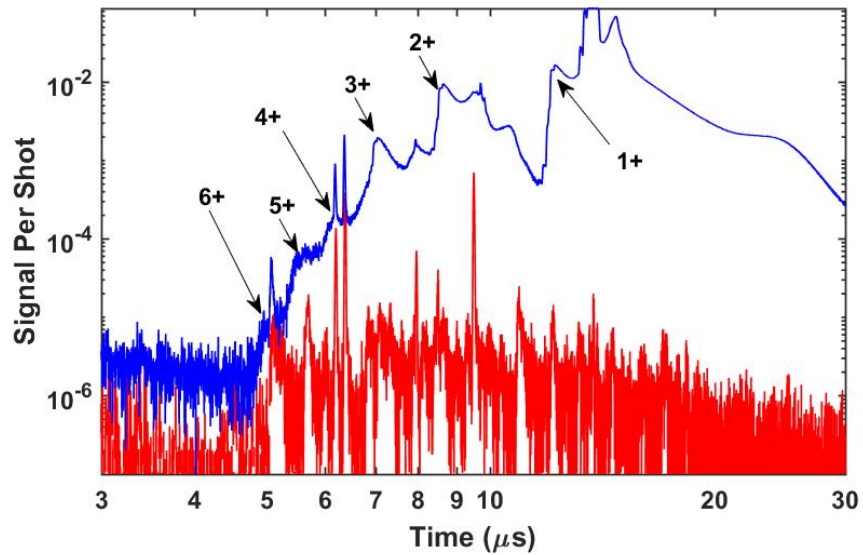


Figure 8.31: ToF m/q spectrum of Kr at $\langle N \rangle = 90,000$ (blue), taken with the 21st harmonic mirror. The gold data set is the chamber background signal.

The data from xenon clusters disturbs the idea that the same amount of continuum lowering applies to each species. In Figure 8.32, we can easily identify the front cluster peak of Xe^{8+} , well above the background levels in the target chamber. The transition from Xe^{7+} to Xe^{8+} requires 106.0 eV of energy. (The next two higher states, which we may arguably see, require 179.8 eV and 202.0 eV, each a much higher jump, due to having to ionize from an inner shell [1].)

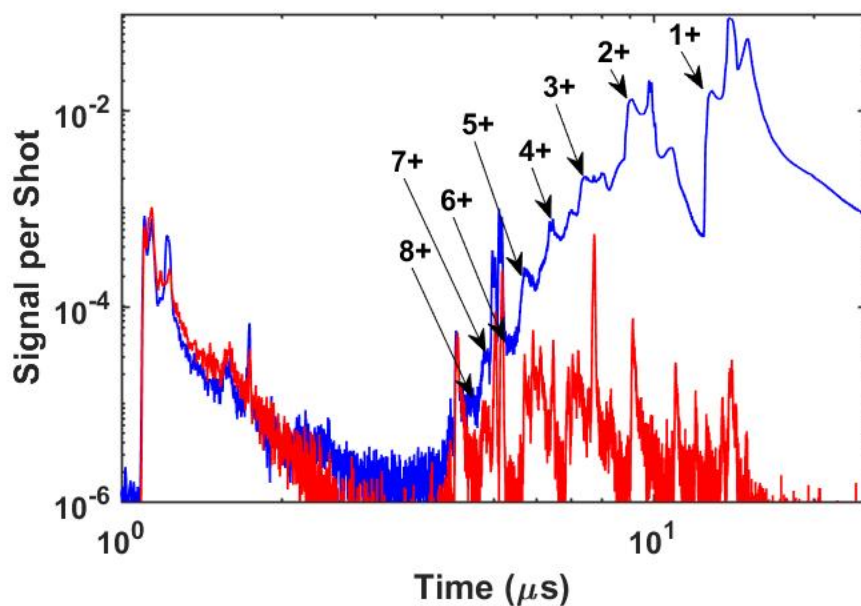


Figure 8.32: ToF m/q spectrum of Xe, taken with the 21st harmonic mirror (blue), and chamber background signal (red). For this data set, we accumulated 40,000 shots of Xe, using the higher plate voltage settings. Front cluster peaks of Xe ions are labeled by charge state.

8.2.3 High Ion Charge States Independent of Cluster Size

While we might expect differently, due to the larger number of “donor” electrons potentially contributing to continuum lowering in large clusters, or simply because intuition suggests that small clusters should play some transitional role between the ionization dynamics of isolated atoms and larger solid-density targets, we find that the high charge states detected in noble gas clusters are largely unaffected by cluster size. Following are some examples with the achievable extremes of cluster size for each atomic species.

Neon, the lightest of the noble gases used in these experiments, is the most resistant to clustering, and most difficult to remove from a high vacuum target chamber. Thus, the achievable range of cluster sizes for this gas was minimal. Nevertheless, as Figure 8.33 shows, we were able to create moderately larger ($\langle N \rangle = 1,000$) clusters by employing cryogenic cooling of the gas jet, as described in Chapter 7. The traces from these two cluster sizes are nearly identical, both in their total and relative ion yields.

Figure 8.33 (a) is zoomed in in the y-axis and plotted on a log scale to best show the Ne^+ , Ne^{2+} , and Ne^{3+} forward-going cluster peaks, which require at least two orders of magnitude in signal-to-noise ratio to resolve. Figure 8.33 (b) presents the same data, but on a linear scale, with no cropping of the sharp, uncondensed atomic Ne^+ peak. Here we see that it is largely the atomic peak and the trailing rear cluster peak of Ne^+ which dominate the signal for these neon ion spectra. No post-processing normalization routines are employed in Figures 8.33 (a) or 8.33 (b), other than averaging the signal over the total number of collected shots. These two plots show remarkable overlap in all atomic and cluster peak landmarks, differing most in the total number of ions from atomic gas detected.

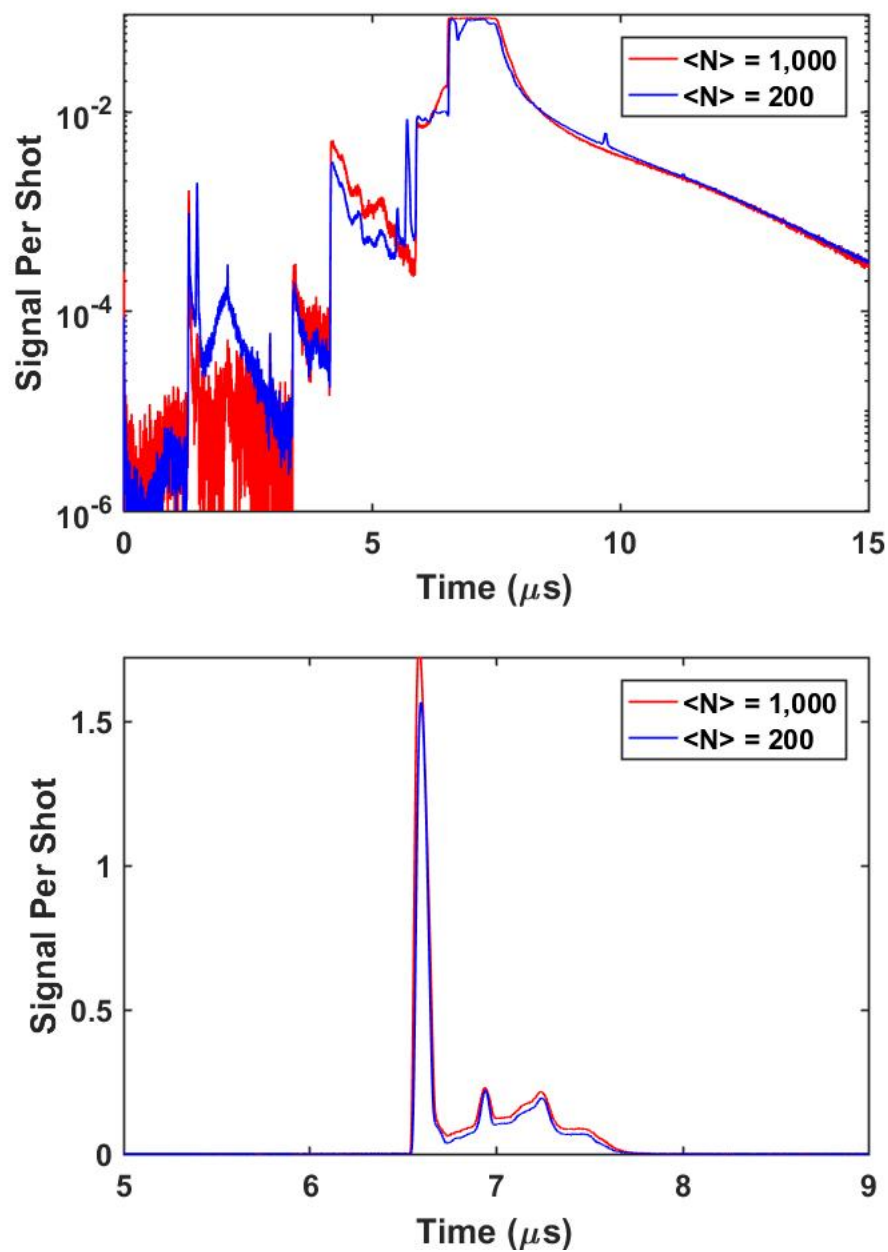


Figure 8.33: ToF m/q spectrum of Ne at two different cluster sizes, $\langle N \rangle = 200$ (red) and $\langle N \rangle = 1,000$ (blue), taken with the 17th harmonic mirror. Data is shown cropped in y, log scale (top), and full-scale linear scale (bottom).

Argon, krypton, and xenon, shown in Figures 8.34 to 8.38, also show similar m/q profiles at different cluster sizes, yielding the same maximal charge state for each cluster size studied. They do not appear as perfectly overlapped as the neon data, in that they may differ slightly in their charge state yield ratios at different cluster sizes, and at larger cluster sizes, the increase in the heights of backward-going cluster peaks to forward-going cluster peaks increases, sometimes overlapping and partially obscuring the easily identifiable sharp front peaks.

A waterfall plot of m/q data from argon clusters of different sizes is shown in Figure 8.34. In each of these plots, Ar^+ to Ar^{5+} is clearly visible, except perhaps where the total signal begins to drop below our noise floor for the smallest clusters. A similar waterfall-style plot for the cluster size span of krypton is shown in Figure 8.35, and for xenon, this data is shown in Figure 8.38. In each of these instances, it is clear that , while the relative peak heights may change, the overall shape of the spectra and existence of high charge states remain. One interesting point to note for the xenon plots, in Figures 8.38 and 8.39, is the presence of xenon Xe_2^+ dimers, arriving here around 25 μs , most visible in the medium-sized clusters, and overshadowed by the long Xe^+ trailing edge in the largest cluster sizes.

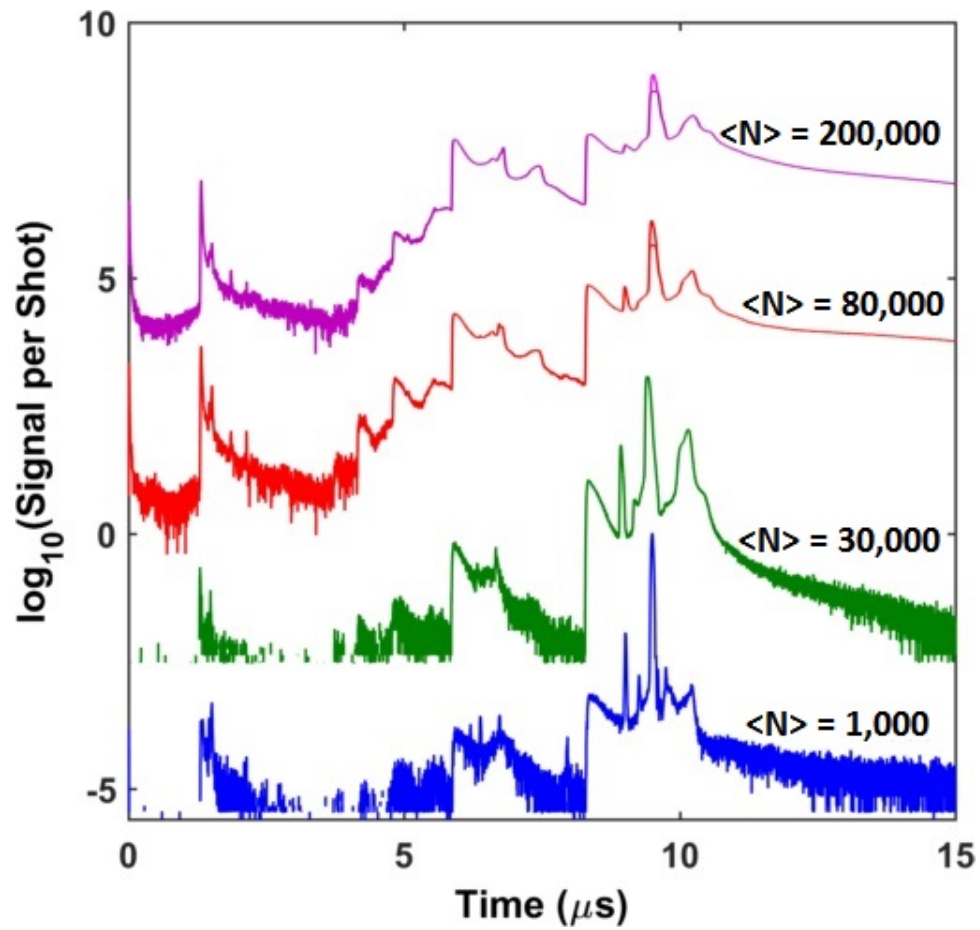


Figure 8.34: ToF m/q spectrum of Ar at different cluster sizes, taken with the 21st harmonic mirror, presented as a log-scale waterfall plot.

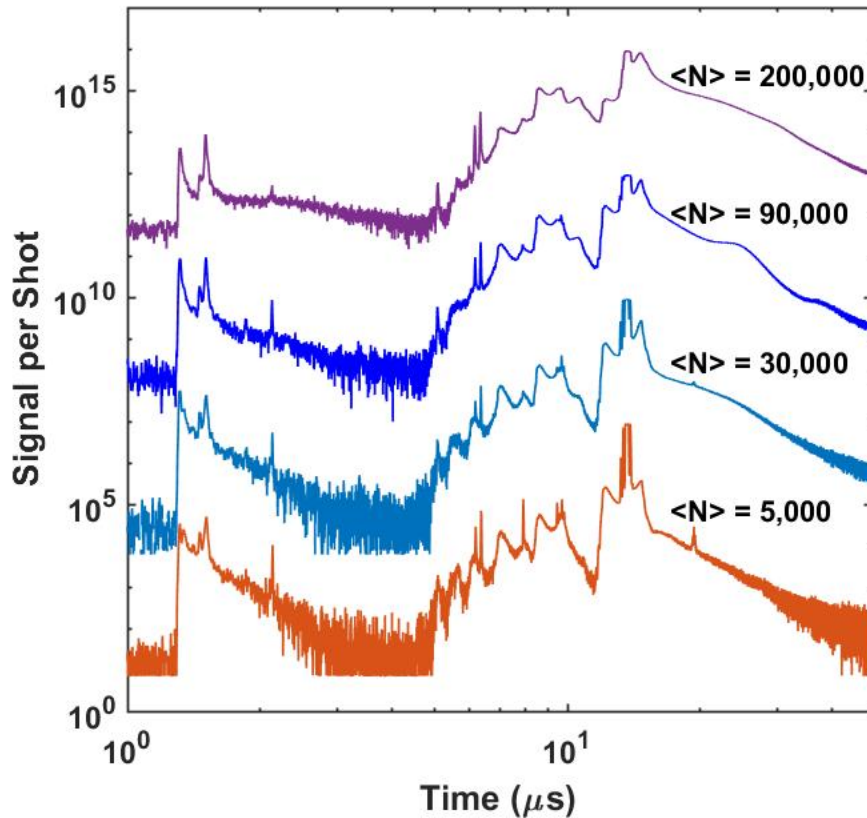


Figure 8.35: ToF m/q spectrum of Kr at different cluster sizes, taken with the 21st harmonic mirror, presented as a log-scale waterfall plot.

An alternative format to the waterfall plots in Figures 8.34, 8.35, and 8.38 are the overlaid plots in Figures 8.36 and 8.38. These figures present the same krypton and xenon data as in Figures 8.35 and 8.38, respectively. The overlay further emphasizes the extraordinary similarities in the spectra from different cluster sizes. In these plots, the precise temporal overlap of the rising edge of the variously charged front cluster peaks is also quite apparent. This

is a surprising feature of each of our m/q ToF spectra obtained with XUV illumination, which will be discussed in greater depth in Section 8.2.5.

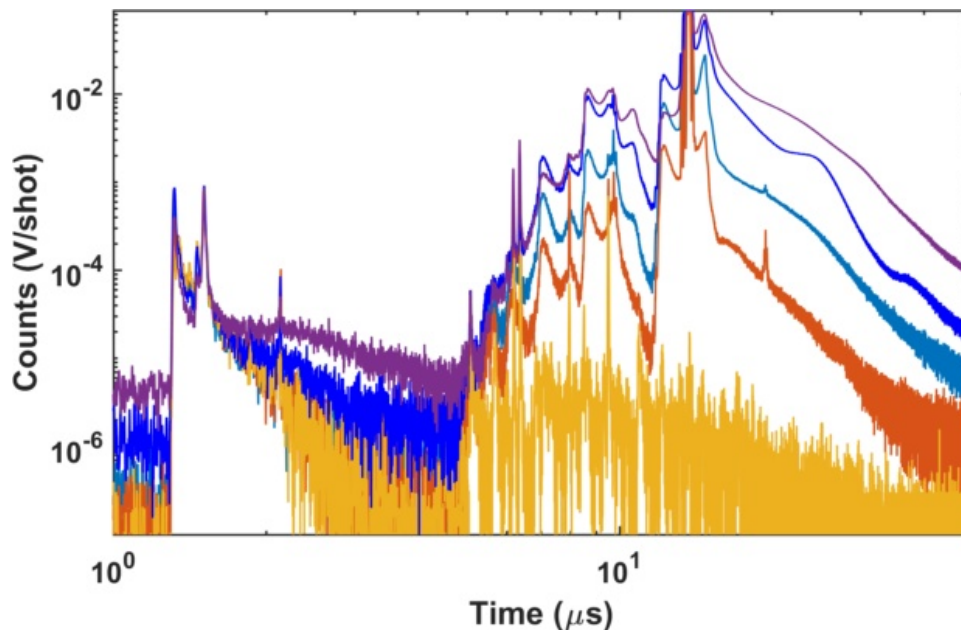


Figure 8.36: ToF m/q spectrum of Kr at different cluster sizes, taken with the 21st harmonic mirror, as shown in Figure 8.35, presented overlaid for direct comparison. Cluster sizes are $\langle N \rangle = 5,000$ (red), 30,000 (teal), 90,000 (blue), and 200,000 (purple). The gold data set is the chamber background signal.

Additional analyses derived from the cluster data already presented in this section are shown in Figures 8.37 and 8.40. In these figures, absolute and relative yields for different charge states of krypton and xenon are presented for different cluster sizes. Absolute yields were determined by the height of the forward-going front cluster peak belonging to a particular isotope of the species (see Section 8.2.5 for more details). These heights were determined to be proportional to the area under the forward-going peaks, so they serve as

an efficient proxy for total ion yield at a particular charge.

Relative yields were determined by dividing the absolute yield at each charge state by the sum of the yields for that cluster size. It is not possible to determine the yields of neutrals within clusters with our detection scheme. The plots of relative yields in Figures 8.37 (b) and 8.40 (b) show an interesting trend. Especially apparent in Figure 8.37 (b), it seems that the relative yields shift towards lower charge states at larger cluster sizes. This may be evidence of electron-ion recombination in large clusters.

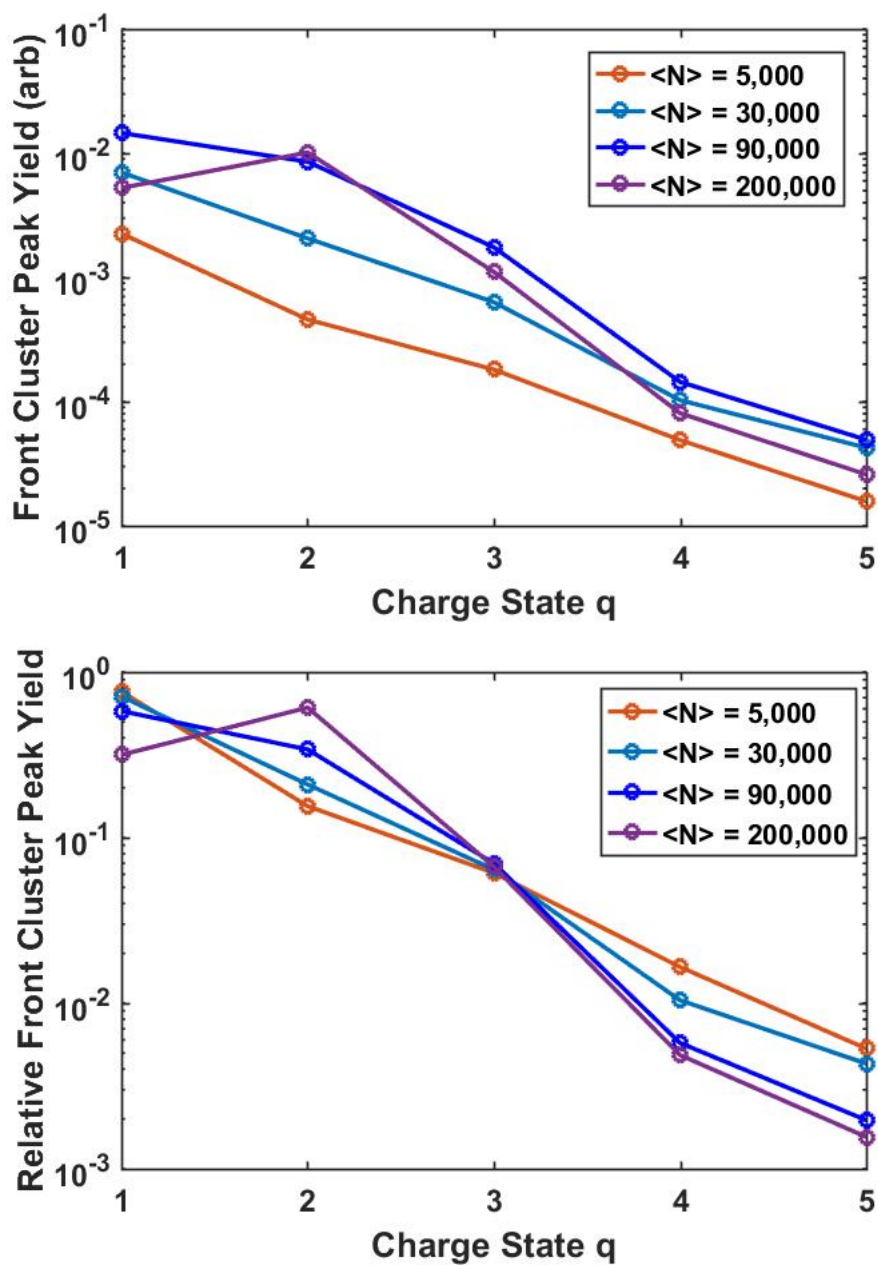


Figure 8.37: Heights of the front cluster Coulomb peaks at different ionic charges from Kr m/q spectra in Figure 8.36, revealing (a) absolute and (b) relative yields ToF m/q spectrum of Kr at different cluster sizes, taken with the 21st harmonic mirror.

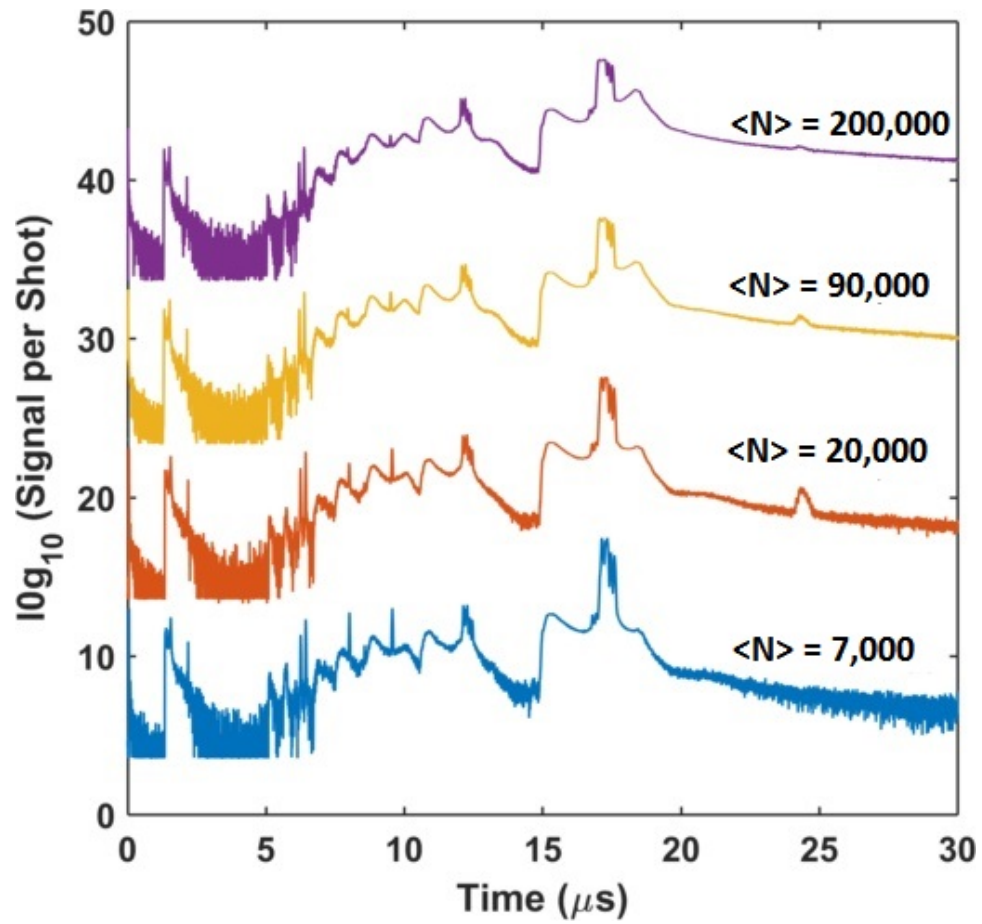


Figure 8.38: ToF m/q spectrum of Xe at different cluster sizes, taken with the 21st harmonic mirror.

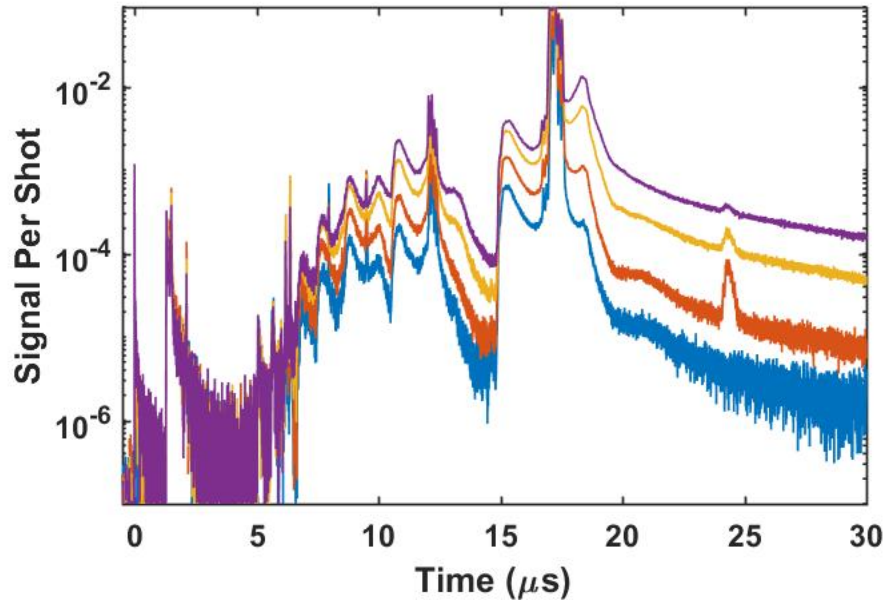


Figure 8.39: ToF m/q spectrum of Xe at different cluster sizes, taken with the 21st harmonic mirror, as shown in Figure 8.38, presented overlaid for direct comparison. Cluster sizes are $\langle N \rangle = 7,000$ (blue), 20,000 (orange), 90,000 (gold), and 200,000 (purple).

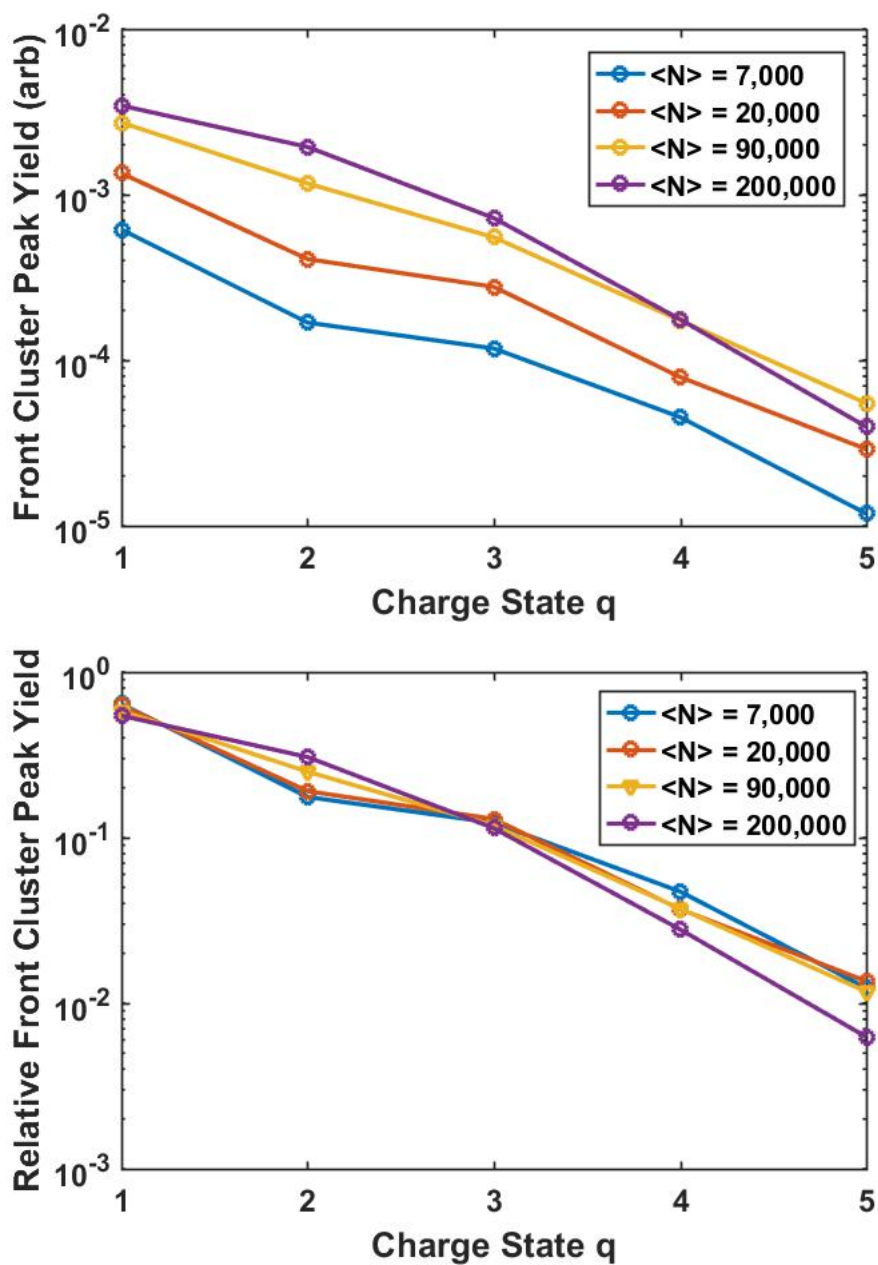


Figure 8.40: Heights of the front cluster Coulomb peaks at different ionic charges from Xe m/q spectra in Figure 8.39, revealing (a) absolute and (b) relative yields ToF m/q spectrum of Xe at different cluster sizes, taken with the 21st harmonic mirror.

8.2.4 Sensitivity of Ion Charge States to Photon Energy

In contrast to the observed relative insensitivity of charge state yield to cluster size discussed in Section 8.2.3, changing the central wavelength of the input laser has a much more dramatic effect. Clusters illuminated primarily by the lower energy, 26 eV 17th harmonic seem to behave in m/q ion ToF investigations similarly to clusters of a much larger size illuminated by the higher energy 33 eV 21st harmonic. This is most readily apparent in Figures 8.41 and 8.43. As shown in Table 8.1, an increase in photoionization cross-section does not account for this effect - in fact, in neon, the photoionization cross-section is actually *lower* for the 17th harmonic than for the 21st. This effect is also seen in nitrogen clusters, as shown in Figure 8.86 in Section 8.3.

It is important to note that although photon energy does change the shape of the m/q profile, as well as the ratios of charge state yields, no change in maximum achievable charge state was observed. This is in contrast to the threshold effect we might expect if continuum lowering were the main driver of these high charge states (if, for example, the ionization potential had been lowered in a particular cluster, resulting in maximum charge state x via photoionization, then a photon providing 6.2 eV less energy might only be able to ionize to charge state $x - 1$).

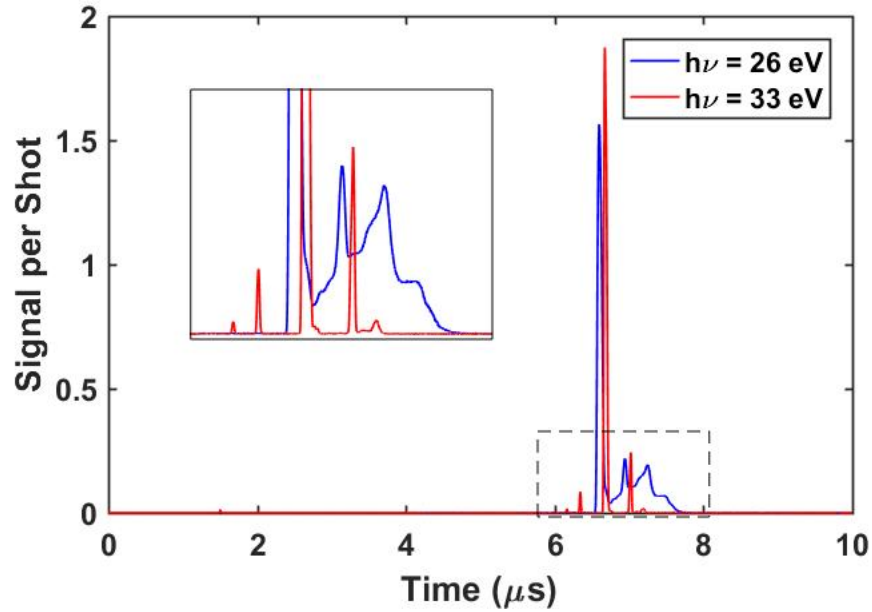


Figure 8.41: ToF m/q spectrum of Ne at $\langle N \rangle = 200$, taken with the 17th (blue) and 21st (red) harmonic mirror at comparable on-target intensities. It seems that the ionization of the clusters increases at the lower photon energy.

Figures 8.41 and 8.43 show the average signal per shot for small neon clusters ($\langle N \rangle = 200$) and medium-large argon clusters ($\langle N \rangle = 30,000$), respectively, each illuminated with the 17th harmonic (26 eV) and 21st harmonic (33 eV) at comparable intensities. The two figures, each shown in an uncropped linear scale, show a strikingly similar pattern. At the higher photon energy, the signals are dominated by unclustered, atomic gas. At the lower photon energy, they appear as if from much larger clusters, with a large backward-going cluster peak.

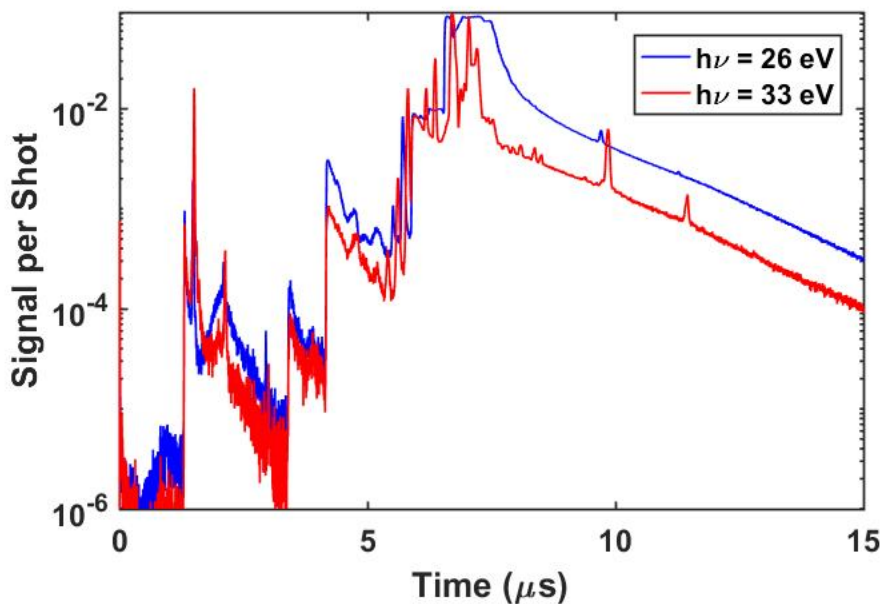


Figure 8.42: ToF m/q spectrum of Ne at $\langle N \rangle = 200$, taken with the 17th (blue) and 21st (red) harmonic mirror at comparable on-target intensities. This plot differs from Figure 8.41 in that it is zoomed in and plotted on a log scale, in order to best display the high charge states. Here, we can see that if we look primarily at the “forward cluster peak,” the signals from the two photon energies are very similar, especially at the higher charge states.

Figures 8.42 and 8.44 present the same data as Figures 8.41 and 8.43, but in a log-scale format cropped in height to show the effects of photon energy on the forward-going cluster peaks which we use to identify high charge states and their relative yields. Figure 8.45 shows an additional plot of argon at small cluster sizes ($\langle N \rangle = 1,000$) in the same format. We can easily see that, for the small neon clusters, while the backward peak may grow dramatically at lower photon energy, all forward peaks (Ne^+ , Ne^{2+} , and Ne^{3+}) overlap nearly perfectly in position as well as absolute and relative yields. Similarly, at the

smaller Ar cluster size, we get more total yield in each forward peak (Ar^+ to Ar^{4+} - Ar^{5+} is difficult to distinguish from noise at this cluster size), but the relative yields remain nearly the same.

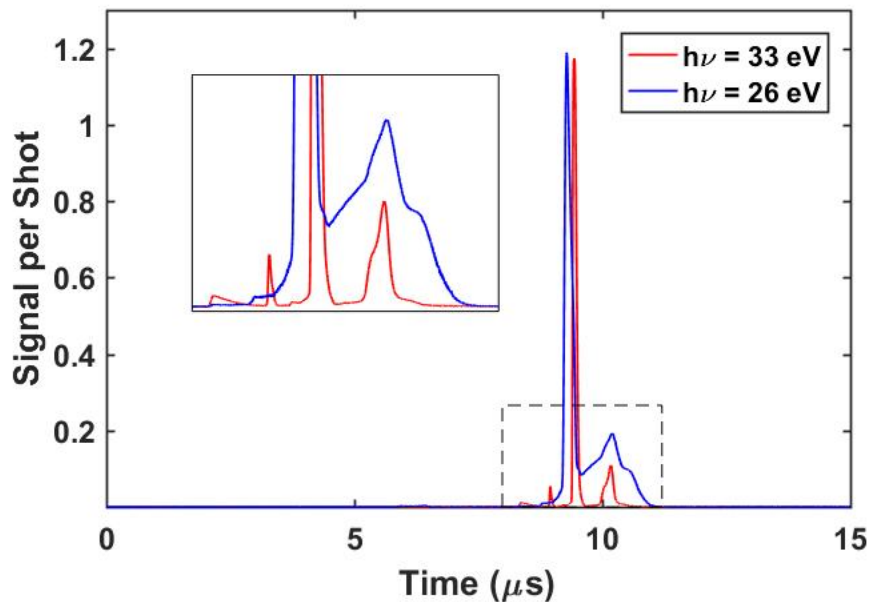


Figure 8.43: ToF m/q spectrum of Ar at $\langle N \rangle = 30,000$, taken with the 17th (blue) and 21st (red) harmonic mirror at comparable on-target intensities. It seems that the ionization of the clusters increases at the lower photon energy. This figure follows the same pattern as Figure 8.41.

In contrast, at the larger Ar cluster size, we see the trend discussed in Section 8.2.3, where larger cluster sizes seem to move towards a more sharply peaked ion yield centered at charge state 2+, suggesting a more highly charged cluster overall, but with elevated rates of recombination. This trend appears amplified at lower photon energies, in that it appears at smaller cluster sizes. Figure 8.48 shows the absolute and relative yields of Ar front cluster peaks

for different cluster sizes when illuminated by the 17th harmonic. Yields are determined from forward peak heights, as described in Section 8.2.3.

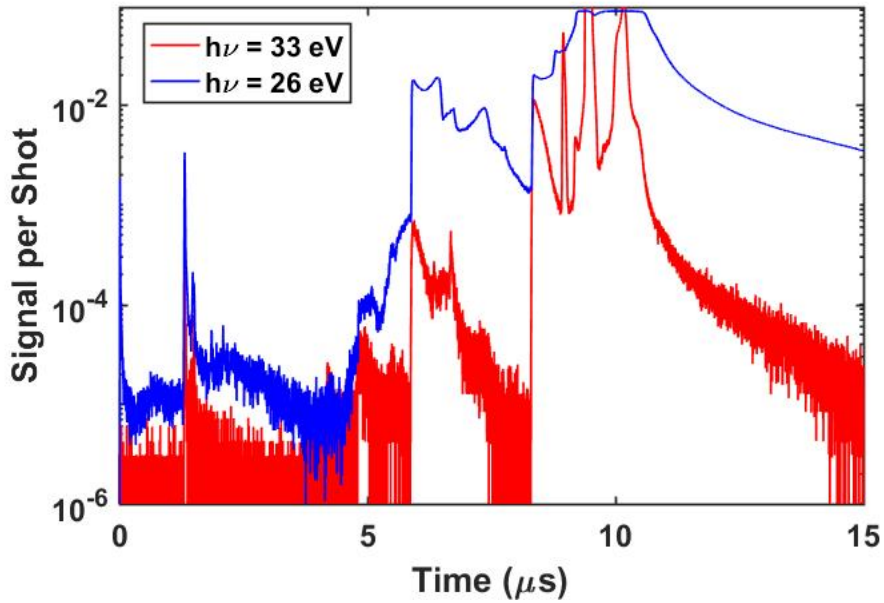


Figure 8.44: ToF m/q spectrum of Ar at $\langle N \rangle = 30,000$, taken with the 17th (blue) and 21st (red) harmonic mirror at comparable on-target intensities. This plot differs from Figure 8.43 in that it is zoomed in and plotted on a log scale, in order to best display the high charge states.

Note that the largest cluster size was left out of the plot of relative yield, as its yields for Ar^{4+} and Ar^+ could not be determined. At the largest cluster sizes, the backwards-going cluster peaks grow and spread out, potentially obscuring the forward-going peaks from later-arriving m/q states. This effect caused the backward-going peak from H^+ contamination to overwhelm the Ar^{4+} peak entirely for the $\langle N \rangle = 200,000$ clusters, and to contribute to a likely overestimation of the Ar^{4+} peak in the $\langle N \rangle = 70,000$ clusters, as well

as the Ar^{3+} peak for the $\langle N \rangle = 200,000$ clusters. Similarly, the forward-going peak for Ar^+ in the $\langle N \rangle = 70,000$ clusters is almost completely obscured by the backward-going Ar^{2+} peak, and is likely overestimated by as much as a factor of 10. These effects are much more of a problem at lower photon energies, where the “effective cluster size” is higher.

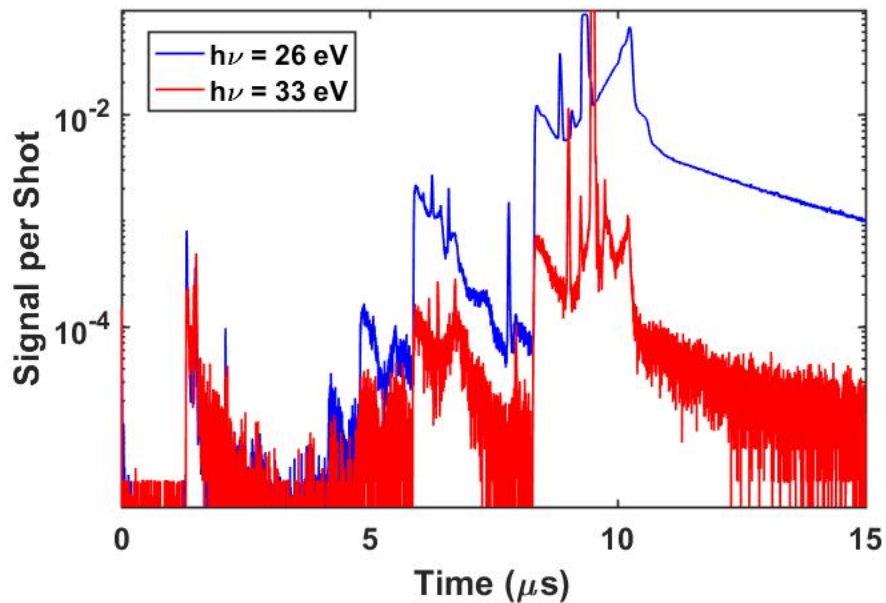


Figure 8.45: ToF m/q spectrum of Ar at $\langle N \rangle = 1,000$, taken with the 17th (blue) and 21st (red) harmonic mirror at comparable on-target intensities. The ratios of the front peaks of Ar^{2+} to Ar^+ are the same, 0.2, for the two photon energies, even though the total yield is much higher for the 26 eV 17th harmonic photons.

Figures 8.46 and 8.47 show the full set of Ar cluster data collected with illumination from the 17th harmonic. The data from the two figures were captured with the same shot conditions. Figure 8.46 shows the full heights and

shapes of the atomic and cluster peaks of the Ar^+ and Ar^{2+} . Here we see the dominance of the backward-going peaks for even moderately-sized clusters at this XUV wavelength. No data is shown below $5 \mu\text{s}$, because all additional peaks in earlier time windows were beneath the dynamic range of our oscilloscope for this set of data.

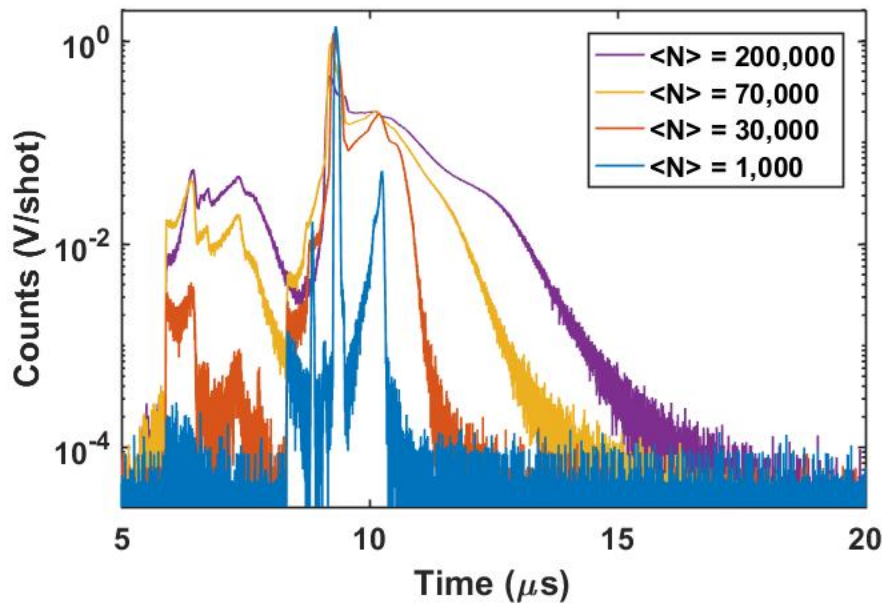


Figure 8.46: ToF m/q spectrum of Ar at $\langle N \rangle = 1,000$ (blue), $30,000$ (orange), $70,000$ (gold), and $200,000$ (purple), taken with the 17th harmonic mirror. Total yield grows much more quickly with illumination from the 17th harmonic than the 21st, rapidly expanding the width of the cluster shoulders, and making high charge states indistinguishable from each other.

Figure 8.47 represents the same data and conditions as Figure 8.46, captured with a different dynamic range, allowing us to see the higher charge states of Ar, as well as the H^+ contamination peak at about $1.5 \mu\text{s}$. Here,

the effect of the backwards cluster peaks in “smearing” the overall shape of the m/q spectrum is very apparent. The forward-going peak heights were extracted from Figures 8.47 and 8.46, and presented in Figure 8.48.

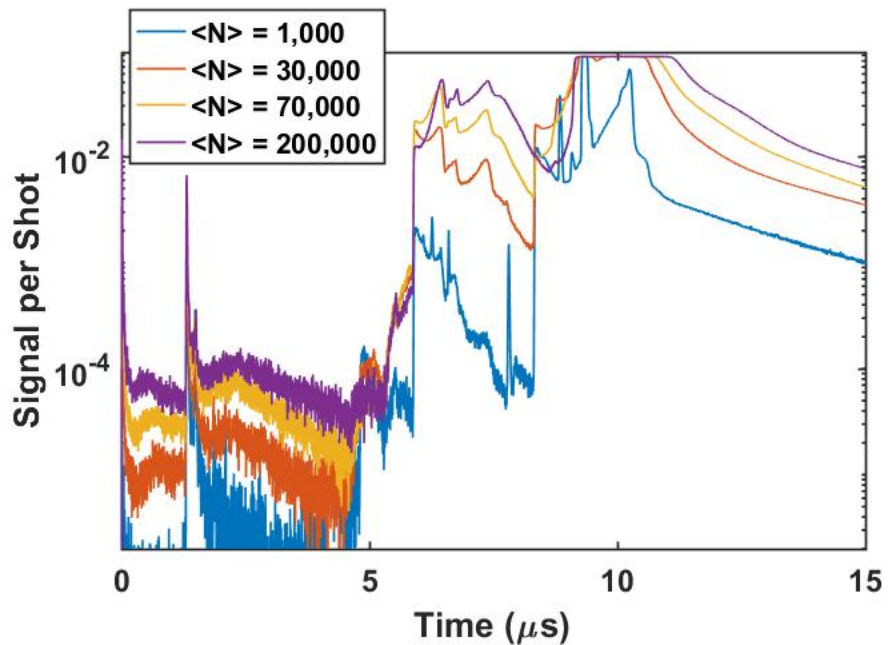


Figure 8.47: ToF m/q spectrum of Ar at $\langle N \rangle = 1,000$ (blue), 30,000 (orange), 70,000 (gold), and 200,000 (purple), taken with the 17th harmonic mirror, zoomed in to show the overlapping shapes of the higher charge states. Total yield grows much more quickly with illumination from the 17th harmonic than the 21st, rapidly expanding the width of the cluster shoulders, and making high charge states indistinguishable from each other.

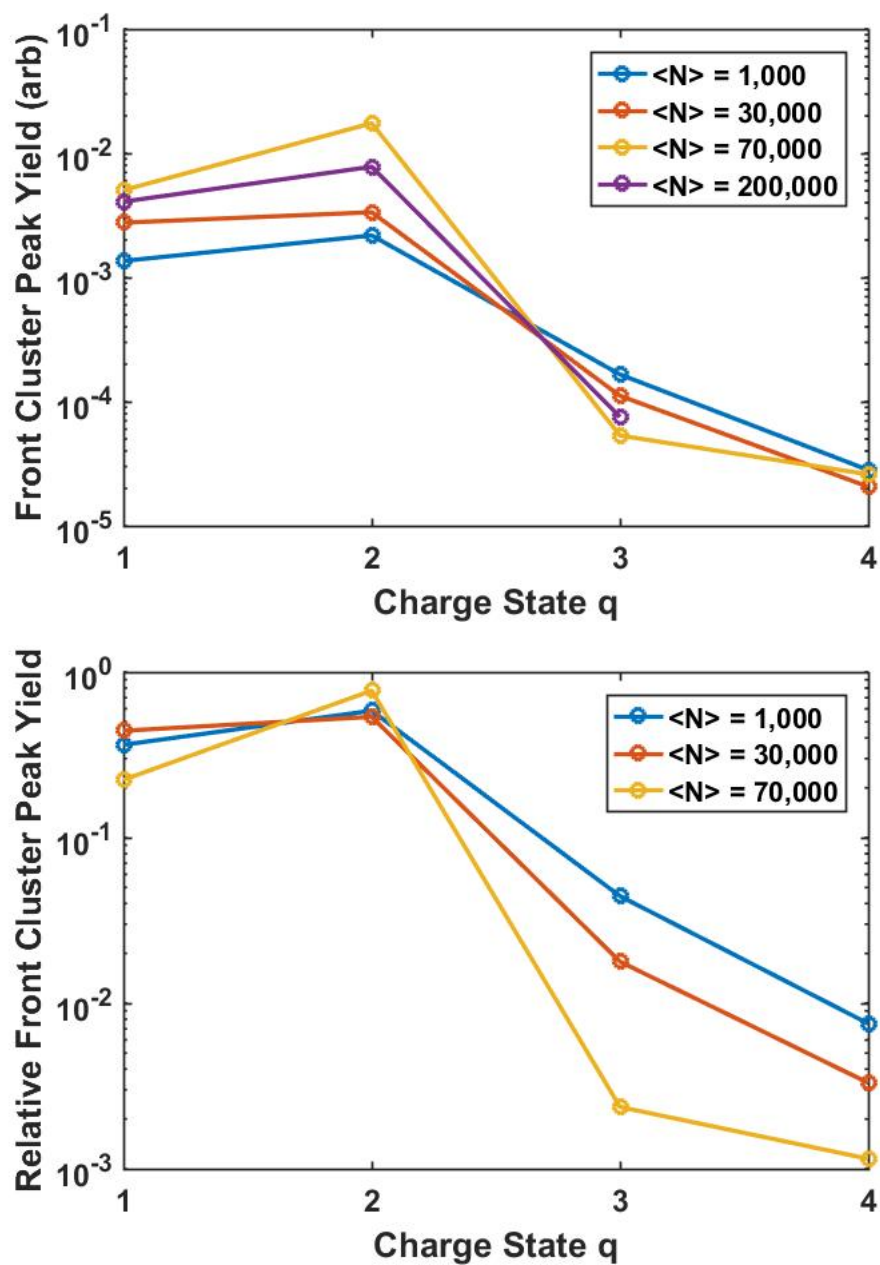


Figure 8.48: Heights of the front cluster Coulomb peaks at different ionic charges from Ar m/q spectra in Figures 8.46 and 8.47, showing (a) absolute and (b) relative yields ToF m/q spectrum of Ar at different cluster sizes, taken with the 17th harmonic mirror.

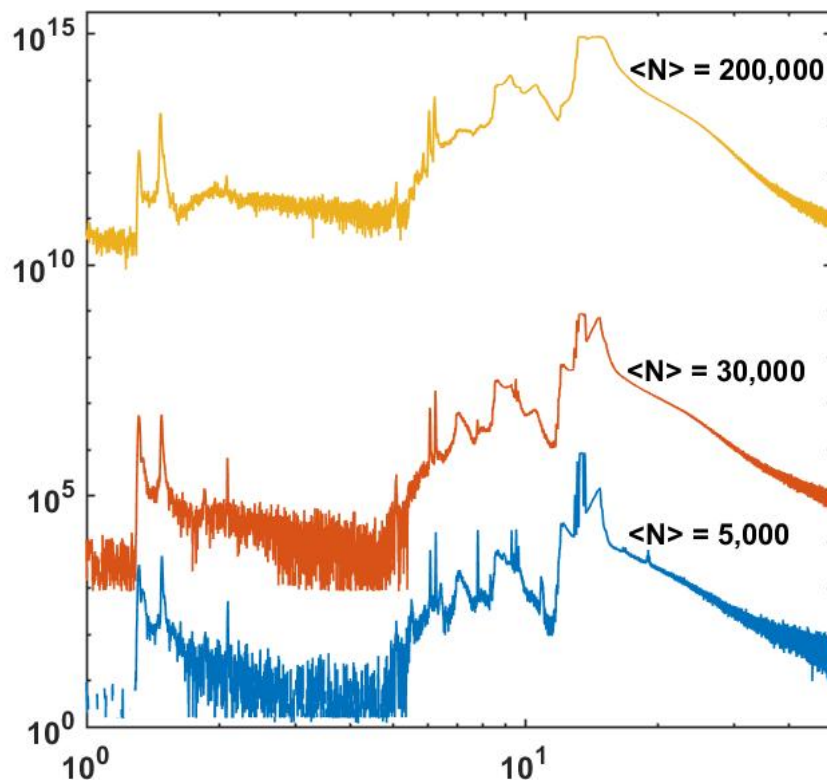


Figure 8.49: ToF m/q spectrum of Kr at different cluster sizes, taken with the 17th harmonic mirror. Compare to Figure 8.35. Note how smeared out the high charge states are, similar to those traces from much larger cluster sizes taken with the 21st harmonic mirror.

Krypton gas shows the same trend of dramatically increasing backward-going cluster peak at larger cluster sizes. Figure 8.49 shows a waterfall-style plot of the m/q spectra of krypton at different cluster sizes, irradiated with the 17th harmonic. When we compare this plot to Figure 8.35, we can see again that the sensitivity to cluster size seems to be magnified at the 17th harmonic

compared to the 21st harmonic.

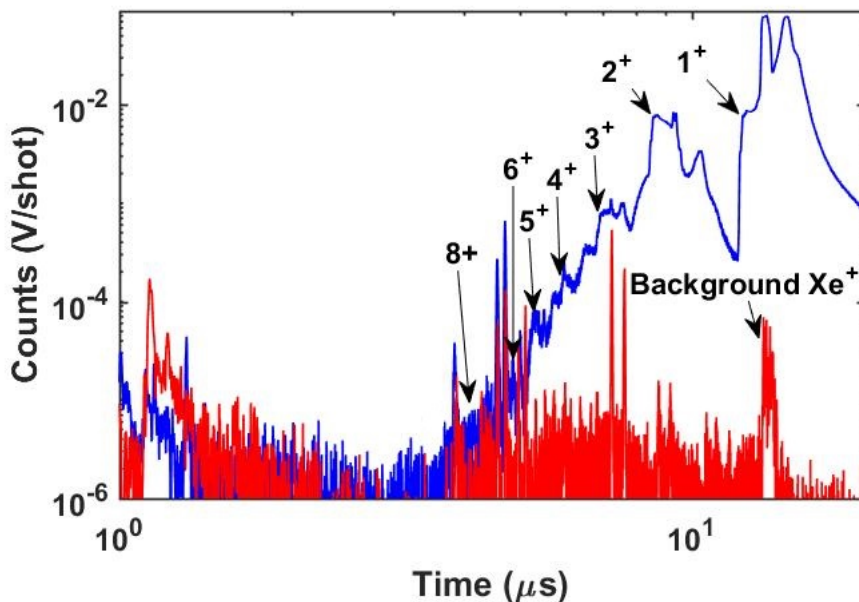


Figure 8.50: ToF m/q spectrum of Xe at $\langle N \rangle = 200,000$ (blue), compared to a background spectrum (red), taken with the 17th harmonic mirror. Front cluster peaks of Xe are labeled. These spectra are taken at the alternate, higher ToF grid voltages, as in Figure 8.32, which was taken with the 21st harmonic mirror. We can see that the same high charge states are present when the clusters are illuminated with the lower energy photons.

In xenon, this effect of a rapidly-increasing backwards cluster peak seems to be less prominent, but still visible. Figures 8.51 and 8.52 compare the Xe m/q spectrum from the two different incident photon energies at large $\langle N \rangle = 200,000$) and medium ($\langle N \rangle = 90,000$) cluster sizes, respectively. While minimal changes in the backwards cluster peaks and total yield are visible, the overall spectral shape and relative charge state yields are remarkably

similar. Figure 8.50 shows confirmation that we still observe the maximal Xe^{8+} charge state with 26 eV photons that we did with 33 eV photons.

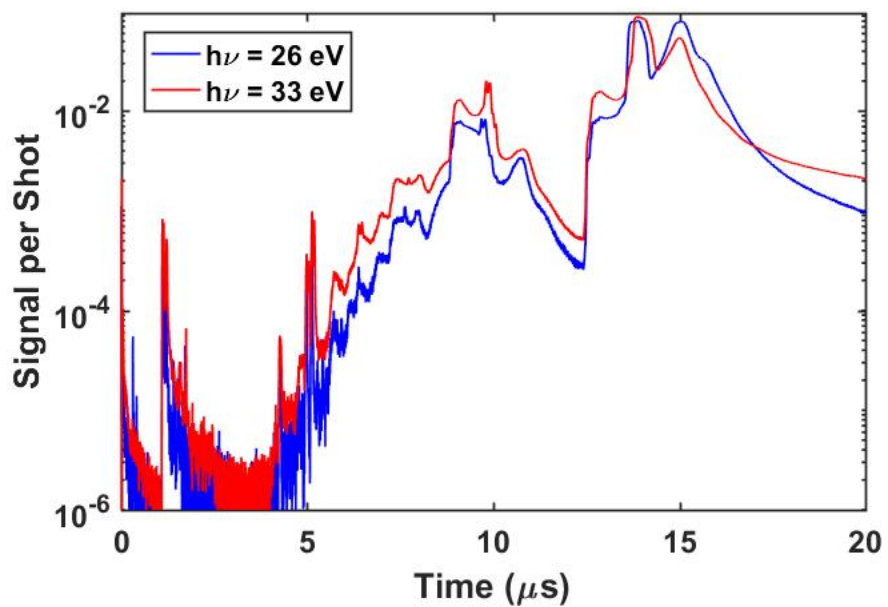


Figure 8.51: ToF m/q spectrum of Xe at $\langle N \rangle = 200,000$, taken with the 17th (blue) and 21st (red) harmonic mirror at comparable on-target intensities. The higher charge states have slightly lower proportional yield in the 17th harmonic data, although the two data sets seem to overlap very well in general.

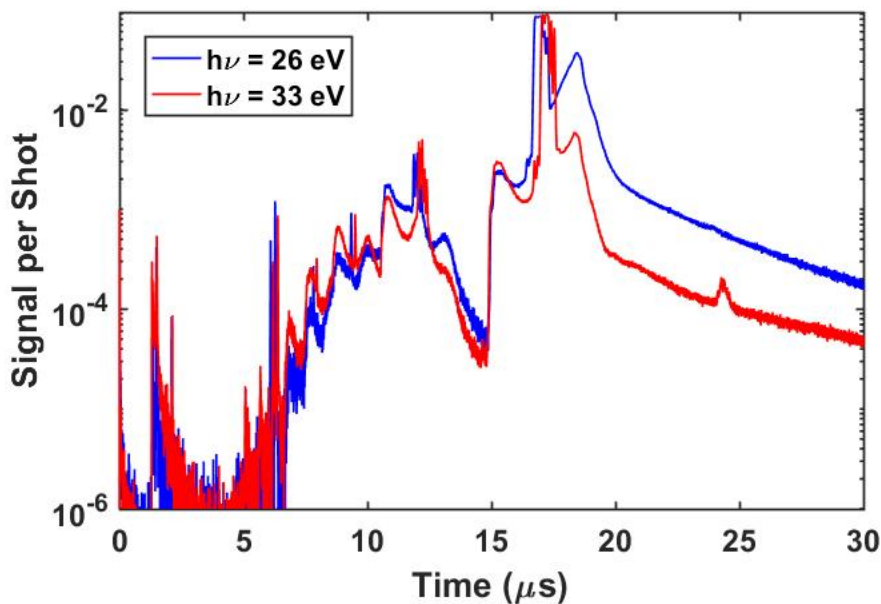


Figure 8.52: ToF m/q spectrum of Xe at $\langle N \rangle = 90,000$, taken with the 17th (blue) and 21st (red) harmonic mirror at comparable on-target intensities. Similarly to Figure 8.51, the higher charge states at this smaller cluster size have slightly lower proportional yield in the 17th harmonic data, although the two data sets seem to overlap very well in general.

Figure 8.53 presents the Xe^+ and Xe^{2+} portion of the m/q spectra for the three cluster sizes obtained with Xe using the 17th harmonic mirror. The relative charge state yields for the data shown in Figure 8.53 are given in Figure 8.54. We can see from these plots that, unlike the yield ratios derived from different species or different incident photon energies, the yields of these Xe charge states, while still maximal at $q = 2$ at large cluster sizes, are not strongly peaked at this charge state, and they fall off only very slowly for higher charges for all cluster sizes.

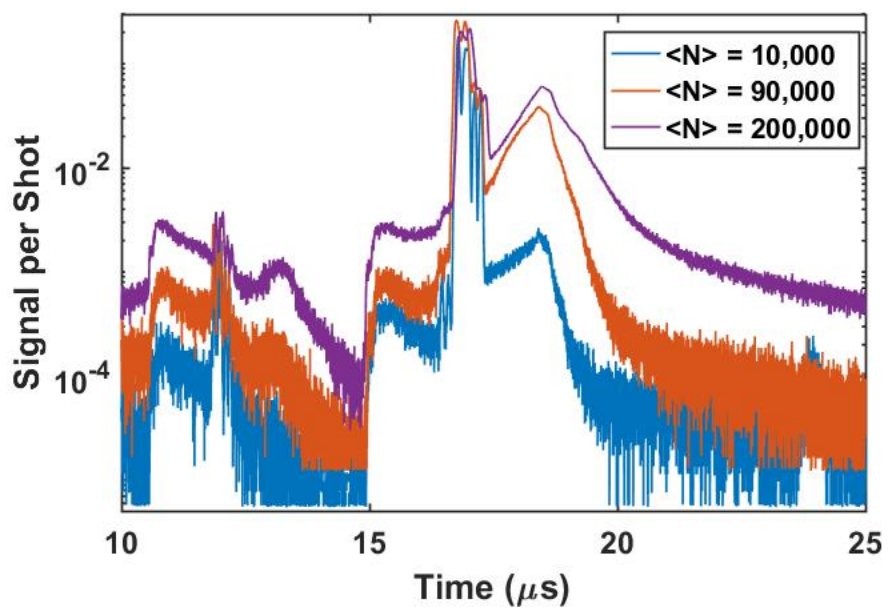


Figure 8.53: ToF m/q spectrum of Xe at $\langle N \rangle = 10,000$ (blue), 90,000 (orange), and 200,000 (purple), taken with the 17th harmonic mirror, cropped to show only the Xe^+ and Xe^{2+} peaks, including the cluster “wings”. This plot shows well how the “back cluster wing” is much more strongly affected by increasing cluster size than the “front cluster wing.”

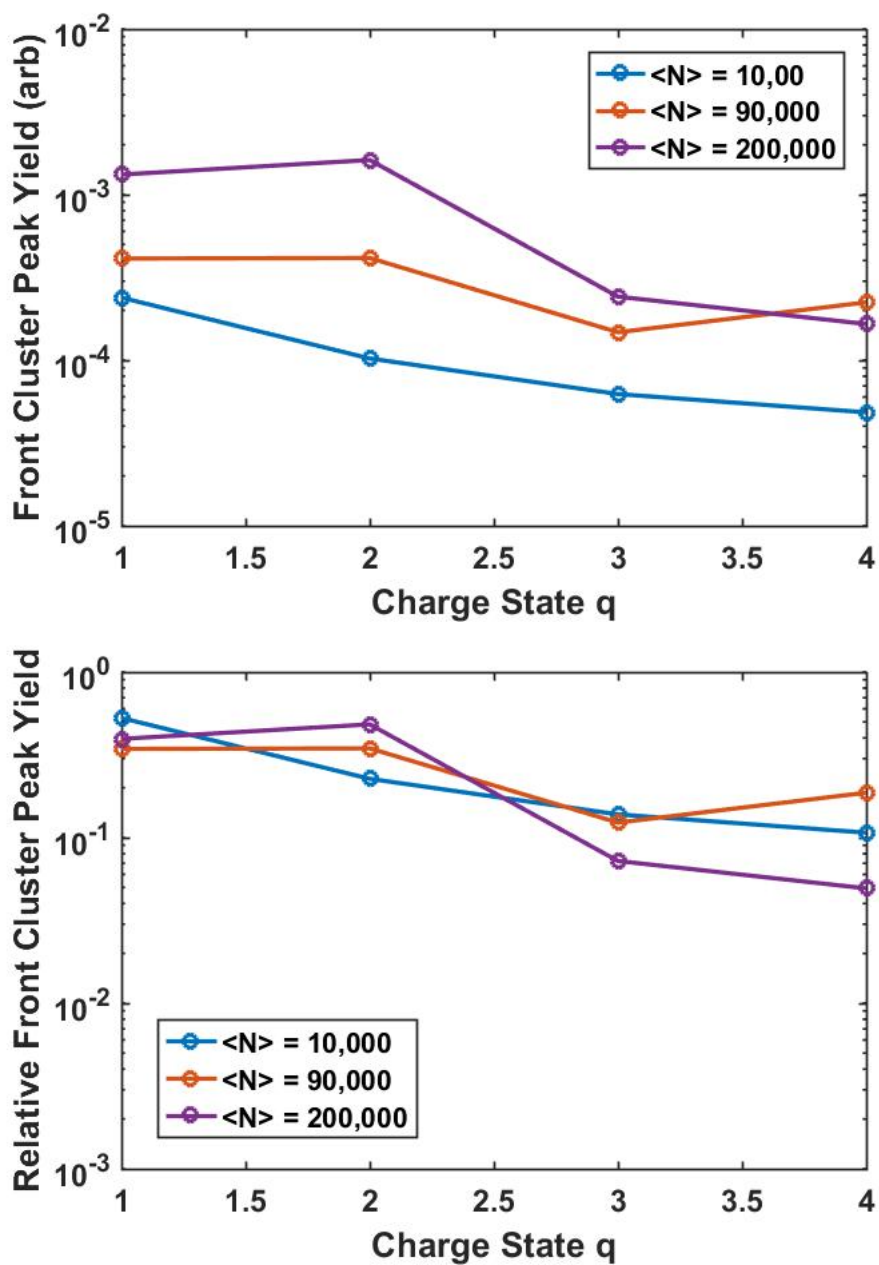


Figure 8.54: Heights of the front cluster Coulomb peaks at different ionic charges from Xe m/q spectra in Figure 8.53, showing (a) absolute and (b) relative yields ToF m/q spectrum of Xe at different cluster sizes, taken with the 17th harmonic mirror.

8.2.5 Cluster Peak Kinetic Energies

As discussed in Sections 8.2.1 through 8.2.4, what we have determined the “forward-going” or “front” cluster peak is the primary indicator of high charge states in our clusters, as the sharp, centered “atomic” peaks are not present at high charge states when the laser photon energy is lower than the sequential ionization potential of an atom at that charge state (typically around $q = +2$). These front cluster peaks have roughly the shape one would expect from a Coulomb explosion, and their behavior as a function of cluster size has been reported by investigators doing experiments similar to ours, with different HHG and ToF detection equipment [52, 68].

In these publications, these forward-going peaks have been referred to as Coulomb explosions of small clusters and of the outer shells of larger clusters. When illuminated with high-intensity infrared (800 nm) light, these front peaks behave as expected, expanding (albeit slowly) as a function of on-target intensity and of cluster size, as the kinetic energy of the explosions increases [46, 68]. However, when illuminated with XUV light, these same experimental circumstances (cluster generation and detectors) show cluster peaks with rigidly fixed rising edge times [46, 68]. As shown in this section, the data presented here follows this trend. While aspects of these front cluster peaks continue to be puzzling, our improved detector resolution may provide some additional information to assist in confidently identifying the physical mechanisms behind their production.

The feature to which I refer is shown most dramatically in Figures

8.55 and 8.56. These figures, presenting the same data set with different emphases, show clear contributions to the forward cluster peaks from different Xe isotopes. Each isotope line appears to have a sharp rising edge and long decay time, so that the contributions from different isotopes “pile up” on one another, creating the appearance of a single peak, if one had lower temporal resolution or slightly noisier data.

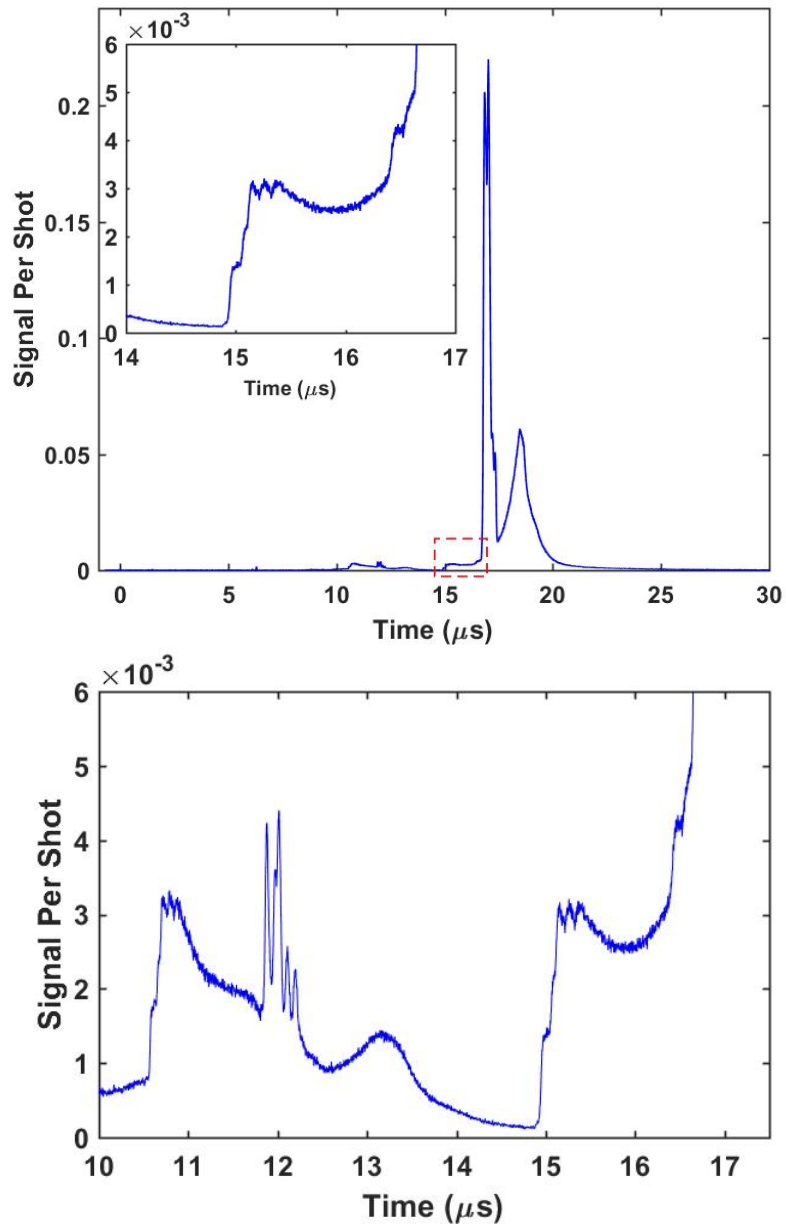


Figure 8.55: ToF m/q spectrum of Xe at $\langle N \rangle = 200,000$, taken with the 17th harmonic mirror. The top plot shows the entire trace on a linear scale, with an inset highlighting the shape of the front cluster peak. The bottom plot expands this highlighted section to show the Xe^+ front cluster peak, as well as the entire Xe^{2+} peak, including front, central atomic, and back peak.

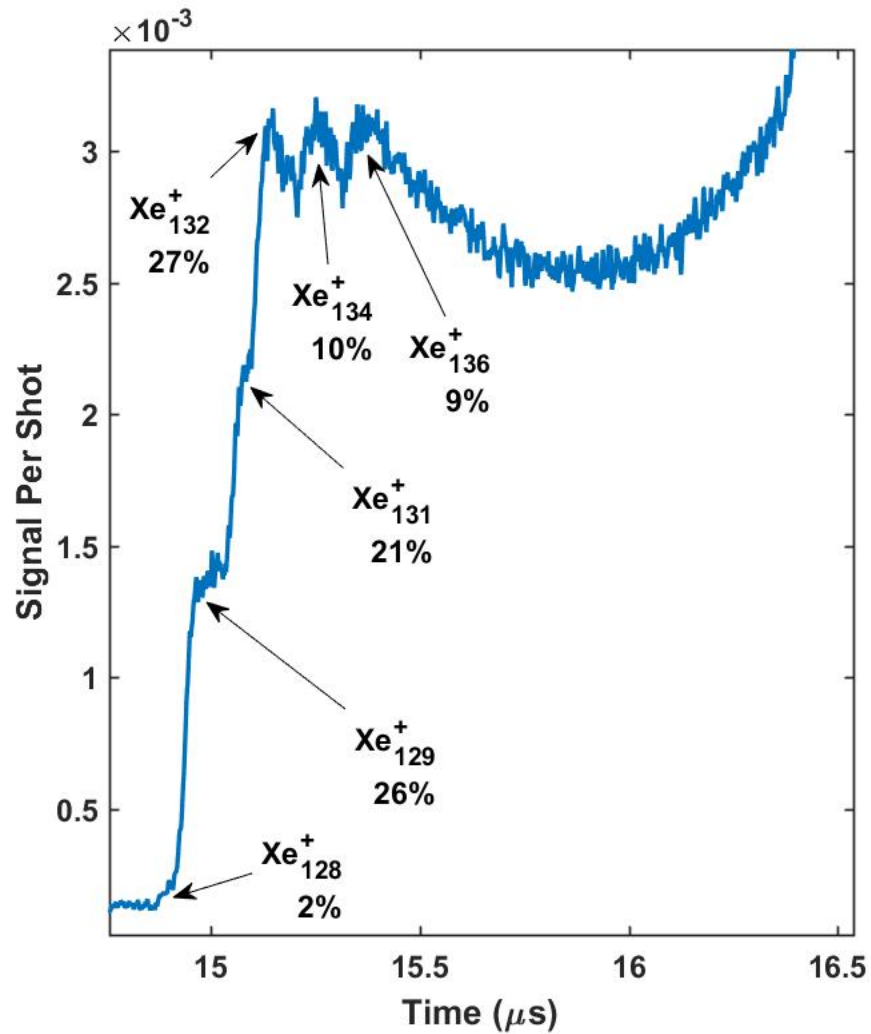


Figure 8.56: ToF m/q spectrum of Xe at $\langle N \rangle = 200,000$, taken with the 17th harmonic mirror, zoomed in to show the isotope peaks present in the Xe^{+} front cluster peak. Data is the same as shown in Figure 8.55. All peaks show an initial kinetic energy of 118.5 ± 1.5 eV.

If we assume that these cluster peaks are evidence of a Coulomb explosion, it makes sense that we should ascertain their initial kinetic energies.

Taking the times of the different isotopes of unclustered Xe^+ and Xe^{2+} found in traces from the lowest-density Xe shots taken with the 17th harmonic mirror, we can obtain a calibration of the dominant uncertainty in our measurements of our detector: the exact position of the laser focus in the extraction region of the ToF spectrometer. We can then use knowledge of the lengths and potentials of each region of the spectrometer to determine the initial kinetic energy of the front cluster peaks.

The energies, determined by this method, of the front cluster peaks of Xe^+ and Xe^{2+} shown in Figure 8.55 are 118.5 eV and 237 eV, respectively. Higher charge states also closely follow this trend ($E_q = q \times E_{1+}$). This would seem to support the conclusion that these peaks represent the maximum kinetic energy obtained from a Coulomb explosion of clusters at the given on-target intensity and cluster size. Each isotope in the forward-going peak represents the same kinetic energy when the mass of the isotope is included in the calculation.

Figure 8.57 presents Xe data similar to Figure 8.55, but ionized by the 21st harmonic rather than the 17th. While the overall shape of the forward-going wing is slightly different, the same isotope peaks are easily identifiable. In fact, as shown in Figure 8.58, they arrive at precisely the same times. The potential complication here is visible when inspecting the peak times of the unclustered Xe between the two data sets. The change in arrival times for the peaks with assumed initial kinetic energy of zero is easily explainable with a shift in the focal spot position caused by the process of physically replacing

one mirror (reflecting, for example, the 21st harmonic) with another (reflecting, for example, the 17th harmonic). However, since the rising edge of the cluster peaks does not show this variability - in fact, it is often completely stable to the resolution of our detector - kinetic energy measurements from this position are suspect. When the position of the laser in the interaction region of the spectrometer is calibrated to the low density data for the 21st harmonic, we obtain “Coulomb wing” kinetic energies of 142 eV for Xe⁺.

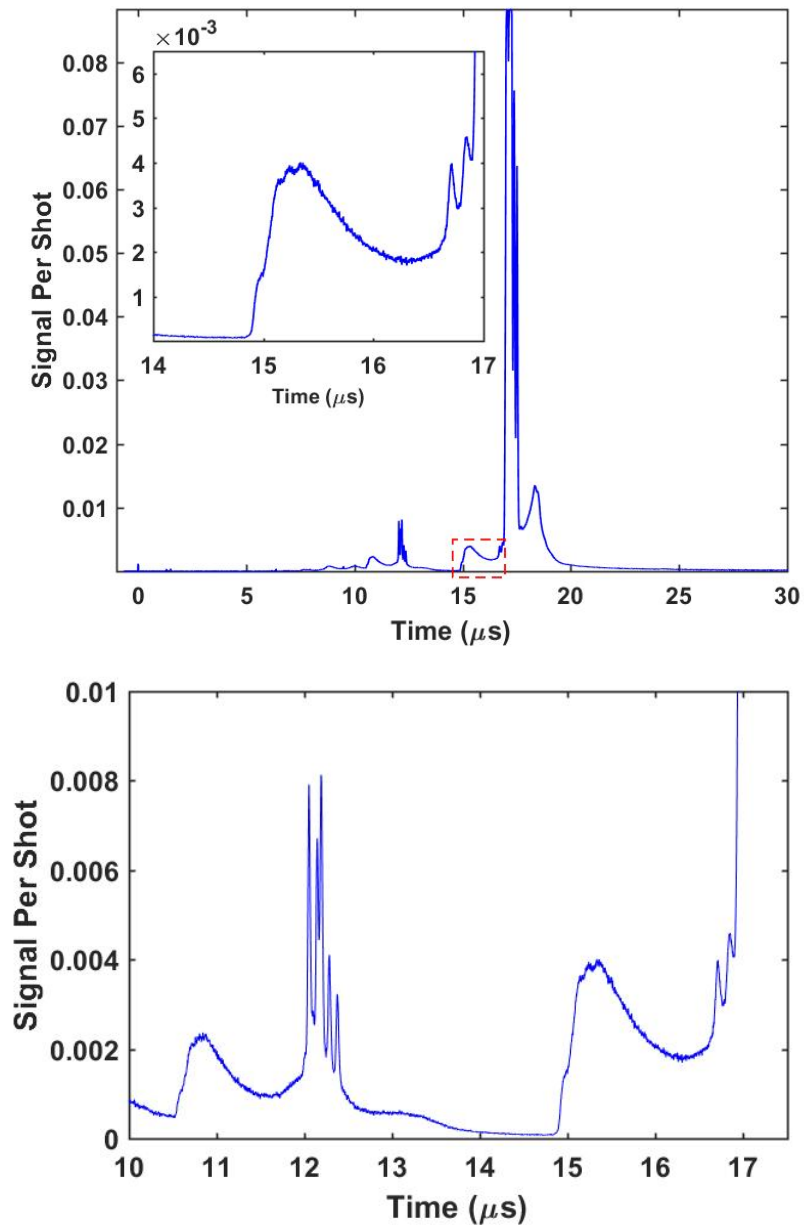


Figure 8.57: ToF m/q spectrum of Xe at $\langle N \rangle = 200,000$, taken with the 21st harmonic mirror. The top plot shows the entire trace on a linear scale, with an inset highlighting the shape of the front cluster peak. The bottom plot expands this highlighted section to show the Xe^+ front cluster peak, as well as the entire Xe^{2+} peak, including front, central atomic, and back peak.

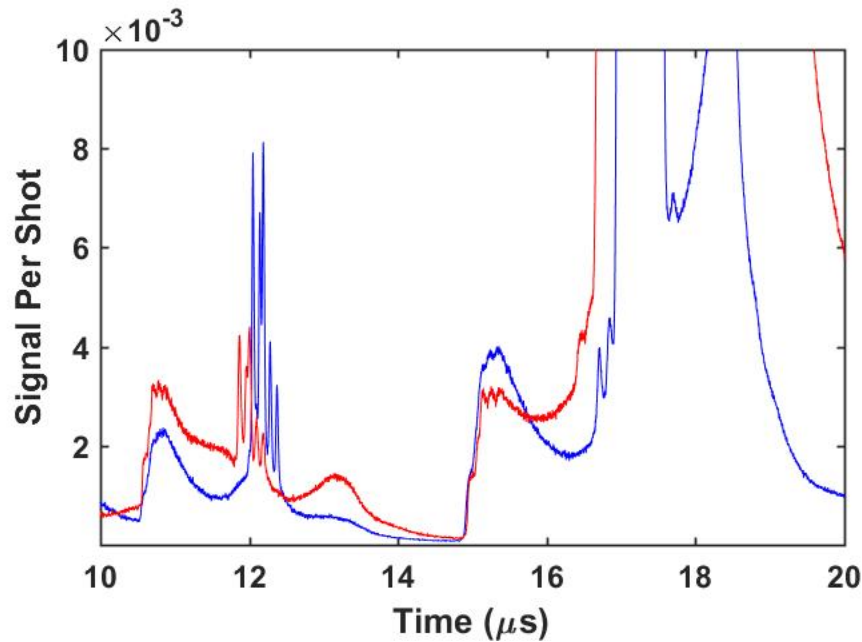


Figure 8.58: ToF m/q spectrum of Xe at $\langle N \rangle = 200,000$, taken with the 17th (red) and 21st (blue) harmonic overlaid. Data are the same as shown in Figures 8.55 and 8.57.

Figure 8.59 shows the Xe atomic and front cluster peaks for different cluster sizes of Xe, taken with the 21st harmonic mirror. This plot identifies a separate interesting feature of these spectra. All kinetic energy measurements listed above were calibrated with low-density gas. The atomic peaks actually seem to grow wider in the forward direction, and hence to shift their center of mass forward, as a function of cluster size/gas density. These peaks shift position, while the forward peaks do not. If we apply the same calibration used to determine the kinetic energy of the forward-going peaks to these central atomic peaks, we obtain 440 meV for the position of the FWHM of the largest ($\langle N \rangle = 200,000$) cluster size in Figure 8.59, and 120 meV for the centroid of

these same peaks.

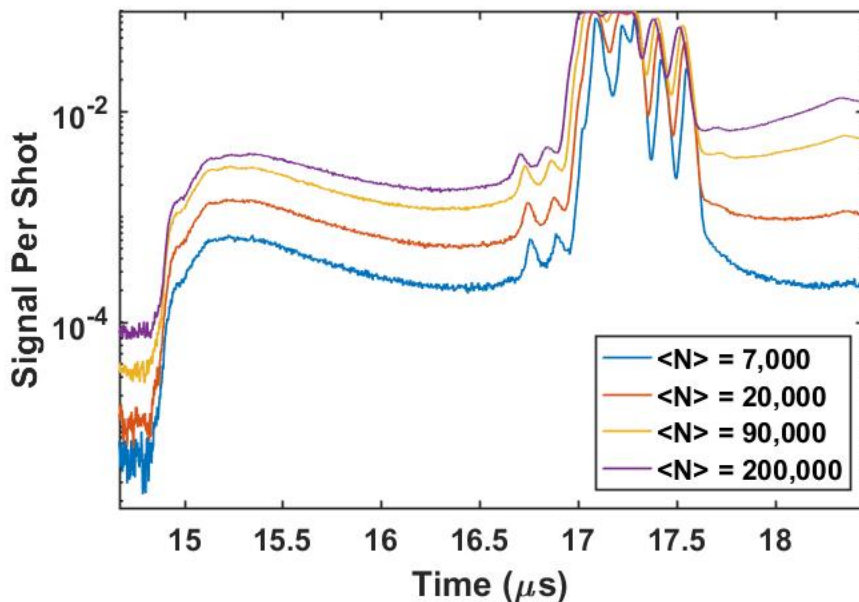


Figure 8.59: ToF m/q spectrum of Xe at multiple cluster sizes, taken with the 21st harmonic mirror, zoomed in to show the Xe⁺ front cluster peak and unclustered atomic peaks. Data is the same as shown in Figure 8.39. While the forward cluster peak occurs at exactly the same time on each trace, the atomic peaks gradually widen and move forward at larger cluster sizes.

Krypton, another gas with multiple prominent isotopes, shows these same features in the forward-going cluster-related peak. Figure 8.60 shows an m/q spectrum of large Kr clusters, illuminated with the 21st harmonic, zoomed in to highlight the front cluster peaks of Kr⁺, Kr²⁺, and Kr³⁺. Identifiable isotopes are labeled in the Kr⁺ peak.

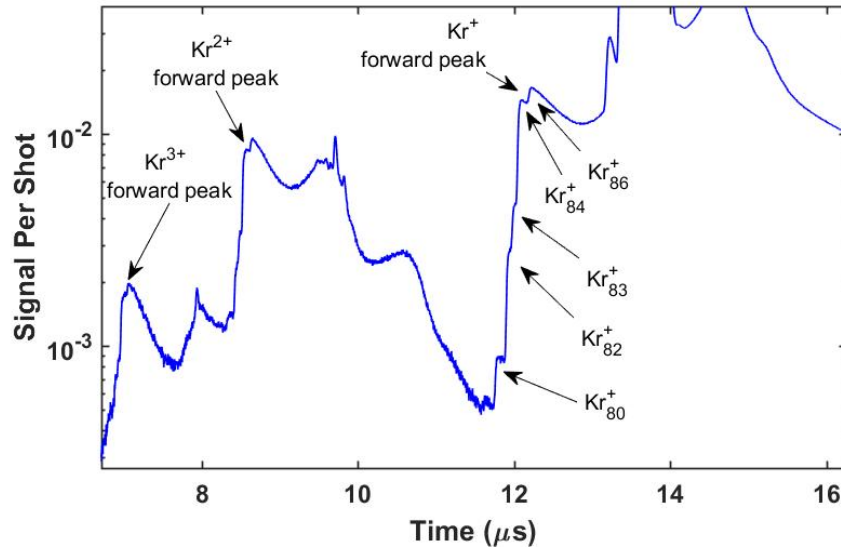


Figure 8.60: ToF m/q spectrum of Kr at $\langle N \rangle = 200,000$, taken with the 21st harmonic mirror, zoomed in to show the isotope peaks present in the Kr^{+} , Kr^{2+} , and Kr^{3+} front cluster peaks.

The Coulomb-suggestive trend of $E_q = q \times E_{1+}$ holds for all noble gas cluster spectra obtained. Using the calibration from the lowest gas density, taken with the 21st harmonic mirror, we obtain a kinetic energy of 108 eV for Ne^{+} , 211 eV for Ne^{2+} , and 310 eV for Ne^{3+} . Similarly, Ar spectra yield 133 eV for Ar^{+} and 264 eV for Ar^{2+} . We hesitate to apply these kinetic energy measurements because of the uncertainty in position of the focal region with respect to the two plates, caused by an apparent effect on the atomic peak position by both photon energy and cluster size. However, the appearance of isotope signatures in the forward-going peaks is a new and interesting addition to the discussion.

8.2.6 Ion Kinetic Energy Profiles

In contrast to the sharply peaked high-energy wings visible in the ion ToF measurements above, the overwhelming majority of the ions collected in a field-free drift measurement of ion kinetic energies are at energies well below 100 eV. The typical observed trend is best shown by argon drift measurements, as in Figure 8.61.

At low cluster sizes, the maximum kinetic energy is very low – about 1 eV. As the cluster size increases, we see a shift of the kinetic energy curve to higher energies, with a maximum around the photoelectron kinetic energy (about 10 eV). As we continue to increase the cluster size, the ion kinetic energy curve broadens at both the high and low energy regimes, and we get a number of electrons in a high energy “tail” above the photoelectron energy, up to around 30 eV. It is important to note that the number of high energy counts maintains a precipitous drop around the 10 eV photoelectron energy.

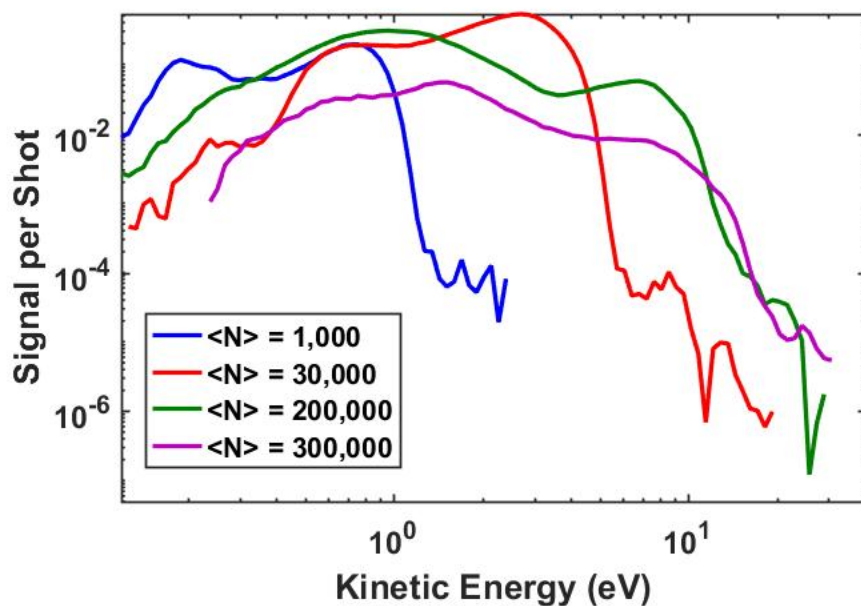


Figure 8.61: Ar ion kinetic energy signatures, obtained with the 17th harmonic laser energy. The constant-in-time background has been subtracted from these plots. Only the low-energy signals which are above the background level are plotted.

We see this trend in more detail in the krypton ion kinetic measurements of Figure 8.62. These data were taken at closely spaced cluster sizes as the gas jet nozzle slowly pumped down, reducing the backing pressure. At the smallest cluster sizes, we have a distribution peaked around 0.3 eV, and as the cluster size grows, the center of the distribution shifts to closer to 0.7 eV, while maintaining a narrow energy distribution. Above a cluster size of about 15,000, the distribution begins to broaden, while continuing to shift the center up to 1.1 eV. At these largest cluster sizes, we can see that there appear to be two overlapped distributions – the original 0.1 eV peak, and the larger peak

around 1.1 eV.

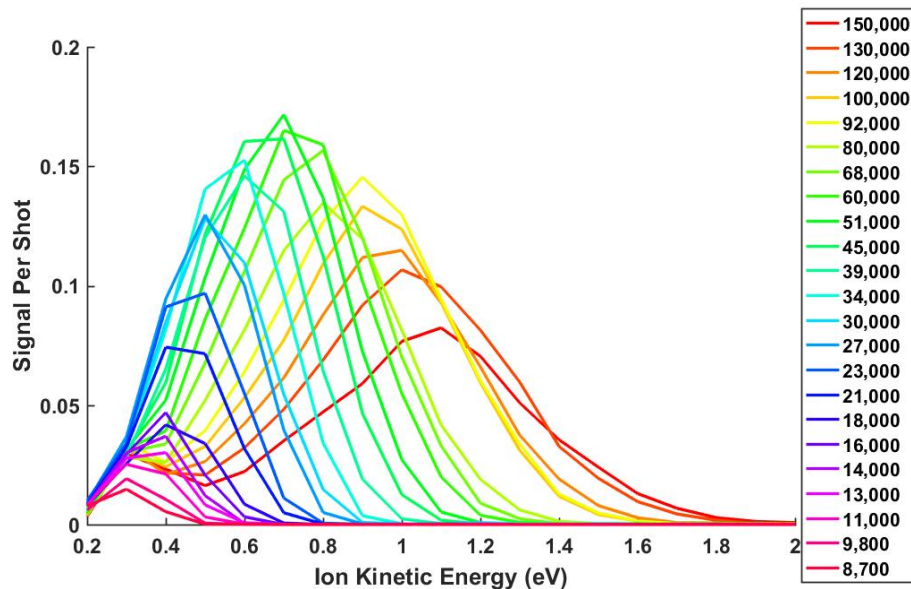


Figure 8.62: Kr ion kinetic energy signatures, obtained with the 17th harmonic laser energy. The figure represents an overview of the trend of cluster size versus kinetic energy, with a scan over cluster sizes from $\langle N \rangle = 8,700$ to $\langle N \rangle = 150,000$, with each cluster size integrating only 200 shots.

Collecting a larger number shots reveals details in these kinetic energy plots. Figure 8.63 shows a comparison of signal from the 17th and 21st harmonics in large krypton clusters. It is interesting that, although their cutoff energies and average kinetic energies are similar, these two display very different profile shapes. While the 17th harmonic data has many small detailed structures, the 21st harmonic data is smooth and relatively featureless.

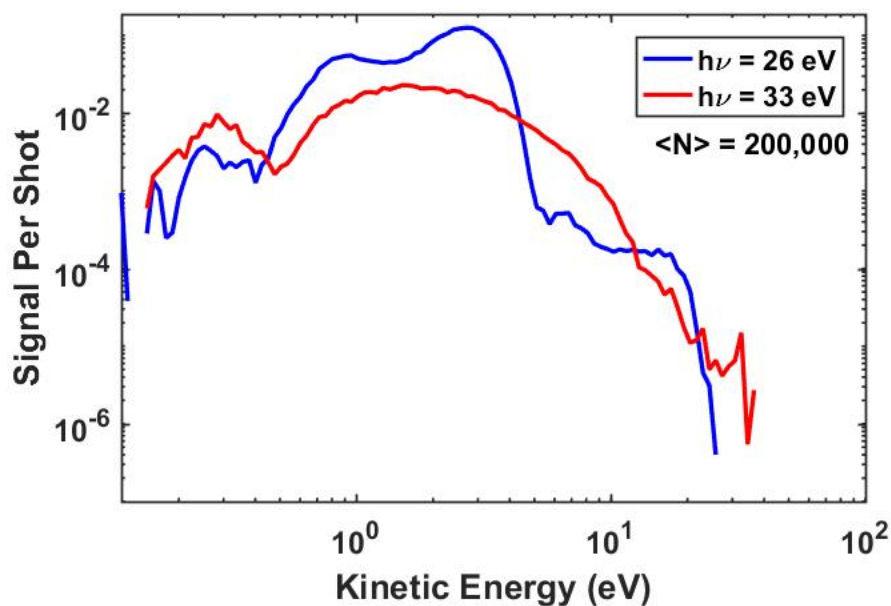


Figure 8.63: Kr ion kinetic energy signatures, at a cluster size of $\langle N \rangle = 200,000$. While the maximum kinetic energies are similar for the two photon energies, the shapes of the two profiles are very different.

As the atomic mass of the target clusters increases, field-free drift measurements become more difficult to obtain. The initial velocity of the clusters from the gas jet is orthogonal to the plane of the laser and the detector, so that for an ion to reach the detector (about half a meter away), the change in momentum imparted by cluster dissociation must overcome this original downward trajectory. This becomes less likely as the atomic mass increases. Because of this, we were only able to obtain a field-free drift kinetic energy measurement for the largest clusters of krypton, as shown in Figure 8.63, and xenon, as shown in Figure 8.64. Still, we may observe that the overall shape and average kinetic energy of the ion distribution from xenon is very similar

to what we observed in both argon and krypton.

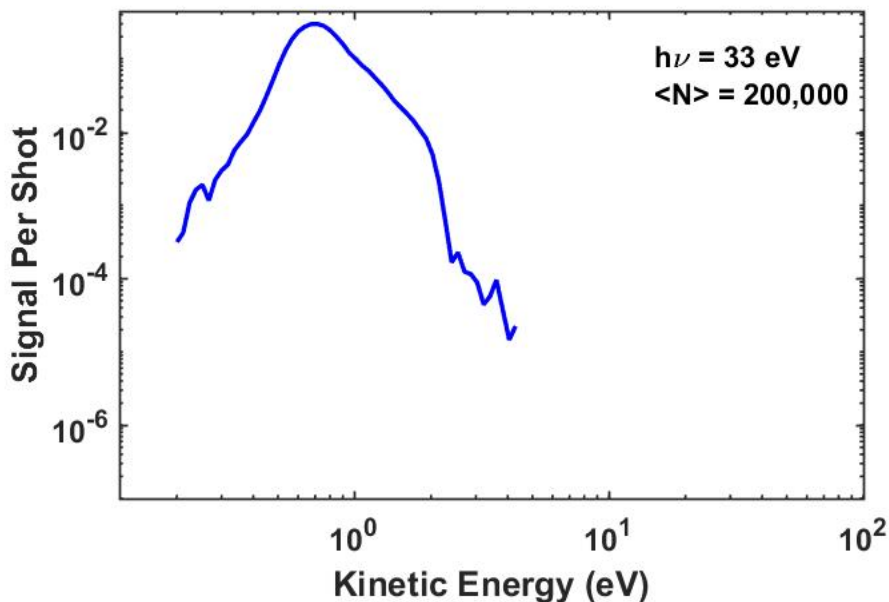


Figure 8.64: Xe ion kinetic energy signature, obtained with the 21st harmonic laser energy, at a cluster size of $\langle N \rangle = 200,000$.

Neon, however, has an entirely different behavior. Because of its resistance to clustering, as well as its difficulty in being pumped out of a vacuum chamber, we were only able to obtain data from very small neon clusters. Nevertheless, both cluster sizes that we investigated yielded similar, striking results. The vast majority of the ions which reached our detector arrived with nearly identical kinetic energies, which were much higher than the energies we observed from similarly sized clusters of other species. The trend of the ions from the smallest clusters arriving with nearly zero kinetic energy, with a plateau and cutoff energy that increases with cluster size, has clearly been

broken. As shown in Figure 8.65, clusters of 200 atoms had a kinetic energy distribution peaked around 2.2 eV, and clusters of 1,000 atoms had a distribution peaked around 2.8 eV. Each of them has a very sparse low-energy tail, which cuts off at around 0.3 eV. Figure 8.66 shows a direct comparison with an argon cluster of the same size as the largest neon clusters studied, in which the stark difference in kinetic energy profiles can be easily observed.

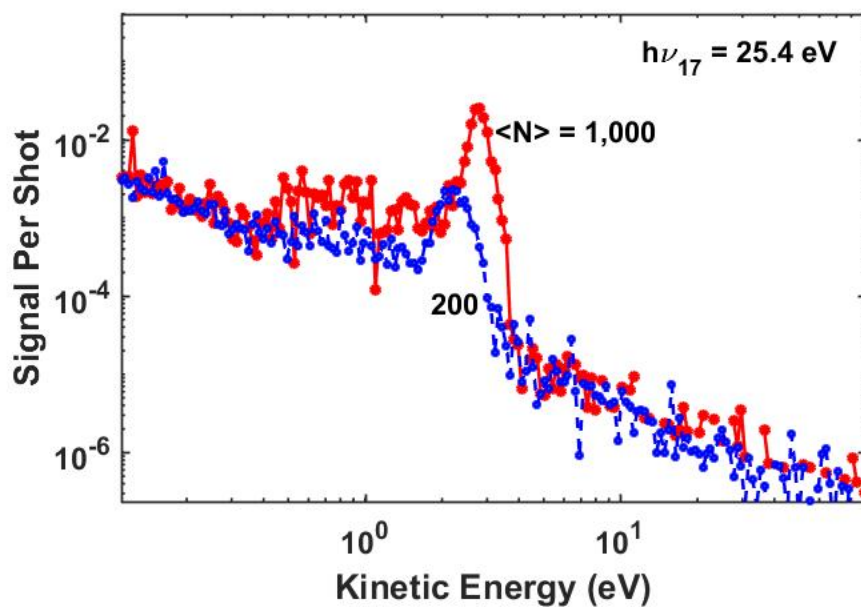


Figure 8.65: Ne ion kinetic energy signatures, obtained with the 17th harmonic laser energy.

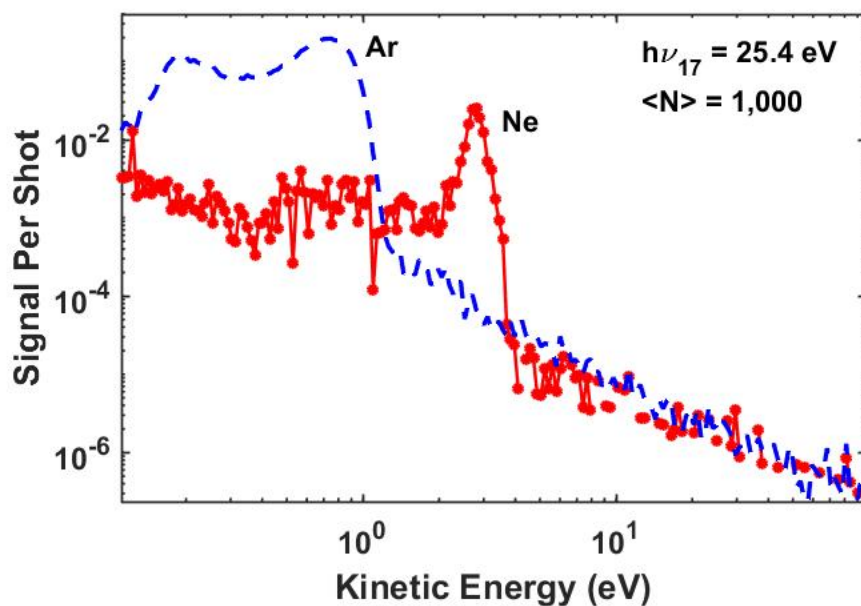


Figure 8.66: Ne and Ar ion kinetic energy signatures, at the same cluster size ($\langle N \rangle = 1,000$) obtained with the 17th harmonic laser energy.

This trend with neon only appears to hold for illumination by the 17th harmonic light. Figures 8.67 and 8.68 show similar ion kinetic energy data, taken with illumination from the 19th harmonic and 21st harmonic. These spectra follow a trend similar to the other noble gases, with low cluster sizes peaked around low kinetic energies, and larger clusters gradually increasing their cutoff energy with cluster size.

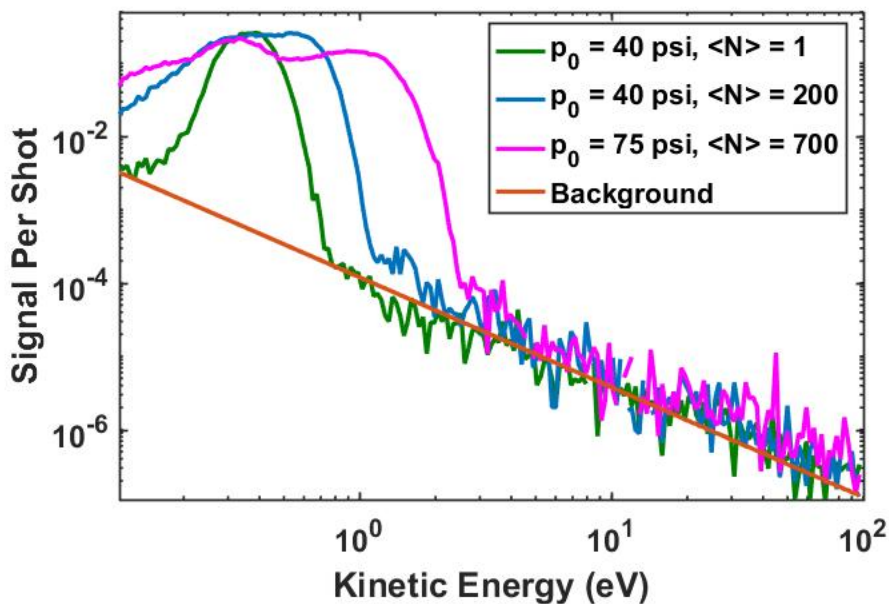


Figure 8.67: Ne ion kinetic energy signatures, at varied cluster sizes, obtained with the 19th harmonic laser energy.

Although the data taken with the 19th harmonic and 21st harmonic involved a new set of turbomolecular pumps, which allowed us to run at higher backing pressures (and generate larger clusters) than we could with the 17th harmonic, we were still not able to observe the ultimate saturation cutoff energy in these plots, as we see with large Ar and Kr clusters. One thing to note, however, is that the ultimate observed cutoff energy from the 19th harmonic data is similar to what we see from the 17th harmonic peak, but with a low-energy plateau. In contrast, the cutoff energy from each cluster size taken with the 21st harmonic is smaller than that from the equal cluster size in the 19th harmonic.

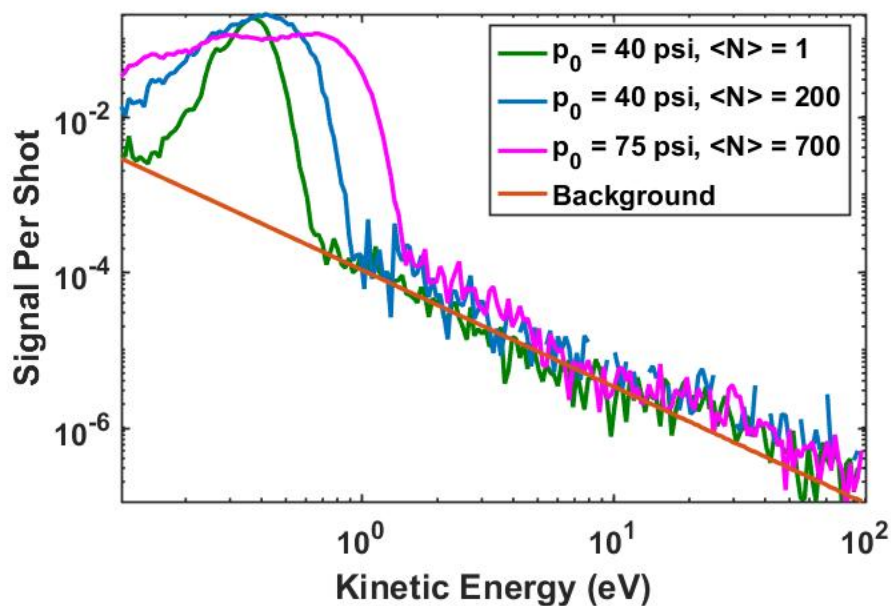


Figure 8.68: Ne ion kinetic energy signatures, at varied cluster sizes, obtained with the 21st harmonic laser energy.

8.2.7 Electron Kinetic Energy Profiles

Electron kinetic energy profiles were initially captured in order to determine the on-target spectrum from our three differently-reflective XUV focusing mirrors. Argon gas was the primary target here, as we had captured this spectrum from the 21st harmonic in previous experiments, and it had yielded good (expected) results, showing a tall central peak at the desired wavelength, and smaller sidebands at the neighboring odd harmonics [46, 68]. Unlike xenon, argon has minimal spin-orbit-splitting of its valence shell level, which makes spectral reconstruction easier.

Results obtained when we used this technique to determine the incident

photon spectrum of the 17th harmonic mirror were much more interesting than we expected. As shown in Figure 8.69, we observed a “filtering” effect at low electron energies, for larger cluster sizes.

At the smallest cluster sizes, (shown in red in Figure 8.69), the spectrum is already modified from our expectations. The photoelectrons from the 17th harmonic (at about 10 eV) dominate the spectrum, as expected, but the ratio between the 17th harmonic and the 19th harmonic is unusually low. Also, no 15th harmonic sideband is observed at all. As the cluster size increases, this trend intensifies. The peak from the 17th harmonic, and eventually the 19th harmonic, broadens as its height dramatically decreases.

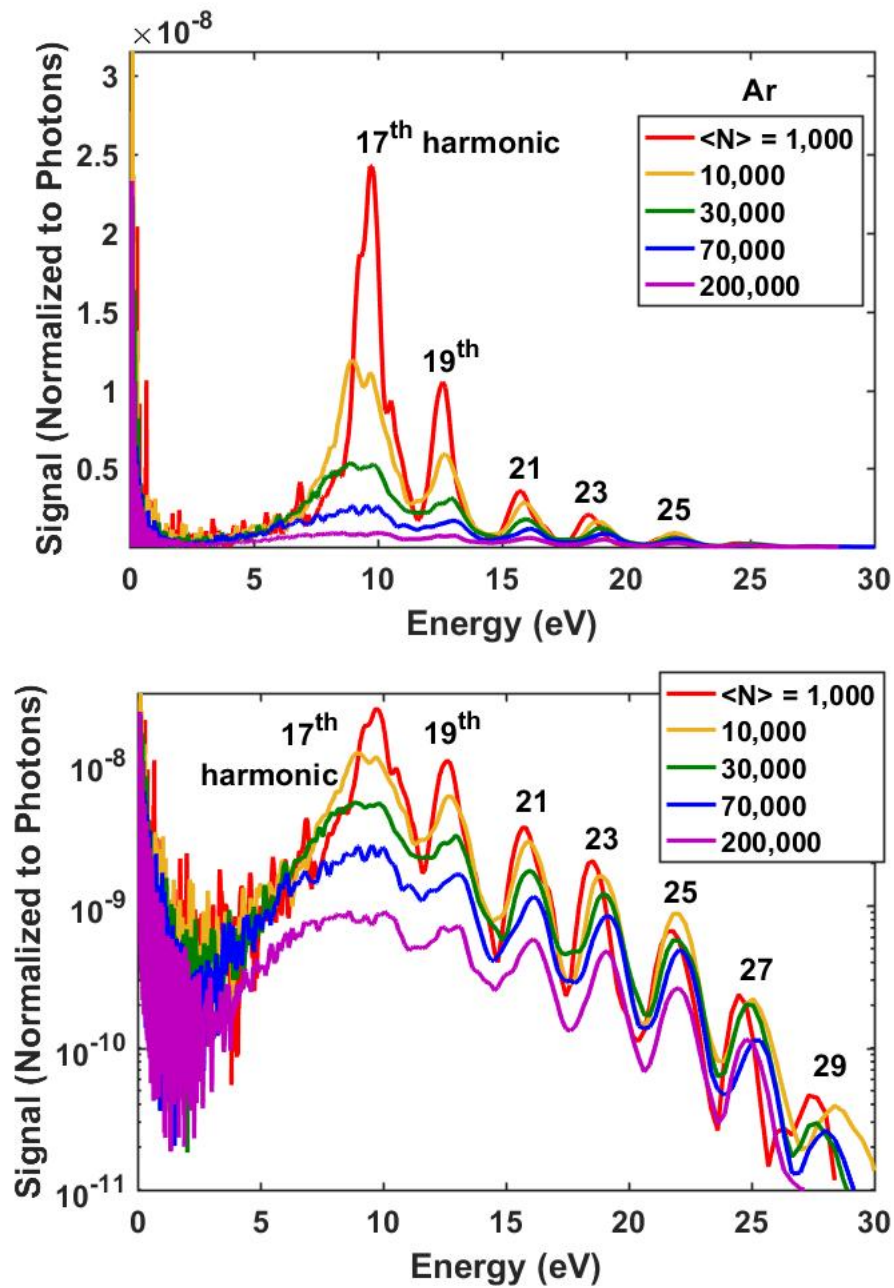


Figure 8.69: Argon electron kinetic energy plots, taken with the 17th harmonic mirror, at different cluster sizes. Data is shown on a linear (a) and log (b) scale. Signals are normalized to their photon peak, effectively normalizing by gas density.

We also observed this trend in krypton, although the effects were much less dramatic. At the smaller cluster size, the ratio of 17th harmonic to 19th harmonic is lower than expected, and some “smearing” of the 17th harmonic peak to lower energies is present. At the larger cluster size, the 17th harmonic “smearing” is much more noticeable, although the higher harmonics appear largely unaffected.

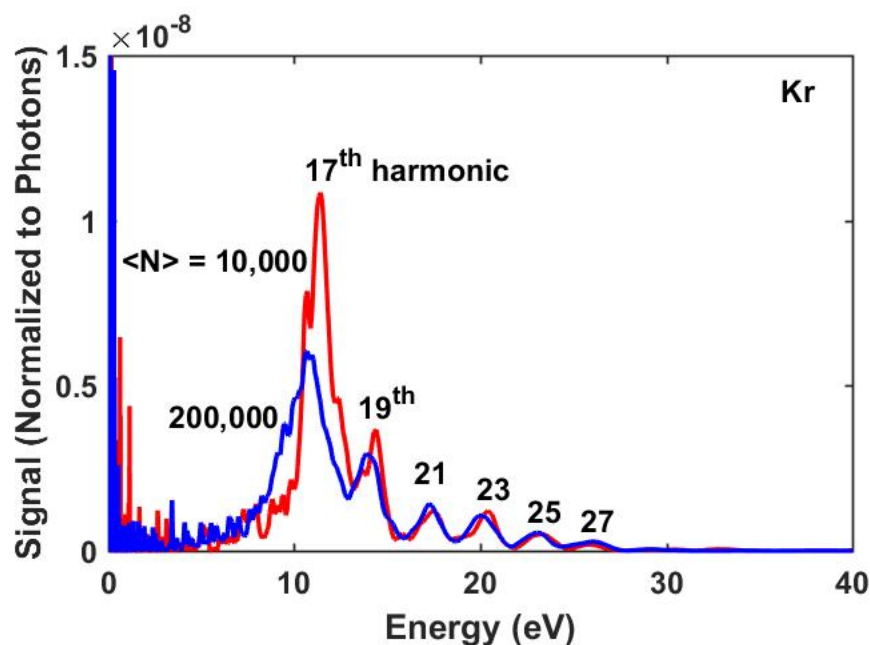


Figure 8.70: Krypton electron kinetic energy plots, taken with the 17th harmonic mirror, at two different cluster sizes. Signals are normalized to their photon peak, effectively normalizing by gas density.

Xenon does not seem to show this effect at all. Figure 8.71 shows xenon photoelectron kinetic energy taken with the largest cluster sizes generated in the experiments detailed here. For reference, both the 17th (blue) and 21st

(green) harmonic data are shown. Note the prominent spin-orbit splitting present in xenon. Small amounts of sidebands containing photoelectrons from the 15th harmonic and (more prominent) 19th harmonic are present in the data taken with the 17th harmonic mirror, in stark contrast to what was observed with the other noble gases in these experiments.

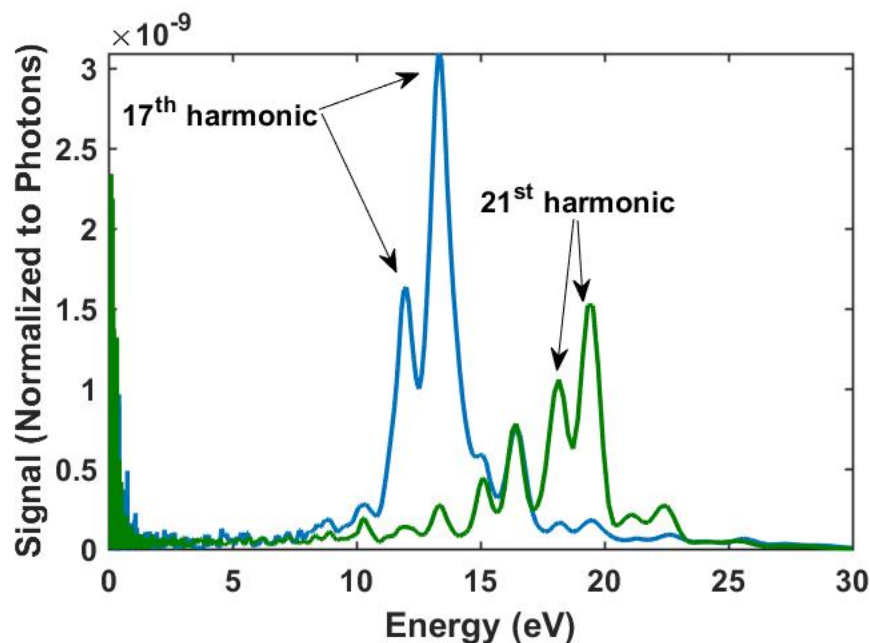


Figure 8.71: Xenon electron kinetic energy plots, taken with the 17th (blue) and 21st (green) harmonic mirror, at large cluster size ($\langle N \rangle = 200,000$). Signals are normalized to their photon peak, effectively normalizing by gas density.

The neon spectra, generated with the 17th harmonic mirror, seem to follow the trend we observe in the lighter noble gases to its extreme. Almost no photoelectrons from the 17th harmonic were detected, and an unusually large number of electrons were detected at very low (< 1 eV) energies. Few electrons

were detected at the nearest higher energy sideband, the 19th harmonic, and none at the nearest lower energy sideband, the 15th harmonic. In contrast, the high energy harmonics, of which we expect to reflect nearly trivial amounts, seem to be unaffected or even amplified. The 23rd harmonic and 25th harmonic are actually the brightest in the spectrum, and harmonics up to the limit of what we generate in the HHG gas jet, the 31st harmonic, are clearly present. These results are shown in Figure 8.72.

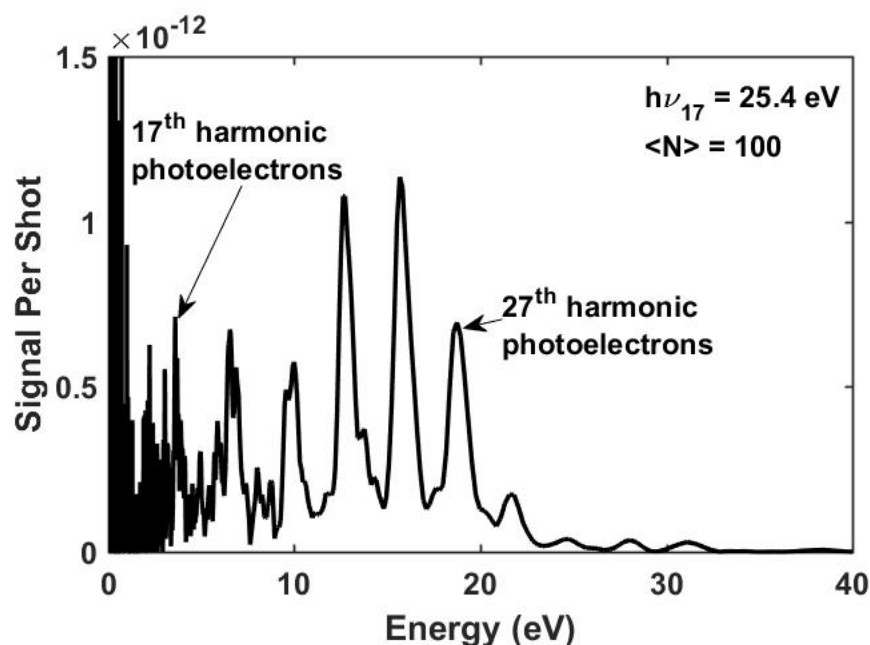


Figure 8.72: Neon electron kinetic energy plots, taken with the 17th harmonic mirror, at small cluster size ($\langle N \rangle = 100$). The photoelectron peak from the 17th harmonic is nearly entirely absent from the spectrum.

At first glance, this data seems to be consistent with the observation of charge buildup on a cluster [2, 3, 83], with electrons from gases with higher

atomic numbers affected less than those with lower numbers due to the lower ionization potential (and thus longer time to full outer ionization frustration). Unfortunately, this theory appears to be incorrect. Firstly, we would expect Coulombic attraction from charge buildup to affect the photoelectrons from each harmonic equally. In our argon, krypton, and neon data, the higher-energy electrons are largely unaffected.

We can also rule out charge buildup on clusters as the cause of this phenomenon because the effect does not grow with intensity. Due to the nonlinear nature of HHG, our shot-to-shot variability on certain days can be quite large (over 50%). Our XUV diode captures on-shot energy measurements for each shot, which we can sort by during data processing. Looking at the electron spectra from the lowest on-shot laser energies versus the highest only results in an overall broadening of all photoelectron peaks for the higher-fluence shots. The energy-selective “smearing” to lower energies is unaffected.

Data from small neon clusters, which is likely dominated by uncondensed atomic gas, seems to suggest that the phenomenon which at first appeared to be cluster size dependent is actually dependent on the unclustered atomic gas density. Figure 8.73 shows the data from above plots, with neon, argon, and xenon electron kinetic energy spectra generated with the 17th harmonic focusing mirror, plotted on the same axes. There is a suggestive trend of photoelectron suppression at and below 10 eV (about 260 ns in Figure 8.73).

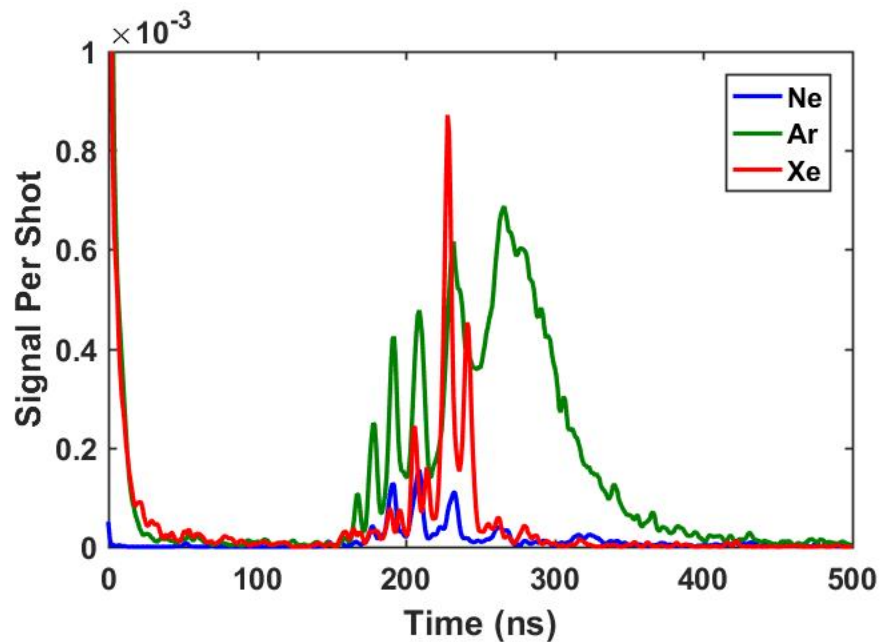


Figure 8.73: Ne, Ar, and Xe electron kinetic energy plots, taken with the 17th harmonic mirror, at 20-30 psig of gas jet backing pressure. Signals are shown on a time, rather than energy, scale, so that their respective photon peaks are visible at $t=0$.

Since neon shows this effect most dramatically, we performed a series of experiments with neon targets to begin to sort out the relevant variables. The most obvious to begin with was a pressure scan. If the effect is amplified at higher gas densities, then we should be able to re-create the systematic suppression of the 17th and 19th harmonic with neon at gradually higher densities, as we did with argon in Figure 8.69. Figure 8.74 shows the results of this gas jet backing pressure scan, taken with illumination of neon by the 17th harmonic mirror. Unfortunately, no similar trend is readily apparent.

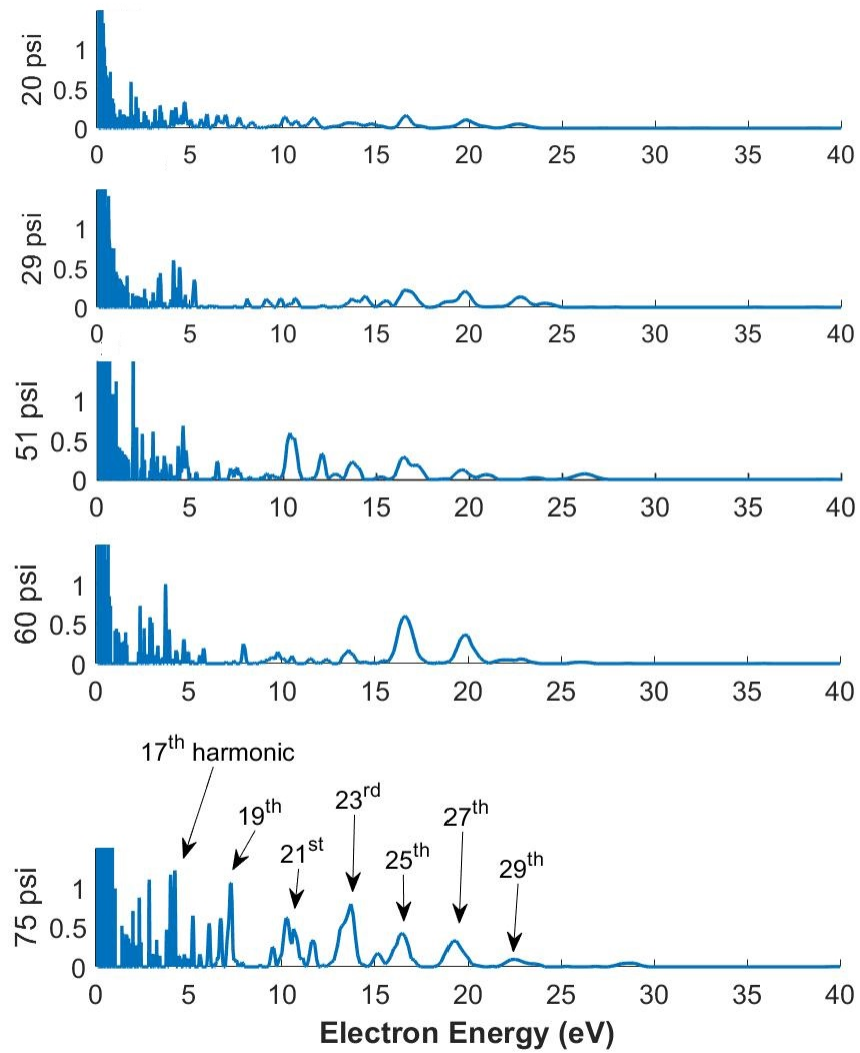


Figure 8.74: Ne electron kinetic energy plots, taken with the 17th harmonic mirror, at different gas jet backing pressures. Signals are normalized to their photon peak.

We repeated this scan of gas jet backing pressure with the 19th and 21st harmonic mirrors, as shown in Figures 8.75 and 8.76, respectively. Here, it seems as if the suppression at lower electron energies actually becomes slightly *less* prominent at higher gas jet backing pressures. The 19th and 21st harmonic seem to grow at higher gas jet densities, with respect to the higher (unsuppressed) harmonics, and despite normalization of these plots to the height of the photon peak in each case. This post-processing serves to normalize the signals to the amount of gas in the target area, as the detected photon peaks result primarily from Rayleigh scattering of the XUV light from uncondensed atomic gas.

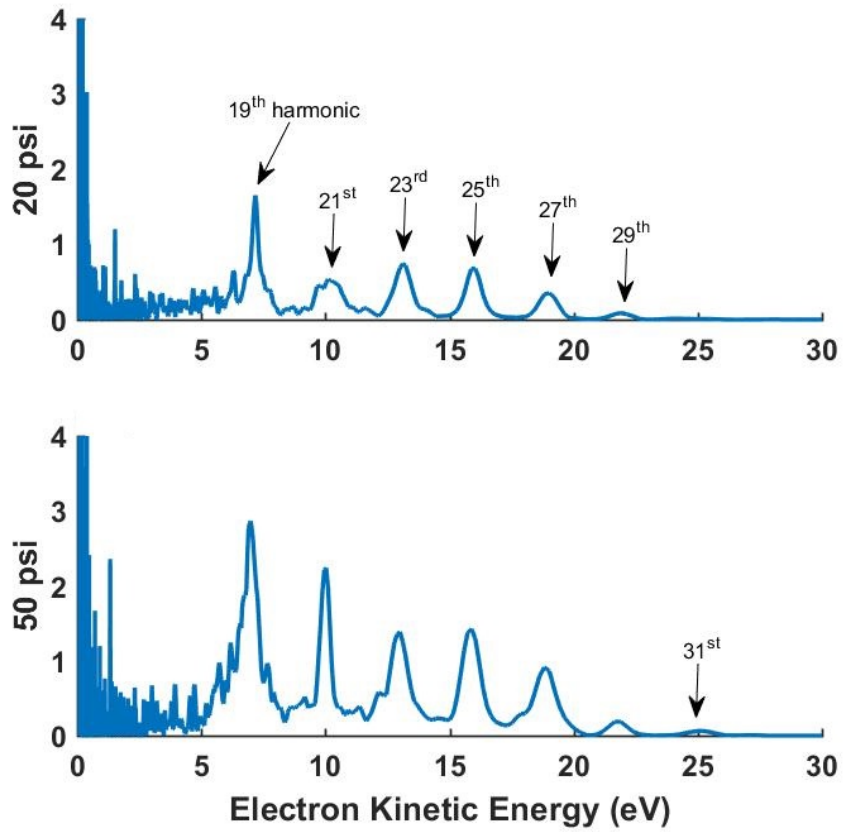


Figure 8.75: Ne electron kinetic energy plots, taken with the 19th harmonic mirror, at different gas jet backing pressures. Signals are normalized to their photon peak.

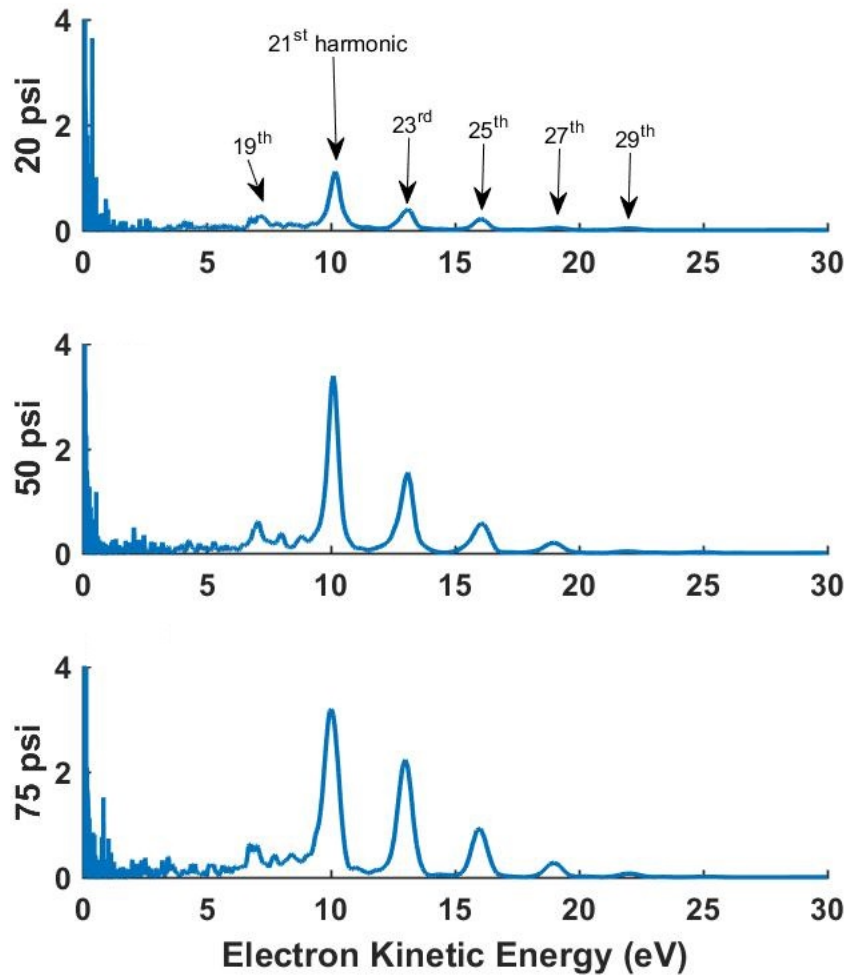


Figure 8.76: Ne electron kinetic energy plots, taken with the 21st harmonic mirror, at different gas jet backing pressures. Signals are normalized to their photon peak.

A timing scan similarly fails to lend concrete support one way or another to the question of whether the low energy photoelectron suppression is a cluster or atomic gas phenomenon, although it points away from the effect being dominated by cluster-based physics. Here, we mis-timed our gas jet to fire much later than it would for optimum cluster signal. This way (labeled “Front” in Figure 8.77), the laser would impact only the very first part of the gas jet which made it to the target area. This gas, released during or shortly after the gas jet poppet opening, and not yet in a steady state, contains mostly atoms, and few clusters. The spectrum labeled “Center” in Figure 8.77 is taken at the common trigger timings, with the laser firing near the center of the gas jet opening time, where more clusters are present. The data taken at the front of the gas jet pulse seems to exhibit more suppression of the 19th harmonic (7 eV) photoelectrons.

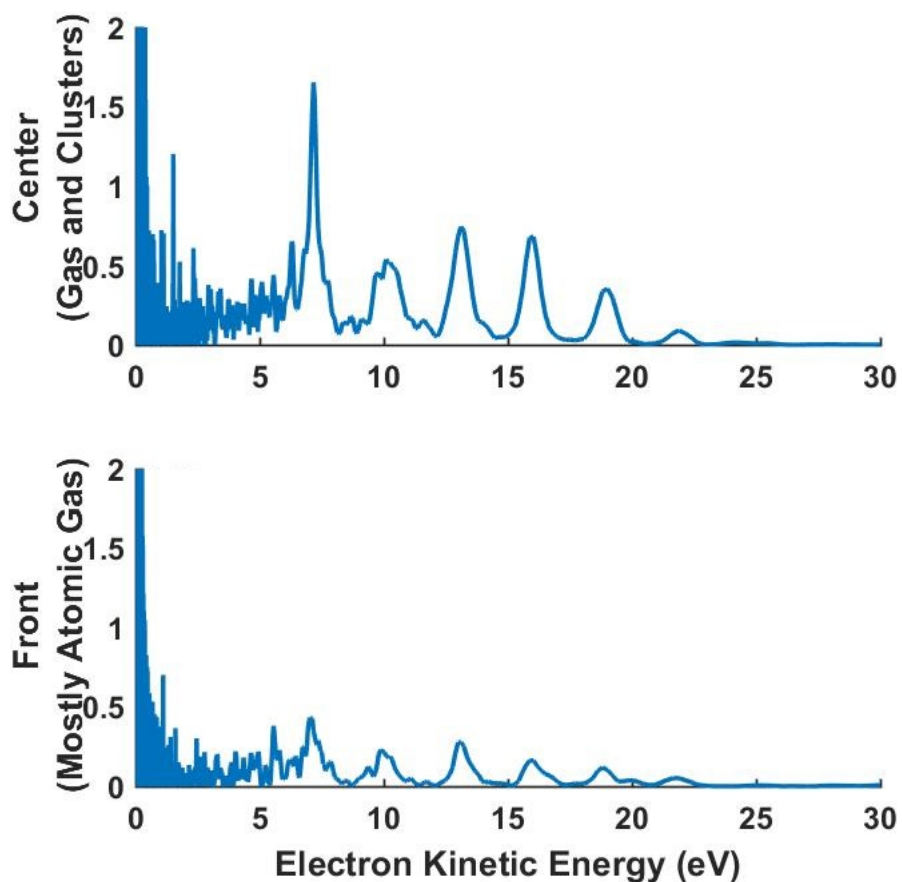


Figure 8.77: Ne electron kinetic energy plots, taken with the 19th harmonic mirror, at different gas jet timings with respect to the XUV laser. This effectively varies the ratio of uncondensed atomic gas to clusters (the clusters being more prevalent in the center of the gas jet opening time than at the front). Data was taken at 20 psi backing pressure. Signals are normalized to their photon peak.

An additional possibility that could help explain the anomalous neon electron data is that there were space charge effects, similar to charge buildup on a cluster, trapping photoelectrons from uncondensed atomic gases in the

focal region of the laser. These effects would be expected, like cluster charge buildup, to affect each photoelectron energy equally, decreasing each electron's energy by the amount of potential built up in the region at its time of "birth." Nevertheless, we performed experiments to definitively determine if this theory held some explanation for our results.

Figures 8.78, 8.79, and 8.80 show the results of defocusing the 17th, 19th, and 21st harmonic beams, respectively, on the neon gas target. This should provide lower fluence, larger focal volume, and hence dramatically less effect of space charge buildup in the region. Unfortunately, as shown, none of these adjustments yielded dramatically different results. These experiments should additionally rule out all nonlinear optical processes such as four-wave mixing to create enhancements in the higher harmonic intensities.

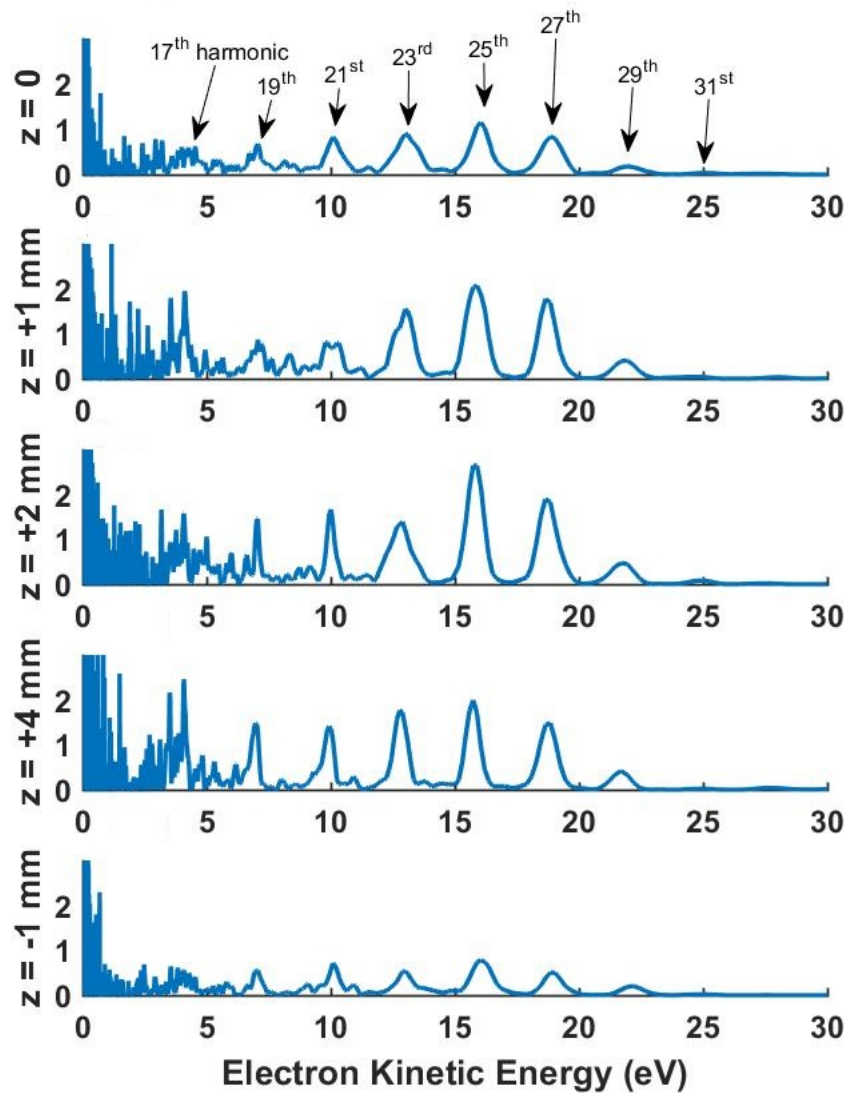


Figure 8.78: Ne electron kinetic energy plots, taken with the 17th harmonic mirror, at different positions of the focusing mirror along the axis of the laser, decreasing the on-target fluence by increasing the laser-gas interaction volume. All data were taken at 50 psi backing pressure. Signals are normalized to their photon peak.

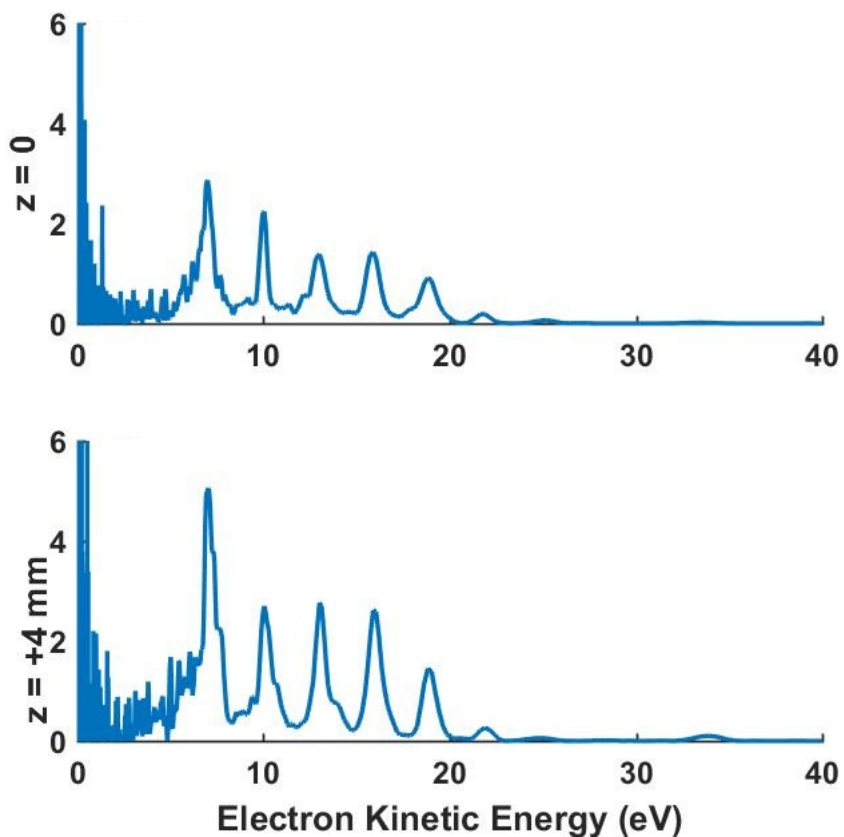


Figure 8.79: Ne electron kinetic energy plots, taken with the 19th harmonic mirror, at different positions of the focusing mirror along the axis of the laser, decreasing the on-target fluence by increasing the laser-gas interaction volume. All data were taken at 50 psi backing pressure. Signals are normalized to their photon peak.

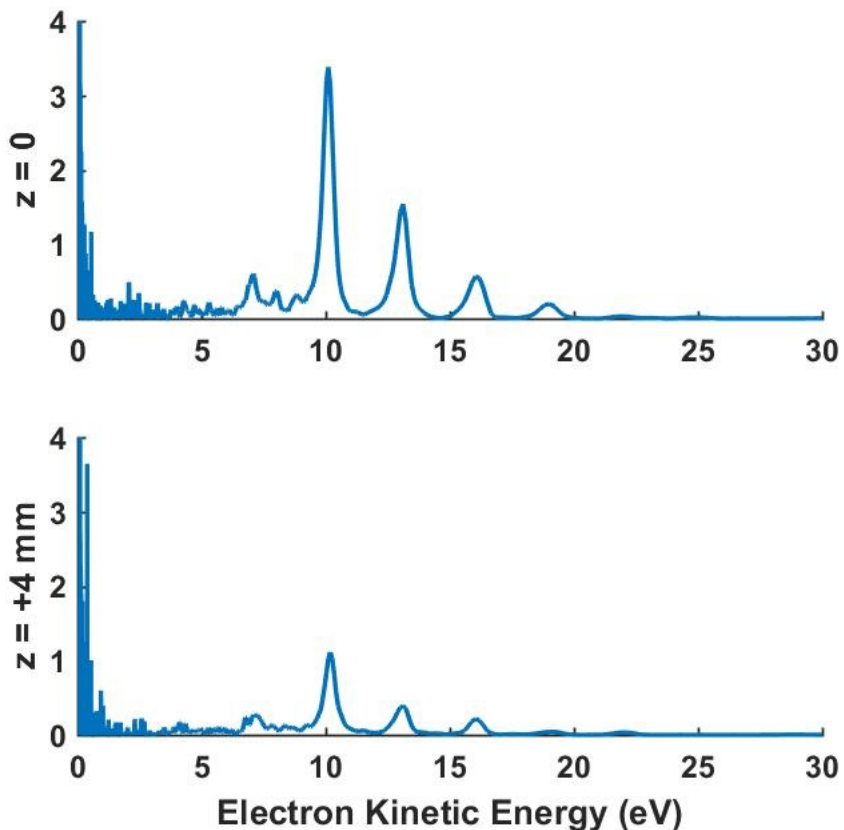


Figure 8.80: Ne electron kinetic energy plots, taken with the 21st harmonic mirror, at different positions of the focusing mirror along the axis of the laser, decreasing the on-target fluence by increasing the laser-gas interaction volume. All data were taken at 50 psi backing pressure. Signals are normalized to their photon peak.

We propose that these trends are due to an as-yet unidentified energy-dependent “filtering” mechanism. This mechanism must be either gas density or cluster size dependent, if it is to explain the argon and krypton spectra as well as the neon spectra. It is possible that we also observe enhancements at

the higher harmonics in addition to suppression at low energies. Figure 8.81 points out a suggestive envelope which appeared when focusing the 19th harmonic onto neon clusters. The regularity of the width and the smooth envelope of heights of the higher harmonics are in sharp contrast to the appearance of the 19th harmonic photoelectron peak. Additionally, it almost appears as if the 21st harmonic is split into two peaks. Two different mechanisms, which overlap or cut off around 10 eV, may explain these trends.

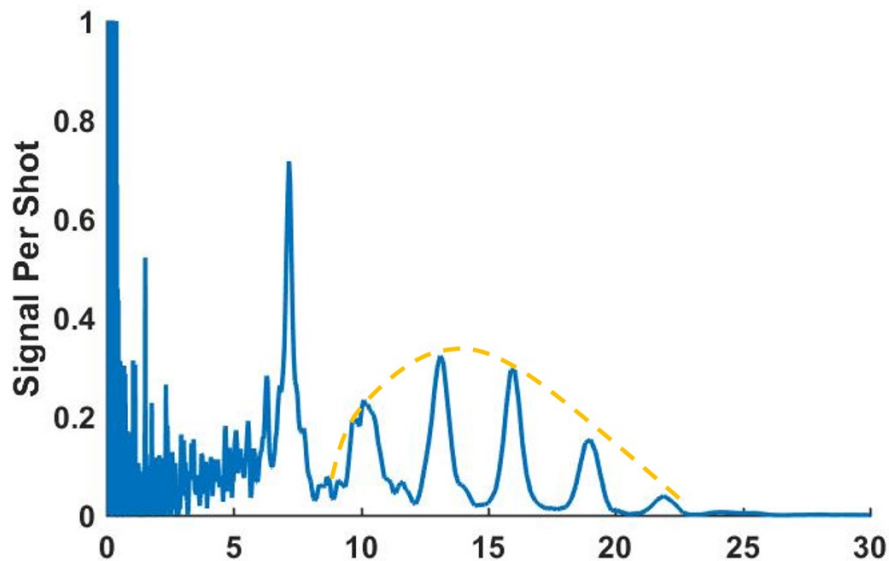


Figure 8.81: Ne electron kinetic energy plot, taken with the 19th harmonic mirror. This data is also shown as the “Center” of the gas jet timing in Figure 8.77. A suggestive envelope is drawn with orange dotted line, which may yield additional hypotheses on the source of our anomalous electron kinetic energy spectra.

8.3 Nitrogen Clusters

Nitrogen is an interesting material for studies of clusters, in that the clusters are made of weakly (van der Waals) bound groups of tightly (triple bond) bound molecules. The ionization and dissociation of isolated N_2 molecules is a current area of scientific interest. Although the molecule may be ionized with 15.6 eV, below 24.3 eV only N_2^+ ions are produced. Between 24.3 eV and 28 eV, separate N^+ and N may be formed on long (picosecond to nanosecond) timescales, and above 28 eV, the dissociation may take only femtoseconds [33]. Therefore, with the full range of our harmonics, we should expect to generate at least some N^+ (as we have indeed seen previously, as referenced in [46]), but we expect the the 21st harmonic, at 33 eV, to be much more efficient at this process than the 17th harmonic, at 26 eV.

Figure 8.82 shows the photoionization cross-sections for N_2^+ and the N^+ , which suggest that although the process of molecular dissociation may be quicker with 21st harmonic light, for comparable photon flux, we expect nearly negligible differences in N^+ detection. Additionally, we should expect to see at least some production of N_2^+ with the 21st harmonic, but not necessarily with the 17th, as the ionization potential for N^+ to N^{2+} is between the two photon energies at 29.6 eV [1]. However, it stands to reason that the electron dynamics present in dense clusters could modify these potentials and cross-sections.

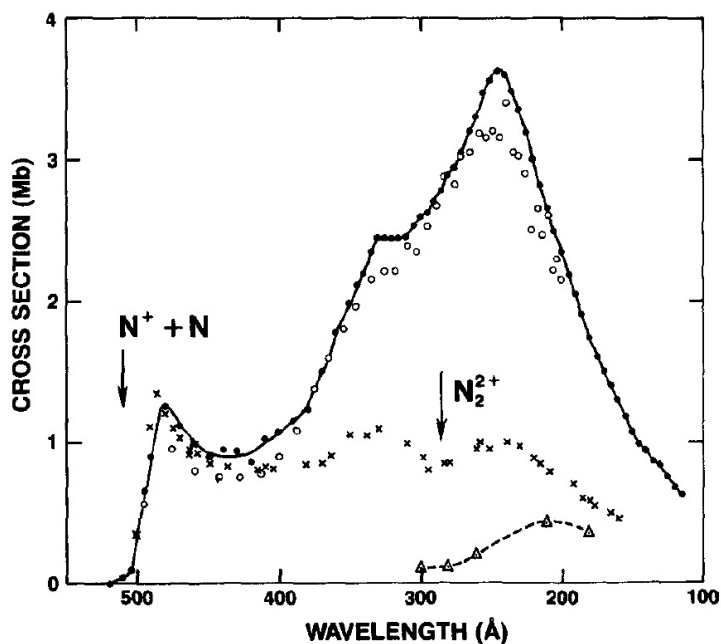


Figure 8.82: Dissociative photoionization cross-sections for N_2 . Figure from Reference [78]. Cross-sections are 22.15 and 1.12 Mb for the N_2^+ and the N^+ pathway, respectively, for illumination with 17th harmonic (26 eV) light. Cross-sections are 16.80 and 1.23 Mb for the N_2^+ and the N^+ pathway, respectively, for illumination with 21st harmonic (33 eV) light

The primary goal of the data presented here, using N_2 cluster targets, was to fill in perceived gaps in data previously generated and presented in Reference [46]. Here, we focus on low cluster sizes, to identify the transitional patterns between atomic and large cluster behavior. Figure 8.83 shows ion kinetic energy spectra, taken with the 21st harmonic, at different cluster sizes. Cluster sizes above and including $\langle N \rangle = 30,000$ are documented in Reference [46] (with cluster sizes re-calibrated from Reference [46] to reflect corrections to the nozzle parameters assumed in that document), while the lower cluster

sizes are unique to this work. In this figure, we can see a transition, from small clusters with spectra sharply peaked at low energies and largely composed of N_2^+ , to spectra at larger cluster sizes, more evenly distributed between N_2^+ and N^+ . At large cluster sizes, both the N^+ and N_2^+ peaks broaden to higher kinetic energies, but the N^+ peak is more strongly affected.

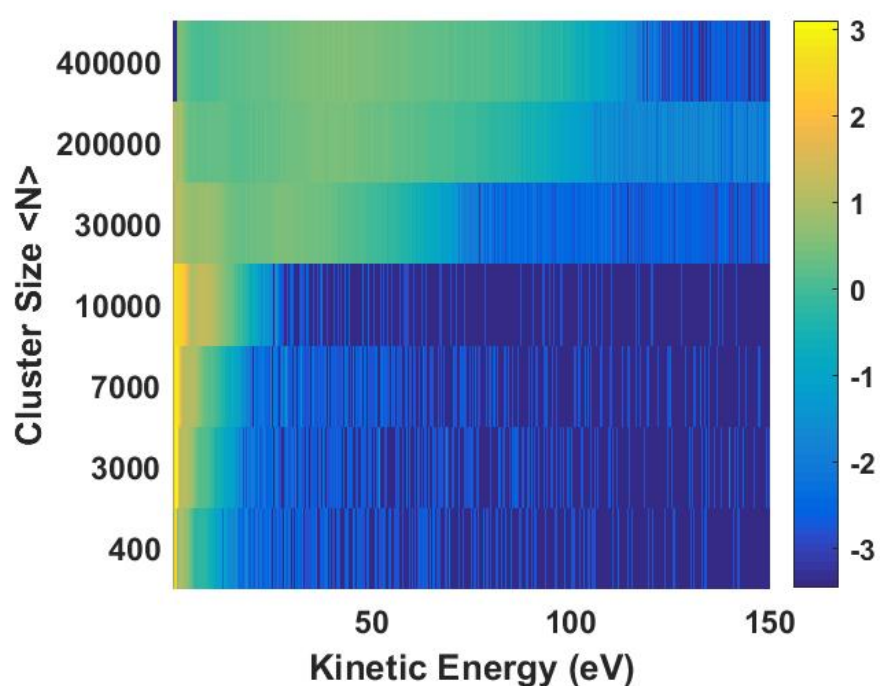


Figure 8.83: N_2 ion kinetic energy signatures, obtained with the 21st harmonic laser energy, for all cluster sizes investigated, including the large sizes in Reference [46].

Figure 8.84 shows the ion kinetic energy spectra for the lower cluster sizes shown in Figure 8.83, presented in a format which aids in distinguishing the different features in the spectra. The smallest cluster size, $\langle N \rangle = 400$,

very closely resembles atomic spectra from low-intensity photoionization at XUV wavelengths [78]. This allows us to easily distinguish the features representing contributions from N_2^+ and N^+ , and to track how these features evolve with increasing cluster size. Both features clearly broaden, shifting to larger kinetic energies at larger cluster sizes.

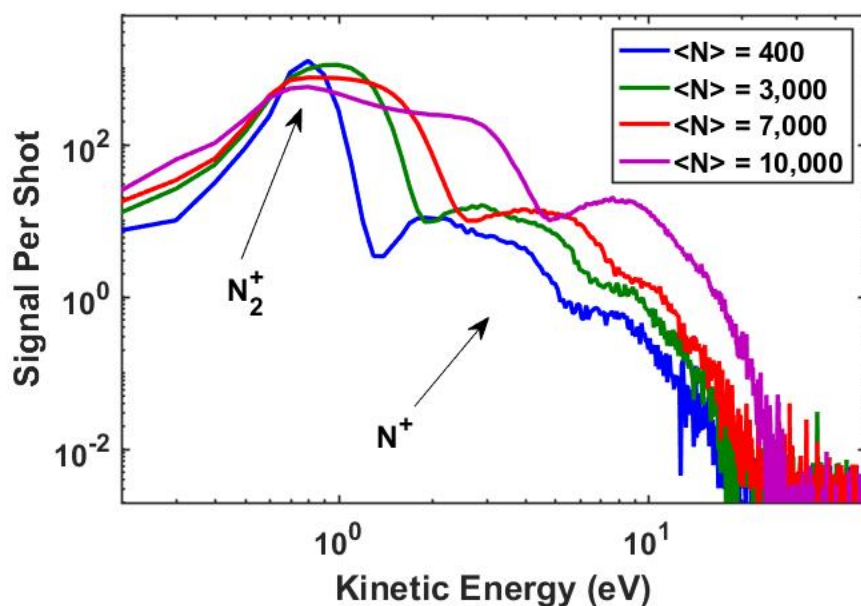


Figure 8.84: N_2 ion kinetic energy signatures, obtained with the 21st harmonic laser energy. Similarities to Reference [78] allow us to identify the portions of the spectra which represent N_2^+ and which represent N^+ .

The features present in ion kinetic energy spectra when N_2 clusters are illuminated with photons of energy barely above the molecular dissociation threshold, shown in Figure 8.85, are much more ambiguous. Nonetheless, the similarities in spectral shape at larger cluster sizes allow us to estimate the

point where the spectra shift from mostly N_2^+ to mostly N^+ , as indicated by arrows on the plots.

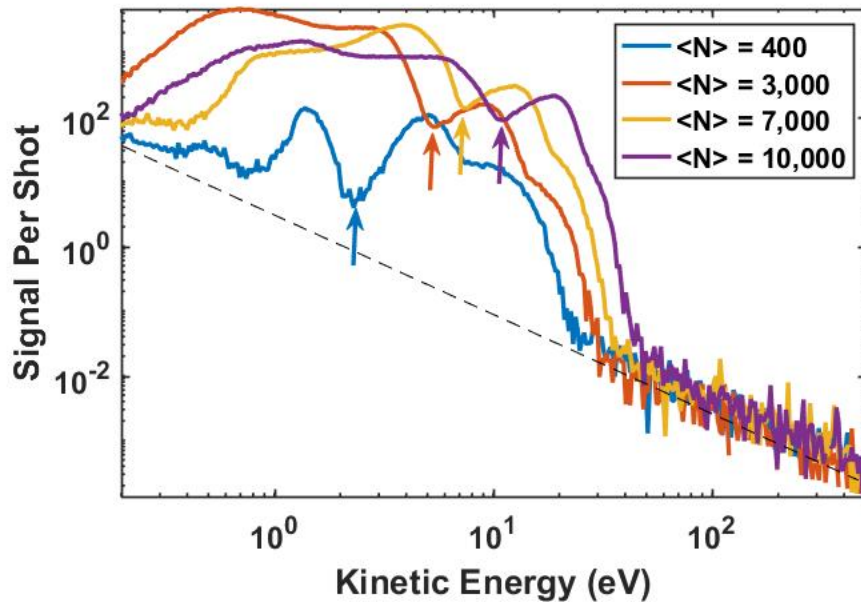


Figure 8.85: N_2 ion kinetic energy signatures, obtained with the 17th harmonic laser energy. The estimated constant-in-time background is plotted as a black dashed line. The estimated break point in the spectra between N_2^+ and N^+ are marked with arrows.

Figure 8.86 presents an overall view of the ion m/q ToF spectra obtained at both photon energies. As is discussed in Reference [46], we see an increase in the ratio of N^+ to N_2^+ at larger cluster sizes. In addition to this, we see a curious trend, also discussed in Section 8.2, where clusters illuminated with the 17th harmonic behave similarly to much larger clusters illuminated with the 21st harmonic. In this case, for almost all sizes observed, the 17th harmonic spectra look nearly identical to spectra of 21st harmonic clusters 5

times their size.

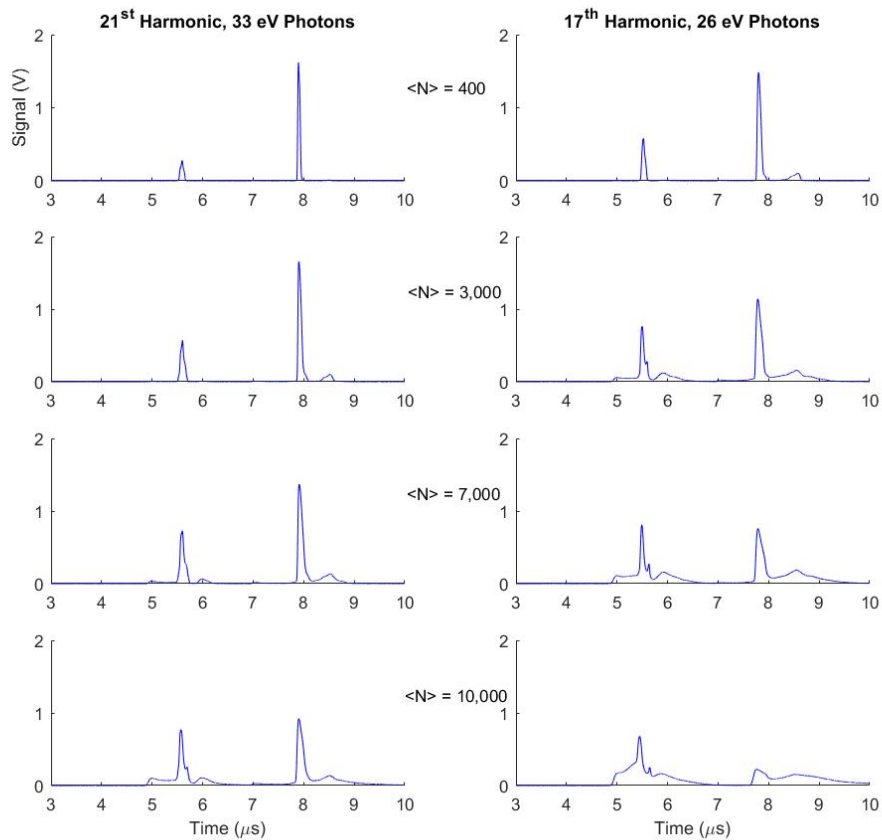


Figure 8.86: N_2 ToF m/q spectra, illuminated by the 17th and 21st harmonics, at different cluster sizes. Notice that the clusters irradiated with the lower energy light source seem to behave like clusters approximately 5 times their size irradiated with the higher energy source.

A similar trend is also visible in the m/q spectra obtained with the different wavelengths. Figures 8.87 and 8.88 show the m/q spectra of differently-sized clusters taken with the 21st harmonic and 17th harmonic, respectively.

These plots present the same data as Figure 8.86, but on a logarithmic, zoomed-in y scale, in order to show the much less intense cluster peaks. Figure 8.87 shows the cluster-related forward-going wing of N_2^+ increasing as a function of cluster size, and then saturating in height, while the backwards-going wing and all portions of the N^+ signal continue to grow. In Figure 8.88, this trend appears to take off where Figure 8.87 left off, with the continued saturation of the forward-going wing of N_2^+ , and the continued increase of the N^+ signal.

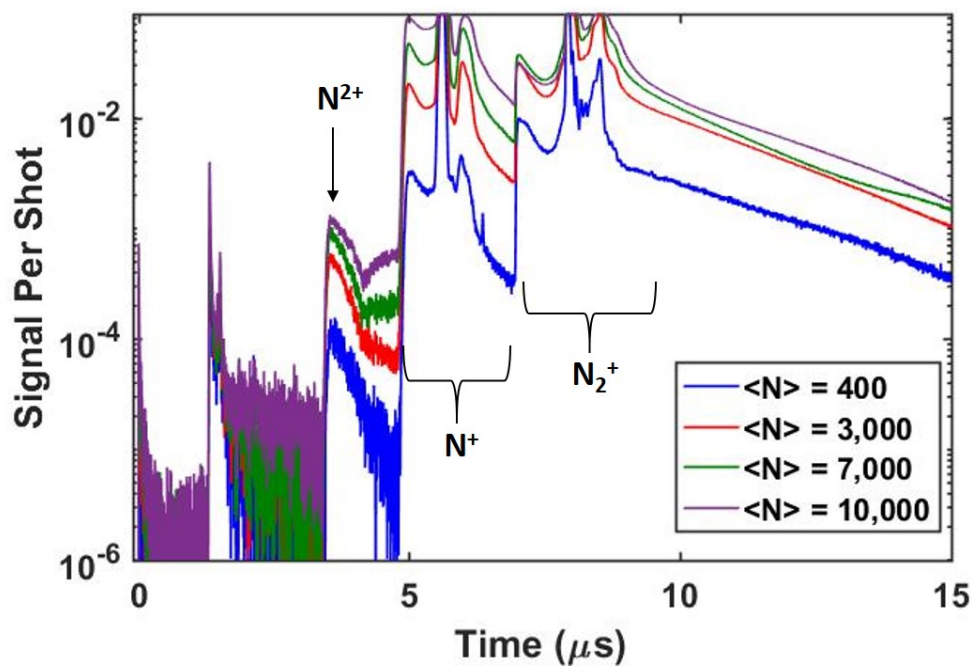


Figure 8.87: N_2 ToF m/q spectra, illuminated by the 21st harmonic, at different cluster sizes, zoomed in to give a better view of branching ratios, as well as the presence of N^{2+} .

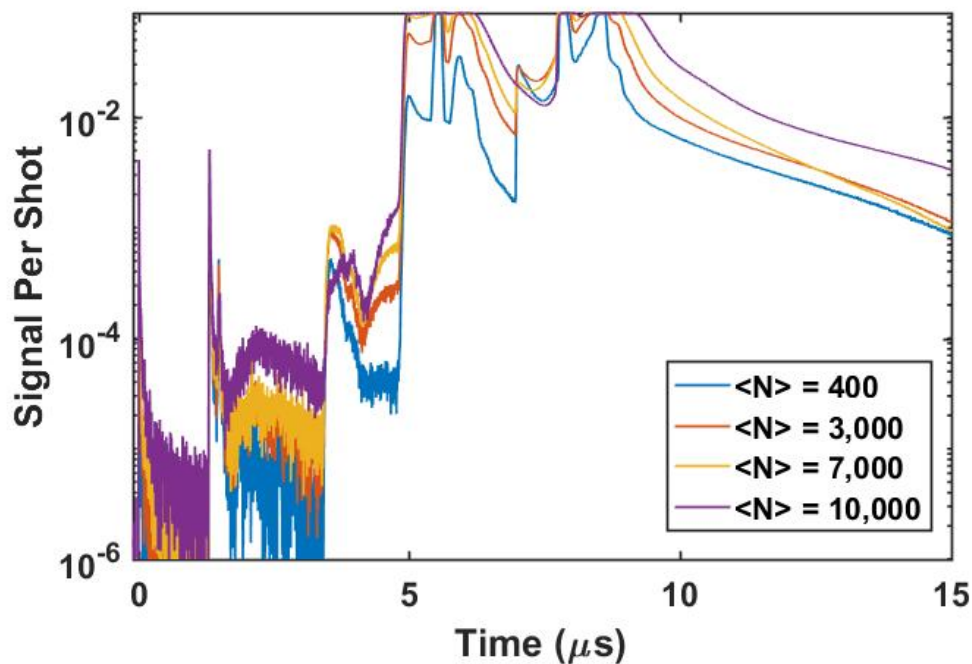


Figure 8.88: N_2 ToF m/q spectra, illuminated by the 17th harmonic, at different cluster sizes, zoomed in to give a better view of branching ratios, as well as the presence of N^{2+} .

Also of note in Figures 8.87 and 8.88 is the prominent N^{2+} signal, visible at all cluster sizes, which was not previously observed. This signal grows as a function of cluster size when ionized by the 21st harmonic. The 17th harmonic photon energy is below the threshold for ionization from N^+ to N^{2+} , however it shows the same yield of N^{2+} as we observe from the 21st harmonic. In fact, production appears to continue to grow with cluster size, saturate around $\langle N \rangle = 3,000$, and then even decrease at $\langle N \rangle = 10,000$. Figure 8.89 shows a direct comparison of m/q yields for the two photon energies at a moderately

small cluster size.

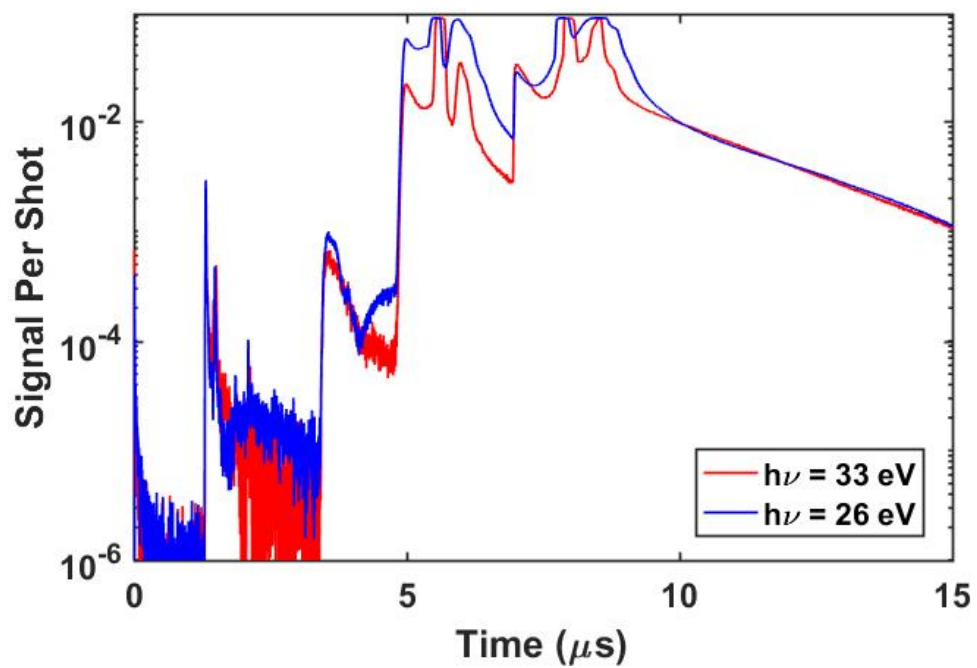


Figure 8.89: ToF m/q spectrum of N_2 at $\langle N \rangle = 3,000$, taken with the 17th (blue) and 21st (red) harmonic mirror at comparable on-target intensities.

Chapter 9

Conclusions

The conclusions which may be drawn from this work are many and varied. The main questions motivating the experiments described here are five-fold:

1. Is it possible to generate high charge states such as those seen in FEL experiments at our HHG frequencies, fluences, and intensities?
2. What is the primary mechanism of ionization in a cluster - photoionization, electron impact ionization, or something else?
3. Which, if any, of the models of continuum lowering best predicts the resulting charge states?
4. What are the main drivers of dissociation at this frequency, fluence, and intensity - can we discern the relative contributions of Coulombic or hydrodynamic expansion mechanisms?
5. Do we see evidence of cluster charge buildup in the electron kinetic energy profiles?

Many of the experiments aiming to answer these questions shed light on the problems they aimed to address, while others proved inconclusive. Still others appear to have opened the door to unanticipated and as of yet unexplained physical phenomena, which could motivate further exploration in the future.

9.1 Solid Targets

Experiments using LAM-generated nanoparticle targets, as well as microparticles and nanoparticles on a solid surface, had as their primary goal to tackle Question 3 above: Which, if any, of the models of continuum lowering best predicts the resulting charge states? Silver nanoparticle targets were employed first, as the LAM apparatus had been well-characterized by previous research teams for use with the DuPont P-311J spherical silver microparticle source stock. Following the silver, we planned to utilize the same LAM apparatus to generate metal oxide nanoparticle targets.

These targets would constitute a unique approach to the problem of continuum lowering. With their known crystalline structure, they have a set distribution of two atomic species: an “electron donor” species and oxygen. These two species are evenly distributed throughout the cluster, in known abundances. The “donor species” would be varied among atoms with different ionization potentials (Si, Ti, Sn), contributing more or fewer electrons to the resulting nanoplasma. Changes in charge state abundances in oxygen resulting from this variation in free electrons within the nanoplasma could point us to a particular model of continuum lowering in these unique dense plasmas.

Unfortunately, we were unable to generate data from solid nanoparticle or microparticle targets using the XUV fluence available to us. Clearly, the physics associated with the dissociation of solid clusters is markedly different than that of the typically used van der Waals-bound gas clusters. The much higher cohesive energy associated with these solid materials may play some role in this. The crystalline structure of the material and mechanism of atomic binding may also play a role.

Silver, specifically, may have been an unusually difficult target in which to affect dissociation due to its metallic properties. The vast majority of ionization of silver would be expected to occur in the already delocalized electrons of the conduction band. Rather than creating “an ion” with the ejection of a single electron, it would be more accurate to characterize the result as “a slightly charged cluster.” Trapped electrons in the charged cluster would behave simply as hot electrons in the conduction band. The large number of delocalized electrons may have provided sufficient shielding to prevent Coulombic dissociation of the outer shells, while the high cohesive energy would have thwarted a hydrodynamic expansion. While these explanations hold for silver, they fail to fully explain the behavior of nonconductive solids, which suggests that there is some additional physical explanation to be investigated by future researchers.

9.2 High Charge States

Upon our return to van der Waals-bound cluster targets, our primary goal became the reliable generation and identification of high charge states

in various cluster species, in order to tackle Questions 1 and 3 above. That is, were previously published reports of Xe^{8+} at 33 eV photon energy and $\sim 10^{11}$ W/cm² accurate [51, 67], or were they, as alleged, evidence of experimental error [83]? Is it really possible to generate high charge states such as those seen in FEL experiments at our XUV frequencies, fluences, and intensities, and if so, what quantity of continuum lowering do the high charge states imply?

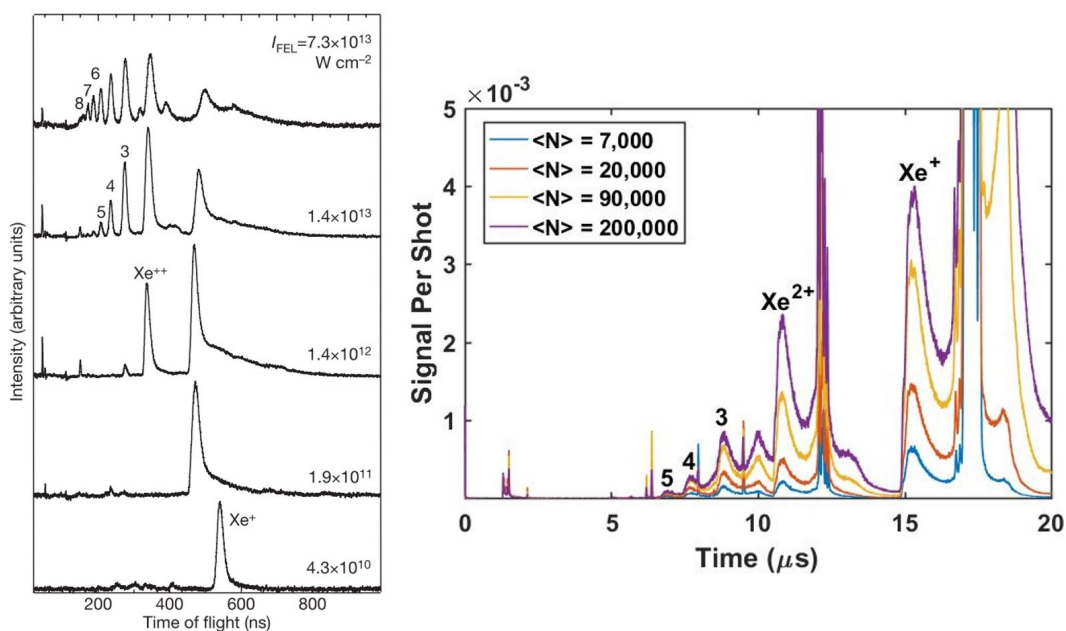


Figure 9.1: A comparison of xenon ion m/q time-of-flight spectra taken by Wabnitz et al. at a wide range of laser intensities (left) with similar data we took using the THOR XUV beamline at nearly 1×10^{13} W/cm² at different cluster sizes [96]. Although the Wabnitz experiment used 12.7 eV photons at a fluence of about 7 J/cm², while we used 33 eV photons at about 0.028 J/cm², the data sets are strikingly qualitatively similar at similar intensities.

As shown in Figure 9.1, our results do parallel those of a FEL (at 12.7 eV photon energies) at similar intensities. This is perhaps unexpected,

as although we achieve similar intensities to those commonly seen with a free electron laser, the fluences produced by a FEL are typically much higher (up to 7 J/cm^2 in the original work by Wabnitz, shown in Figure 9.1, compared to our 0.028 J/cm^2) [96]. Given that the physics we expect to observe is in the linear regime, we expect fluence to matter far more than intensity.

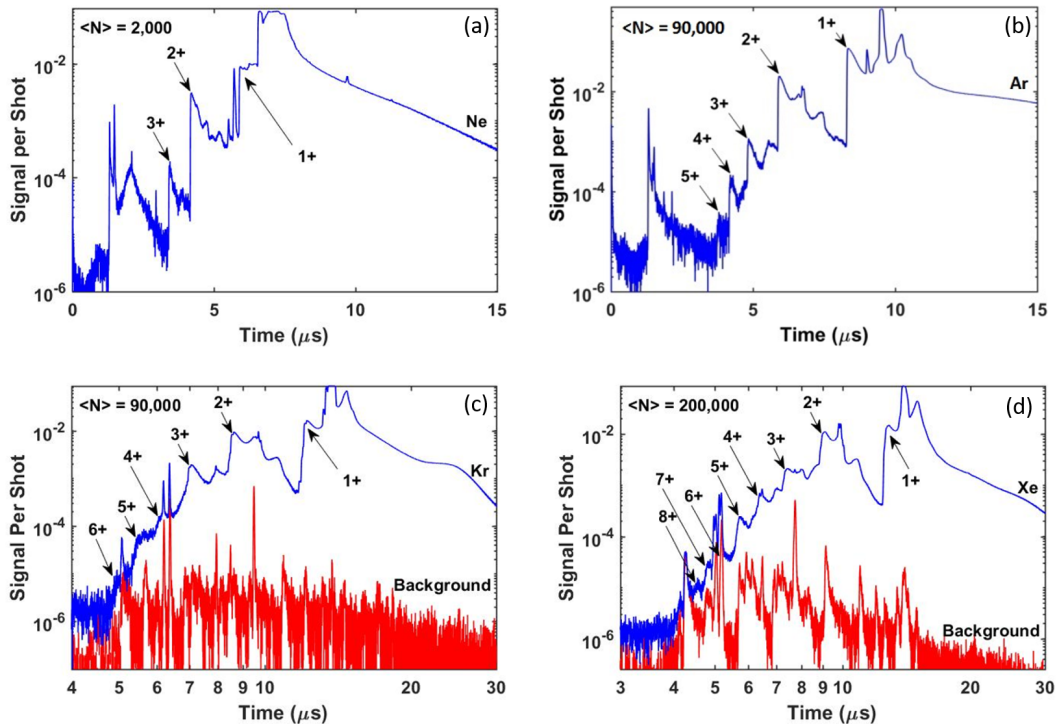


Figure 9.2: We observe high charge states, necessitating some amount of continuum lowering to produce, in each noble gas cluster species studied. Maximal observed charge states are (a) Ne^{3+} , (b) Ar^{5+} , (c) Kr^{6+} , and (d) Xe^{8+} .

When we look closely at the high charge states produced in each species, as shown in Figure 9.2 and in Section 8.2.2, we see a consistent pattern. The charge states observed in each species could not be generated via photoion-

ization or electron impact ionization by nonthermalized photoelectrons without significant amounts of ionization potential depression. Maximal observed charge states are Ne^{3+} , Ar^{5+} , Kr^{6+} , and Xe^{8+} , which would require an “instantaneous” input of 63, 75, 79, and 106 eV, respectively, to ionize isolated atoms from Ne^{2+} , Ar^{4+} , Kr^{5+} , and Xe^{7+} .

Each maximal observed charge state was unaffected by changes in cluster size or on-target fluence, which stands in stark contrast to the observations of Wabnitz and other researchers in this area. However, it is also true that our dynamic range for these factors was low. The maximum change in on-target fluence which we were able to achieve with sufficient signal-to-noise ratio was about a factor of two. Likewise, for easily-clustering gases such as Ar, Kr, and Xe, we found it difficult to produce clusters of fewer than 1,000 atoms (7-8 shells), whereas for neon, which is resistant to clustering, we had a difficult time making cluster sizes larger than 1,000 atoms. Still, the persistence of Ne^{3+} at cluster sizes of $\langle N \rangle = 200$ (4-5 shells) suggests a rapid onset of high density plasma-based continuum lowering at small cluster sizes.

9.3 Mechanism of Ionization

We can potentially explain these high charge states via a combination of factors related to the development of a dense plasma in our photon-dominated ionization regime. The process supported by the known physical mechanisms, as well as by our data, is as follows (Xe will be used as a representative model for a quantitative examination of the system):

1. Single photon photoionization removes an electron from the potential well of a few atoms (about 3% in Xe, using the gas-phase photoionization cross-section). The kinetic energy of the resulting electron is equal to $(h\nu - I_g)$, the difference between the photon energy and the band gap energy of the liquid-density species, if the electron is ejected near the center of the cluster. If the electron is ejected from an atom near to the surface of the cluster, the electron kinetic energy is likely at some intermediate value between $(h\nu - I_g)$ and $(h\nu - I_p)$, the difference between the photon energy and the ionization potential of an isolated atom. For a core atom in a xenon cluster, irradiated with the 21st harmonic, the electron would have 23 eV of kinetic energy.
2. The removal of an electron contributes to a form of barrier suppression, promoting ionization in neighboring atoms due to the new Coulombic potential well of the parent ion. In solid-density xenon, the maximal barrier between atoms, at half of the nearest neighbor distance of solid xenon (nearest neighbor distance 4.49 Å[48]) would be expected to be depressed by 6.40 eV, leaving an interatomic potential barrier of only 2.93 eV. This may also be expected to polarize nearby atoms.
3. Electron impact ionization, facilitated by the lowered potential barriers and the high electron impact ionization cross-section, ionizes neighboring atoms. The large electron elastic scattering cross-section leads to the free electrons remaining localized near their parent ions. We predict a

mean free path for elastic scattering in xenon of about 2 \AA , as shown in Figure 3.4, indicating that an electron would immediately be scattered by a nearest neighbor atom. The high electron impact ionization cross-section makes it likely that atoms close to the parent ion will be ionized first. In xenon, the mean free path for electron impact ionization by a $\sim 20 \text{ eV}$ electron is about 3 nm , or about every seven elastic collisions with nearby neutral atom.

4. A localized “metal-like” region of liquid density plasma with $Z^* = 1$ begins to form via a cascade of electron impact ionization, as described in Item 3 above. The resulting electron screening lowers the potential for both electron impact ionization and photoionization, while largely screening (and thus cancelling) the original barrier suppression.

As a consequence of electron screening, the cross-section for photoionization in these regions increases [97]. As shown in Figure 4.1, a xenon plasma with $Z^* = 1$ can depress the local continuum potential to facilitate direct photoionization up to Xe^{5+} , using the ion sphere model. If we allow for the possibility that a Xe^{5+} ion would attract at least three screening electrons to its vicinity, rather than the local average of one, the ion sphere model permits photoionization up to charge states of Xe^{6+} . This model of photoionization in a continuum-lowered plasma matches our observations of xenon charge state abundances very closely, as shown in Figure 9.3.

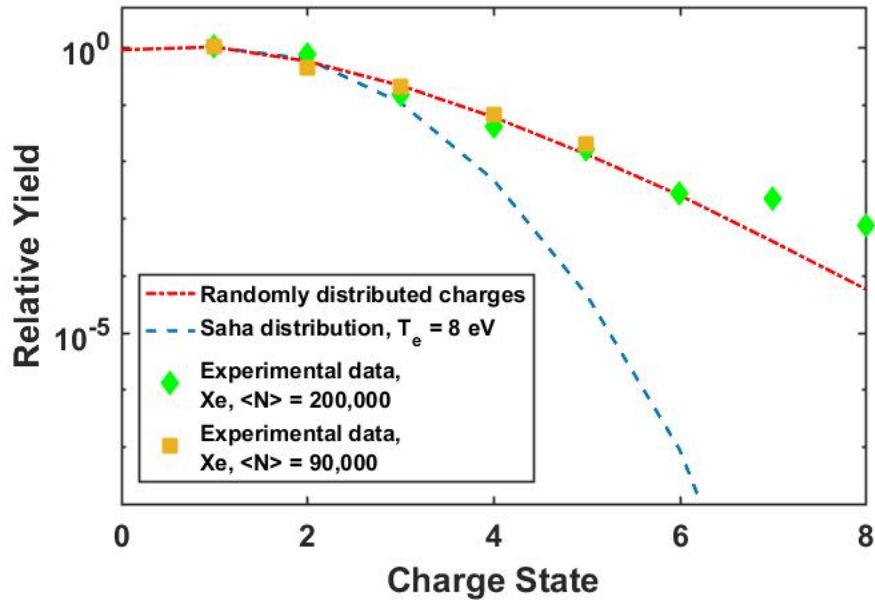


Figure 9.3: Charge state abundances, determined by the relative heights of forward-giong cluster peaks of different charge states for Xe ion m/q spectra, for cluster sizes of $\langle N \rangle = 90,000$ (gold squares) and $\langle N \rangle = 200,000$ (green diamonds). Two model fits for the yield ratios are also shown. The first model (red dot-dashed line) shows the result of a purely random distribution of “lost electrons” for an average ionization state of $Z^* = 1.1$, as might be expected if above-threshold single-photon ionization were dominant. The second model (blue dashed line) shows the results of a Saha distribution, with electron temperature of 8 eV and an average charge state of $Z^* = 1$.

The model shown with the red dot-dashed line in Figure 9.3 represents the random distribution of charge states given an average charge state of 1.1. This purely random distribution of “missing electrons” would be the expected result of sequential photoionization within a plasma with ionization potentials sufficiently lowered to allow photoionization to occur, as long as the cross-section for photoionization remained constant

with charge state, as is likely the case [98].

This photoionization model does not predict the abundances of charge states Xe^{7+} and Xe^{8+} as well as it does the lower charge states, suggesting that some new physical process may contribute disproportionately to these high charge states.

5. At larger cluster sizes, we see evidence of a greater contribution from electron impact ionization and recombination, as shown in Figure 9.4. These plots of charge state abundances for different cluster sizes appear to shift towards being more sharply peaked around charge state $2+$, with decreasing contributions from $1+$ and from the highest charge states, at larger cluster sizes.

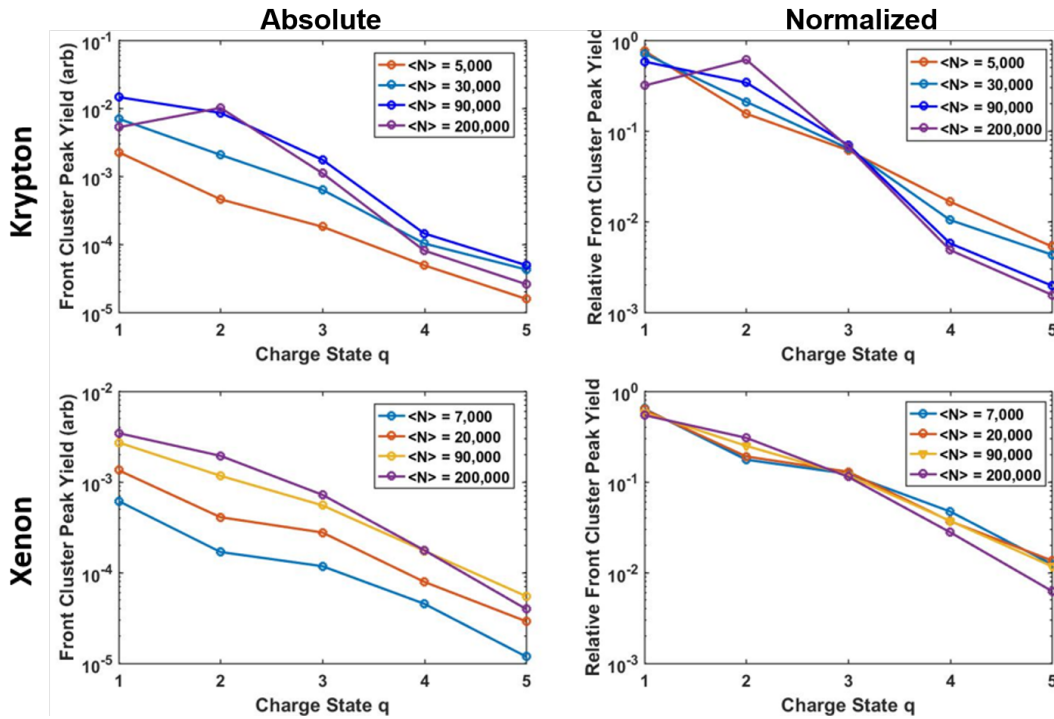


Figure 9.4: Absolute (left column) and relative (right column) yields of different charge states of krypton (top row) and xenon (bottom row), at different cluster sizes. These data correspond to ionization by the 21st harmonic.

9.4 Continuum Lowering

The high charge states observed for each cluster species, especially in abundances suggesting the facilitation of direct photoionization, would require large amounts of continuum lowering, from at least 30 eV in neon to at least 73 eV in xenon. This suggests that the ion sphere, Ecker Kröll, or spectroscopic IPD models, which each yield similar results in our plasma regimes, may be more accurate than the Stewart Pyatt model. These three models would predict sufficient continuum lowering to photoionize up to Xe^{6+} (and,

in fact, the SP model does so as well, if you assume that a Xe^{5+} ion attracts five screening electrons to its vicinity rather than its “equal share” of one, or the smaller assumption of three, as required by the IS model). However, we note that none of these available models provides sufficient ionization potential depression to allow for the direct photoionization from Xe^{6+} to Xe^{7+} or Xe^{7+} to Xe^{8+} . These charge states may be evidence of electron impact ionization by the hot tail of thermalizing electrons, or, more likely given their relatively high abundances, evidence of new physics, to be explored more fully in future experiments.

To assist in determining a more accurate model of continuum lowering in our dense plasmas, we attempted to pin down the exact amount of IPD using mirrors reflecting primarily the 17th, 19th, and 21st harmonic, at 26 eV, 29 eV, and 33 eV, respectively. Unfortunately, within the 6 eV span of our primary on-target photon energy, we were unable to discern any changes to the high charge state abundances which would allow us to place stricter limits on the amount of IPD present.

9.5 Cluster Dissociation

Previously published research suggests that ionic dissociation of large clusters is a multi-step process. Electron holes, generated primarily by photoionization, migrate preferentially to the surface of the cluster, creating a highly charged outer shell and a quasineutral inner core [91]. This highly charged outer layer or layers explodes Coulombically, leaving behind a neutral

plasma core to expand hydrodynamically, dragged outward at much longer time scales by the expansion of the hotter electrons [3, 82, 101]. The long time scales associated with this hydrodynamic expansion lead to significant amounts of electron impact ionization and recombination, the effects of which are nearly negligible in the outer shell, due to its shorter time scale for expansion, as well as the increased probability of electron impact ionization in the core (caused by a harmonic oscillator-like motion of hot electrons trapped in the Coulomb field of the charged cluster) [101]. Our data may lend support to these predicted processes.

The shape of the forward-going cluster peaks shown throughout Chapter 8, and more closely in Section 8.2.5, suggest that these features are primarily due to a Coulomb shell explosion, with kinetic energies of about 100 eV. In each atomic species, $E_q = qE_+$, that is, the kinetic energy of the q^{th} charge state is linear with q , as might be expected from a Coulomb expansion. A plot of kinetic energy of these forward-going peaks as a function of charge state for xenon clusters is shown in Figure 9.5.

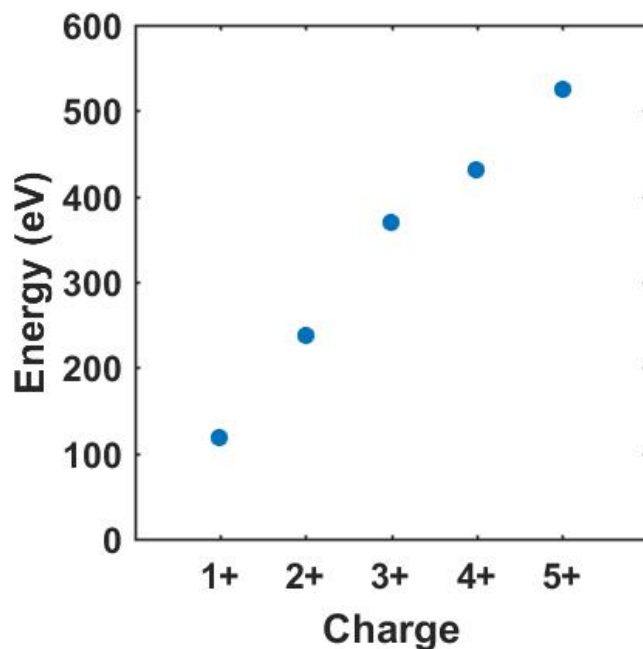


Figure 9.5: Calculated average kinetic energies of individual isotopes within the forward-going cluster peaks of xenon ion m/q spectra, at different charge states. These data correspond to ionization by the 21st harmonic

This may also explain why the charge state distributions, shown in Figure 9.4, so closely resemble photoionization-based distributions. Larger cluster sizes, higher ionization potentials (neon, argon or krypton, instead of xenon, for example) and lower photon energies (as shown in the distributions from the 17th harmonic data presented in Figure 9.6) seem to shift the distribution away from a purely random distribution to one which more closely resembles the results of electron impact ionization, as we might expect given the current models of cluster dissociation mechanisms.

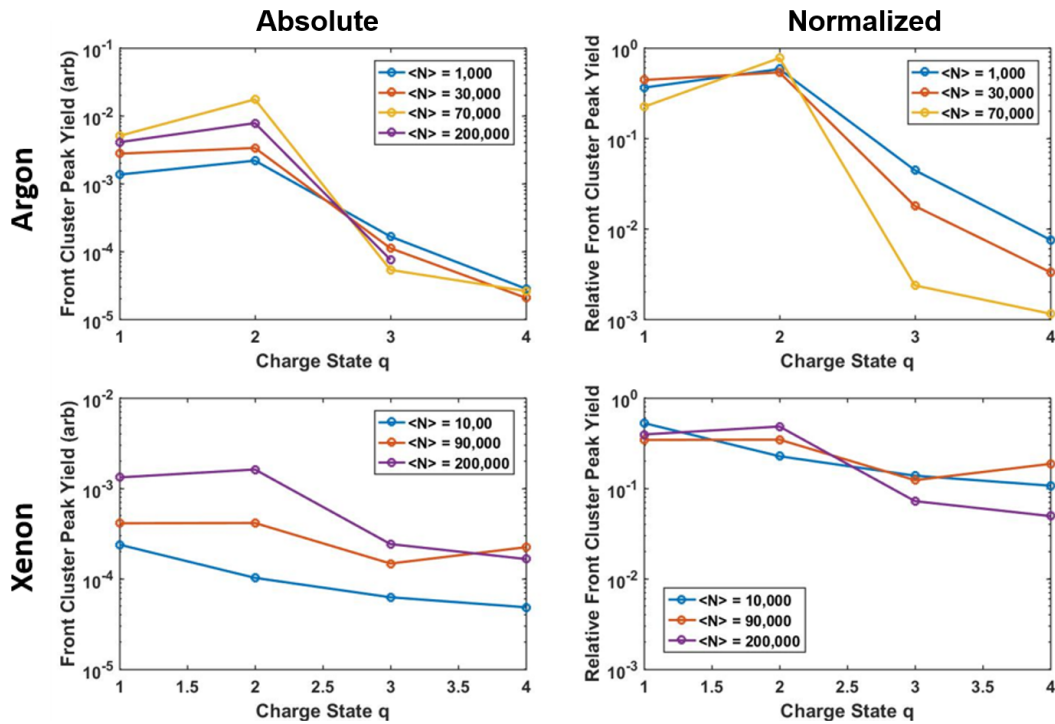


Figure 9.6: Absolute (left column) and relative (right column) yields of different charge states of argon (top row) and xenon (bottom row), at different cluster sizes. These data correspond to ionization by the 17th harmonic.

Ion kinetic energy spectra, shown in Section 8.2.6, with their multi-lobed profiles (rather than an amplitude uniformly decreasing with kinetic energy, as would indicate a hydrodynamic expansion), further support the view that the dominant source of ion signals at our detector are from Coulombic cluster expansion. It should be noted, however, that these kinetic energies from field-free drift measurements do not correspond to the calculated kinetic energies from our m/q spectra. Further experiments may be necessary to positively identify the physical mechanisms between these two types of signals.

9.6 Photoelectron Behavior

With the expectation of observing evidence of charge buildup on clusters, we examined the photoelectron spectra of each of our noble gas cluster species. While initial analyses of the resulting data seemed to show evidence of this mechanism, additional examinations and data collection revealed something altogether different, unexpected, and thus far unexplained. Examples of expected photoelectron spectra are shown in Figure 9.7.

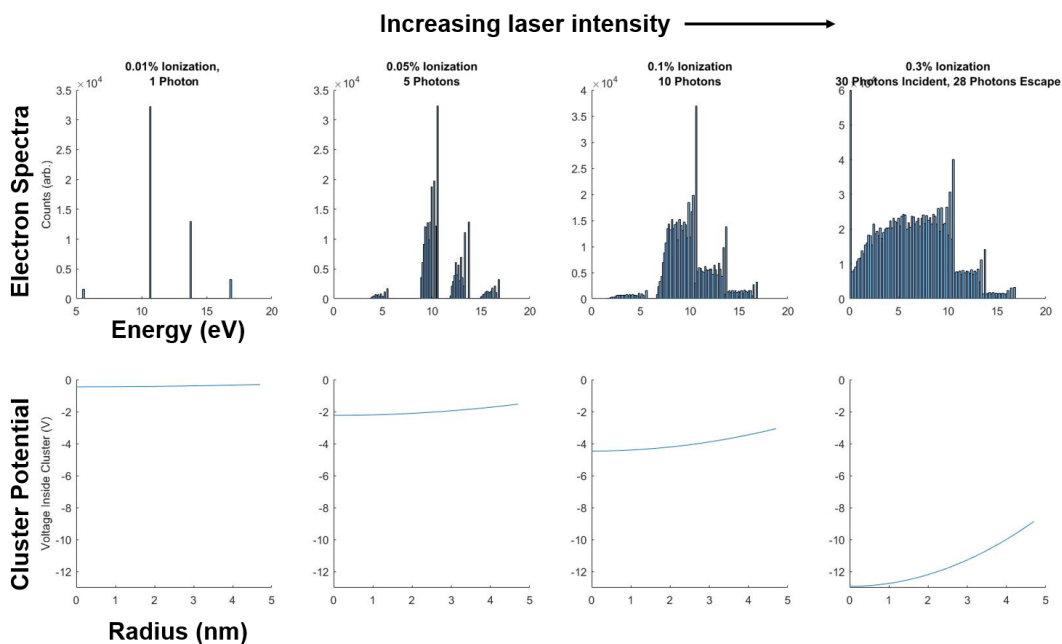


Figure 9.7: Simulated photoelectron kinetic energy spectra (top row) and the associated ultimate cluster potential as a function of radius (bottom row), resulting from different numbers of cluster photoionization events (columns left to right). Simulation is of an argon cluster of 10,000 atoms, irradiated with the expected incident photon spectrum reflected by our 21st harmonic mirror.

As shown in Section 8.2.7, rather than the photoelectron kinetic energy from each harmonic being extended into a plateau, we observed this behavior from low energy photoelectrons only. This decrease in amplitude, along with a growing plateau to lower energies, was affected by cluster size in argon and krypton. Experiments in neon showed the effect to be independent of on-target intensity, but attempts to tease out effects from cluster size and local gas density were inconclusive. Rather than being an effect of cluster charge buildup, it appeared instead to be a “filtering” mechanism, affecting photoelectrons below 10 eV kinetic energy, while leaving higher energy electrons unaffected. Since xenon 17th harmonic photoelectrons are ejected with energies of more than 10 eV, we were able to extract the incident photon spectrum from this data (this spectrum is used to create the simulations in Figure 9.7). Further research is needed to determine the physical mechanisms causing this electron behavior.

Chapter 10

Future Work

The results here yield many potential follow-up experiments which may further illuminate XUV-cluster dynamics. First, the disappointing results of our solid nano-clusters, such as silver, suggest exciting results if XUV fluence may be raised. Improving HHG generation conversion, perhaps to include longer interaction length with the generating medium, changing IR-XUV separation techniques, or boosting the initial IR laser energy may result in the desired on-target fluence which could overcome the high cohesive energy of solid targets. If this is not possible, adjusting the experiment to a pump-probe geometry, using the unconverted 30 fs 800 nm THOR laser as a pump, may allow experimenters to probe cluster explosion dynamics.

Using a wider range of harmonics to illuminate the target could also yield interesting results. This could be accomplished by, for example, utilizing helium instead of argon as the HHG-generating medium. A slightly higher range, spanning 50-100 eV, would allow researchers to observe the rising edge of the Xe $4d$ giant resonance. Ionization rates should be higher, and pinning down the onset of the resonance in the dense cluster/plasma medium would shed light on the effects of continuum lowering in XUV-generated plasmas.

Appendices

Appendix A

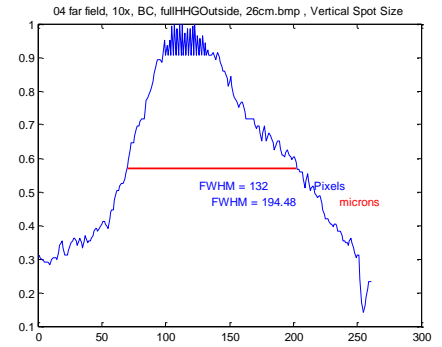
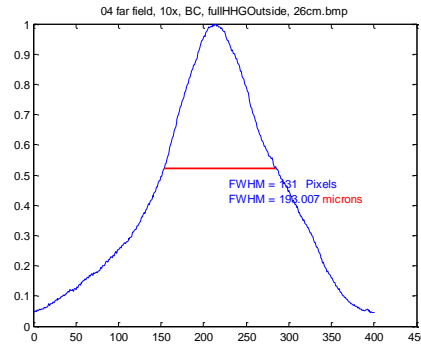
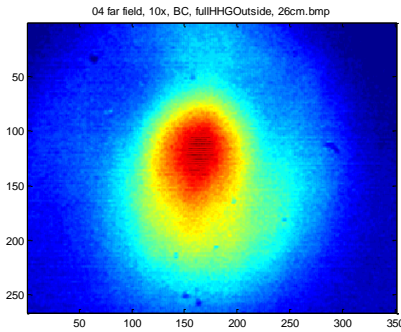
Far Field Analysis of the Astigmatic Beam Out of the THOR Compressor

The following is the full far field analysis done on the beam out of the THOR compressor, as focused by the HHG beamline long focus mirror. The labels above the images represent distances traveled backward by the camera as it moved through the focus of the beam. Two line focuses, at orthogonal angles, are visible. As we demonstrate in the section labeled “Blocking Parts of the Beam,” at the camera distance corresponding to the “circle of least confusion,” blocking the top half or the bottom half of the beam on input to the compressor removes one or the other of these line foci, suggesting wavefront aberrations in the beam. This document was produced in partnership with Dr. Ahmed Helal.

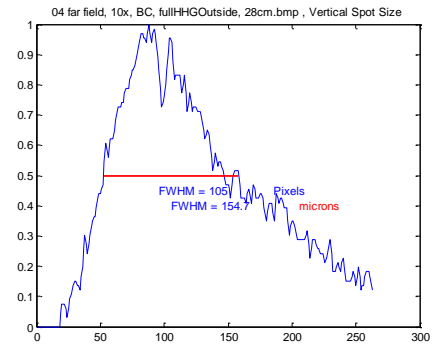
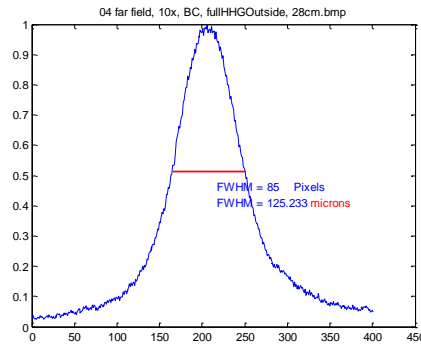
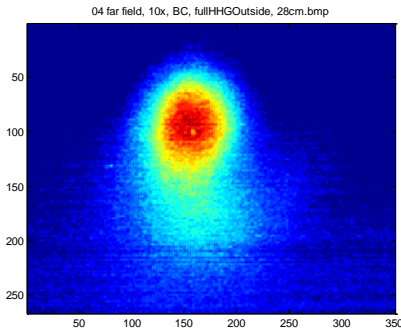
THOR –Far Field analysis 06/13/2014

1- Before the Compressor, we build the HHG line outside (with 10X microscope objective) 06/11/2014

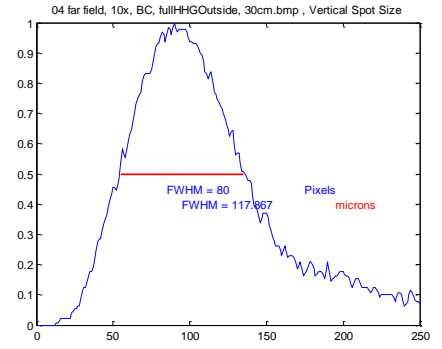
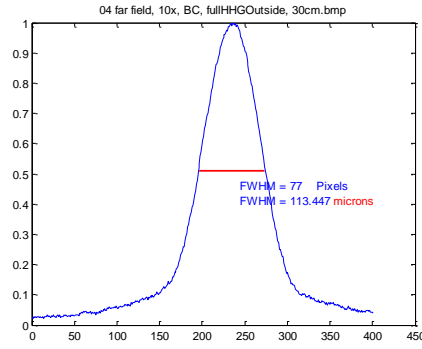
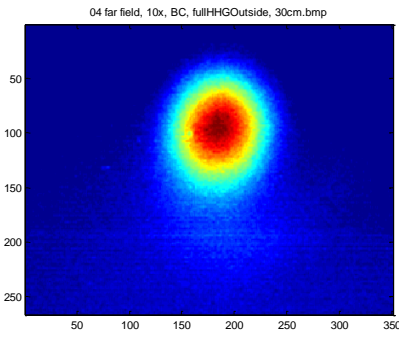
04 far field, 10x, BC, fullHHGOutside, 26cm



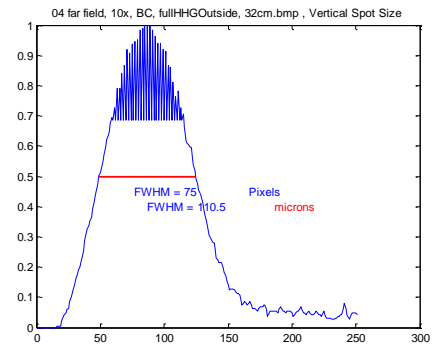
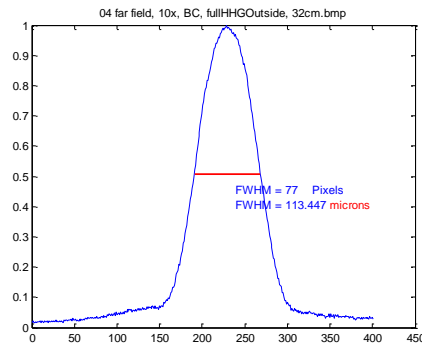
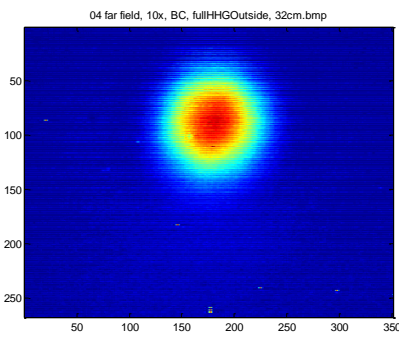
04 far field, 10x, BC, fullHHGOutside, 28cm



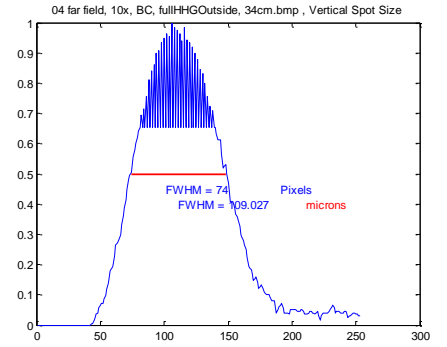
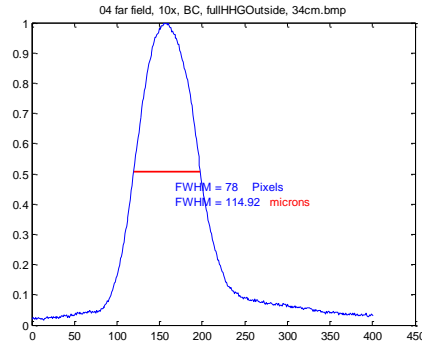
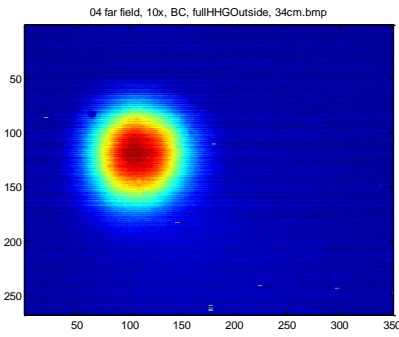
04 far field, 10x, BC, fullHHGOutside, 30cm



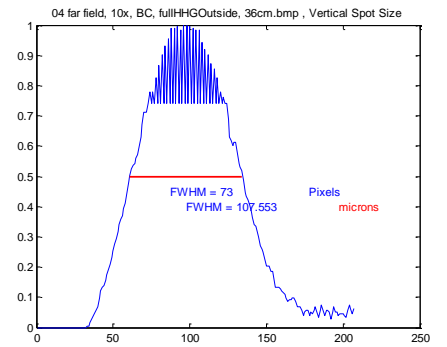
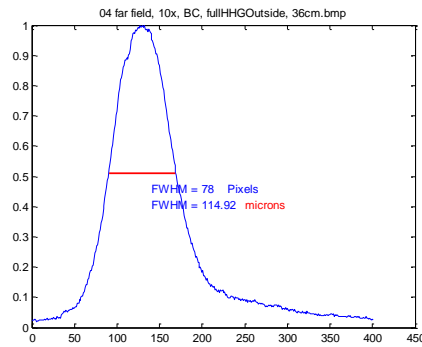
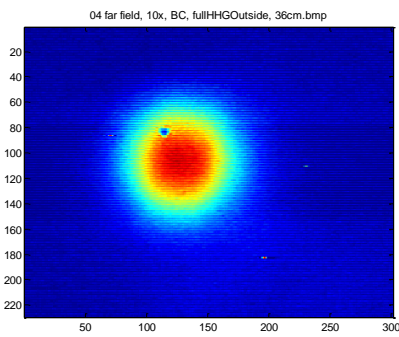
04 far field, 10x, BC, fullHHGOutside, 32cm



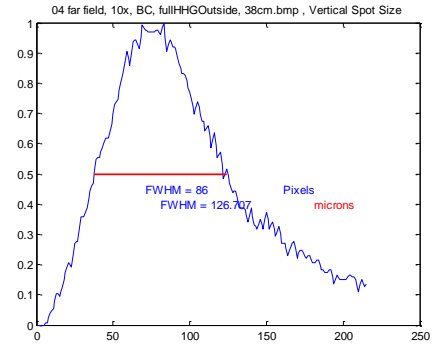
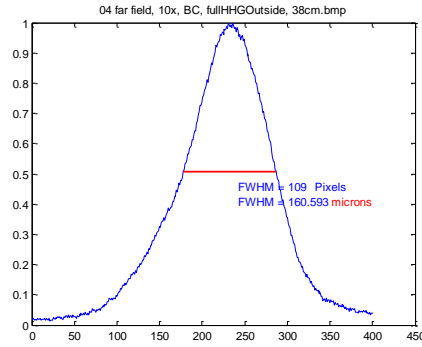
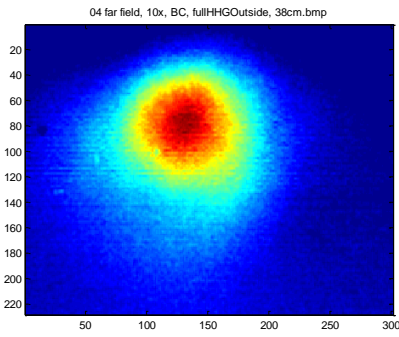
04 far field, 10x, BC, fullHHGOutside, 34cm



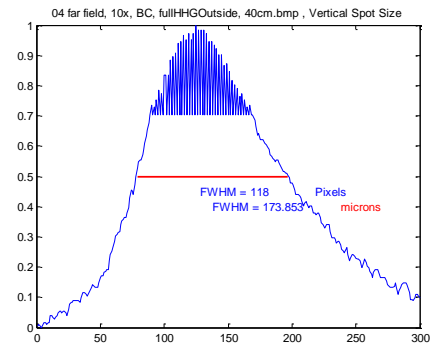
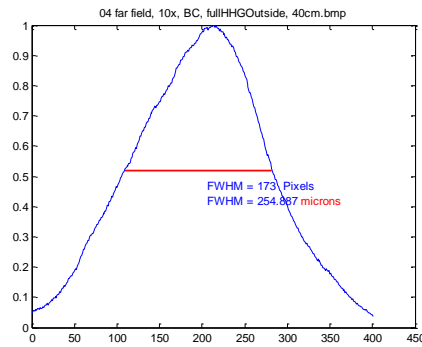
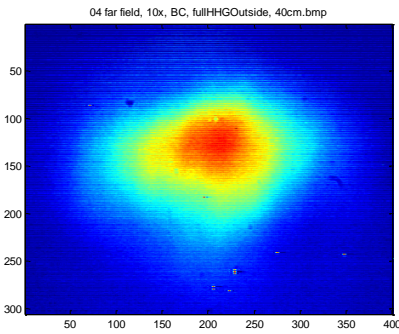
04 far field, 10x, BC, fullHHGOutside, 36cm



04 far field, 10x, BC, fullHHGOutside, 38cm

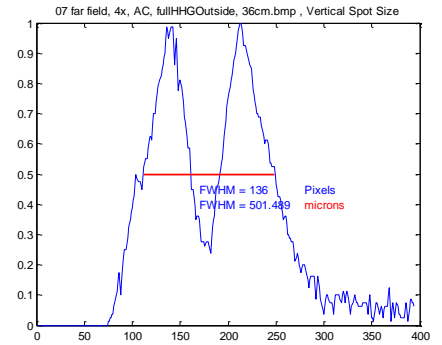
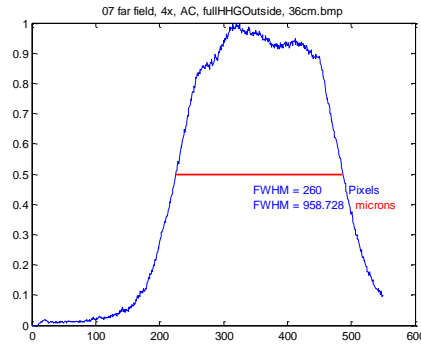
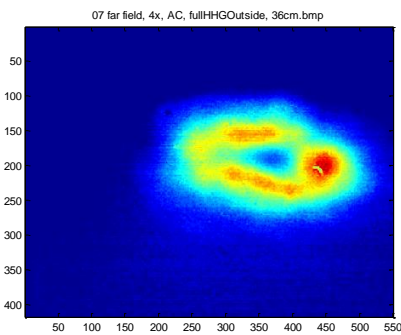


04 far field, 10x, BC, fullHHGOutside, 40cm

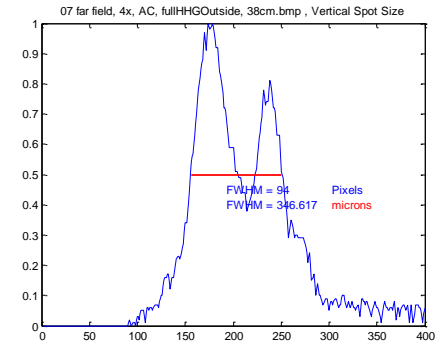
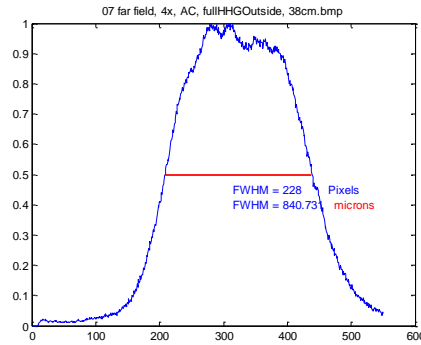
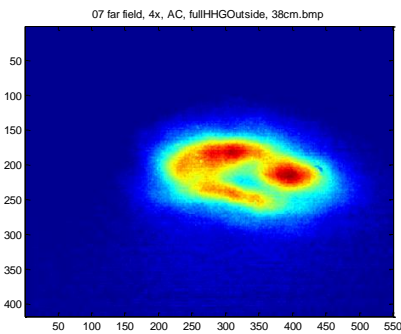


2- After the Compressor, we build the HHG line outside (with 4X microscope objective) 06/11/2014, Setup did not change from the previous one especially the camera position and the focusing mirror.

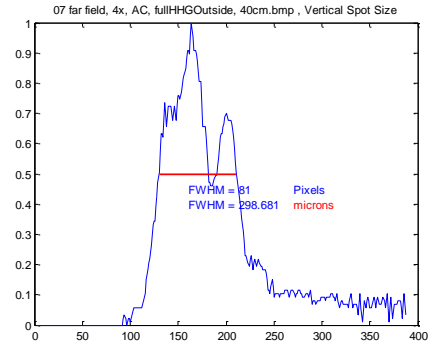
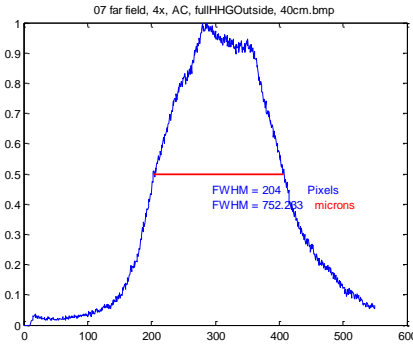
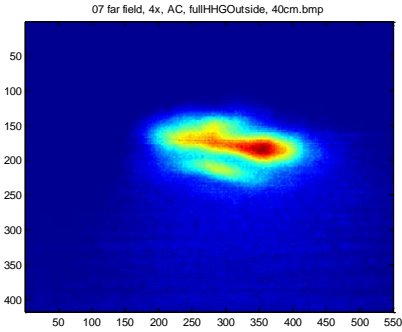
07 far field, 4x, AC, fullHHGOutside, 36cm



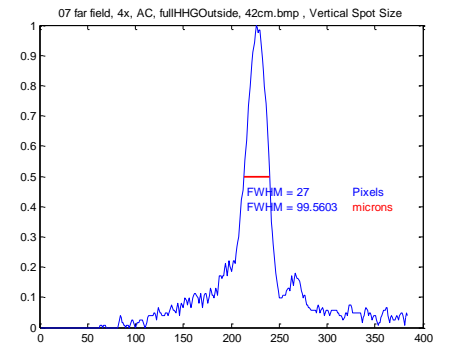
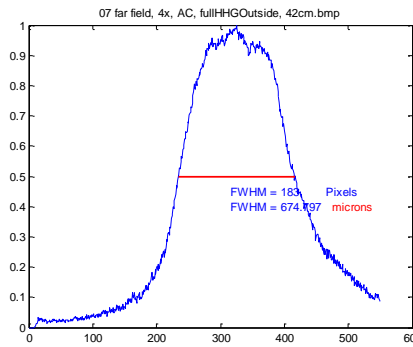
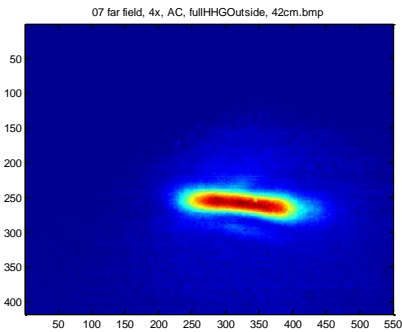
07 far field, 4x, AC, fullHHGOutside, 38cm



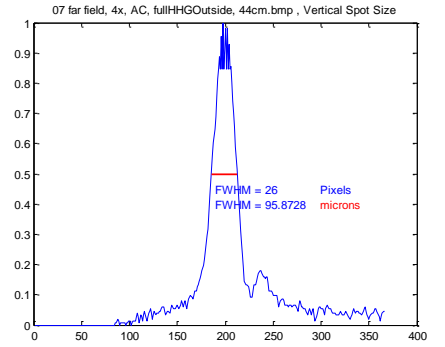
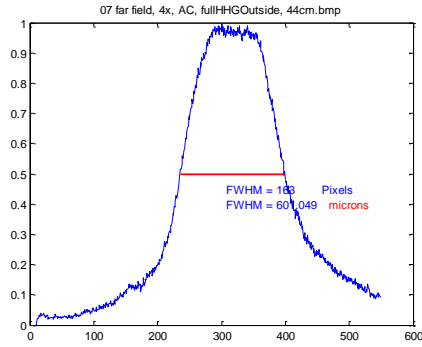
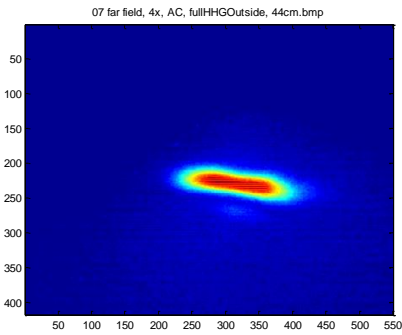
07 far field, 4x, AC, fullHHGOutside, 40cm



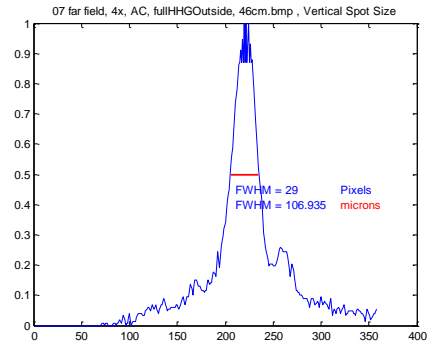
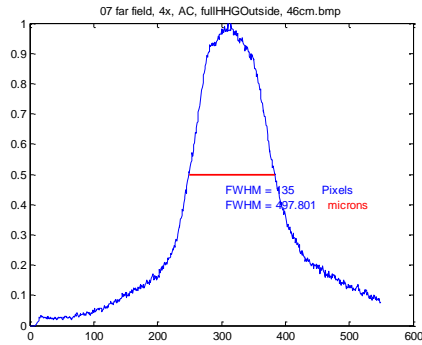
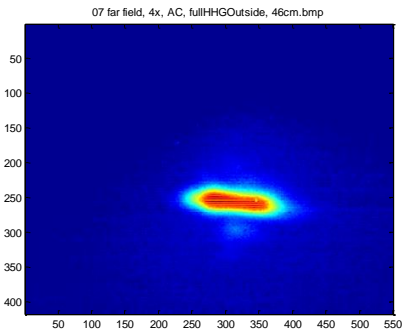
07 far field, 4x, AC, fullHHGOutside, 42cm



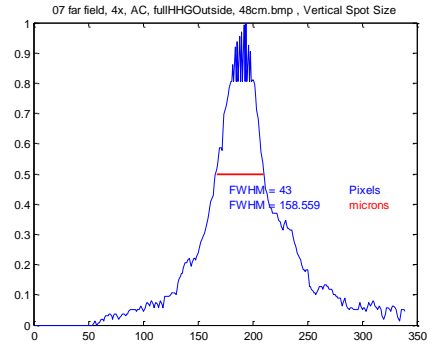
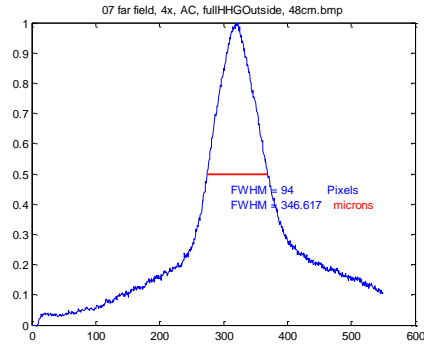
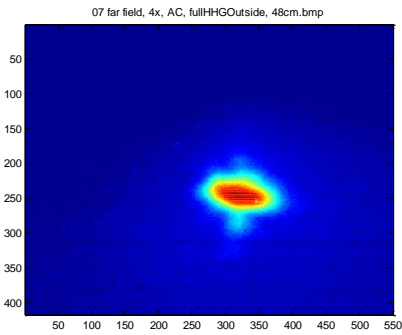
07 far field, 4x, AC, fullHHGOutside, 44cm



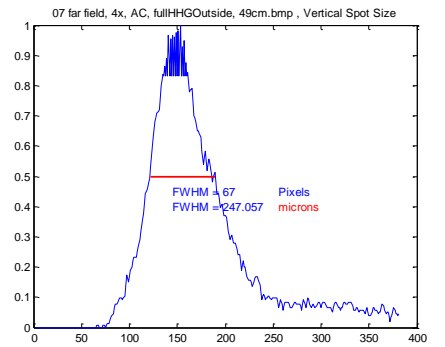
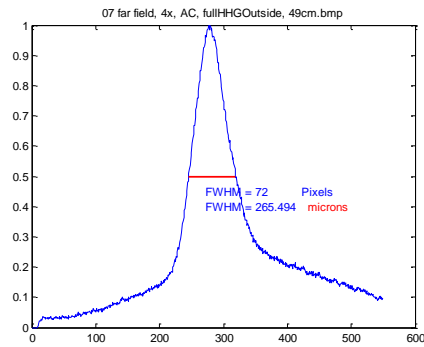
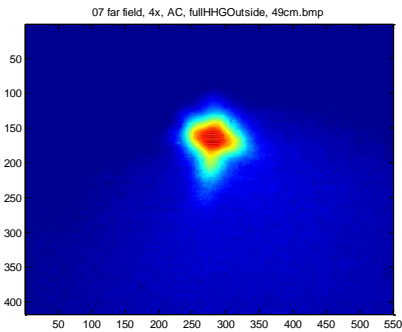
07 far field, 4x, AC, fullHHGOutside, 46cm



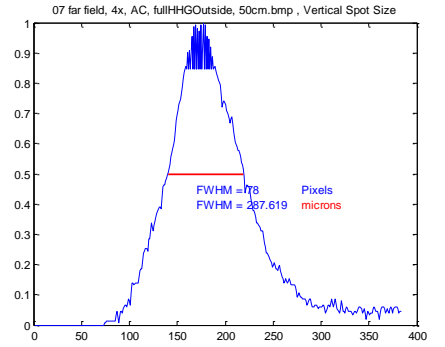
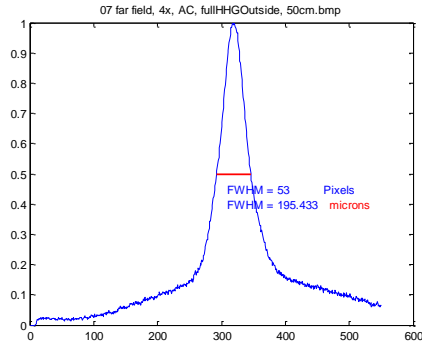
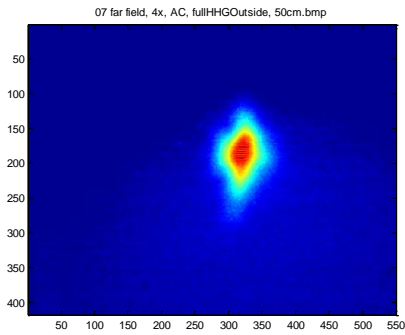
07 far field, 4x, AC, fullHHGOutside, 48cm



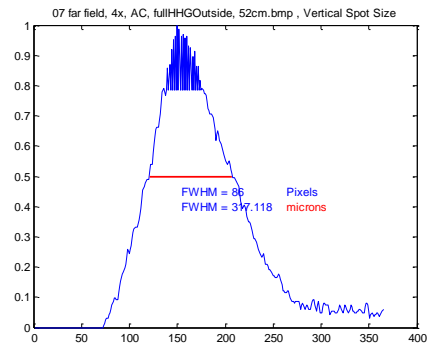
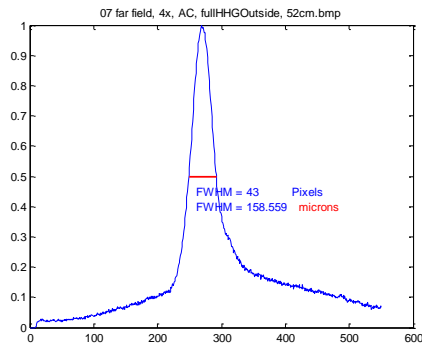
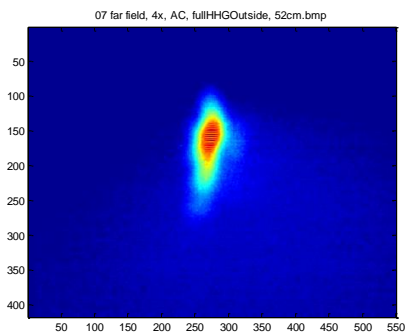
07 far field, 4x, AC, fullHHGOutside, 49cm



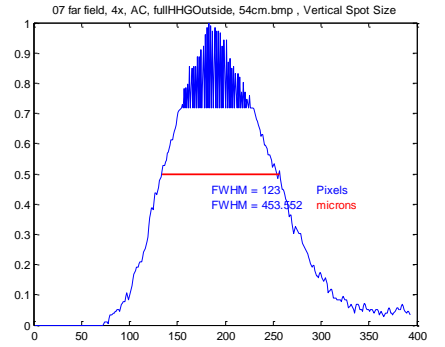
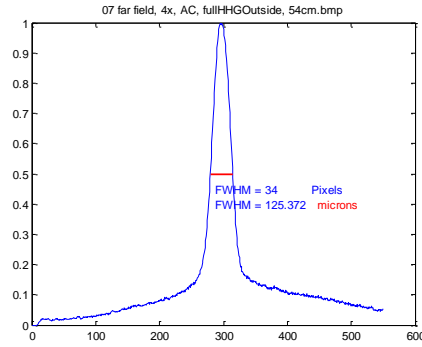
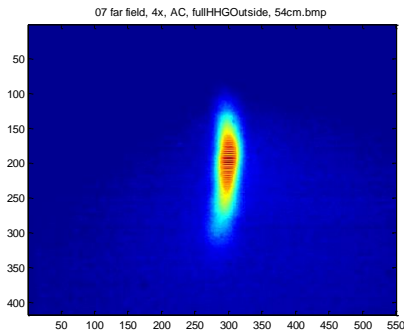
07 far field, 4x, AC, fullHHGOutside, 50cm



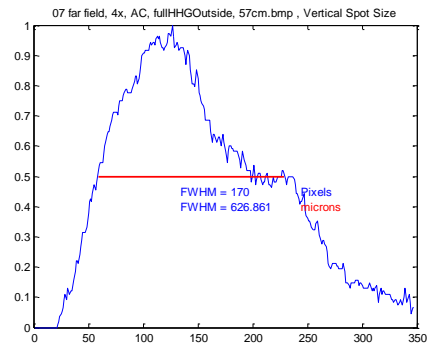
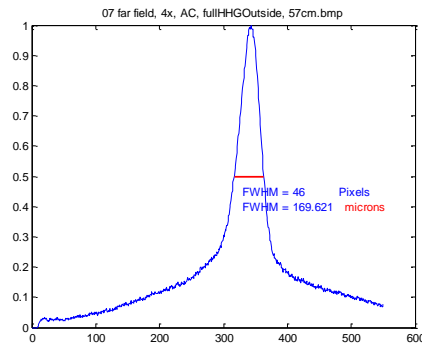
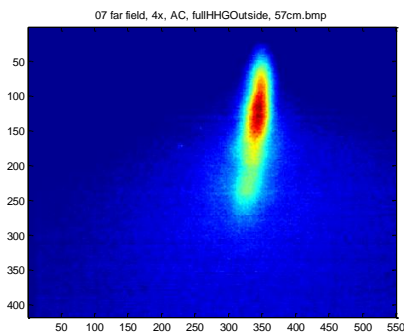
07 far field, 4x, AC, fullHHGOutside, 52cm



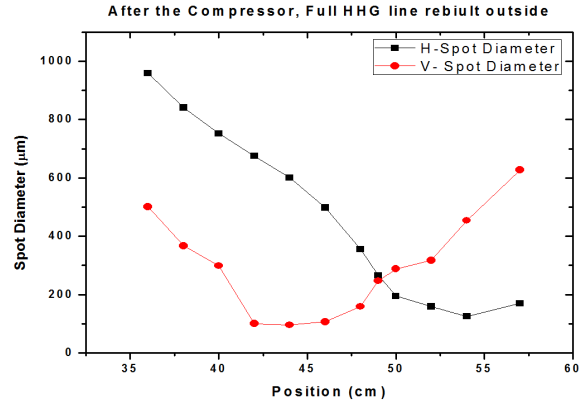
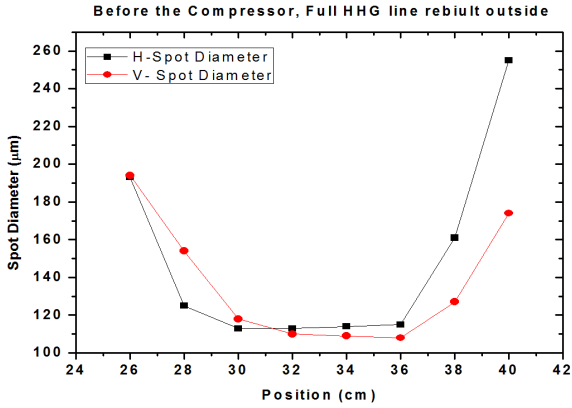
07 far field, 4x, AC, fullHHGOutside, 54cm



07 far field, 4x, AC, fullHHGOutside, 57cm



Full Comparizon shows the change of the focus before and after the THOR-Compressor



Best focus:

Before the Compressor at: nearly 33 cm

After the compressor at: 49 cm

the focus shifts about = 16 cm

Size of best focus:

Before the Compressor: Horizontal = 113 microns

vertical= 110 microns

After the compressor at: Horizontal = 266 microns

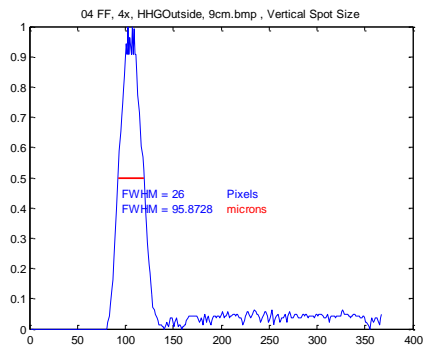
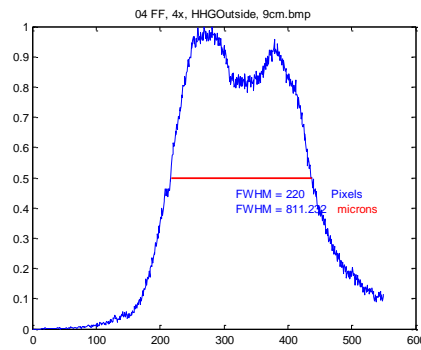
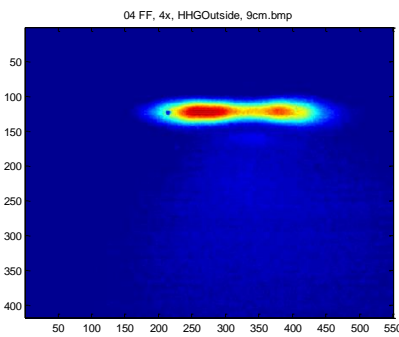
vertical= 247 microns

Horizontal focus= 125 microns

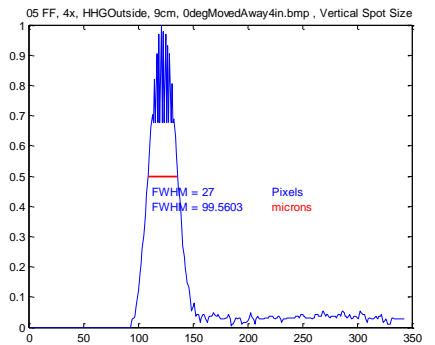
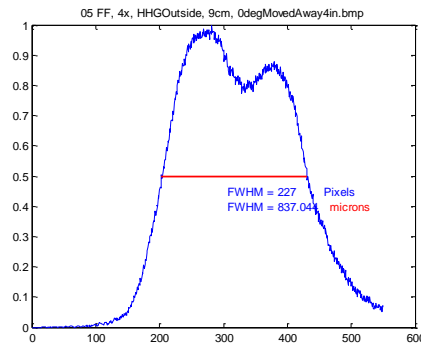
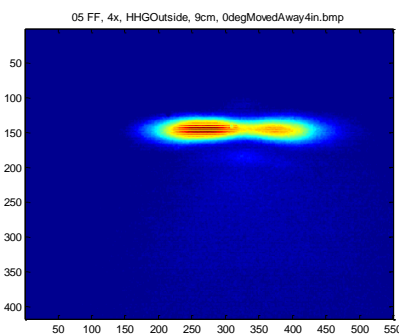
vertical focus = 96 microns

3- After the Compressor, we build the HHG line outside (with 4X microscope objective) 06/13/2014, Tweaking the separation of the zero degree mirror to introduce a larger angle than it should be in the main HHG line.

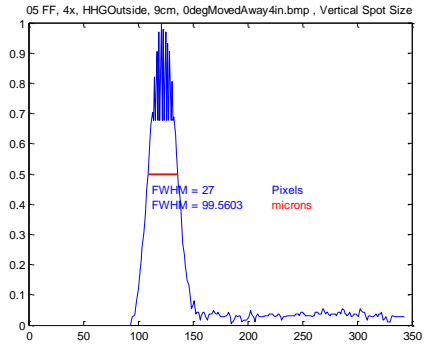
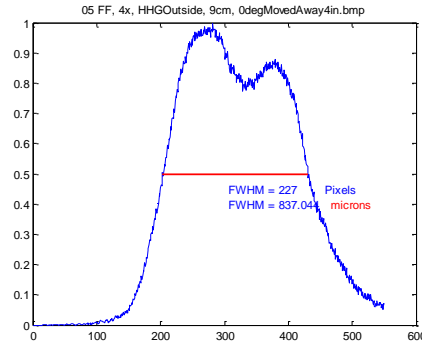
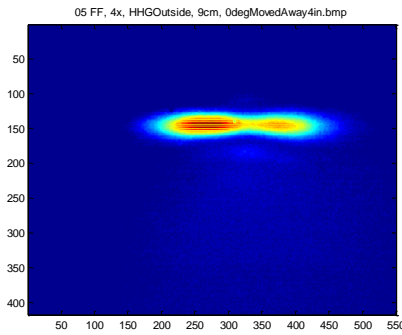
04 FF, 4x, HHGOutside, 9cm



05 FF, 4x, HHGOutside, 9cm, 0degMovedAway4in

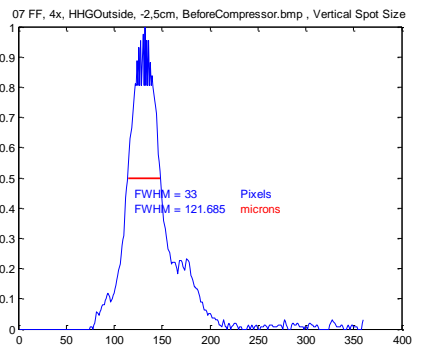
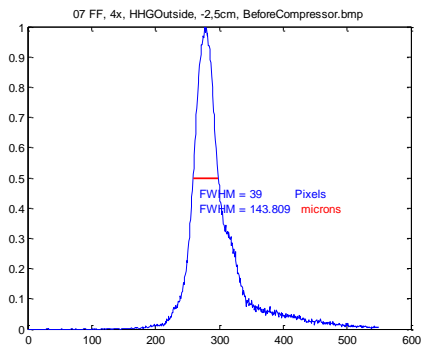
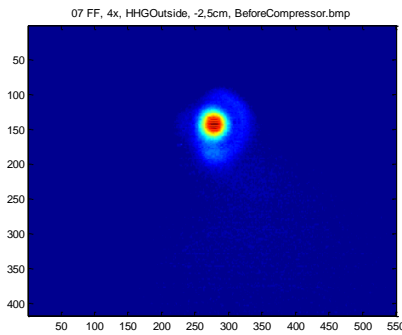


06 FF, 4x, HHGOutside, 9cm, 0degAnd45degMovedOpposite9in

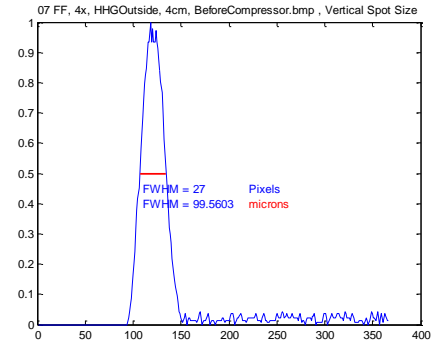
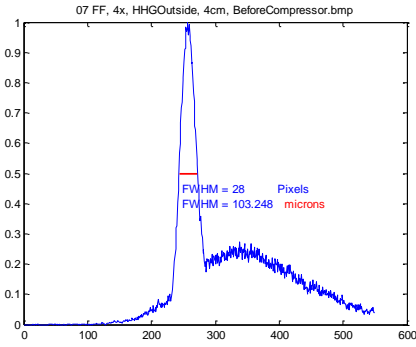
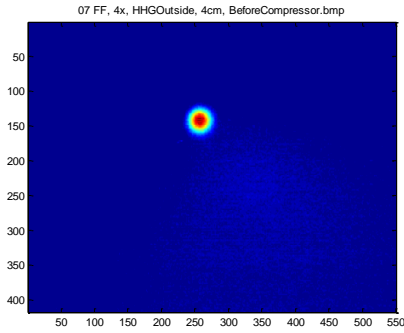


4- Again before the Compressor, (with 4X and 10Xmicroscope objective) 06/13/2014, to check if we have astigmatic beam or not.

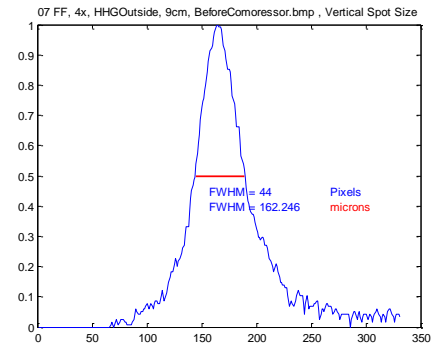
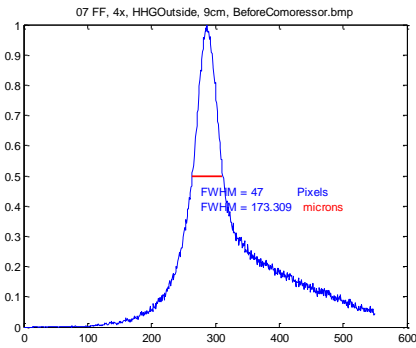
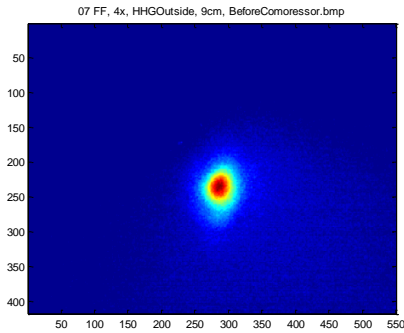
07 FF, 4x, HHGOutside, -2,5cm, BeforeCompressor



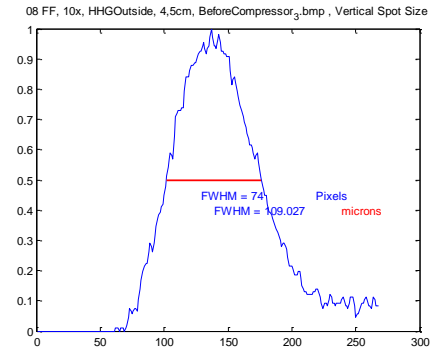
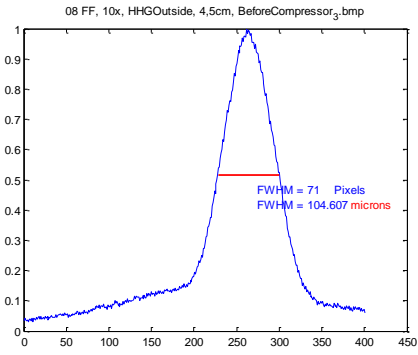
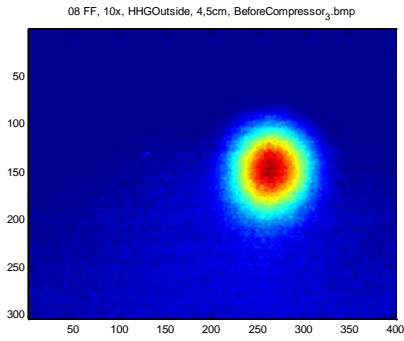
07 FF, 4x, HHGOutside, 4cm, BeforeCompressor



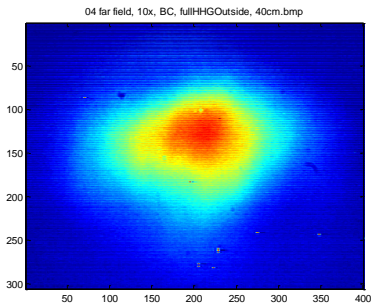
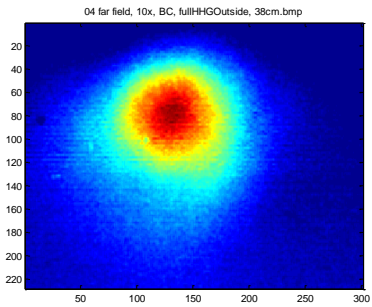
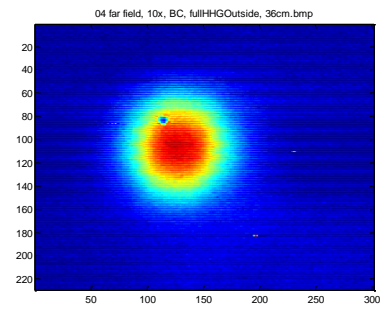
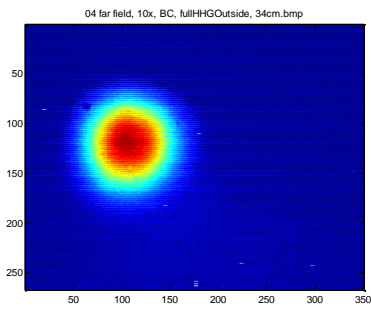
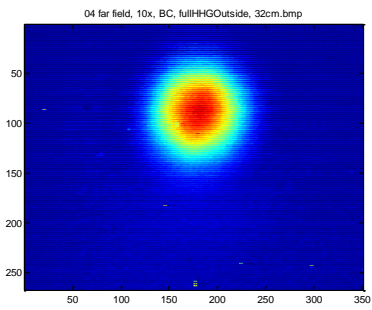
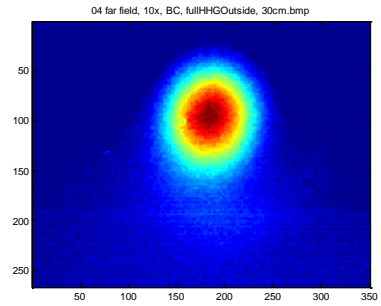
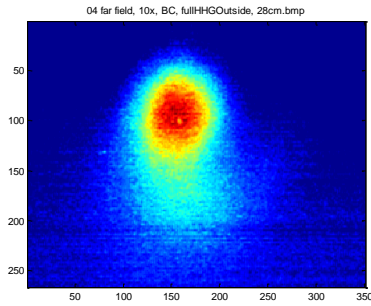
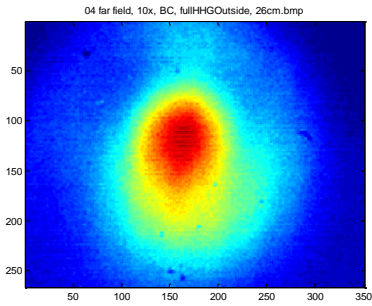
07 FF, 4x, HHGOutside, 9cm, BeforeCompressor



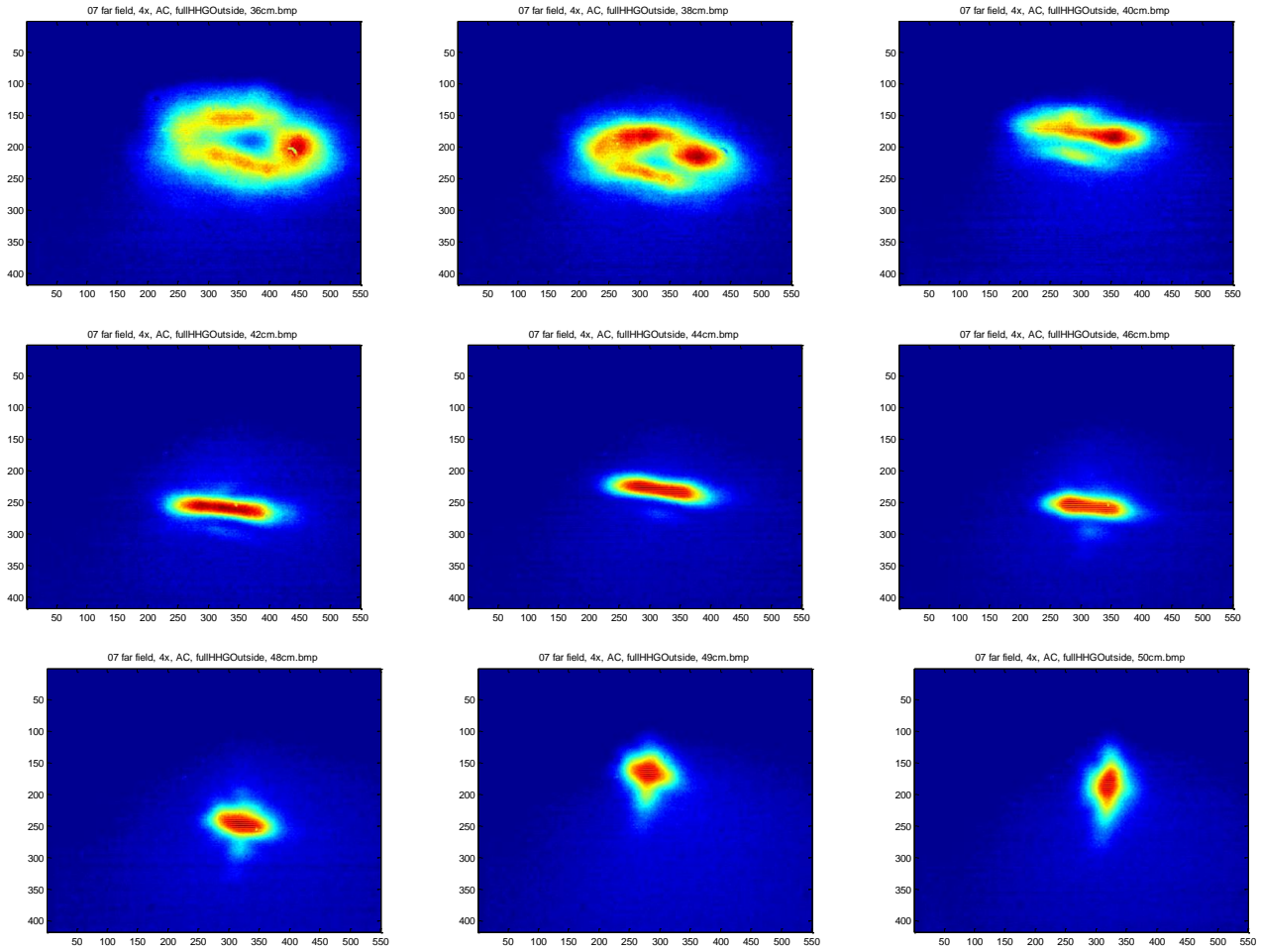
08 FF, 10x, HHGOutside, 4,5cm, BeforeCompressor_3



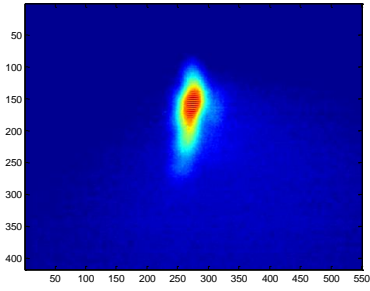
Before the Compressor, Using the Full HHG-line rebuilt outside.



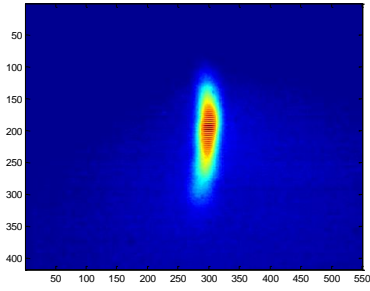
After the Compressor, Using the Full HHG-line rebuilt outside.



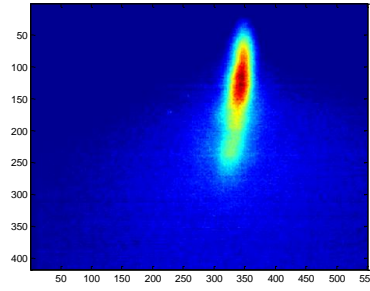
07 far field, 4x, AC, fullHGOoutside, 52cm.bmp



07 far field, 4x, AC, fullHGOoutside, 54cm.bmp



07 far field, 4x, AC, fullHGOoutside, 57cm.bmp



Appendix B

Standard Operating Procedure for LAM Nanoparticle Generator

The following is the Standard Operating Procedure (SOP) generated for the safe operation of the Laser Ablation of Microparticles (LAM) Nanoparticle Generator, used with the THOR XUV target chamber. This document was generated in partnership with the CHEDS research staff.

Standard Operating Procedure

Laser Ablation of Microparticles (LAM) Nanoparticle Generator

THOR Lab Operations

Center for High Energy Density Science
University of Texas at Austin



Prepared by: Aaron Bernstein, Hernan Quevedo, Sandi Bruce, Ahmed Helal, Thanh Ha.

Standard Operating Procedure for Laser-Ablation of Microparticles (LAM) Nanoparticle Generator

Name	Signature	Date
John Keto		
Aaron Bernstein		
Hernan Quevedo		
Sandi Bruce		
Ahmed Helal		
Thanh Ha		

LAM Operators:

Name	Signature	Date
Hernan Quevedo		
Sandi Bruce		
Ahmed Helal		
Thanh Ha		

Approved by:

Todd Ditmire:

John Keto:

Aaron Bernstein:

1. Contents

2.	Introduction:	1
3.	Hazards:	1
3.1.	Laser Optical Hazards:	1
3.1.1.	Ablation Laser:	1
3.1.2.	HeNe Used for Scattering Measurements:	1
3.1.3.	Class 3R Laser Pointers:	1
3.2.	Particle Hazards:	1
3.2.1.	Particle Generation:	1
3.2.2.	Inhalation Hazards:	3
3.2.3.	Eye and Skin Hazards:	4
4.	Safety Controls:	4
4.1.	Personal Protective Equipment:	4
4.1.1.	Respirator:	4
4.1.2.	Nitrile Gloves:	5
4.1.3.	Lab Coats:	5
4.1.4.	Goggles:	5
4.2.	Engineering Controls:	6
4.2.1.	Vacuum Exhaust:	6
4.2.2.	Particle Detector:	7
4.2.3.	Emergency Spill Kit:	7
5.	Safe Operating Protocols:	8
5.1.	Designated Work Area:	8
5.2.	Signage and Operation Modes:	8
5.2.1.	“In Use” Mode:	8
5.2.2.	“Maintenance/Filling” Mode:	8
5.2.3.	“Spill” Mode:	9
5.3.	Labeling:	9
5.4.	Disposal of Contaminated Materials:	9
5.5.	Approved Materials and Material Storage:	10
6.	LAM Description and Operating Principles:	10
7.	Protocol for Changing Operating Modes:	13
7.1.	“In Use” Mode:	13
7.2.	“Maintenance/Filling” Mode:	13

Standard Operating Procedure for Laser-Ablation of Microparticles (LAM) Nanoparticle Generator

7.3.	“Spill” Mode:	14
8.	Standard Operating Procedure:	14
8.1.	LAM Testing:	14
8.1.1.	Procedure for LAM Ablation Testing:.....	14
8.1.2.	To Shut Down:.....	17
8.1.3.	Procedure for Collecting Nanoparticle Samples :	17
8.2.	LAM Experimental Operations:.....	18
9.	Emergency Procedures:	21
9.1.	Emergency Shutdown of the LAM:	21
9.2.	Spill Incident Instructions:.....	21
10.	Maintenance:	23
10.1.	HEPA Filters:.....	23
10.2.	Cleaning the Apparatus:.....	23
10.3.	Filling the LAM Microparticle Bed:.....	24
10.3.1.	Procedure for Filling the Particle Bed:	24
11.	Appendix A:.....	27
11.1.1.	Quick-Installation Instructions for Sierra Instruments Mass-Trak 810 Controllers:	27

Standard Operating Procedure for the LAM Nanoparticle Generator

2. Introduction:

This document outlines procedures for safe operation of the Laser Ablation of Microparticles (LAM) apparatus in RLM 12.210. To qualify to be present in the THOR lab during normal LAM operation, an on-site operational and safety briefing must be performed, and Sections [1-6] of this document must be read and signed. To qualify as a LAM Operator, a more thorough on-site safety briefing must be performed, and the entire following document must be read and signed. Additionally, all Operators must have their own 3M 7500 series respirator, professionally fit-tested (See Section [4.1.1] for further information). Proper performance of these procedures is mandatory to be a qualified THOR user during LAM operations. While it is our goal to provide engineered controls to physically limit the possibility of accident, these cannot ensure by themselves a completely safe environment. Personnel and visitors must therefore adhere to safe standard operational procedures.

It is expected that everybody in the lab is concerned for each other's safety, *however* each person is ultimately responsible for their own safety. If any worker in the lab has a concern regarding safety, that worker is qualified to safely halt work until such time that there is no cause for concern.

3. Hazards:

3.1. Laser Optical Hazards:

Standard operation mode goggle procedures apply. See THOR Laser Standard Operating Procedure for details. All Operators of this laser must have followed the procedure for becoming a qualified laser user in the THOR lab.

3.1.1. Ablation Laser:

The Quanta-Ray GCR is a frequency-doubled YAG laser. It is a Class 4 laser, outputting a maximum of 500 mJ per pulse at 532 nm when Q-switched, at a repetition rate of 10 Hz. It optionally has the capability of outputting 1 J per pulse at 1064 nm. When used as the ablation laser in the LAM setup, it will operate at 532 nm.

The GCR will be focused into a stream of microparticles in order to ablate them to nanoparticles. This involves the laser entering a glass tube, which imparts a curvature to the reflected beam wavefront, essentially reflecting that wave backward and forward over a range of angles. This reflected light must be blocked, and follow procedures for operating the laser consistent with the THOR Laser SOP protocol. Furthermore, when the LAM is attached to the main target chamber, the laser beam will have to be routed to a level above the chamber, focused into the microparticle stream, and blocked.

3.1.2. HeNe Used for Scattering Measurements:

In order to determine the size of the nanoparticles generated with the LAM method, a HeNe will be routed into the vacuum chamber, beneath the supersonic nozzle at the exit of the ablation cell. This laser operates continuously (not pulsed) at a wavelength of 633 nm, and 17 mW power, making it a Class 3B laser. For initial alignment, this laser will be attenuated by ND filters to achieve an effective Class I laser. During normal operation, the ND filters will be removed, and all scatter from the vacuum chamber windows, as well as all residual (unscattered) beam will be blocked.

3.1.3. Class 3R Laser Pointers:

In order to visually observe microparticle and nanoparticle flow in the LAM system, Class 3R laser pointers will be employed. Care should be taken to ensure eye hazard from direct or reflected beams.

3.2. Particle Hazards:

3.2.1. Particle Generation:

It is important to note that individual particles are not readily visible if they are less than 150 microns in size! As such, it is impossible to visually determine whether you are inhaling small quantities of these particles.

While the equipment and procedures in this document are designed to minimize exposure levels, the LAM may still produce airborne nano- and microparticles during normal operations. In this SOP we adopt the usual convention of defining nanoparticles as those <100 nm in size. Figure 1 shows common sources of inhalation hazards. In this experiment it is possible to produce inhalation hazards that span this entire range and the filtration range of HEPA and ULPA filters. Figure 2 shows the results of an experimental determination of the effectiveness of these common filters on even smaller nanoparticles.

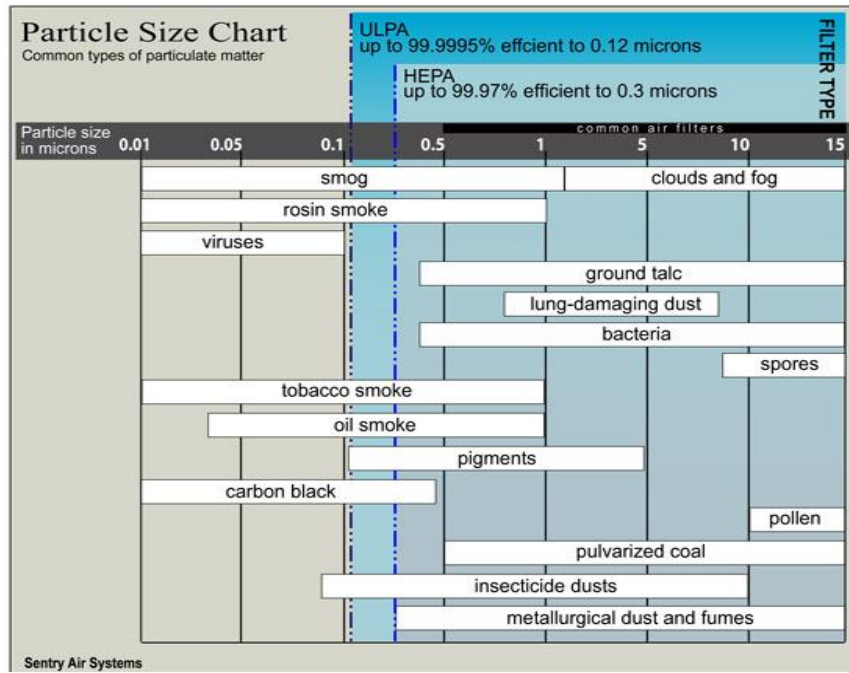


Figure 1: Rated filter effectiveness on different particle sizes.¹ Nanoparticles generated by the LAM are at the leftmost of this scale (0.01 microns). It is worth noting that some filters do become effective again at the very low range of 10s of nanometers.

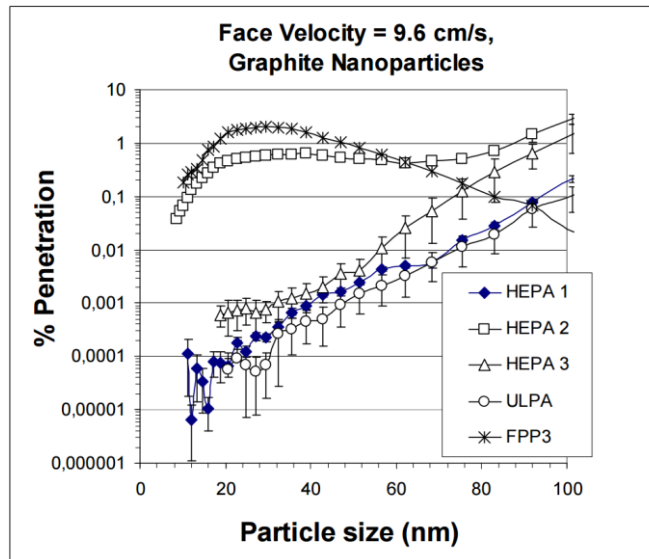


Figure 2: Experimentally determined filter effectiveness on different particle sizes of graphite nanoparticles.²

¹ Reproduced from <http://www.sentryair.com/hepa-filter.htm>

² Golanski, L., A. Guiot, and F. Tardif [2008]. "Experimental evaluation of personal protection devices against graphite nanoaerosols: fibrous filter media, masks and protective clothing."

Nano-science is a burgeoning field with many workers. Despite this, there is still a lack of knowledge regarding effects of nanoparticles on the human body. Currently, higher rates of lung cancer are considered a ubiquitous feature among those exposed to significant levels of nanoparticles, irrespective of their material makeup. See "Occupational Exposure to Titanium Dioxide", currently at <http://www.cdc.gov/niosh/docs/2011-160/pdfs/2011-160.pdf>.

Most of the studies of nanoparticles' effect on health have been performed on TiO₂. The results of a variety of inhalation studies have indicated that toxicity is directly related to the overall surface area of the particles introduced into the lungs. Therefore, on a per-mass basis, microparticles are considered less toxic than nanoparticles. To mitigate risks in the face of incomplete understanding of the health risks of nano- and micro-particles, nano-technology workers have leveraged the existing safety systems and protocols developed for toxic chemical work, including the use of fume hoods and personal protective equipment such as gloves and masks.

In the absence of protocols developed for each material, we adopt conclusions from guidelines developed over the years for nanometer-sized TiO₂, which is considered a poorly soluble, low toxicity substance. These operations are approved for the research materials specified in Section [5.5]. Materials currently approved for research are, similarly to TiO₂, considered low-toxicity materials in bulk samples. Introducing additional materials must be approved.

In other labs, nanoparticle research is usually performed in solution and under fume-hoods. Both of these factors mitigate exposure risk. In this lab, we do not operate under an enclosed fume-hood and our nanoparticles are not in solution. **We are therefore using nanoparticles in a manner that is not typical among those in the nano-sciences.** The safety protocol in place at LCLS/SLAC national laboratory classifies work outside of fume-hoods at the High Risk level; these are "Dry dispersible nanoparticles, nanoparticles agglomerates, or nanoparticles aggregates." **For the work described here, the importance of proper use of personal protective equipment (PPEs), such as respirators, is elevated.**

3.2.2. Inhalation Hazards:

Under normal operations the LAM entirely closes the micro- and nanoparticles. We expect micro- and nanoparticles to potentially be released only upon disconnecting a component, potentially becoming airborne from any site where they have accumulated. It is difficult to establish an expected number of airborne particles per unit volume in such a case, for the following reasons:

1. Significant accumulation of nanoparticles requires impaction, which usually entails high velocity. There is a large range of velocities and angles of incidence of particles within the LAM, making prediction of rates of accumulation difficult.
2. Nanoparticles accumulate into aggregates, which strongly adhere to each other. As such, they become films or collections of microparticles.
3. Some nanoparticles will come out of suspension during our purging procedure (see below), and these may or may not agglomerate or adhere strongly to surfaces. As such, they may be more easily removed by variations in air pressure.

Because the release of particles depends largely upon opening the apparatus, exposure will depend in part on how long particles have been allowed to accumulate, including the in-line vacuum pump exhaust filter.

It is important to note that pump exhaust containing any unfiltered micro- or nanoparticles may have higher toxicity effects than dry particles, as oil may have condensed on their surfaces, increasing the

likelihood of their adhering to surfaces, including lungs. Previous studies have shown toxicity to be higher for fine particles that have been coated.^{3,4}

The nanoparticle and microparticle production rate and filtration rate are calculated in Section [4.2.1].

3.2.3. Eye and Skin Hazards:

The microparticles or nanoparticles themselves could pose an eye hazard. These standard operating procedures are designed to help avoid contact of nano- and microparticles with the eyes. The brown goggles worn during normal conditions of laser hazard serve a dual purpose of protecting the eyes from particle exposure. This practice has been approved by EHS. When brown goggles are unnecessary because there is no laser hazard, users should wear standard clear work goggles whenever the LAM apparatus and/or directly affected vacuum chamber are not 100% sealed (such as maintenance or filling of the apparatus), or in case of a spill.

Nanoparticles may be able to be absorbed through the skin, and the health repercussions of this form of contact are largely unknown. Avoid touching any nanoparticles which may be deposited in filters or in various areas of the vacuum chamber/pump system. Wear nitrile gloves and lab coats when working with both microparticles and nanoparticles.

When contact exposure is likely (when re-filling the microparticle bed, or when opening any part of the apparatus for inspection or cleaning), nitrile or latex gloves and a supplied long-sleeved lab coat will be worn. Additionally, the use of a snorkel extractor will be used when appropriate to mitigate exposure to airborne particles in these instances.

4. Safety Controls:

4.1. Personal Protective Equipment:

4.1.1. Respirator:

This lab uses 3M 7500 series half-face respirators (see Figure 3 below), with 3M model 60921 P100 plus organic vapor filter cartridges. To become a LAM Operator, or to be present in lab when any but the standard LAM "In Use" conditions are met, user must be medically cleared by the UT Occupational Health Program (OHP, see <http://www.utexas.edu/hr/current/services/ohp.html>) to wear a 7500 series half-mask, and have it professionally fit-tested by the staff at OHP. (Note: only University of Texas employees are eligible to be fit-tested at OHP. Alternative fitting must be arranged for non-employees.) Sizes small, medium, and large correspond to 3M model numbers 7501, 7502, and 7503 respectively. OHP will confirm the appropriate size, and give instructions on proper mask use.

³ NIOSH [2011]. *Current Intelligence Bulletin 63*, "Occupational exposure to Titanium Dioxide."

⁴ Warheit DB, Brock WJ, Lee KP, Webb TR, Reed KL [2005]. Comparative pulmonary toxicity inhalation and instillation studies with different TiO₂ particle formulations: impact of NIOSH CIB 63 • Titanium Dioxide 103 surface treatments on particle toxicity. *Toxicol Sci* 88(2):514–524.



Figure 3. The 3M 7500 series respirator used in our lab (shown without filters installed).

For reasons of sanitation, all qualified users will have their own respirator. When the LAM is not in use, or is in “In Use” mode (See Section [5.2.1]), respirators will be stored in plastic drawers inside the entryway of the THOR lab. When the LAM is in “Maintenance/Filling” mode or “Spill” mode (See Sections [5.2.2] and [5.2.3]), those drawers will be moved outside the lab, next to the main THOR entryway door. Additional respirator filter cartridges will be available in the drawers as well.

When a LAM Operator enters the lab during normal “In Use,” operation, he will bring his respirator with him. Respirators for all Operators currently in the lab will then be stored in the top drawers of the plastic drawers located near the LAM apparatus. During “Maintenance/Filling” mode or “Spill” mode, only qualified users are permitted to enter the lab, and these users must properly put on their respirator before entry (See Section [5.2] and Section [7] for more information on protocol for different operation modes). A spill kit in these drawers will in addition contain two unassigned emergency-use respirators for use in case of emergency.

4.1.2. Nitrile Gloves:

Nitrile gloves will be available in the drawer kit near the LAM. They protect against skin exposure to the particles. They are to be put on overlapping the sleeves so that particles are prevented from traveling into the sleeve of the lab coat.

4.1.3. Lab Coats:

The supplied lab coats will be worn when handling unenclosed microparticles in any way. Primary use of lab coats will be while re-filling the microparticle bed in the LAM apparatus. They will also be worn in a spill situation. The spill kit, located in plastic drawers near to the LAM apparatus, will contain a supply of disposable clean room gowns. If a gown is exposed to a microparticle spill, or has been used at least 4 times during ordinary microparticle transportation or particle bed filling, it should be disposed of in a gallon-sized plastic Ziploc bag, which should be properly labeled with its possible contaminants. EHS will be called to dispose of these and all other bags of contaminated materials.

4.1.4. Goggles:

The vast majority of research on micro- and nanoparticle toxicity has been conducted on the hazards of inhalation, and not on their contact with eyes. Other than acute irritation or a scratched eye lens, toxicity of the bulk material is the most important consideration regarding contact with the eye. Our

plans are to initially use silver and metal oxide microparticles which are considered poorly soluble, low toxicity substances.

Goggles will be worn when the LAM is in “Maintenance/Filling” mode, or “Spill” mode (See Section [5.2] and Section [7] for more information on protocol for different operation modes). In these modes, the microparticles/nanoparticles are not 100% enclosed.

In order to mitigate exposure hazard without creating new optical exposure hazard, laser goggles will be sufficient when the standard THOR Laser SOP indicates that laser goggles are necessary. Otherwise, clear work goggles, stored in the plastic storage drawers near the LAM apparatus, will be worn.

4.2. Engineering Controls:

4.2.1. Vacuum Exhaust:

The vacuum pump which removes the micro- and nanoparticles generated by the LAM can be contaminated by the particles. To keep particles from simply venting through the exhaust, we have a system of filters in the intake of the pumps as well as in the exhaust.

About 10% of the nanoparticles generated in the ablation cell will first be sent by a virtual impactor into the inline Whatman HEPA filters. With a ¼ duty cycle at 100% efficiency in producing nanoparticles, a total of ~0.5 mg/h (out of the 18 mg/h microparticle feed rate) are expected to be directed into these filters. Assuming 99.97% removal efficiency of nanoparticles for each HEPA filter, ~0.05 ng/h is expected to pass the filters, that is, 10^8 particles per hour considering 4 nm diameter nanoparticles. Studies have shown that the efficiency of these types of filters increases for nanometer particles due to the capture through the diffusion process.⁵

Additionally, THOR is in the process of getting a negative pressure fume hood exhaust line for all pumps in the lab, which, when it is constructed, will ensure that any remaining microparticles or nanoparticles not trapped by the filters at the back of a vacuum pump are not exhausted into the building.

⁵ See doi: 10.1177/0960327109105157

4.2.2. Particle Detector:

In order to detect exposure limits in near-real time, we will use the HACH ULTRA Analytic, model Met-One HHPC-6 (Serial No. 050609134, Part No. 2087815-01). This unit measures particles and bins them into 6 channels, each for a different size. The particle size channels are for particles 0.3, 0.5, 0.7, 1, 2, 5 microns. This unit has a 50% sensitivity for 300 nm particle sizes, so it is likely not to be very sensitive for <100 nm particles. However, exposure during any normal maintenance procedure will also involve microparticles well within the efficient detection range. We will rely on microparticle measurements throughout the HHPC-6 detection range to indicate the possibility of the presence of nanoparticles.

The manual for this unit is available online, and is also available in THOR lab in hardcopy. We will operate this unit to alarm personnel of particle counts exceeding limits.



Figure 4. The HACH ULTRA Analytic, model Met-One HHPC-6. This unit indicates a spill if it alarms, at which the user refers to “Spill Incident Instructions.”

4.2.3. Emergency Spill Kit:

We will mitigate the risk to health due to the failure of any single control, by having on-hand a Spill Kit. This kit will be used in case of visible contamination, or if the particle counter alarms. See also Sections [4.2.2] and [9].

The Kit will contain:

- Emergency use respirators, with P100 particulate filters – Qty. 2
- Clear work goggles – Qty. 2
- Cleanroom gowns – Qty. 2
- Cleanroom wet wipes – Qty. 1 container
- Handheld HEPA vacuum – Qty. 1
- Rubber or nitrile gloves, size small – Qty. 1 box
- Rubber or nitrile gloves, size medium – Qty. 1 box
- Rubber or nitrile gloves, size large – Qty. 1 box
- Gallon size plastic bags – Qty. 1 box
- Labels and pen for labeling hazardous waste.

5. Safe Operating Protocols:

5.1. Designated Work Area:

This is the area designated for the micro- and nanoparticles work to be performed. It will be designated by signs posted outside the innermost reasonable air-barrier. For operations inside the THOR lab, this will be the outer door of the lab. To maintain verbal communications throughout the lab, we will conform to the THOR Laser SOP and keep doors interior to the lab open, such as the door separating the XUV target area from the main room (Note: This does not apply to the black plastic door at the lab entrance).

5.2. Signage and Operation Modes:

The following signs are to be placed outside of the two laboratory doors during operations using the LAM. Their presence warns people of the LAM operating status.

5.2.1. “In Use” Mode:

The most common sign corresponds to the “In Use” mode, which indicates standard operation of the LAM apparatus. In this mode, the LAM apparatus is 100% sealed (rubber stopper in, and no openings to air between the particle bed and the vacuum chamber). **In “In Use” mode, only personnel who have read and signed this SOP will permitted entry to the lab.** There is no requirement for personnel to wear respirators in this mode.



Figure 5. The “In Use” warning sign for display outside the door during normal LAM operations. This indicates standard (fully sealed) operation.

5.2.2. “Maintenance/Filling” Mode:

The second sign corresponds to “Maintenance/Filling” mode, which indicates that some part of the LAM is not sealed. This is most likely to occur when opening the particle bed stopper to refill the microparticles, opening the LAM apparatus for cleaning, or opening a directly contaminated vacuum chamber for particle sample retrieval. In this mode, only LAM Operators are permitted entry to the lab, and these Operators must wear their respirators before entry.



Figure 6. The “Maintenance/Filling” warning sign for display outside the door during LAM maintenance or filling operations. This indicates that some part of the LAM apparatus is open to air.

5.2.3. “Spill” Mode:

The last sign corresponds to “Spill” mode, which indicates that a microparticle or nanoparticle spill has occurred. In this mode, only LAM Operators are permitted entry to the lab, for the purposes of cleaning the spill, and these Operators must wear their respirators, lab coats, and nitrile gloves before entry.



Figure 7. The “Spill” warning sign for display outside the door during emergency situations. This indicates that a microparticle or nanoparticle spill has occurred.

5.3. Labeling:

Nanoparticle and microparticle containers or contaminated equipment will be specifically labeled as such, including the various bulk substances from which the nanoparticles are comprised. The nanoparticles will be stored on the bottom drawer of the drawer set nearest the LAM.

5.4. Disposal of Contaminated Materials:

Contaminated materials, such as wipes and filters, will be enclosed and placed in plastic bags and labeled for chemical waste pickup. Labels will indicate the size and bulk material of the possible particulate contaminants (for example, “Nanosize SiO₂ waste”). See <http://www.utexas.edu/safety/ehs/disposal/> for more information.

5.5. Approved Materials and Material Storage:

The current SOP relates to the following materials: Ag, SiO₂, TiO₂, SnO₂, MnO₂, and ZrO₂.

The introduction of new micro- and nano-materials must be approved by the authors of this SOP, and their presence indicated in this section of the SOP.

Unused microparticles will be stored in individual sealed, labeled containers, inside the bottom drawer of the plastic LAM kit drawers.

6. LAM Description and Operating Principles:

The operating principle of the LAM device, shown in Figure 8, is described in detail in Gleason⁶ and summarized here. A buffer gas, in our case helium, is initially introduced into the apparatus at a pressure less than 30 psi, set by the “Buffer Gas Bottle Pressure Regulator.” This flow is then regulated by the flow controller “A” to ~2500 sccm. Part of this gas flows through the “Particle Bed Line” to the glass particle bed containing the microparticles. In the “Particle Bed Line” there is a flow controller, F, with a valve. This valve, in conjunction with the setting of the “Buffer Gas Bottle Pressure Regulator” and the “Bypass Line Valve” controls the aerosol density and particle feed rate.

A continuous-flow nozzle of ~250 micron diameter is located at the bottom of the particle bed, which concentrates gas flow through the particles to create the aerosol (by “fluidization”) of particles, with the help of a vibrating motor. The glass Particle Bed also serves as a gravitational settling chamber to remove large agglomerates.

The aerosol particles are size-filtered by the “Cascaded Pair of Virtual Impactors.” Flows containing oversized particles and agglomerates are discarded through line “q2,” regulated by flow controller C, and undersize particles and excess buffer gas is discarded through line “Q3,” and is regulated by flow controller D. HEPA filters placed before the controllers are expected to remove 99.97% of these particles. Both these lines then flow through another Whatman HEPA filter to a vacuum pump.

The particle size-selected aerosol enters the ablation cell where a Q-switched laser, a Quanta-Ray GCR, hits the particles to generate nanoparticles by ablation and subsequent condensation. Currently, the period of the laser is such that ~¼ of the total flow is ablated. A controller, “B,” injects buffer gas into the ablation cell. This buffer gas may originate from the same bottle feeding controller “A.” This gas is regulated such that the nanoparticles are generated and carried in a laminar flow. The excess of this gas is discarded, while the rest of the flow carries nanoparticles and non-ablated microparticles into the “Virtual Impactor.” In the Virtual Impactor, ~ 90% of the nanoparticles are separated from the microparticles and are injected into a vacuum chamber (either a test chamber or the XUV target chamber) through a small continuous-flow nozzle. Approximately 10% of the nanoparticles and a majority of the microparticles are discarded by a vacuum pump or pumps through the “rejected micro-particle line” and flow controller E.

The configuration of the vacuum pumps attached to the final vacuum chamber is detailed in Sections [8.1] and [4.2.1].

⁶ K.L. Gleason, PhD. Dissertation, The University of Texas at Austin (2011).

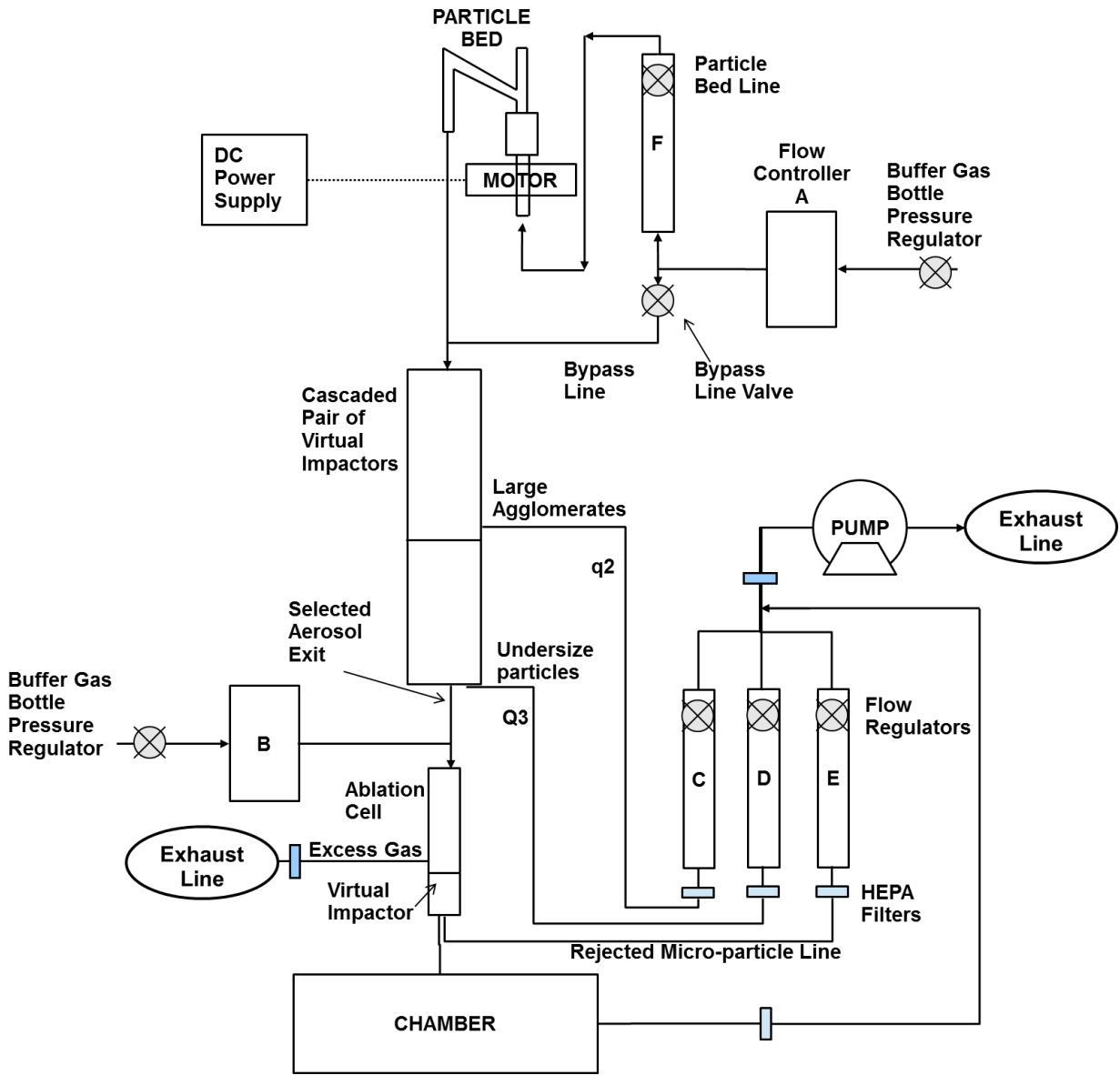




Figure 8. Schematic of the LAM in testing mode. Valves are represented by , while HEPA filters are represented by .

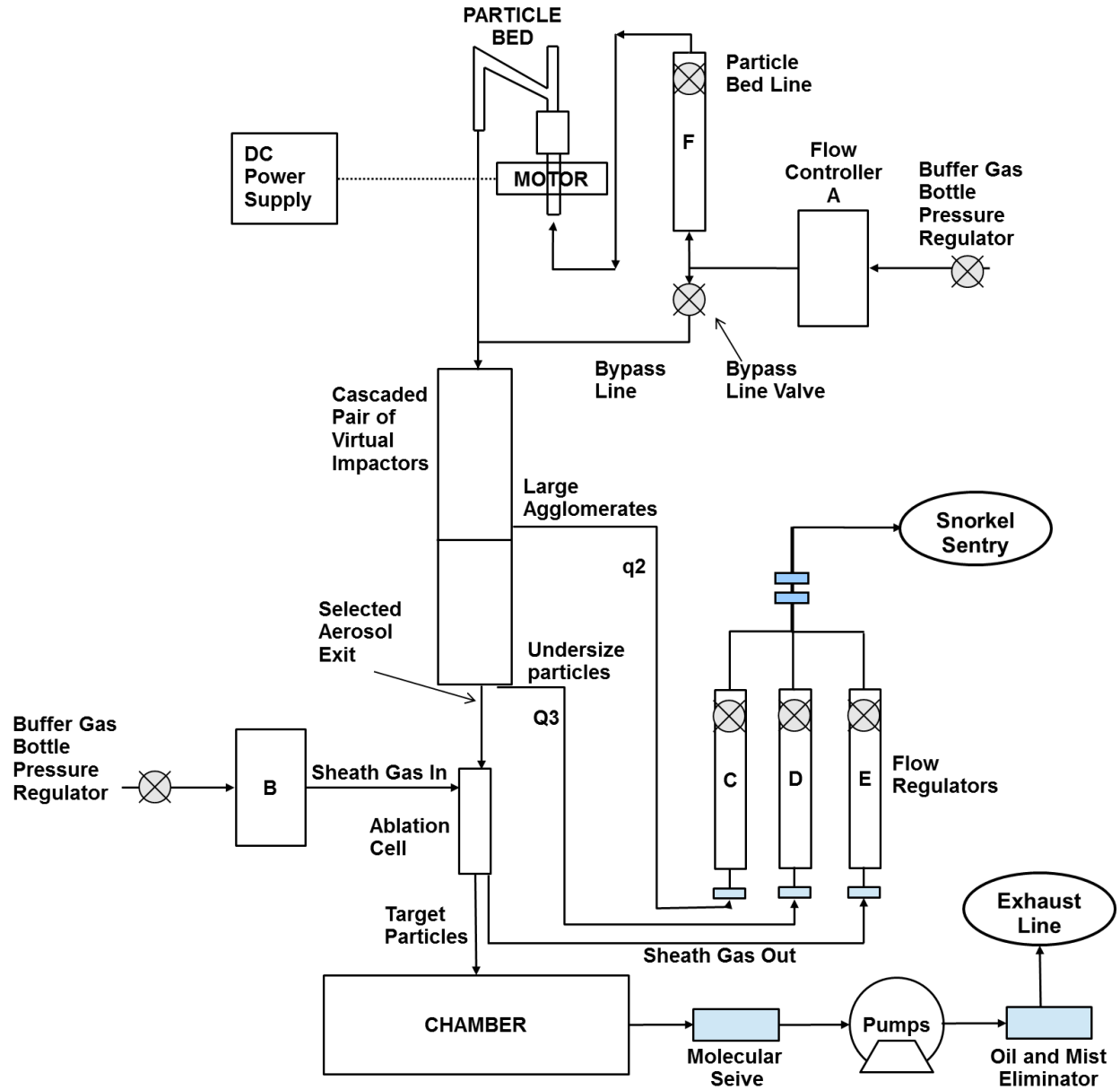




Figure 9. Schematic of the LAM in experimental mode. Valves are represented by , while HEPA filters are represented by .

7. Protocol for Changing Operating Modes:

7.1. “In Use” Mode:

The following procedure should be used when changing to “In Use” mode. This mode should be used whenever running the LAM apparatus while it is fully sealed.

1. Put up the “In Use” sign on the entry door to the THOR lab [Figure 5].
2. Perform a sweep to ensure that the lab is cleared of individuals who have not read and signed Sections [1-6] of this SOP.
3. Move the masks for current Operators to the plastic storage drawers near the LAM apparatus.
4. Make sure the spill kit is stocked.
5. Take a reading with the particle counter and log it into the logbook.
6. Proceed with running the LAM apparatus.
7. Promptly take a reading with the particle counter and log it into the logbook.
8. Once the testing is done and the apparatus is shut off, the “In Use” sign may be removed from the door.

7.2. “Maintenance/Filling” Mode:

The following procedure should be used when changing to “Maintenance/Filling” mode. This mode should be used when the LAM apparatus is going to be opened, such as when filling the microparticle bed, or opening the LAM apparatus for cleaning.

1. Put up the “Maintenance/Filling” sign on the entry door to the THOR lab [Figure 6].
2. Make the respirator mask station available outside the main entrance door.
3. Perform a sweep to ensure that the lab is clear of all personnel who are not certified LAM Operators.
4. All remaining personnel should wear their fitted respirator.
5. Operators who will touch any interior chamber surface or particle-contaminated sample slide will wear nitrile/latex gloves, work goggles or laser goggles, as described in Section [4.1.4], and a clean room gown.
6. Take a reading with the particle counter and log it into the logbook.
7. Proceed with opening the LAM apparatus and performing necessary maintenance/filling procedures.
8. Once maintenance is done and the apparatus is re-sealed, wipe down all possibly contaminated instruments and surfaces with a wet wipe, and dispose of wet wipes in sealed, labeled waste

bags (See Section [5.4] for disposal instructions). Remove nitrile gloves, and dispose of them in a similarly labeled bag.

9. Take a reading with the particle counter and log it into the logbook.
10. If the particle counter reading is within the normal range for the room, the “Maintenance/Filling” sign may be removed from the door. Otherwise, employ the Snorkel Sentry in the affected area until the particle count decreases. Maintain the “Maintenance/Filling” sign for 20 minutes after particle counts have returned to normal. Log the new particle counter reading in the logbook.
11. Once the “Maintenance/Filling” sign has been removed, LAM Operators may remove their respirators and other PPE.

7.3. “Spill” Mode:

See Section [9.2] for spill incident instructions.

8. Standard Operating Procedure:

The LAM may only be operated by LAM Operators, authorized individuals who have been fitted for a respirator and cleared to maintain and operate the LAM. The procedures are outlined below for **general information**. As is common in experimental research, these procedures are not unchangeable, and they **do not** supersede the guidelines in Sections [5] and [7]. Common sense, along with the standard THOR SOP guidelines, and the guidelines in Section [5] and [7], should guide any necessary deviations in these procedures.

These procedures are separated into LAM Testing and LAM Experimental Operations. These differ primarily in the description of the pump configuration attached to the final vacuum chamber. In case of a spill, please refer to Section [9].

8.1. LAM Testing:

These procedures will be used while the LAM apparatus is in THOR, assembled on a tabletop for testing purposes.

8.1.1. Procedure for LAM Ablation Testing:

1. Follow the procedure for transitioning to “In Use” mode (See Section [7.1]).
2. Make sure there is a sufficient level of microparticles in the particle bed. If not, refer to “Filling the LAM Microparticle Bed” instructions in Section [10.3]. Note: Filling the particle bed is “Maintenance/Filling” mode.
3. Make sure the vacuum pump is operating.
4. Connect a gas cylinder (He) with a pressure regulator with range for 20-30 psi to Sierra instruments Mass-Trak controllers A and B.
5. Set the pressure regulator to about 20 psi. **Do NOT exceed 30 psi. This will damage the controllers.**

Standard Operating Procedure for Laser-Ablation of Microparticles (LAM) Nanoparticle Generator

6. Apply gas to the controllers.
7. Plug in controllers A and B.
8. Let the controllers calibrate for 15 minutes.

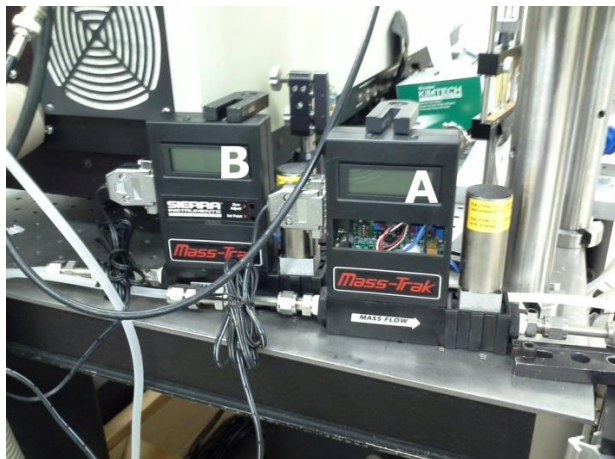


Figure 10. A and B – Sierra Instruments, Inc. 810 Mass-Trak Flow Controller.

9. Set the zero point for each controller (if necessary) by adjusting the upper screw (see Figure 11).



Figure 11. Sierra Instruments, Inc. 810 Mass-Trak Flow Controller. The screws referred to in the Procedure are indicated by arrows and labelled.

10. Set the flow for controller A with potentiometer screw [Figure 11]. This controller regulates the input flow for the particle bed and the virtual impactor assembly. Flow is dependent on particle size, composition, and valve settings.
11. Set the flow for controller B. This controller will regulate the major input flow for the ablation cell.



Figure 12. C, D, E, and F – Omega FT-062-01-ST-BN flow controllers.

12. Use regulator C [Figure 12] to set the flow q_2 containing particles larger in size than those desired and agglomerates.
13. Use regulator D [Figure 12] to set the flow Q_3 containing particles smaller in size than those desired.
14. Use regulator E [Figure 12] to set the output flow containing unablated particles.
15. Turn on and set the DC power supply to 7 volts in “Volts mode.”
16. Set the flow for regulator F. This controls the bypass flow to the particle bed.
17. Ensure that microparticles are flowing into the ablation cell using a laser pointer.
18. If not already in “Operation” mode, switch the lighted laser sign in the lab entryway to “Operation” mode, and do a verbal and visual sweep of the lab to confirm that there are no un-goggled personnel in the lab. Standard operation mode goggle procedures apply.
19. Turn on the HeNe for scattering measurements.
20. Make sure HeNe alignment is correct, and all stray reflections are blocked.
21. Make sure the PMT and photodiode are powered on, and plugged into an oscilloscope. A change in scattering signal should be discoverable while the laser is ablating microparticles.
22. Turn on the ablation laser, and unblock the beam. See Section [11.1]. See also the manual for this laser, available in the laboratory.

23. Look for plasma in the ablation cell, in the microparticle stream. This indicates good overlap, and ablation.
24. Adjust the mirror before the cylindrical lens to optimize overlap with the microparticle stream.
25. Replace the shroud over the ablation cell area.

8.1.2. To Shut Down:

1. Power off the ablation laser. See Section [11.2].
2. Stop microparticle feeding by setting the flow regulator F to zero.
3. Turn off the DC power supply for the vibration motor.
4. Turn off the vacuum pump.
5. Continue gas flow for ~2 minutes to let the chamber reach to atmospheric pressure (based on 1-2k sccm flowing into a 1-2 L chamber).
6. Set flows for controllers A and B to zero.

8.1.3. Procedure for Collecting Nanoparticle Samples :

1. Follow the procedure for transitioning to “Maintenance/Filling” mode (See Section [7.2]).
2. If the LAM apparatus is running, follow the shutdown procedure (See Section [8.1.2]).
3. Open the quick-release ISO flange on the chamber that is blanked off.
4. Insert a TEM grid or glass slide through the open port for collection. It should be positioned under the micro/nanoparticle jet, in order to collect the particles.
5. Close and secure the blank on the vacuum port.
6. Follow the procedures in Sections [7.1] and [7.2] to transition out of “Maintenance/Filling” mode, and into “In Use” mode.
7. Turn the vacuum pump back on, and start the LAM apparatus as usual. Collect sample.
8. Follow the procedures in Section [7.1] and [7.2] to transition out of “In Use” mode, and into “Maintenance/Filling” mode.
9. Follow standard LAM shutdown procedures to shut down the apparatus (See Section [8.1.2]).
10. Open the quick-release ISO flange on the chamber that is blanked off.
11. Remove the TEM grid or glass slide through the open port.
12. Place sample in a sealed, marked plastic box.

13. Close and secure the blank on the vacuum port.

14. Follow the procedures in Section [7.2] to transition out of “Maintenance/Filling” mode.

8.2. LAM Experimental Operations:

These procedures will be used while the LAM apparatus is attached to the THOR XUV target chamber for full experimental operations.

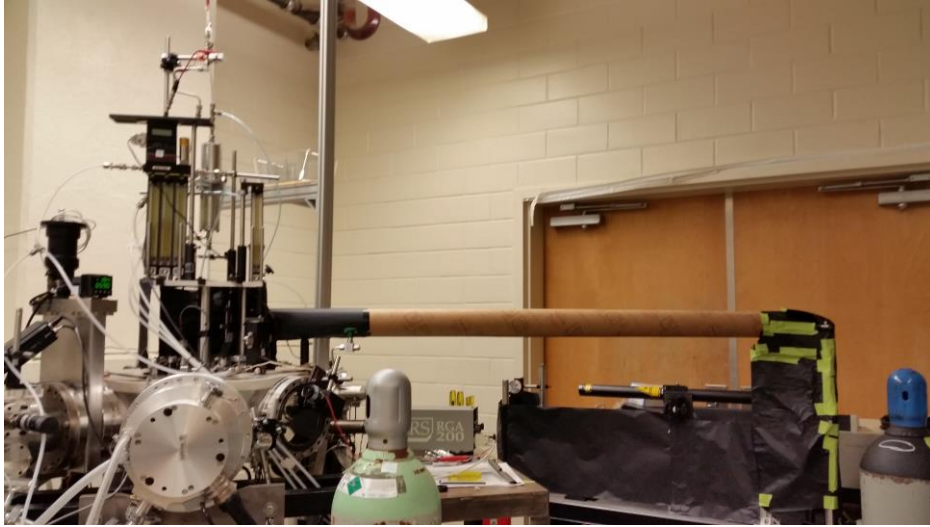


Figure 13. Full setup for nanoparticle XUV experiment.

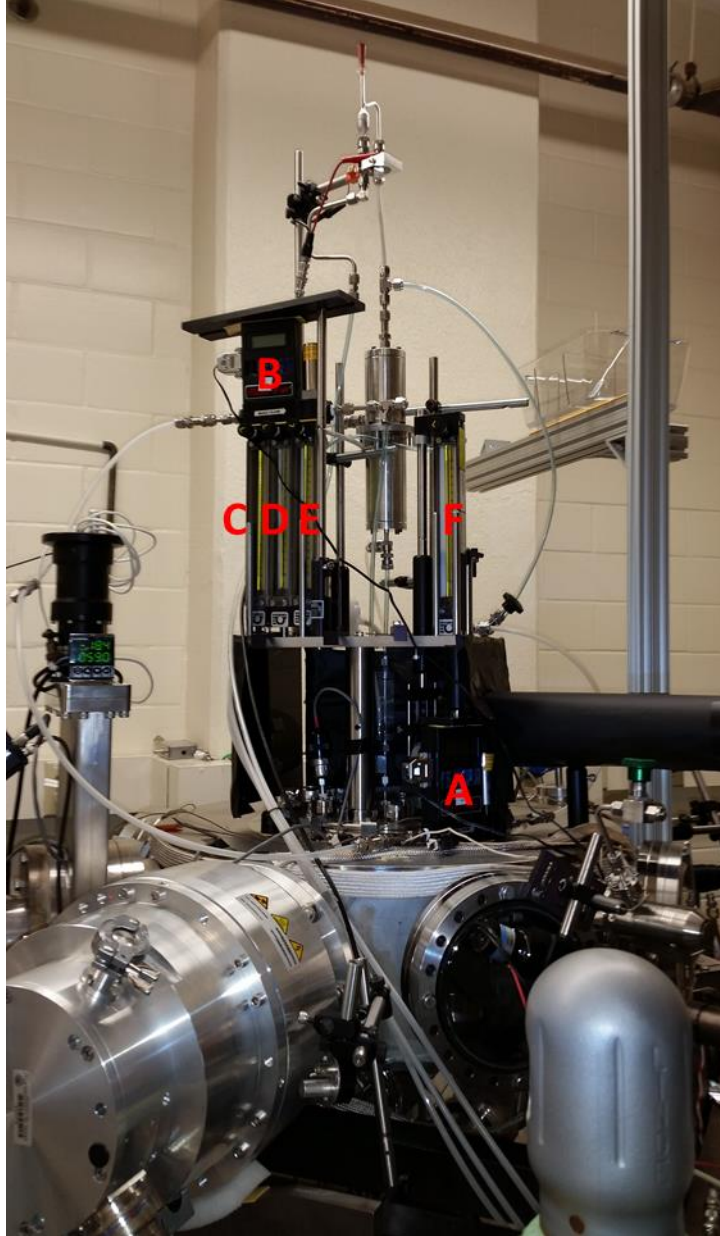


Figure 14. Experimental setup with flow regulators labeled in red.

8.2.1. Procedure for LAM Ablation Experiment on XUV Target Chamber:

1. Follow the procedure for transitioning to “In Use” mode (See Section [7.1]).
2. Make sure there is a sufficient level of microparticles in the particle bed. If not, refer to “Filling the LAM Microparticle Bed” instructions in Section [10.3]. Note: Filling the particle bed is “Maintenance/Filling” mode.
3. Make sure the black vacuum pump and roots blower are operating, and the gate valve is open.
4. Connect a gas cylinder (N_2 or Ar) with a pressure regulator with range for 20-30 psi to Sierra instruments Mass-Trak controllers A and B.

5. Set the pressure regulator to about 20 psi. **Do NOT exceed 30 psi. This will damage the controllers.**
6. Apply gas to the controllers.
7. Turn on the power switch to supply power and turn on controllers A and B, as well as the snorkel sentry.
8. Let the controllers calibrate for 15 minutes.
9. Set the zero point for each controller (if necessary) by adjusting the upper screw (see Figure 11).
10. Set the flow for controller A with potentiometer screw [Figure 11]. This controller regulates the input flow for the particle bed and the virtual impactor assembly. Flow is dependent on particle size, composition, and valve settings.
11. Set the flow for controller B. This controller will regulate the sheath flow for the ablation cell.
12. Use regulator C [Figure 14] to set the flow q_2 containing particles larger in size than those desired and agglomerates.
13. Use regulator D [Figure 14] to set the flow Q_3 containing particles smaller in size than those desired.
14. Use regulator E [Figure 14] to set the output ablation cell sheath flow.
15. Turn on and set the DC power supply to 7 volts in "Volts mode."
16. Set the flow for regulator F [Figure 14]. This controls the bypass flow to the particle bed.
17. Ensure that microparticles are flowing into the ablation cell using a laser pointer.
18. If not already in "Operation" mode, switch the lighted laser sign in the lab entryway to "Operation" mode, and do a verbal and visual sweep of the lab to confirm that there are no un-goggled personnel in the lab. Standard operation mode goggle procedures apply.
19. Turn on the HeNe for scattering measurements.
20. Make sure HeNe alignment is correct, and all stray reflections are blocked.
21. Make sure the PMT and photodiode are powered on, and plugged into an oscilloscope. A change in scattering signal should be discoverable while the laser is ablating microparticles.
22. Make sure there is cooling water flowing to the GCR.
23. Make sure there is purging nitrogen flowing to the GCR.
24. Make sure the shroud on the ablation area is in place and secure.
25. Turn on and unblock the ablation laser. See Section [11.1]. See also the manual for this laser, available in the laboratory.

26. Look for plasma in the ablation cell, in the microparticle stream, using a camera. This indicates good overlap, and ablation.
27. Adjust the mirror before the cylindrical lens to optimize overlap with the microparticle stream.

8.2.2. To Shut Down:

1. Power off the ablation laser. See Section [11.2].
2. Stop microparticle feeding by setting the flow regulator F to zero.
3. Turn off the DC power supply for the vibration motor.
4. Set flows for controllers A and B to zero.
5. Close the valve between the ablation cell and the chamber.
6. Wait 5 minutes, then close the gate valve to the black pump and roots blower.
7. Switch off the power supply to flow controllers A and B, and the snorkel sentry.

9. Emergency Procedures:

These procedures will be followed during any situation involving unplanned, uncontained release of micro- or nanoparticles.

9.1. Emergency Shutdown of the LAM:

1. Set flow regulator F to zero.
2. Unplug electric plugs for flow controllers A and B.
3. Turn off the vacuum pump.
4. Set the pressure regulator(s) for the buffer gas to zero, and close gas tanks.
5. Turn off the DC power supply for the vibration motor.

9.2. Spill Incident Instructions:

In case of a microparticle and/or nanoparticle leak or spill, as detected by sight, or by the particle counter, the procedure is as follows:

1. If the spill was discovered visually, inspect the spill. This is a quick visual inspection. Skip to step 3.
2. If the particle-counter is producing an alarm, that is sufficient to proceed with all of the following.
3. All non-essential personnel shall be notified of the incident and immediately exit the lab.
4. Switch to emergency "Spill" sign on the entry door to the THOR lab [Figure 7]
5. The qualified LAM Operators shall immediately put on their respirator(s), or one of the emergency-use respirators.
6. If not already wearing them, users shall put on clear work goggles. If laser goggles are being used, these shall remain on.

7. If the LAM apparatus is in operation, initiate emergency shutdown procedures. See Section [9.1]. If there is visible contamination on any surface which must be touched for emergency shutdown, Operators shall first put on nitrile gloves before touching these surfaces.
8. If not otherwise being worn, Operators shall put on cleanroom gown and nitrile gloves.
9. Turn on the vacuum extractor and direct the tube to approach as close as possible the spill location.
10. Determine the extent of the spill.
11. To remove visible accumulations of particles, employ the handheld HEPA vacuum. This vacuum shall remain on as additional filtration during the entire cleaning procedure.
12. Users shall then use cleanroom wet wipes to wipe all possibly affected surfaces. Wipes will be used as a single-use items and discarded in gallon-sized zip-lock bags. Wipes should be employed until they show no visible dust/dirt/particles after wiping.
13. Once all surface-cleaning wipes are discarded, additionally wipe the exterior of the plastic bags and, finally, the gloves themselves (using single-wipe protocol). Using the gloves, zip the bags.
14. Remove by inverting the gloves and discard in a new plastic bag. Zip the bag.
15. Label all plastic bags according to material and size of possible particle contaminants. These bags will be disposed of by contacting EHS.
16. Once the leak has been thoroughly cleaned, and there is no sign of continuing respiratory or tactile hazard as determined by the particle counter, turn off the vacuum extractor and handheld HEPA vacuum. If the particle counter detects additional particles, turn on the vacuum extractor and handheld HEPA vacuum again. Continue this process until additional particles are not detected for 20 minutes after turning off the extractor and handheld vacuum. Sweep the area for particles using the particle counter to assure no additional particles are read.
17. Upon completion of step 16, users may remove their masks and other PPE. After this time, the emergency "Spill" sign may be removed from the door.

10. Maintenance:

10.1. HEPA Filters:

All HEPA filters should be checked every day during normal (daily) operation. Clogged filters will be visible by eye.

To change a filter:

1. Follow the procedure for transitioning to “Maintenance/Filling” mode (See Section [7.2]).
2. Obtain a replacement filter for that unit.
3. Make sure all flow through the apparatus has been shut off, and the area around the filter is at atmospheric pressure.
4. Open filter holder and replace the filter.
5. Dispose of old filter, as well as gloves, into appropriate disposal bag labeled, for example, “SiO₂ Microparticles and Nanoparticles Waste,” or otherwise as appropriate.
6. Follow the procedure for transitioning out of “Maintenance/Filling” mode (See Section [7.2]).

10.2. Cleaning the Apparatus:

Cleaning should be performed any time the microparticle material will be changed, or when an obstruction caused by microparticle buildup in some part of the system is suspected.

1. Follow the procedure for transitioning to “Maintenance/Filling” mode (See Section [7.2]).
2. Evacuate the system of all buffer gas, in order to help any entrained nanoparticles to settle onto surfaces.
3. Introduce the buffer gas in quantities sufficient to bring the apparatus to atmospheric pressure.
4. Carefully disassemble the apparatus only as much as is necessary to facilitate transport, and wrap in a plastic bag.
5. Move the parts to a location with a fume hood.
6. Rinse the parts with distilled water or other appropriate solvent such as alcohol, and wipe with Kimwipes.
7. Collect all rinse water in a container marked to identify the microparticle/nanoparticle contaminants. Minimize the volume of solvent by allowing to evaporate in the fume hood, and then pour the solution into a disposal bottle and attach the safety office disposal tag to the bottle. Keep a running record in the card of quantities and dispose with the safety office when full.
8. Collect all Kimwipes in a bag marked to identify the microparticle/nanoparticle contaminants.
9. Transport the cleaned apparatus back to the lab, and re-assemble the apparatus.

10. Dispose of gloves, as well as any contaminated wipes/bags/etc. in the properly marked disposal bag.
11. When the LAM apparatus in the THOR lab is re-sealed, follow the procedure for transitioning out of “Maintenance/Filling” mode (See Section [7.2]).

10.3. Filling the LAM Microparticle Bed:

Of all the operations in the lab, this procedure has the highest chance of resulting in inhalation and contact exposure to microparticles. In this operation, two vessels containing microparticles will be open to the air, and particles will be manually transferred in bulk from one container to the other. Furthermore, this will take place, during normal operations, approximately seven feet above the ground. During the transfer, sudden gusts or hand motions can scatter the particles into the air and onto the surrounding apparatus. The following procedure is designed to mitigate this risk. Should exposure occur, refer to Section [9.2], “Spill Incident Instructions.”

The vial holding the replacement microparticles, will be small and one that has been filled (if necessary) using a fume hood and protective gloves. The small size mitigates the contamination in the case of a spill.

When the LAM apparatus is mounted on the THOR XUV target chamber for an experiment, a platform will be available that provides for safely ascending to the level of the apparatus (approximately seven feet). The Operator will be able to use two hands, a convenient horizontal surface, and wipes, in order to fill the particle bed. Using measurements of Sandi, we determined she will be able to conveniently handle the materials.

10.3.1. Procedure for Filling the Particle Bed:

1. Follow the procedure for transitioning to “Maintenance/Filling” mode (See Section [7.2]).
2. Make sure you have a “buddy” present that is attentive to what is going on. In the event of a spill, this person will secure the area of personnel, switch to the “Spill” warning sign, and assist in cleanup.
3. Before starting, both Operators should don their respirator, lab coat, and gloves.
4. Make sure all flows are off, and the particle bed assembly is at atmospheric pressure.
5. Start with the vial and spatula placed on a convenient surface.
6. Remove the particle bed stopper with a gentle twisting motion with one hand, while supporting the glass apparatus with the other, and place the stopper on a convenient surface.
7. Pick up the vial, and, using both hands, open the vial, and place the lid on a convenient surface.
8. Position the mouth of the vial directly above the particle bed funnel.
9. Tip the vial sideways slightly, and use the small spatula to transfer level amounts of the microparticles from the vial into the funnel.
10. Place the spatula on a convenient surface.
11. Using both hands, replace the vial lid and place the vial on a convenient surface.

12. Put the spatula in the plastic bag.
13. With one hand replace the particle bed stopper with a gentle twisting motion while supporting the glass apparatus with the other hand.
14. Follow the procedure for transitioning out of “Maintenance/Filling” mode (See Section [7.2])

11. Operating the Quanta-Ray GCR Ablation Laser:

11.1. Starting the Quanta-Ray GCR Ablation Laser:

1. Make sure there is cooling water flowing to the GCR.
2. Make sure there is purging nitrogen flowing to the GCR.
3. Place a beam block as close as reasonably possible to the output of the GCR.
4. Turn GCR power supply switches on.



Figure 13. GCR oscillator control panel.

5. Make sure Oscillator and amplifier “LAMP ENERGY ADJUST” knobs are set to “START,” and the Q-switch control knob is set to “OFF.”
6. Set the pulse repetition rate to “OFF/EXT” or “VARIABLE,” depending on whether you will be running in triggered mode.
7. Press and hold the green oscillator “ON” button. Release button and wait for the green light to turn on, to indicate the lamps are simmering.



Figure 13. GCR amplifier control panel.

8. Press and hold the green amplifier “ON” button. Release button and wait for the green light to turn on, to indicate the lamps are simmering.
9. Slowly rotate the oscillator “LAMP ENERGY ADJUST” knob until there is IR light visible on an IR card at the output.
10. Using the IR card, remove the beam block and trace the beam from the laser output to the final beam dump after the ablation cell, ensuring that there are no major misalignments.
11. Using the IR card or IR viewer, look at the fan-shaped reflection from the ablation cell, and ensure that it is fully blocked when the laser shroud is in place. You may need to slowly increase the oscillator “LAMP ENERGY ADJUST” knob until this reflection is visible.
12. Slowly increase the oscillator “LAMP ENERGY ADJUST” knob to full power.
13. Slowly increase the amplifier “LAMP ENERGY ADJUST” knob to full power.
14. Set the Q-switch to “NORMAL” or “EXT,” depending on whether you will be running in triggered mode.

11.2. Shutting Down the Quanta-Ray GCR Ablation Laser:

1. Turn the amplifier Q-switch to “OFF.”
2. Turn the oscillator Q-switch to “OFF.”
3. Turn down the amplifier and oscillator “LAMP ENERGY ADJUST” knobs to “START.”
4. Press the amplifier and oscillator “OFF” buttons.
5. After 15 minutes, the GCR power supply may be turned off.

12. Appendix A:

12.1. Quick-Installation Instructions for Sierra Instruments Mass-Trak 810 Controllers:

These instructions were provided by Sierra Instruments, Inc.

1. If equipped with a black nylon flow body, DO NOT OVERTIGHTEN your fittings or pipes when installing into the hexed-portions of the flow body. Use two wraps of Teflon tape on each of your fittings, hold the plastic hexagonal nuts with a wrench, and tighten your fittings no more than one (1) turn past hand tight.
2. NEVER TEST FOR LEAKS WITH LIQUID LEAK DETECTOR. If liquid seeps into the electronics or the sensor compartment below, the instrument may be damaged. Use a pressure-decay test instead.
3. Install an appropriate in-line filter upstream if the gas contains any particulate matter or condensed moisture. (A 15-micron particulate filter for full-scale flows up to 30 liters/minute is recommended, 30-micron for flows above 30).
4. Mount with a horizontal gas-flow. This orientation is preferable unless the factory calibration was specifically performed for a vertical flow. Consult the "Comment" section of your calibration certificate. (Horizontal flow is assumed unless vertical flow upward or downward is specified).
5. DO NOT APPLY POWER TO THE OUTPUT LOOP on units equipped and calibrated for a 4-20 mA output signal. This is NOT a loop-powered device. Damage will occur.
6. Confirm that the DIPswitch settings are in the correct position for your chosen setpoint source by removing the front access panel. (The DIPswitches are located in the left of the opening).
7. Wire the instrument per the diagram on the back of this card, or the Operator's Manual, Chapter 2. Connect the Setpoint signal wire if an external source is to be used to control flow. (Note: In External Source mode, if no wire is connected to the Setpoint pin, the valve may float open).
8. Apply the gas to the inlet at the recommended inlet pressure as listed on the label and the calibration certificate. On a controller, confirm that there is no gas flowing through it with a zero setpoint and under the operating pressure. (If there is a flow, consult the valve adjustment procedure found in the Operator's Manual, Chapter 4).
9. Apply power and verify or adjust the zero setting after allowing a 15-minute warm-up period. The zero adjustment potentiometer is accessed through the upper-right hole in the front panel. Adjust until the reading on the display is within 0.5% of the full scale value.

For instruments without a display, monitor the output signal and adjust DOWNWARD from a positive output, stopping at 4 mA (a V4 instruments) or 15 mV (V1 instruments). (See the Operator's Manual, Chapter 3).
10. DO NOT LEAVE A SETPOINT APPLIED TO A CONTROLLER WHEN NO GAS IS AVAILABLE TO THE INLET FITTING. The control circuit will apply the maximum voltage to the valve coil resulting in

eventual overheating. Damage may occur. (Instead, consult the Operator's Manual, Chapter 3, for use of the "Valve Override" feature).

11. An ANNUAL factory evaluation and calibration is recommended.

EMAIL Technical Support: Service@sierrainstruments.com

Website Self Service: www.sierrainstruments.com (Click "Sales & Service" Button)

Phone Technical Support:

SIERRA FACTORY: 800-866-0200 OR 831-373-0200

SIERRA EUROPE: +31 72 5071 400

Appendix C

Calculation of Flows and Microparticle Diameters

The MATLAB code to calculate the flows and cutoff diameters of the microparticles in the virtual impactor is as follows:

```
function [mQ1, mQ2, q2, mQ3, q3, d1,d2] = Flows(metal, particleSize, gas)
% metal is a string, referring to the microparticle material.
% 'Ag', 'Si' (SiO2), 'Ti' (TiO2), 'Sn' (SnO2), 'Mn' (MnO2), 'Zr' (ZrO2)
% particleSize is microparticle diameter in microns.
% Gas is the buffer gas type: 'He' for helium, 'Ar' for argon, 'at' for air

sizeRange = 0.5; % radius in microns that you're willing to tolerate is
    % particleSize - sizeRange to particleSize + sizeRange

pMetal = 0; %Metal density in g/cm3
if metal == 'Ag'
    pMetal = 10.49; %g/cm3, for pure Ag
elseif metal == 'Au'
    pMetal = 19.32; %g/cm3, for pure Ag
elseif metal == 'Si'
    pMetal = 2.648; %g/cm3, for SiO2
elseif metal == 'Ti'
    pMetal = 3.78; %g/cm3, for TiO2
elseif metal == 'Sn'
    pMetal = 6.95; %g/cm3, for SnO2
elseif metal == 'Mn'
    pMetal = 5.03; %g/cm3, for MnO2
elseif metal == 'Zr'
    pMetal = 5.68; %g/cm3, for ZrO2
end
```

```

mu = 0; % Viscosity in Poise
alpha = 0;
gasDensity = 0; % in g/cm^3
gasWeight = 0; % Molecular weight of gas in g/mol
gamma = 0;
lambda = 0; % Mean free path at 20 deg. C, 1 bar, in microns
if gas == 'He'
    mu = 199.01*10(-6); %
    alpha = 1.277;
    gasDensity = 1.64*10(-4);%0.0001768;
    gasWeight = 4;
    gamma = 1.66;
    lambda = 0.1943; %0.196;
elseif gas == 'Ar'
    mu = 222.00*10(-6);
    alpha = 1.227;
    gasDensity = 0;
    gasWeight = 39.948;
    gamma = 1.66;
    lambda = 0.0703; %0.072;
elseif gas == 'at'
    mu = 183.14*10(-6);
    alpha = 1.207;
    gasDensity = 0;
    gasWeight = 28.967;
    gamma = 1.40;
    lambda = 0.0674; %0.068;
elseif gas == 'N2'
    gamma = 1.40;
    lambda = 0.067;
end

flowRatio = 0.08;
q3 = 200;%204; % sccm (use 200 for He, 150 um nozzle, 204 for N2, 250 um)

% Find all of the flows (in sccm)

```

```

% Confirmed: These reproduce Kristopher Gleason's flow table (Table 2.1).
mQ2 = q3/flowRatio;
mQ3 = (1-flowRatio)*mQ2;
mQ1 = mQ2/(1-flowRatio);
q2 = flowRatio*mQ1;

% Find the nozzle diameters
% Confirmed: These reproduce Krostopher Gleason's nozzle diameter table
%(Table 2.2)
a1 = (particleSize + sizeRange)/2; % min particle radius in microns
a2 = (particleSize - sizeRange)/2; % max particle radius in microns
k1 = lambda/a1;
k2 = lambda/a2;
csf1 = 1+ alpha*k1; %Cunningham slip factor
csf2 = 1+ alpha*k2;

particleSize1 = (2*a1)*10^(-4); % microns to cm, oversized cut point
particleSize2 = (2*a2)*10^(-4); % microns to cm, undersized cut point

d1 = ((pMetal*csf1*particleSize1^2*4*(mQ1/60))/(9*mu*pi*0.83^2))^(1/3);
d2 = ((pMetal*csf2*particleSize2^2*4*(mQ2/60))/(9*mu*pi*0.83^2))^(1/3);

% If we use Gleason's virtual impactor, our cut point diameters for this
% gas and this particle material are:
dG1 = 0.268;
dG2 = 0.163;
x = pMetal*4*(mQ1/60)/(9*mu*pi*0.83^2);
y = 2*(lambda*10^-4)*alpha;
particleCut1 = (-x*y+(x^2*y^2+4*x*dG1^3)^(1/2))/(2*x)*10^4;
particleCut2 = (-x*y+(x^2*y^2+4*x*dG2^3)^(1/2))/(2*x)*10^4;
disp(['If you use Gleason's virtual impactor for this gas '...
      'and this metal']);
disp(['Your cut point diameters will be ',num2str(particleCut1),...
      ' microns and ',num2str(particleCut2),' microns']);

```


Index

- $\gamma > 1$, 10
- $\gamma \gg 1$, 11
- $\gamma \ll 1$, 8
- 5-Pass Amplifier*, 86
- 6-Pass Amplifier*, 83

- Ablation Cell*, 145, 148
- Abstract, viii
- Acknowledgments*, v
- Aligning the Compressor*, 102
- Appendices*, 291
- Appendix
 - Calculation of Flows and Microparticle Diameters*, 345
 - Far Field Analysis of the Astigmatic Beam Out of the THOR Compressor*, 292
 - SOP for LAM Nanoparticle Generator*, 311

- Benefits and Drawbacks of OPCPA*, 72
- Bibliography*, 367

- Cascaded Virtual Impactor Assembly*, 140
- Cluster Dissociation*, 44, 284
- Cluster Gas Jet*, 148
- Cluster Peak Kinetic Energies*, 227
- Cluster Theory*, 25
- Collisions in a Plasma*, 16
- commands
 - environments
 - table, 41, 44, 48, 49, 142, 190
- Compression*, 92
- Conclusions*, 273
- Conduction Bands and Solid State Phenomena*, 41
- Continuum Lowering in High-Density Plasmas*, 27
- Continuum Lowering*, 283
- Coulomb Collisions*, 17
- Coulomb Explosion*, 44

- Debye Shielding*, 13
- Dedication*, iv
- Detection of High Ion Charge States*, 195

- Ecker Kröll Model*, 32
- Electron Kinetic Energy Profiles*, 245
- Enhanced Photon Absorption in Clusters*, 26
- Experimental Setup*, 123

- Fiber*, 62
- Formation of Condensed Gas Clusters*, 47
- Formation of Metal and Metal Oxide Clusters*, 50
- Future Work*, 290

- HHG Optimization*, 121
- High Charge States*, 275
- High Charge-to-Mass Ratio Resolution*, 191
- High Ion Charge States Independent of Cluster Size*, 200

High-Order Harmonic Generation, 109
Hydrodynamic Explosion, 46
Inelastic Collisions, 22
Inner and Outer Ionization, 37
Introduction, 1
Ion Kinetic Energy Profiles, 237
Ion Sphere Model, 28
Irradiation with Intense 800 nm Pulses, 161
Irradiation with XUV, 177
Keldysh Parameter, 7
LAM Setup, 138
Laser Ablation of Microparticles, 51
Laser-Matter Interaction, 6
Mechanism of Ionization, 278
Nanoparticles, 156
Nitrogen Clusters, 264
Noble Gas Clusters, 188
On-Target Beam Characteristics, 130
OPCPA, 66
Oscillator, 59
Oxygen-Containing Molecular Cluster Data, 156
Parametric Amplification, 66
Particle Bed, 139
Photoelectron Behavior, 288
Plasma Coupling, 15
Plasma Theory, 12
Results, 153
Second-Order Autocorrelator, 98
Sensitivity of Ion Charge States to Photon Energy, 212
Solid Targets, 274
Solid Targets Mounted on Glass, 178
Spectroscopic IPD, 35
Stewart Pyatt Model, 33
Stretcher, 60
The Design and Construction of THOR's OPCPA, 74
The Front End, 58
The THOR Compressor, 96
The THOR Laser, 55
Theory, 111
THOR HHG Beamline, 116
Ti:Sapph Multipass Amplifiers, 83
ToF Spectrometer, 134
Transform Limited Compression, 93
Virtual Impactors and Gas Flows, 51
XUV Focusing Mirrors, 129
XUV Target Chamber, 124

Bibliography

- [1] NIST Atomic Spectra Database.
- [2] Mathias Arbeiter and Thomas Fennel. Ionization heating in rare-gas clusters under intense XUV laser pulses. *Physical Review A - Atomic, Molecular, and Optical Physics*, 82(1):1–7, 2010.
- [3] Mathias Arbeiter and Thomas Fennel. Rare-gas clusters in intense VUV, XUV and soft x-ray pulses: Signatures of the transition from nanoplasma-driven cluster expansion to Coulomb explosion in ion and electron spectra. *New Journal of Physics*, 13, 2011.
- [4] Mathias Arbeiter, Christian Peltz, and Thomas Fennel. Electron-relocalization dynamics in xenon clusters in intense soft-x-ray fields. *Physical Review A - Atomic, Molecular, and Optical Physics*, 89(4), 2014.
- [5] Alexey V. Arefiev, Xiaohui Gao, Mikhail R. Tushentsov, Xiaoming Wang, Bonggu Shim, Boris N. Breizman, and Michael C. Downer. Size distribution and mass fraction of microclusters in laser-irradiated plasmas. *High Energy Density Physics*, 6(2):121–127, 2010.
- [6] Paul Christopher Arpin. *Generation and Characterization of Coherent Soft X-Ray Light with High Harmonic Generation*. PhD thesis, University of Colorado, 2011.

- [7] Durham University Atomic and Molecular Physics Group. Gaussian Beams and the Knife-Edge Measurement. [Online; accessed 3-June-2017].
- [8] Scott D Baalrud and Scott D Baalrud. Transport coefficients in strongly coupled plasmas Transport coefficients in strongly coupled plasmas. 030701, 2012.
- [9] Philippe Balcou, Pascal Salières, Anne L’Huillier, and Maciej Lewenstein. Generalized phase-matching conditions for high harmonics: The role of field-gradient forces. *Physical Review A*, 55(4):3204–3210, 1997.
- [10] A Baltuška, Th Udem, M Uiberacker, M Hentschel, E Goulielmakis, Ch Gohle, R Holzwarth, V S Yakovlev, A Scrinzi, T W Hänsch, and F Krausz. Attosecond control of electronic. *Nature*, 421(February), 2003.
- [11] P. S. Banks, M. D. Perry, V. Yanovsky, S. N. Fochs, B. C. Stuart, and J. Zweiback. Novel all-reflective stretcher for chirped-pulse amplification of ultrashort pulses. *IEEE Journal of Quantum Electronics*, 36(3):268–274, 2000.
- [12] Paul M Bellan. *Fundamentals of plasma physics*. Cambridge University Press, 2008.
- [13] Robert E. Benfield. Mean Coordination Numbers and the Nonmetal Metal Transition in Clusters. *Journal of the Chemical Society-Faraday*

- Transactions*, 88(8):1107–1110, 1992.
- [14] C. Bostedt, H. Thomas, M. Hoener, E. Eremina, T. Fennel, K. H. Meiwes-Broer, H. Wabnitz, M. Kuhlmann, E. Plönjes, K. Tiedtke, R. Treusch, J. Feldhaus, A. R B De Castro, and T. Möller. Multistep ionization of argon clusters in intense femtosecond extreme ultraviolet pulses. *Physical Review Letters*, 100(13):12–14, 2008.
- [15] Robert W. Boyd. *Nonlinear Optics, Third Edition*. Academic Press, 3rd edition, 2008.
- [16] Udo Buck and Reinhard Krohne. Cluster size determination from diffractive He atom scattering. *The Journal of Chemical Physics*, 105(13):5408–5415, 1996.
- [17] J D Callen. Coulomb Collisions. In *Fundamentals of Plasma Physics*. 2006.
- [18] B. T. Chen and H. C. Yeh. An improved virtual impactor: Design and performance. *Journal of Aerosol Science*, 18(2):203–214, 1987.
- [19] Ivan P. Christov, Margaret M. Murnane, and Henry C. Kapteyn. High-Harmonic Generation of Attosecond Pulses in the Single-Cycle Regime. *Physical Review Letters*, 78(7):1251–1254, 1997.
- [20] P. B. Corkum. Plasma Perspective on Strong-Field Multiphoton Ionization. *Physical Review Letters*, 71(13):1994–1997, 1993.

- [21] B. J B Crowley. Continuum lowering - A new perspective. *High Energy Density Physics*, 13:84–102, 2014.
- [22] T Ditmire. Simulations of heating and electron energy distributions in optical field ionized plasmas. *Physical Review E*, 54(6):6735–6740, 1996.
- [23] T. Ditmire, T. Donnelly, A. M. Rubenchik, R. W. Falcone, and M. D. Perry. Interaction of intense laser pulses with atomic clusters. *Physical Review A*, 53(5):3379–3402, 1996.
- [24] T. Ditmire, E. T. Gumbrell, R. a. Smith, a. Djaoui, and M. H. R. Hutchinson. Time-Resolved Study of Nonlocal Electron Heat Transport in High Temperature Plasmas. *Physical Review Letters*, 80:720–723, 1998.
- [25] T Ditmire, E T Gumbrell, R a Smith, J W G Tisch, D D Meyerhofer, and M H R Hutchinson. Spatial Coherence Measurement of Soft X-Ray Radiation Produced by High Order Harmonic Generation. *Physical Review Letters*, 77(23):4756 – 4759, 1996.
- [26] T. Ditmire, K. Kulander, J. K. Crane, H. Nguyen, and M. D. Perry. Calculation and measurement of high-order harmonic energy yields in helium. *Journal of the Optical Society of America B*, 13(2):406, 1996.
- [27] T. Ditmire, E. Springate, J. W. G. Tisch, Y. L. Shao, M. B. Mason, N. Hay, J. P. Marangos, and M. H. R. Hutchinson. Explosion of atomic

- clusters heated by high-intensity femtosecond laser pulses. *Physical Review A*, 57(1):369–382, 1998.
- [28] T. Ditmire, J. W. G. Tisch, E. Springate, M. B. Mason, N. Hay, J. P. Marangos, and M. H. R. Hutchinson. High Energy Ion Explosion of Atomic Clusters: Transition from Molecular to Plasma Behavior. *Physical Review Letters*, 78(14):2732–2735, 1997.
- [29] F. Dorchies, F. Blasco, T. Caillaud, J. Stevefelt, C. Stenz, A. S. Boldarev, and V. A. Gasilov. Spatial distribution of cluster size and density in supersonic jets as targets for intense laser pulses. *Physical Review A*, 68(2):023201, 2003.
- [30] M Drescher, M Hentschel, R Kienberger, M Uiberacker, V Yakovlev, a Scrinzi, Th Westerwalbesloh, U Kleineberg, U Heinzmann, and F Krausz. Time-resolved atomic inner-shell spectroscopy. *Nature*, 419(6909):803–807, 2002.
- [31] Gilliss McNaughton Dyer. *Experimental Study of the Equation of State of Isochorically Heated Warm Dense Matter*. PhD thesis, The University of Texas at Austin, 2007.
- [32] G. Ecker and W. Kröll. Lowering of the Ionization Energy for a Plasma in Thermodynamic Equilibrium. *The Physics of Fluids*, 6(62):62–69, 1963.

- [33] Martin Eckstein, Chung Hsin Yang, Markus Kubin, Fabio Frassetto, Luca Poletto, Hans Hermann Ritze, Marc J J Vrakking, and Oleg Kornilov. Dynamics of N₂ dissociation upon inner-valence ionization by wavelength-selected XUV pulses. *Journal of Physical Chemistry Letters*, 6(3):419–425, 2015.
- [34] Nathan William Erickson, John Keto, and Michael Becker. *Size Distributions and Nonlinear Optical Enhancement of Silver Nanoparticles Produced by LAM*. PhD thesis, The University of Texas at Austin, 2011.
- [35] B. Erk, K. Hoffmann, N. Kandadai, A. Helal, J. Keto, and T. Ditmire. Observation of shells in coulomb explosions of rare-gas clusters. *Physical Review A - Atomic, Molecular, and Optical Physics*, 83(4):1–5, 2011.
- [36] J. Farges, M. F. de Feraudy, B. Raoult, and G. Torchet. Noncrystalline structure of argon clusters. II. Multilayer icosahedral structure of Ar_N clusters 50 < N < 750. *The Journal of Chemical Physics*, 84(6):3491, 1986.
- [37] Simin Feng and Herbert G. Winful. Physical origin of the Gouy phase shift. *Optics Letters*, 26(8):485, 2001.
- [38] Thomas Fennel, Lora Ramunno, and Thomas Brabec. Highly charged ions from laser-cluster interactions: Local-field-enhanced impact ionization and frustrated electron-ion recombination. *Physical Review Letters*, 99(23):1–4, 2007.

- [39] David N Fittinghoff, Barry C Walker, Jeff A Squier, S T Csaba, Christoph Rose-petruck, and Christopher P J Barty. Dispersion Considerations in Ultrafast CPA Systems. 4(2):430–440, 1998.
- [40] Paul Gibbon. *Short pulse laser interactions with matter*. World Scientific Publishing Company, 2004.
- [41] Kristofer L Gleason. *Engineering Nanocomposite Polymer Membranes for Olefin / Paraffin Separation*. PhD thesis, The University of Texas at Austin, 2011.
- [42] Will Robert Grigsby. *Experimental Studies of High Energy Density Silicon Using Ultra-Fast Lasers*. PhD thesis, The University of Texas at Austin, 2007.
- [43] O. F. Hagen. Cluster Formation in Expanding Supersonic Jets: Effect of Pressure, Temperature, Nozzle Size, and Test Gas. *The Journal of Chemical Physics*, 56(5):1793, 1972.
- [44] O. F. Hagen. Condensation in free jets: Comparison of rare gases and metals. *Zeitschrift für Physik D Atoms, Molecules and Clusters*, 4(3):291–299, 1987.
- [45] Otto F. Hagen. Cluster ion sources (invited). *Review of Scientific Instruments*, 63(4):2374–2379, 1992.

- [46] Ahmed Mohammed Helal. *Explosion Dynamics of van der Waals Clusters Using 38 nm XUV Laser Pulses*. PhD thesis, The University of Texas at Austin, 2016.
- [47] D. G. Henshaw. Atomic distribution in liquid and solid neon and solid argon by neutron diffraction. *Physical Review*, 111(6):1470–1475, 1958.
- [48] Oliver Hilt and Werner F. Schmidt. Positive hole mobility in liquid xenon. *Chemical Physics*, 183(1):147 – 153, 1994.
- [49] M. Hirokane, S. Shimizu, M. Hashida, S. Okada, S. Okihara, F. Sato, T. Iida, and S. Sakabe. Energy distributions of ions emitted from argon clusters Coulomb-exploded by intense femtosecond laser pulses. *Physical Review A - Atomic, Molecular, and Optical Physics*, 69(6):12–15, 2004.
- [50] Matthias Hoener, Christoph Bostedt, H. Thomas, L. Landt, E. Eremina, H. Wabnitz, T. Laarmann, R. Treusch, A. R. B. De Castro, and Thomas Möller. Charge recombination in soft x-ray laser produced nanoplasmas. *Journal of Physics B: Atomic, Molecular and Optical Physics*, 41(18):181001, 2008.
- [51] K. Hoffmann, B. Murphy, B. Erk, A. Helal, N. Kandadai, J. Keto, and T. Ditmire. High intensity femtosecond XUV pulse interactions with atomic clusters. *High Energy Density Physics*, 6(2):185–189, 2010.
- [52] K. Hoffmann, B. Murphy, N. Kandadai, B. Erk, A. Helal, J. Keto, and T. Ditmire. Rare-gas-cluster explosions under irradiation by intense

- short XUV pulses. *Physical Review A - Atomic, Molecular, and Optical Physics*, 83(4):1–9, 2011.
- [53] Christian Jungreuthmayer, Lora Ramunno, Jürgen Zanghellini, and Thomas Brabec. Intense VUV laser cluster interaction in the strong coupling regime. *Journal of Physics B: Atomic, Molecular and Optical Physics*, 38:3029–3036, 2005.
- [54] I. V. Khyzhniy, O. N. Grigorashchenko, E. V. Savchenko, A. N. Ponomaryov, and V. E. Bondybey. Thermally stimulated exoelectron emission from solid Xe. *Low Temperature Physics*, 33(6):529–531, 2007.
- [55] C. Kittel. *Introduction to solid state physics*. Wiley, 1976.
- [56] Ferenc Krausz and Misha Ivanov. Attosecond physics. *Reviews of Modern Physics*, 81(1):163–234, 2009.
- [57] P. Kruit, J. Kimman, H. G. Muller, and M. J. Van Der Wiel. Electron spectra from multiphoton ionization of xenon at 1064, 532, and 355 nm. *Physical Review A*, 28(1):248–255, 1983.
- [58] Jon Larsen. *Foundations of High-Energy-Density Physics: Physical Processes of Matter at Extreme Conditions*. Cambridge University Press, 2017.
- [59] Isidore Last and Joshua Jortner. Dynamics of the Coulomb explosion of large clusters in a strong laser field. *Physical Review A*, 62(November 1999):1–9, 2000.

- [60] Jaemyoung Lee, Michael F. Becker, and John W. Keto. Dynamics of laser ablation of microparticles prior to nanoparticle generation. *Journal of Applied Physics*, 89(12):8146–8152, 2001.
- [61] Stephen R. Leone, C. William McCurdy, Joachim Burgdörfer, Lorenz S. Cederbaum, Zenghu Chang, Nirit Dudovich, Johannes Feist, Chris H. Greene, Misha Ivanov, Reinhard Kienberger, Ursula Keller, Matthias F. Kling, Zhi-Heng Loh, Thomas Pfeifer, Adrian N. Pfeiffer, Robin Santra, Kenneth Schafer, Albert Stolow, Uwe Thumm, and Marc J. J. Vrakking. What will it take to observe processes in ‘real time’? *Nature Photonics*, 8(3):162–166, 2014.
- [62] Matthew Warren McCormick. *Study of Picosecond-Scale Electron Dynamics in Laser-Produced Plasmas with and without an External Magnetic Field*. PhD thesis, The University of Texas at Austin, 2013.
- [63] A. McPherson, G. Gibson, H. Jara, U. Johann, T. S. Luk, I. A. McIntyre, K. Boyer, and C. K. Rhodes. Studies of multiphoton production of vacuum-ultraviolet radiation in the rare gases. *Journal of the Optical Society of America B*, 4(4):595, 1987.
- [64] H. M. Milchberg, S. J. McNaught, and E. Parra. Plasma hydrodynamics of the intense laser-cluster interaction. *Physical Review E*, 64(5 Pt 2):056402, 2001.
- [65] M Müller, L Schroedter, T Oelze, L Nösel, A Przystawik, A Kicker-
mann, M Adolph, T Gorkhover, L Flückiger, M Krikunova, M Sauppe,

- Y Ovcharenko, S Schorb, C Bostedt, D Rupp, T Laarmann, and T Möller. Ionization dynamics of XUV excited clusters: the role of inelastic electron collisions. *Journal of Physics B: Atomic, Molecular and Optical Physics*, 48(17):174002, 2015.
- [66] Margaret M. Murnane, Henry C. Kapteyn, Mordecai D. Rosen, and Roger W. Falcone. Ultrafast x-ray pulses from laser-produced plasmas. *Science*, 251(4993):531–536, 1991.
- [67] B F Murphy, K Hoffmann, A Belolipetski, J Keto, and T Ditmire. Explosion of Xenon Clusters Driven by Intense Femtosecond Pulses of Extreme Ultraviolet Light. 203401(November):1–4, 2008.
- [68] Brendan Francis Murphy. *Dynamics of noble gas cluster expansion driven by intense pulses of extreme ultraviolet light*. PhD thesis, The University of Texas at Austin, 2009.
- [69] R Neutze, R Wouts, D van der Spoel, E Weckert, and J Hajdu. Potential for biomolecular imaging with femtosecond X-ray pulses. *Nature*, 406(6797):752–757, 2000.
- [70] W. T. Nichols, J. W. Keto, D. E. Henneke, J. R. Brock, G. Malayanatham, M. F. Becker, and H. D. Glicksman. Large-scale production of nanocrystals by laser ablation of microparticles in a flowing aerosol. *Applied Physics Letters*, 78(8):1128–1130, 2001.

- [71] William T. Nichols. *Production and Controlled Collection of Nanoparticles: Toward Manufacturing of Nanostructured Materials*. PhD thesis, The University of Texas at Austin, 2002.
- [72] William T. Nichols, Gokul Malyavanatham, Dale E. Henneke, James R. Brock, Michael F. Becker, John W. Keto, and Howard D. Glicksman. Gas and Pressure Dependence for the Mean Size of Nanoparticles Produced by Laser Ablation of Flowing Aerosols. *Journal of Nanoparticle Research*, 2(2):141–145, 2000.
- [73] William T. Nichols, Gokul Malyavanatham, Dale E. Henneke, Daniel T. O’Brien, Michael F. Becker, and John W. Keto. Bimodal nanoparticle size distributions produced by laser ablation of microparticles in aerosols. *Journal of Nanoparticle Research*, 4(5):423–432, 2002.
- [74] J Peatross, J L Chaloupka, and D D Meyerhofer. High-order harmonic generation with an annular laser beam. 19(13):942–944, 1994.
- [75] Tenio Popmintchev, Ming-Chang Chen, Paul Arpin, Margaret M. Murnane, and Henry C. Kapteyn. The attosecond nonlinear optics of bright coherent X-ray generation. *Nature Photonics*, 4(12):822–832, 2010.
- [76] Daniela Rupp. *Ionization and Plasma Dynamics of Single Large Xenon Clusters in Superintense XUV Pulses*. 2016.
- [77] Ulf Saalmann and Jan-Michael Rost. Ionization of Clusters in Intense Laser Pulses through Collective Electron Dynamics. *Physical review*

- letters*, 91(22):223401, 2003.
- [78] James A. R. Samson, T. Masuoka, P. N. Pareek, and G. C. Angel. Total and dissociative photoionization cross sections of N_2 from threshold to 107 eV. *The Journal of Chemical Physics*, 86(11):6128–6132, 1987.
- [79] J.A.R. Samson and W.C. Stolte. Precision measurements of the total photoionization cross-sections of He, Ne, Ar, Kr, and Xe. *Journal of Electron Spectroscopy and Related Phenomena*, 123(2-3):265–276, 2002.
- [80] Robin Santra and Chris H. Greene. Xenon clusters in intense VUV laser fields. *Physical review letters*, 91(23):233401, 2003.
- [81] Werner F. Schmidt and E. Illenberger. *Electronic excitations in liquefied rare gases*. American Scientific Publishers, Stevenson Ranch, Calif, 2005.
- [82] L. Schroedter, M. Müller, A. Kickermann, A. Przystawik, S. Toleikis, M. Adolph, L. Flückiger, T. Gorkhover, L. Nösel, M. Krikunova, T. Oelze, Y. Ovcharenko, D. Rupp, M. Sauppe, D. Wolter, S. Schorb, C. Bostedt, T. Möller, and T. Laarmann. Hidden charge states in soft-x-ray laser-produced nanoplasmas revealed by fluorescence spectroscopy. *Physical Review Letters*, 112(18):1–5, 2014.
- [83] B. Schütte, M. Arbeiter, Th Fennel, M. J J Vrakking, and A. Rouzée. Rare-gas clusters in intense extreme-ultraviolet pulses from a high-order harmonic source. *Physical Review Letters*, 112(7):1–5, 2014.

- [84] M. Marvin Seibert, Tomas Ekeberg, Filipe R. N. C. Maia, Martin Svenda, Jakob Andreasson, Olof Jönsson, Duško Odić, Bianca Iwan, Andrea Rucker, Daniel Westphal, Max Hantke, Daniel P. DePonte, Anton Barty, Joachim Schulz, Lars Gumprecht, Nicola Coppola, Andrew Aquila, Mengning Liang, Thomas A. White, Andrew Martin, Carl Caleman, Stephan Stern, Chantal Abergel, Virginie Seltzer, Jean-Michel Claverie, Christoph Bostedt, John D. Bozek, Sébastien Boutet, A. Alan Miahnahri, Marc Messerschmidt, Jacek Krzywinski, Garth Williams, Keith O. Hodgson, Michael J. Bogan, Christina Y. Hampton, Raymond G. Sierra, Dmitri Starodub, Inger Andersson, Saša Bajt, Miriam Barthelmess, John C. H. Spence, Petra Fromme, Uwe Weierstall, Richard Kirian, Mark Hunter, R. Bruce Doak, Stefano Marchesini, Stefan P. Hau-Riege, Matthias Frank, Robert L. Shoeman, Lukas Lomb, Sascha W. Epp, Robert Hartmann, Daniel Rolles, Artem Rudenko, Carlo Schmidt, Lutz Foucar, Nils Kimmel, Peter Holl, Benedikt Rudek, Benjamin Erk, André Hömke, Christian Reich, Daniel Pietschner, Georg Weidenspointner, Lothar Strüder, Günter Hauser, Hubert Gorke, Joachim Ullrich, Ilme Schlichting, Sven Herrmann, Gerhard Schaller, Florian Schopper, Heike Soltau, Kai-Uwe Kühnel, Robert Andritschke, Claus-Dieter Schröter, Faton Krasniqi, Mario Bott, Sebastian Schorb, Daniela Rupp, Marcus Adolph, Tais Gorkhover, Helmut Hirsemann, Guillaume Potdevin, Heinz Graafsma, Björn Nilsson, Henry N. Chapman, and Janos Hajdu. Single mimivirus particles intercepted and imaged with an X-ray laser. *Nature*, 470(7332):78–

81, 2011.

- [85] Y L Shao, T Ditmire, J W G Tisch, E Springate, J P Marangos, and M H R Hutchinson. Multi-keV Electron Generation in the Interaction of Intense Laser Pulses with Xe Clusters. *Physical Review Letters*, 77(16):3343–3346, 1996.
- [86] Christian Siedschlag and Jan Michael Rost. Small rare-gas clusters in soft x-ray pulses. *Physical Review Letters*, 93(4):043402–1, 2004.
- [87] Igor I Smolyaninov. Electrons on Solid Hydrogen and Solid Neon Surfaces. *International Journal of Modern Physics B*, 15(15):2075, 2001.
- [88] KS Song and Richard T Williams. *Self-trapped excitons*, volume 105. Springer Science & Business Media, 2013.
- [89] John C. Stewart and Kedar D. Pyatt, Jr. Lowering of Ionization Potentials in Plasmas. *Astrophysical Journal*, 144:1203, 1966.
- [90] Donna Strickland and Gerard Mourou. Compression of amplified chirped optical pulses. *Optics Communications*, 56(3):219–221, 1985.
- [91] A. Sugishima, H. Iwayama, S. Yase, H. Murakami, K. Nagaya, M. Yao, H. Fukuzawa, X. J. Liu, K. Motomura, K. Ueda, N. Saito, L. Foucar, A. Rudenko, M. Kurka, K. U. Kühnel, J. Ullrich, A. Czasch, R. Dörner, R. Feifel, M. Nagasono, A. Higashiya, M. Yabashi, T. Ishikawa, T. Togashi, H. Kimura, and H. Ohashi. Charge and energy transfer in argon-core-neon-shell clusters irradiated by free-electron-laser pulses at 62 nm.

- Physical Review A - Atomic, Molecular, and Optical Physics*, 86(3):1–6, 2012.
- [92] Czeslaw Szmytkowski, Krzysztof Maciąg, and Grzegorz Karwasz. Absolute Electron-Scattering Total Cross Section Measurements for Noble Gas Atoms and Diatomic Molecules. 54:271–280, 1996.
- [93] Franz Tavella. *Multiterawatt few-cycle pulse OPCPA*. PhD thesis, Ludwig Maximilian University of Munich, 2007.
- [94] M. Tchapyguine, R. R. Marinho, M. Gisselbrecht, J. Schulz, N. Mårtensson, S. L. Sorensen, A. Naves de Brito, R. Feifel, G. Öhrwall, M. Lundwall, S. Svensson, and O. Björneholm. The size of neutral free clusters as manifested in the relative bulk-to-surface intensity in core level photoelectron spectroscopy. *Journal of Chemical Physics*, 120(1):345–356, 2004.
- [95] H Thomas, C Bostedt, M Hoener, E Eremina, H Wabnitz, T Laarmann, E Plönjes, R Treusch, a R B de Castro, and T Möller. Shell explosion and core expansion of xenon clusters irradiated with intense femtosecond soft x-ray pulses. *Journal of Physics B: Atomic, Molecular and Optical Physics*, 42(13):134018, 2009.
- [96] H Wabnitz, L Bittner, a R B de Castro, R Döhrmann, P Gürtler, T Laarmann, W Laasch, J Schulz, A Swiderski, K von Haefen, T Möller, B Faatz, A Fateev, J Feldhaus, C Gerth, U Hahn, E Saldin, E Schneidmiller, K Sytchev, K Tiedtke, R Treusch, and M Yurkov. Multiple

- ionization of atom clusters by intense soft X-rays from a free-electron laser. *Nature*, 420(6915):482–5, 2002.
- [97] Zachary B. Walters, Robin Santra, and Chris H. Greene. Interaction of intense vuv radiation with large xenon clusters. *Physical Review A - Atomic, Molecular, and Optical Physics*, 74(4):1–14, 2006.
- [98] J B West. Photoionization cross sections of atomic ions. *Journal of Electron Spectroscopy and Related Phenomena*, 123:247–256, 2002.
- [99] W. C. Wiley and I. H. McLaren. Time-of-flight mass spectrometer with improved resolution. *Review of Scientific Instruments*, 26(12):1150–1157, 1955.
- [100] B. Ziaja, T. Laarmann, H. Wabnitz, F. Wang, E. Weckert, C. Bostedt, and T. Möller. Emission of electrons from rare gas clusters after irradiation with intense VUV pulses of wavelength 100 nm and 32 nm. *New Journal of Physics*, 11, 2009.
- [101] B Ziaja, H Wabnitz, E Weckert, and T Möller. Femtosecond non-equilibrium dynamics of clusters irradiated with short intense VUV pulses. *New Journal of Physics*, 10, 2008.
- [102] B. Ziaja, F. Wang, H. Wabnitz, E. Weckert, and T. Möller. Ionization and expansion dynamics of atomic clusters irradiated with short intense VUV pulses. *AIP Conference Proceedings*, 1161:105–112, 2009.

- [103] Beata Ziaja, Zoltan Jurek, Nikita Medvedev, Sang-Kil Son, Robert Thiele, and Sven Toleikis. Photoelectron spectroscopy method to reveal ionization potential lowering in nanoplasmas. *Journal of Physics B: Atomic, Molecular and Optical Physics*, 46:164009, 2013.

Vita

Sandra Allison Bruce was born in Baltimore, Maryland on 5 October 1986, the daughter of Robert J. Bruce and Morita C. Bruce. She graduated from Harvey Mudd College with a Bachelor of Science degree in Physics (with Distinction) in 2008. After graduation, she accepted a position as a Scientist at Southwest Research Institute, Applied Physics Division, Department of Engineering Applications and Systems Development, in San Antonio, Texas, eventually rising to the position of Research Scientist. After three years at SwRI, she chose to further her formal education. She began her graduate studies in August of 2011, in the Department of Physics, Center for High Energy Density Science, at The University of Texas at Austin.

Permanent address: 4505 Duval St.
Austin, Texas 78751

This dissertation was typeset with L^AT_EX[†] by the author.

[†]L^AT_EX is a document preparation system developed by Leslie Lamport as a special version of Donald Knuth's T_EX Program.